A high-magnification electron micrograph of cytoskeletal filaments, likely microtubules, showing their characteristic hollow tubular structure and periodic lattice. The filaments are arranged in a complex, overlapping network, with some appearing as parallel bundles and others as individual strands. The image is rendered in a monochromatic teal and light blue color scheme, highlighting the intricate details of the filamentous structures.

STATISTICAL MECHANICS OF CYTOSKELETAL FILAMENTS

HARMEN WIERENGA

**STATISTICAL MECHANICS OF CYTOSKELETAL
FILAMENTS**

HARMEN WIERENGA

This thesis was reviewed by:

prof.dr. L.C. Kapitein	Universiteit Utrecht
prof.dr. G.H. Koenderink	Technische Universiteit Delft
prof.dr.ir. E.J.G. Peterman	Vrije Universiteit Amsterdam
dr. C.P. Broedersz	Vrije Universiteit Amsterdam
dr. Z. Lánský	Institute of Biotechnology CAS, Prague
dr. F.J. Nédélec	University of Cambridge



The work described in this thesis was performed at AMOLF, Science Park 104, 1098 XG Amsterdam, The Netherlands, part of the Dutch Research Council (NWO). This work was part of the research performed at the Technische Universiteit Delft, Faculty of Applied Sciences, Department of Bionanoscience, Marileen Dogterom group, and it was supported by European Research Council (ERC) Synergy Grant 609822. Financial support from the TU Delft for the printing of this thesis is gratefully acknowledged.

© H. Wierenga, 2021

Cover image: Karolina Grabowska
Printed by: Ipskamp Printing, Enschede

ISBN 978-94-92323-52-1

A digital version of this thesis is available online at www.ub.vu.nl and ir.amolf.nl.
Printed copies can be obtained by request via library@amolf.nl.

VRIJE UNIVERSITEIT

**STATISTICAL MECHANICS OF CYTOSKELETAL
FILAMENTS**

ACADEMISCH PROEFSCHRIFT

ter verkrijging van de graad Doctor
aan de Vrije Universiteit Amsterdam,
op gezag van de rector magnificus
prof.dr. V. Subramaniam,
in het openbaar te verdedigen
ten overstaan van de promotiecommissie
van de Faculteit der Bètawetenschappen
op maandag 17 mei 2021 om 11.45 uur
in de aula van de universiteit,
De Boelelaan 1105

door

Harmen Wierenga

geboren te Zutphen

promotor: prof.dr. P.R. ten Wolde
copromotor: prof.dr. A.M. Dogterom

PREFACE

All eukaryotic cells contain a structure called the cytoskeleton, which is a collection of filamentous networks that consist of microtubules, actin filaments, and intermediate filaments. At the molecular level, the filaments are made up of protein polymers, and the filaments interconnect via other proteins to form functional networks. Cytoskeletal structures are important for cell stability, sustaining the cellular shape, and providing resilience against external forces. The cytoskeleton also plays a key role in cell signalling by transmitting mechanical forces, trafficking lipid vesicles and signalling proteins, and providing binding scaffolds at specific sites [1, 2]. Furthermore, the filaments provide tracks for motor proteins, which can transport cargo through the cell, and even lead to the large scale contraction of muscles [3].

The cytoskeleton is not a static network, because the filaments that constitute it continuously grow or shrink at one or both ends. Combined with the action of motor proteins, this allows cytoskeletal networks to contract and remodel, driving the movement of cells [4]. The cytoskeleton also plays an important role in controlling cell division. The signalling functions of the cytoskeleton influence the location of the cell division plane and the polarisation of the dividing cell [5–7]. Moreover, cytoskeletal structures mechanically perform the division itself. Microtubules form the mitotic spindle that drives chromosome segregation and cytokinesis [8, 9], and actin filaments form the cytokinetic ring that cleaves the cell [10].

Cytoskeletal filaments have a diameter in the order of nanometres, but can grow up to several micrometres in length [11–14]. Intermediate filaments are the most flexible with thermal persistence lengths of up to $1\ \mu\text{m}$, actin filaments are less flexible with a thermal persistence length of roughly $10\ \mu\text{m}$, and microtubules form stiff hollow tubes with a thermal persistence length of more than $1\ \text{mm}$ [15]. These filaments occur at a length scale where thermal fluctuations influence all dynamics, not only stochastically bending the filaments, but also causing friction forces and diffusive motion. In general, the dynamics of the filaments can be driven by the ATP hydrolysis of motor proteins or by the ATP or GTP hydrolysis occurring in the growth dynamics of the filaments themselves [16], leading to a non-equilibrium dynamics for these filaments.

The extent to which equilibrium thermodynamics fails in biological non-equilibrium systems is often mitigated by several conditions, providing general techniques to describe these systems. First, we see that even though cytoskeletal filaments are only nanometres in thickness, they constantly collide with water molecules and other components of the cytosol on very short time scales. Hence, their mechanical movement and chemical modification reactions are often memoryless on the time scales of interest. We can describe such continuous memoryless processes using a Fokker-Planck equation, which describes diffusion and drift. Furthermore, discrete memoryless processes such as chemical reactions can be described using Markov chains. In recent years, a framework called stochastic thermodynamics has been developed to find a general descrip-

tion for non-equilibrium systems [17]. Hence, we can use tools provided by statistical mechanics to characterise the movement and function of cytoskeletal filaments.

The movement of cytoskeletal filaments is influenced by their growth dynamics, by motor proteins, but also by passive cross-linkers. These cross-linkers interconnect filaments to create networks or bundles, but the filaments can still move when the cross-linkers diffuse on the filaments or unbind stochastically. When two filaments overlap partially and are bound by a fixed number of diffusing cross-linkers, these cross-linkers cause an entropic force that expands the overlap between the filaments [18]. Additionally, the cross-linkers generate a condensation force when the cross-linkers can bind to and unbind from the overlap. Hence, passive cross-linkers can generate driving forces in addition to the driving forces generated by motor proteins that use chemical fuel to do work. Simultaneously, the cross-linkers that drive the motion of the filaments also cause an opposing friction force between the filaments. In this thesis, we will study the interplay between these different cross-linker generated forces. We will derive an expression for the friction coefficient between two filaments that are connected by cross-linkers, taking into account the discrete nature of the cross-linker binding sites arising from the protein lattices that make up cytoskeletal filaments. Further, we use methods from statistical mechanics to study the interplay between the friction forces and entropic or condensation forces that are all generated by the passive cross-linkers.

Finally, we will also study a minimal model of cell polarisation based on a combination of active transport and membrane-cytosol protein shuttling. This mechanism is used in various biological systems, such as the Pom1/Tea1/Tea4 system in fission yeast and the Cdc42 system in budding yeast [19, 20]. In this mechanism, proteins are transported actively along filaments from the cytoplasm to the membrane. There, these proteins bind to the membrane or drive the binding of other proteins to the membrane close to the end of the filament. The proteins that are bound to the membrane diffuse away from their site of delivery, after which they will dissociate back into the cytoplasm, creating a finite high density spot on the membrane that polarises the cell. Cell polarisation is a symmetry breaking transition that requires energy input, and interestingly, these systems are driven out of equilibrium in two ways. The active transport of the proteins requires the turnover of fuel, but in addition the proteins can undergo an activation-deactivation cycle, which is driven by nucleotide hydrolysis. We can use a memoryless description of the transport and binding reactions to quantify the free-energy costs of this cell polarisation, and compare which mechanism is the most efficient at creating a polarised protein distribution on the membrane. Hence, statistical mechanics is an instrument that can provide novel and interesting insights into the movement and functioning of cytoskeletal filaments, and the theoretical predictions it provides can be tested by experiments.

In chapter 1, we summarise and derive the concepts from statistical mechanics that we use in this thesis. Specifically, we discuss equilibrium mechanics, the Fokker-Planck equation, and how to predict the rates of rare events that are caused by the crossing of a free-energy barrier. Then, we apply these techniques to the movement of two cross-linked cytoskeletal filaments in chapter 2. It has been observed that the friction between microtubules that are connected by diffusible cross-linkers increases exponentially with the number of cross-linkers, and we investigate the mechanism behind this exponential

increase. We find that the relative movement of the filaments occurs via discrete steps that are caused by free-energy barriers, leading to experimentally testable predictions on how the friction coefficient between the filament scales with the density of cross-linkers. In chapter 3, we show that Kramers theory, which calculates the rates at which the filaments jump over the free-energy barriers, breaks down in the model presented in chapter 2. We review each assumption of Kramers theory and discuss why this breakdown occurs. Then, in chapter 4 we examine how entropic and condensation forces depend on the number and density of cross-linkers, and how the interplay between these forces and the exponentially increasing friction coefficient shapes the movement of the filaments. The predicted trajectories of the filaments can be compared to experimental data to test our prediction that the friction scales exponentially with the number of cross-linkers. In this chapter we also study the effect of cooperative interactions between the passive cross-linkers and of multiple protofilaments taking part in the binding of these cross-linkers. In chapter 5 we show how actin filaments can be transported by growing microtubules and passive cross-linkers that connect the actin filaments with the tips of the growing microtubules. The actin filament tracks the moving microtubule tip via a condensation force, which tends to maximize the overlap between the actin filament and the chemically distinct tip region of the microtubule, but this transport is opposed by friction forces caused by the cross-linkers. From this model, we predict how the average transport time of these actin filaments depends on the growth velocity of the microtubule and the length of the actin filament, and we test the predicted trends experimentally. Finally, inspired by the Pom1 and Cdc42 systems, we investigate in chapter 6 if a protein distribution on the membrane can be polarised by the transport of the proteins along filaments that point towards a spot on the membrane. Using a minimal model, we find that polarisation requires detailed balance to be broken either by motor proteins that carry the proteins to the membrane or by a chemical modification of the proteins driving a flux from the filament to the membrane. We compare these two mechanisms by quantifying the amount of free energy that is dissipated by each, showing that the processes are not equally efficient in creating a dense protein spot on the membrane.

CONTENTS

1	Thermodynamics and stochastic processes	1
1.1	Equilibrium distribution	2
1.1.1	Boltzmann distribution from explicit bath description	4
1.2	Local detailed balance	6
1.3	Fokker-Planck equation from master equation	8
1.3.1	Comparison with general derivation	11
1.4	Kolmogorov backward equation	12
1.5	Kramers rate theory	14
2	Diffusible cross-linkers cause superexponential friction forces	17
2.1	Model.	19
2.2	Barrier crossings cause microtubule jumps	20
2.3	Jump rate decreases superexponentially	23
2.4	Discussion	25
2.A	Estimate of spring constant revisited	27
2.B	Simulation dynamics	29
2.C	Microtubule jump rate sets the diffusion constant	31
2.D	Deviations from the Einstein relation	39
2.E	Configuration combinatorics for entropy calculation	41
2.F	Numerical confirmation of free-energy equation	44
2.G	Determination of reaction coordinate.	44
2.H	Microtubule jump rate follows Arrhenius' law.	49
2.I	Exponential approximation of free-energy barrier	49
2.J	Overlap length range for observing superexponential friction.	56
2.K	Cooperative interactions increase friction.	58
3	Breakdown of simple diffusion impairs Kramers theory	61
3.1	Microtubule jump rates from Kramers theory.	62
3.2	The short-time effective diffusion constant	63
3.3	Prefactor of the filament jump rate	67
3.4	Discussion	78
4	Condensation forces and entropic forces on overlapping microtubules	81
4.1	Friction coefficient and entropic forces	82
4.2	Friction coefficient and condensation forces	88
4.3	Cooperative interactions reduce the entropic force	95
4.4	Cooperative interactions increase the condensation force	99
4.5	Effects of multiple protofilaments.	101
4.6	Discussion	104

5	Passive cross-linkers drive actin transport by growing microtubules	107
5.1	Growing Microtubules Plus Ends Can Transport Actin Filaments	109
5.2	Simulations Reproduce Microtubule-Mediated Actin Transport	111
5.3	The Actin Filament Displays Effective Diffusion and Drift.	113
5.4	Actin Transport Is A Meta-Stable State	115
5.5	Simulations and theory predict correct trends in transport times	117
5.6	Cross-linker Binding Creates A Significant condensation Force	121
5.7	Discussion	122
5.A	Protein Isolation and Preparation	125
5.B	Dynamic Microtubule Assay	125
5.C	Microscopy	126
5.D	Image and Data Analysis	126
5.E	Optical Tweezers	126
5.F	Microtubule catastrophes affect the transport time distribution	127
5.G	Details of the simulated model	129
5.H	Actin diffusion measurements	131
5.I	Simulation parameter value estimation	132
5.J	Analytical expression for condensation force	136
5.K	condensation force in the optical tweezer experiments	139
5.L	Binding probability scales exponentially with actin length	140
5.M	Kramers theory	140
5.N	Rate of actin unbinding	141
5.O	Algorithms	143
6	Energetic constraints on filament mediated membrane polarisation	159
6.1	Minimal model for membrane spot formation	161
6.2	Biologically relevant parameter values	171
6.3	A finite bulk diffusion constant is beneficial for cell polarisation	174
6.4	Free-energy is dissipated to form a membrane spot.	179
6.5	Driven binding kinetics is more efficient than motor transport	181
6.6	Discussion	184
6.A	Integration constants of analytical solutions	187
6.B	Reflecting boundary algorithms.	189
	references	193
	Summary	207
	Samenvatting	210
	Curriculum Vitæ	213
	List of Publications	214
	Acknowledgements	215

1

THERMODYNAMICS AND STOCHASTIC PROCESSES

We summarise several key concepts from statistical mechanics that are used in this thesis. We present a derivation of the Boltzmann distribution and the detailed balance condition, and generalise these relations to find the local detailed balance relation that defines free-energy differences in Markovian non-equilibrium systems. Then, we discuss that a memoryless continuous process can be described as a limiting case of a discrete system, providing derivations of the Fokker-Planck equation, the Kolmogorov backward equation, and the Einstein relation. Finally, we treat Kramers theory in the overdamped regime, which calculates the transition rates over free-energy barriers that separate different attractor regions, transforming a continuous Fokker-Planck description to a coarse-grained discrete Markov process.

Cytoskeletal filaments consist of protein polymers that have a diameter in the order of nanometres and that can grow to several micrometres in length. At these length scales, the dynamics of the filaments is strongly influenced by thermal fluctuations, and because they are embedded in the cytosol, their constant interaction with surrounding water molecules and biomolecules causes a friction force that brings them to the overdamped regime [21]. Therefore, we use statistical mechanics to describe the motion and reactions of cytoskeletal filaments. In this chapter, we discuss the derivations of several important concepts from statistical mechanics that will be used in the later chapters of this thesis.

We follow Jaynes [22] to find a derivation of the Boltzmann distribution, and we discuss how Maxwell [23] derived the detailed balance condition. Then, we show how thermodynamics can provide information on the dynamics of Markovian systems that are out of equilibrium via the local detailed balance relation, which is discussed for example by Maes et al. [24, 25]. These relations are true for Markov chains with a discrete state space, and we show that Markov processes with a continuous state space are governed by the Fokker-Planck equation [26, 27]. Starting from a continuous time Markov chain on a discrete regular lattice and taking the limit of a vanishing lattice spacing, the Fokker-Planck equation emerges when we scale the transition rates properly. Furthermore, this derivation shows that the continuous equivalent of the local detailed balance relation is the Einstein relation [28], which connects diffusion constants with friction coefficients. Related to the Fokker-Planck equation, we also discuss a derivation of the Kolmogorov backward equation [29]. Then, we end this chapter by following Kramers [30] to derive the Kramers theory of reaction rates. In summary, we start from a continuous overdamped diffusion process on a free-energy landscape containing different regions of attraction separated by barriers, which is described by a Fokker-Planck equation. This system can be coarse-grained into a continuous time Markov chain with rates that follow from the free energy and the diffusion constant. All these concepts are then used in the following chapters, where we discuss models for cytoskeletal systems that observe the rules set by statistical mechanics.

1.1. EQUILIBRIUM DISTRIBUTION

EQUILIBRIUM thermodynamics aims to describe the macroscopic behaviour of a system using a minimal set of parameters. To achieve this, all details about the dynamics of the system are ignored, such that the focus is on the equilibrium state. This is the steady state that the system relaxes to when it is left alone long enough. Equilibrium is important because the system becomes independent of the initial state. When we consider a system that is interacting with its environment in an arbitrary fashion, there is little we can assume about its time evolution. However, usually we know of the existence of some quantity that is conserved by the global (system+environment) dynamics, and that is shared between the system and environment. Energy can play this role in thermodynamic systems, and other examples can be the system volume or the number of particles.

To calculate the probability that we will find the system in a specific state, we have to take into account all information that we know, and acknowledge our ignorance about

all other degrees of freedom. In thermodynamics, our knowledge can consist of a set of possible states, their individual energies and degeneracies, and the first law which states that energy is a conserved quantity. The probability distribution over the states i with energies U_i and degeneracies g_i follows from the maximisation of the entropy, under the constraints set by our knowledge of the system [22]. In this case, that corresponds to maximising

$$\mathcal{L} = -k_B \sum_i p_i \log\left(\frac{p_i}{g_i}\right) - \lambda_1 \left(\sum_i p_i - 1\right) - \lambda_2 \left(\sum_i p_i U_i - E\right). \quad (1.1)$$

Here, λ_1 and λ_2 are the Lagrange multipliers for the constraints that certainty corresponds to unit probability and that the mean energy is fixed to E . The formula differs from that of Jaynes [22] by the degeneracy term g_i . This factor takes into account any prior information on the states. For example, you would take $g_i = 2$ and $g_j = 1$ if you knew that state i actually represents two equivalent distinguishable configurations with the same energy, and state j only represents one such configuration. In particular, if no prior knowledge besides the energies discriminates the different states i , g_i can be taken to be unity. The form of Eq. 1.1 follows from the information gained when measuring the system in state i , and with no prior knowledge, this equals $-\log(p_i)$. However, when it is known that state i is degenerate, there is an extra source of uncertainty and a measurement would possibly also reveal the specific subsystem. Therefore, the information gained from a measurement is increased to $-\log(p_i/g_i)$.

Why should we constrain the mean energy of the system to a fixed value? To investigate this question, we can first have a look at the entirety of system and bath. Imagine that the bath actually consists of some number of systems that is identical to the system we have been looking at. Further, we know the total energy that is shared between the subsystems. In this setup, the average energy per system equals the energy of the entirety divided by the number of subsystems. Then, if we bring our focus back to the single system, and describe the rest as a bath of unknown size, all that we can assume is that our system still has some average energy. This is a consequence of the extensiveness of energy, which means that doubling the system size generally also doubles the energy contained by the system. Sec. 1.1.1 also addresses this question in a more specific setting. In summary, fixing the mean energy of the system represents our knowledge that the bath shares its scarce energy with the system.

The maximum entropy principle leads us to maximising Eq. 1.1 over the space of probabilities and the Lagrange multipliers. First, we optimise with respect to p_i ,

$$\frac{\partial \mathcal{L}}{\partial p_i} = -k_B \left(1 + \log\left(\frac{p_i}{g_i}\right)\right) - \lambda_1 - \lambda_2 U_i = 0. \quad (1.2)$$

We solve this equation for p_i , after which the entropy function reduces to

$$\mathcal{L} = k_B \sum_i g_i \exp\left(-\frac{\lambda_1}{k_B} - \frac{\lambda_2 U_i}{k_B} - 1\right) + \lambda_1 + \lambda_2 E. \quad (1.3)$$

Then, we optimise over λ_1 ,

$$\frac{\partial \mathcal{L}}{\partial \lambda_1} = -\sum_i g_i \exp\left(-\frac{\lambda_1}{k_B} - \frac{\lambda_2 U_i}{k_B} - 1\right) + 1 = 0. \quad (1.4)$$

Combined, Eq. 1.2 and Eq. 1.4 set the relations

$$\exp\left(\frac{\lambda_1}{k_B} + 1\right) = \sum_i g_i \exp\left(-\frac{\lambda_2 U_i}{k_B}\right) \equiv \mathcal{Z} \quad (1.5)$$

and

$$p_i = \frac{g_i \exp\left(-\frac{\lambda_2 U_i}{k_B}\right)}{\mathcal{Z}} = \frac{\exp\left(-\frac{\lambda_2 \mathcal{F}_i}{k_B}\right)}{\mathcal{Z}}. \quad (1.6)$$

In the second step, we defined the free energy of state i as

$$\mathcal{F}_i = U_i - \frac{k_B}{\lambda_2} \log(g_i). \quad (1.7)$$

The temperature of the system is given by

$$\frac{1}{T} = \frac{\partial S}{\partial E} = \frac{\partial \mathcal{L}_{opt}}{\partial E} = \lambda_2, \quad (1.8)$$

where S and E are the equilibrium entropy and mean energy of the system. Hence, Eq. 1.6 shows that the p_i follow the Boltzmann distribution.

Finally, the relation between the temperature and the mean energy is given by the final maximisation of the entropy over λ_2 ,

$$\frac{\partial \mathcal{L}}{\partial \lambda_2} = k_B \frac{\partial \log(\mathcal{Z})}{\partial \lambda_2} + E = 0. \quad (1.9)$$

This general equation cannot be solved without knowledge about the state space $\{i\}$ and the energies and degeneracies U_i and g_i . Nevertheless, it is clear that our assumed knowledge of the average energy E is equivalent to knowledge about the temperature T through this relation.

1.1.1. BOLTZMANN DISTRIBUTION FROM EXPLICIT BATH DESCRIPTION

IN Sec. 1.1, we showed that the general maximum entropy distribution of a system in contact with a heat bath is given by the Boltzmann distribution. Here, we would like to show this in a more concrete toy example, without the need for explicit distribution optimisation. Imagine an isolated system with M different subsystems, which can exchange energy freely, and where each system i is only described by its potential energy U_i . All systems can have a spectrum of energies,

$$U_i \geq 0 \quad \forall i, \quad (1.10)$$

and energy conservation implies

$$\sum_{i=1}^M U_i = U. \quad (1.11)$$

The only property of the subsystems that we know of is their energy, and there is nothing else that can distinguish the likelihood of certain states to the observer. Then, we have

to assume a uniform probability density over the constrained state space of the entire isolated system,

$$f_{\{U,M\}}(v_1, v_2, \dots, v_M) \propto \delta\left(\sum_{i=1}^M v_i - U\right) \prod_{i=1}^M \mathbb{1}(v_i \geq 0). \quad (1.12)$$

Here, $f_{\{U,M\}}(v_1, v_2, \dots, v_M)$ is the probability density to find subsystem i with energy v_i when there are M subsystems with total energy U . Further, $\delta(x)$ represents the Dirac delta function peaked at $x = 0$, and $\mathbb{1}(C)$ represents the indicator function which is 1 when the condition C is true and 0 otherwise. The proportionality constant is found by integrating over all parameters. The first integration step is the marginalisation over v_M ,

$$f_{\{U,M\}}(v_1, v_2, \dots, v_{M-1}) = \int_0^U f_{\{U,M\}}(v_1, v_2, \dots, v_M) dv_M, \quad (1.13)$$

which applied to Eq. 1.12 gives

$$\int_0^U \delta\left(\sum_{i=1}^M v_i - U\right) \prod_{i=1}^M \mathbb{1}(v_i \geq 0) dv_M = \mathbb{1}\left(\sum_{i=1}^{M-1} v_i \leq U\right) \prod_{i=1}^{M-1} \mathbb{1}(v_i \geq 0). \quad (1.14)$$

The integrals over the remaining $M - 1$ dimensions calculate the volume of a standard simplex embedded in $M - 1$ dimensions,

$$\int_0^U dv_1 \int_0^{U-v_1} dv_2 \dots \int_0^{U-v_1-v_2-\dots-v_{M-2}} dv_{M-1} \mathbb{1} = \frac{U^{M-1}}{(M-1)!}. \quad (1.15)$$

The last expression can be verified by induction, adding an integral over v_0 around all other integrals in the inductive step. Eq. 1.15 gives us the normalisation constant of the probability density,

$$f_{\{U,M\}}(v_1, v_2, \dots, v_M) = \frac{(M-1)!}{U^{M-1}} \delta\left(\sum_{i=1}^M v_i - U\right) \prod_{i=1}^M \mathbb{1}(v_i \geq 0). \quad (1.16)$$

Now, we would like to know the distribution of energies in system 1, given only the information about the number of subsystems M and the total energy U , and not the specific states of all other subsystems. This amounts to marginalising out all but one parameter from the full distribution Eq. 1.16. In other words, we have to perform all integrals except for the last in Eq. 1.15, and choosing $v = v_1$, we have

$$f_{\{U,M\}}(v) = (M-1) \frac{(U-v)^{M-2}}{U^{M-1}} \quad (1.17)$$

This formula simplifies significantly when we further limit our information about the "bath" of subsystems surrounding the one subsystem. Instead of assuming we know the exact number of subsystems, we can say that we know that there are many: in this thermodynamic limit we let M approach infinity. The actual number will be large enough such that this approximation is valid. However, when we lose the information about the number of subsystems, we also lose the information about the total energy in the

system. Therefore, we have to replace our exact knowledge of U by the knowledge that the energy is an extensive quantity that scales with the number of subsystems in the bath. The proportionality constant u is then the average energy per subsystem, and

$$U = Mu. \quad (1.18)$$

Combining this, we get

$$\begin{aligned} f_u(v) &= \lim_{M \rightarrow \infty} f_{(Mu, M)}(v) \\ &= \lim_{M \rightarrow \infty} (M-1) \frac{(Mu-v)^{M-2}}{(Mu)^{M-1}} \\ &= \lim_{M \rightarrow \infty} \frac{M-1}{Mu} \left(1 - \frac{v}{Mu}\right)^{M-2} \\ &= \frac{1}{u} e^{-v/u} \end{aligned} \quad (1.19)$$

In the final line, we recognise the Boltzmann distribution for a continuous spectrum degree of freedom with mean energy $u = k_B T$.

This may not be the most general derivation of this quantity, but it does provide some insight in the role of the thermodynamic limit in the applicability of the Boltzmann factor. In this limit we can extend the border of the potential energy spectrum to infinity, and we can ignore the exact size of the bath. Our knowledge is reduced to "the bath is large enough". Finally, the fact that we have to take into account the extensiveness of the potential energy makes it clear why we have to assume knowledge about the average potential energy for the system state. This mean energy, which turns out to be $k_B T$, describes a property of the bath. For a general system, the mean energy has a more complex relationship with the temperature, as described in the first part of Sec. 1.1, but the constraint on the mean system energy remains the proper way to describe the bath.

1.2. LOCAL DETAILED BALANCE

SEC. 1.1 showed how we can calculate the equilibrium distribution of states, but it did not show anything about the dynamics of thermodynamic systems. Sometimes, we are interested in the dynamics of thermally activated processes in equilibrium, such as diffusion. More often still, we would like to describe systems that are driven out of equilibrium, for example by a bath of chemicals that is constantly replenished. When we talk about diffusive systems, we can assume that there are no inertial effects and that the dynamics is memoryless. This leads us to describe the stochastic dynamics of Markov models.

A continuous time Markov chain model can exhibit both in and out of equilibrium behaviour. To distinguish between the two, we need a condition that describes a property of equilibrium dynamics. This condition is known as detailed balance, and it can be derived using the principle of sufficient reason [23]. Since all states in an equilibrium system have a fixed probability of occurring, and there are transitions between these states, the probability flux into one state should equal the probability flux out of that state. In a general network of states, it is possible to obey this stationarity condition by having

cycles, in which a current flows around the cycle. However, physical principles give us no reason to prefer one direction of this flux over another. Therefore, the only dynamics that represents our knowledge about an equilibrium system is one where there are no cycles, and where the direct flux between any two states is the same in both directions. In a Markov chain with transition rates $k_{i,j}$ from state i to state j , this means that

$$p_i k_{i,j} = p_j k_{j,i}, \quad (1.20)$$

where p_i is the equilibrium probability of state i . Detailed balance implies that for thermodynamic consistency, it is necessary to have microscopic reversibility,

$$k_{i,j} \neq 0 \iff k_{j,i} \neq 0. \quad (1.21)$$

Without this condition, the model would imply that there are infinite free-energy differences between certain states, since one would be completely empty while another has a finite probability. This is even true for non-equilibrium systems without detailed balance, meaning that it would never be possible to calculate free-energy costs for systems with microscopically irreversible transitions.

Using the Boltzmann distribution for equilibrium systems Eq. 1.6, we can rearrange Eq. 1.20 to arrive at a relation between the rates and equilibrium free-energy differences,

$$\frac{k_{i,j}}{k_{j,i}} = \frac{p_j}{p_i} = \exp(-\beta \Delta \mathcal{F}_{i,j}), \quad (1.22)$$

where $\beta = 1/k_B T$ and $\Delta \mathcal{F}_{i,j} = \mathcal{F}_j - \mathcal{F}_i$ is the increase in free energy when going from state i to state j . This equation holds in equilibrium, but we would like to extend its validity to non-equilibrium systems.

There are different ways to bring a system out of equilibrium. When you prepare a system in a certain state, this will generally not be the equilibrium state of that system. However, when the system is left alone, its dynamics will move towards the steady state and reach equilibrium eventually. This relaxation is a non-equilibrium process. For a Markov chain, the dynamics is fully described by the reaction rates between the states. Therefore, when the system is not yet in a steady state, the rates do not change, only the probabilities and fluxes change. Hence, we can generalise Eq. 1.22 to

$$\frac{k_{i,j}}{k_{j,i}} = \exp(-\beta \Delta \mathcal{F}_{i,j}). \quad (1.23)$$

Here, there is no relation with the probabilities p_i any more, since they do not follow the Boltzmann distribution when the system leaves equilibrium. However, we can define free-energy differences out of equilibrium using Eq. 1.23, which we call local detailed balance [25]. This definition makes sense, since it formalises our intuition that free-energy differences between states should not depend on the initial distribution that you choose to impose on the system. And since both the transition rates and these free-energy differences remain unchanged during the dynamics, the relation between them should always be the same as it is in equilibrium.

This holds when the system is brought out of equilibrium by preparing it in a certain initial state. It is also possible to bring the entire bath to a non-equilibrium initial

state, and let the entirety of system and bath relax to equilibrium. When the bath is large enough and the only relaxation happens within the system, for example when a non-equilibrium reaction of a chemical species is only catalysed within the system, then the bath will stay approximately constant. In this case, the dynamics is still a result of the relaxation towards equilibrium. However, the transition rates are generally different from the rates found with an equilibrium bath. Still, we define the free-energy change due to a system transition using Eq. 1.23. It is possible that the actual free-energy dissipation in the entirety of system and bath is larger than $\Delta\mathcal{F}_{i,j}$ due to different irreversible transitions that are not part of the system description, but Eq. 1.23 provides a definition of the minimal free-energy dissipation in a non-equilibrium Markov system.

We make the generalisation of the applicability of Eq. 1.23 based on the idea that a local transition can be considered irrespective of the rest of the system. Whether the system obeys detailed balance or not, the relation between the rates and the free-energy change should stay the same.

1.3. FOKKER-PLANCK EQUATION FROM MASTER EQUATION

HERE, we will show how to properly take the limit from a Markov chain with discrete states to a continuous space Markov system, which is described by the Fokker-Planck equation [26, 27]. This limit clarifies the relation between the drift parameter in the Fokker-Planck equation and forces, and gives us the proper version of the Einstein relation in case of a position-dependent diffusion constant.

Consider a discrete Markov chain with sites $i \in \mathbb{Z}$, and with transition rates

$$k_{i,j} = \begin{cases} k_{i+} & \text{if } j = i + 1 \\ k_{i-} & \text{if } j = i - 1 \\ -(k_{i+} + k_{i-}) & \text{if } j = i \\ 0 & \text{otherwise.} \end{cases} \quad (1.24)$$

Again, the probability to be in state i is called $p_i(t)$. Then, the master equation for the continuous time Markov chain is given by

$$\partial_t p_i(t) = -(k_{i+} + k_{i-}) p_i(t) + k_{i-1} p_{i-1}(t) + k_{i+1} p_{i+1}(t). \quad (1.25)$$

The free-energy differences in this system are given by local detailed balance, as shown in Eq. 1.23,

$$\frac{k_{i+}}{k_{i+1-}} = \exp(\beta(\mathcal{F}_i - \mathcal{F}_{i+1})). \quad (1.26)$$

To bring this system to a continuous line, we assume that the states are equally spaced from each other with a lattice spacing δ . We need to take a limit of $\delta \rightarrow 0$ for a continuous description, and assume that the transition rates diverge in that limit. Specifically, we start with a parameter transformation,

$$\tilde{v}(i\delta) = \delta(k_{i+} - k_{i-}), \quad (1.27)$$

$$D(i\delta) = \frac{\delta^2}{2}(k_{i+} + k_{i-}). \quad (1.28)$$

Here, \tilde{v} represents the drift velocity and D is the local diffusion constant. The notation anticipates that these will become continuous functions, because we assume that the parameters \tilde{v} and D will reach finite values in the continuum limit. The inverse of these relation gives

$$k_{i+} = \frac{D(i\delta)}{\delta^2} + \frac{\tilde{v}(i\delta)}{2\delta}, \quad (1.29)$$

$$k_{i-} = \frac{D(i\delta)}{\delta^2} - \frac{\tilde{v}(i\delta)}{2\delta}. \quad (1.30)$$

Then, we define the probability density as

$$p(x, t) = \lim_{\delta \rightarrow 0} \frac{p_{x/\delta}}{\delta}, \quad (1.31)$$

where x/δ should be rounded to an integer value using any choice of rounding. Using Eq. 1.27 and Eq. 1.28 to replace the rates in Eq. 1.25, we have

$$\begin{aligned} \partial_t p(x, t) &= \lim_{\delta \rightarrow 0} -\frac{2}{\delta^2} D(x) p(x, t) \\ &\quad + \left(\frac{D(x-\delta)}{\delta^2} + \frac{\tilde{v}(x-\delta)}{2\delta} \right) p(x-\delta, t) \\ &\quad + \left(\frac{D(x+\delta)}{\delta^2} - \frac{\tilde{v}(x+\delta)}{2\delta} \right) p(x+\delta, t) \\ &= \lim_{\delta \rightarrow 0} \frac{D(x+\delta) p(x+\delta, t) + D(x-\delta) p(x-\delta, t) - 2D(x) p(x, t)}{\delta^2} \\ &\quad - \frac{\tilde{v}(x+\delta) p(x+\delta, t) - \tilde{v}(x-\delta) p(x-\delta, t)}{2\delta} \\ &= \partial_x^2 (D(x) p(x, t)) - \partial_x (\tilde{v}(x) p(x, t)). \end{aligned} \quad (1.32)$$

This is one representation of the Fokker-Planck equation. The equation specifies the time evolution of the probability density function, and can be generalised to higher dimensions. Using this equation, it is possible to describe the time evolution of the mean position too. We write down the definition of the mean position and apply partial integration and the assumption that the probability density and its derivatives vanish at infinity,

$$\partial_t \langle x(t) \rangle = \int_{-\infty}^{\infty} x \partial_t p(x, t) dx = \int_{-\infty}^{\infty} \tilde{v}(x) p(x, t) dx. \quad (1.33)$$

This equation shows that $\tilde{v}(x)$ describes the drift of the mean position. To investigate its relation with the force, we have to derive the Einstein relation for this system. Note that by l'Hôpital's rule,

$$\lim_{\delta \rightarrow 0} \frac{\exp(\beta(\mathcal{F}(x) - \mathcal{F}(x+\delta))) - 1}{\delta} = -\beta \partial_x \mathcal{F}(x). \quad (1.34)$$

Then, using Eq. 1.26, we also have

$$\begin{aligned}
\lim_{\delta \rightarrow 0} \frac{\exp(\beta(\mathcal{F}(x) - \mathcal{F}(x + \delta))) - 1}{\delta} &= \lim_{\delta \rightarrow 0} \frac{k_{x/\delta+} - k_{x/\delta+1-}}{\delta k_{x/\delta+1-}} \\
&= \lim_{\delta \rightarrow 0} \frac{D(x)/\delta^2 + \tilde{v}(x)/(2\delta)}{D(x + \delta)/\delta - \tilde{v}(x + \delta)/2} \\
&\quad - \frac{D(x + \delta)/\delta^2 + \tilde{v}(x + \delta)/(2\delta)}{D(x + \delta)/\delta - \tilde{v}(x + \delta)/2} \\
&= \lim_{\delta \rightarrow 0} -\frac{D(x + \delta) - D(x)}{\delta(D(x + \delta) - \delta\tilde{v}(x + \delta)/2)} \\
&\quad + \frac{\tilde{v}(x + \delta) + \tilde{v}(x)}{2D(x + \delta) - \delta\tilde{v}(x + \delta)} \\
&= -\frac{\partial_x D(x)}{D(x)} + \frac{\tilde{v}(x)}{D(x)}
\end{aligned} \tag{1.35}$$

In the second line, we used the inverse Eq. 1.29 and Eq. 1.30 to replace the rates, and then we used the assumption that the functions $D(x)$ and $\tilde{v}(x)$ and their derivatives remain finite in the continuum limit. We can rewrite the final line by introducing the function

$$v(x) = \tilde{v}(x) - \partial_x D(x). \tag{1.36}$$

Using this parameter, the Fokker-Planck equation, Eq. 1.32, takes a different form,

$$\partial_t p(x, t) = \partial_x (D(x) \partial_x p(x, t)) - \partial_x (v(x) p(x, t)). \tag{1.37}$$

Combining the results of Eq. 1.34 and Eq. 1.35, we find,

$$\beta D(x) F(x) = -\beta D(x) \partial_x \mathcal{F}(x) = v(x). \tag{1.38}$$

Here, $F(x) = -\partial_x \mathcal{F}(x)$ is the force, and we recognise the friction coefficient

$$\zeta(x) = \frac{k_B T}{D(x)}. \tag{1.39}$$

This is called the Einstein relation [28]. We see that $v(x)$ is the contribution of the force to the drift, while $\tilde{v}(x)$ also takes into account the drift term that is due to the varying diffusion constant. This term, the derivative of the diffusion constant, has a transient effect on the mean position. Initially, the mean moves in the direction of the fastest diffusion, and the distribution "equilibrates" earlier in the direction of faster diffusion. However, in the long time limit, this term has no effect on the equilibrium distribution, which is set by the force through the Boltzmann distribution, so the mean regresses back to the expected position. Eq. 1.38 can be used to rewrite the Fokker-Planck equation Eq. 1.37 once more,

$$\begin{aligned}
\partial_t p(x, t) &= \partial_x (D(x) \partial_x p(x, t)) + \partial_x (\beta D(x) \partial_x \mathcal{F}(x) p(x, t)) \\
&= \partial_x [\exp(-\beta \mathcal{F}(x)) D(x) \partial_x (\exp(\beta \mathcal{F}(x)) p(x, t))] \\
&= -\partial_x J(x, t).
\end{aligned} \tag{1.40}$$

The first line is known as the Smoluchowski equation. The last line shows the definition of the flux, and compared with the second line one can verify that the flux vanishes if and only if the equilibrium distribution is the Boltzmann distribution.

1.3.1. COMPARISON WITH GENERAL DERIVATION

IN the previous section, we derived the Fokker-Planck equation Eq. 1.37 and the Einstein relation Eq. 1.39 as the continuous limit of the master equation for continuous time Markov chains. In general, the Fokker-Planck equation does not require this underlying mechanism, and is based on more abstract assumptions. Specifically, the Fokker-Planck equation starts from the conservation of probability,

$$\partial_t p(x, t) = -\partial_x J(x, t), \quad (1.41)$$

where $J(x, t)$ is the probability flux related to the position x . The main assumption is Fick's law, which says that diffusion leads to a probability flux which is proportional to the derivative of the probability density,

$$J(x, t) = -D(x) \partial_x p(x, t) + v(x) p(x, t). \quad (1.42)$$

The proportionality constant equals the diffusion constant $D(x)$, and the second term on the right hand side follows from the definition of the flux. The combined equations Eq. 1.41 and Eq. 1.42 lead to the Fokker-Planck equation Eq. 1.37.

As explained in the derivation of Eq. 1.20, detailed balance says that the flux Eq. 1.42 vanishes in equilibrium. Furthermore, in equilibrium the probability distribution must follow the Boltzmann distribution Eq. 1.6,

$$p(x, t) \propto e^{-\mathcal{F}(x)/k_B T}. \quad (1.43)$$

Since $\mathcal{F}(x)$ is the free-energy profile that determines all forces acting on the particle, and the particle undergoes overdamped dynamics, the drift velocity is set by the free energy and a friction coefficient $\zeta(x)$,

$$v(x) = \frac{-\partial_x \mathcal{F}(x)}{\zeta(x)}. \quad (1.44)$$

The numerator on the right hand side equals the definition of the force, and hence Eq. 1.44 defines the friction coefficient. Combining Eq. 1.42, Eq. 1.43, and Eq. 1.44 with the detailed balance condition $J(x, t) = 0$, we see

$$\left(\frac{D(x)}{k_B T} - \frac{1}{\zeta(x)} \right) \partial_x \mathcal{F}(x) e^{-\mathcal{F}(x)/k_B T} = 0. \quad (1.45)$$

Hence, we retrieve the Einstein relation Eq. 1.39, which also shows the general validity of Eq. 1.40. This derivation shows the generality of these equations, but it does not make clear what the relation is to Eq. 1.32, and why $\tilde{v}(x)$ is the wrong function to use in Eq. 1.44. Sec. 1.3 clearly shows that $\tilde{v}(x)$ is the full drift velocity, which contains the force contribution Eq. 1.44 and a contribution due to the positional changes in the diffusion constant, as shown in Eq. 1.36. These latter contributions only cause a transient drift that has no effect on the steady state distribution, and only the force driven drift $v(x)$ determines the final Boltzmann distribution.

1.4. KOLMOGOROV BACKWARD EQUATION

THE Fokker-Planck equation, given in Eq. 1.37, determines the probability that a particle is at a certain position given a specific initial condition. If a particle is at point x' at time t' , then the Fokker-Planck equation determines the probability density $p(x, t | x', t')$ that the particle is at x at time $t > t'$. This equation is also known as the Kolmogorov forward equation [29], since the operator in the equation propagates the probability density forward in time. Similarly, there is an operator that propagates the probability density backward in time. To find it, we use the Chapman–Kolmogorov equation which relates the probabilities at times $t'' < t' < t$,

$$p(x, t | x'', t'') = \int p(x, t | x', t') p(x', t' | x'', t'') dx'. \quad (1.46)$$

Then, we apply a time derivative operator with respect to t' to both sides of this equation,

$$\begin{aligned} 0 &= \int \partial_{t'} p(x, t | x', t') p(x', t' | x'', t'') + p(x, t | x', t') \partial_{t'} p(x', t' | x'', t'') dx' \\ &= \int \partial_{t'} p(x, t | x', t') p(x', t' | x'', t'') + p(x, t | x', t') \partial_{x'} (D(x') \partial_{x'} p(x', t' | x'', t'')) \\ &\quad - p(x, t | x', t') \partial_{x'} (v(x') p(x', t' | x'', t'')) dx' \\ &= \int [\partial_{t'} p(x, t | x', t') + \partial_{x'} (D(x') \partial_{x'} p(x, t | x', t')) + v(x') \partial_{x'} p(x, t | x', t')] \\ &\quad \times p(x', t' | x'', t'') dx'. \end{aligned} \quad (1.47)$$

In the second step, we apply the Fokker-Planck equation Eq. 1.37 to resolve the second time derivative, and in the third step we apply partial integration to apply the partial derivatives with respect to x' to the function $p(x, t | x', t')$. We ignore the boundary terms, which are assumed to vanish because of the form of the probability distribution. Eq. 1.47 can only be satisfied if

$$\partial_{t'} p(x, t | x', t') = -\partial_{x'} (D(x') \partial_{x'} p(x, t | x', t')) - v(x') \partial_{x'} p(x, t | x', t'). \quad (1.48)$$

This is the Kolmogorov backward equation [29].

For completeness, we give a separate derivation of the backward equation for the Smoluchowski equation, Eq. 1.40. In contrast to the derivation of Eq. 1.48, this derivation is only valid when the detailed balance condition holds,

$$p(x, t | x', t') e^{-\mathcal{F}(x')/k_B T} = p(x', t' | x, t) e^{-\mathcal{F}(x)/k_B T}. \quad (1.49)$$

In this case, the order of t and t' is irrelevant. Then, Eq. 1.40 shows that

$$\begin{aligned}
 \partial_{t'} p(x, t | x', t') &= e^{-(\mathcal{F}(x) - \mathcal{F}(x'))/k_B T} \partial_{t'} p(x', t' | x, t) \\
 &= e^{-(\mathcal{F}(x) - \mathcal{F}(x'))/k_B T} \\
 &\quad \times \partial_{x'} \left[e^{-\mathcal{F}(x')/k_B T} D(x') \partial_{x'} \left(e^{\mathcal{F}(x')/k_B T} p(x', t' | x, t) \right) \right] \\
 &= e^{-(\mathcal{F}(x) - \mathcal{F}(x'))/k_B T} \\
 &\quad \times \partial_{x'} \left[e^{-\mathcal{F}(x')/k_B T} D(x') \partial_{x'} \left(e^{\mathcal{F}(x)/k_B T} p(x, t | x', t') \right) \right] \\
 &= e^{\mathcal{F}(x')/k_B T} \partial_{x'} \left[e^{-\mathcal{F}(x')/k_B T} D(x') \partial_{x'} p(x, t | x', t') \right]. \quad (1.50)
 \end{aligned}$$

This derivation is more direct, but it also requires the stronger assumption that the system will eventually reach the equilibrium distribution where detailed balance holds Eq. 1.49. If external driving forces are present that break detailed balance in steady state, Eq. 1.48 is still valid.

The backward equation is useful for calculating the mean first passage time T at which a particle leaves a region A . Following [31], we define the survival probability

$$S(t) = \mathbb{P}(T > t) = \int_A p(x, t | x', 0) dx. \quad (1.51)$$

Since the region A has absorbing boundaries, the probability density will eventually become 0. The first relation in Eq. 1.51 shows that the negative derivative of the survival probability equals the first passage time density, which we can use to find a relation for the mean first passage time,

$$\langle T \rangle(x') = \int_0^\infty t (-\partial_t S(t)) dt = \int_0^\infty S(t) dt = \int_0^\infty \int_A p(x, t | x', 0) dx dt, \quad (1.52)$$

where the second step requires a partial integral. The average depends implicitly on the initial position x' through Eq. 1.51. Then, we find an equation for this mean first passage time by applying the operator from Eq. 1.48 to $\langle T \rangle(x')$,

$$\begin{aligned}
 &[-\partial_{x'} D(x') \partial_{x'} - v(x') \partial_{x'}] \langle T \rangle(x') \\
 &= \int_0^\infty \int_A [-\partial_{x'} D(x') \partial_{x'} - v(x') \partial_{x'}] p(x, t | x', 0) dx dt \\
 &= \int_0^\infty \int_A \partial_{t'} p(x, t | x', t') |_{t'=0} dx dt \\
 &= - \int_0^\infty \int_A \partial_t p(x, t | x', 0) dx dt. \quad (1.53)
 \end{aligned}$$

In the second step, we apply the backward Kolmogorov equation, Eq. 1.48. The last step follows from the time homogeneity of the system,

$$p(x, t | x', t') = p(x, t - t' | x', 0). \quad (1.54)$$

By first applying the integral over time in the last line of Eq. 1.53, and using that the probability density vanishes for $t \rightarrow \infty$ and equals a Dirac delta function at $t = 0$, we find an

equation for the mean first passage time,

$$\partial_{x'} (D(x') \partial_{x'} \langle T \rangle(x')) + \nu(x') \partial_{x'} \langle T \rangle(x') = -1. \quad (1.55)$$

Together with the boundary condition $\langle T \rangle(x') = 0$ when $x' \notin A$, this equation gives the mean first passage time when $D(x)$ and $\nu(x)$ are known.

1.5. KRAMERS RATE THEORY

OFTEN, a system contains several meta-stable states, and time scale of transitions between these states is large compared to the time scales of the microscopic dynamics. Then, we are interested in the effective rates at which these rare transitions occur, since they give the full dynamics at the macroscopic level. Focussing on a thermodynamic system, the meta-stable states are regions of low free energy, and free-energy barriers exist between these states. In principle, this is a high-dimensional free-energy landscape with many meta-stable states. Transitions between these states often follow approximately one dimensional regions in phase space, which we call transition paths. There can exist several transition paths between two meta-stable states, and to describe the macroscopic dynamics, one needs to specify all transition paths and the rates at which these paths are taken in either direction. Since the system will equilibrate when it is left unperturbed for long enough, the free energy sets the equilibrium probabilities for all states, including the unstable states along transition paths. The simplest method to predict the rate at which a single path between meta-stable states is taken, is to assume that the peak of the barrier forms the bottleneck in the dynamics, and that the rate of taking a certain transition path is proportional to the equilibrium probability at the peak of barrier. Hence, we write

$$r = r_0 \exp(-\beta \mathcal{F}^\ddagger), \quad (1.56)$$

where \mathcal{F}^\ddagger is the activation energy for the transition, which is the free energy of the bottleneck of a transition path. To calculate this free energy properly, we need to find the reaction coordinate for this specific transition path, which captures its one-dimensional shape. Different methods exist to identify the reaction coordinate and the transition state, the bottleneck in a transition path [32, 33].

Eq. 1.56 seems not to make a prediction about r_0 , but if no constraints are placed on this prefactor, then the prefactor is allowed to cancel the exponential factor and the equation is a tautology. Actually, what is meant by Eq. 1.56 is that any parameter that influences \mathcal{F}^\ddagger has at most a similar influence on r_0 . In other words, if the transition rate depends exponentially on some parameter, this dependence should be captured by the free-energy barrier, and not by the prefactor. Even more loosely speaking, the prefactor changes less fast than the exponential term. In case this is found not to be the case, and the prefactor does contain an exponential term, it provides a strong hint that the proposed reaction coordinate is not correct.

Hence, Eq. 1.56 is simple and does not strongly restrict r_0 , but it is also the most generally applicable equation for the reaction rate behaviour. If we wish to predict the prefactor, then we require more assumptions about the dynamics of the system. One commonly made assumption is that the underlying dynamics can be described by a Fokker-

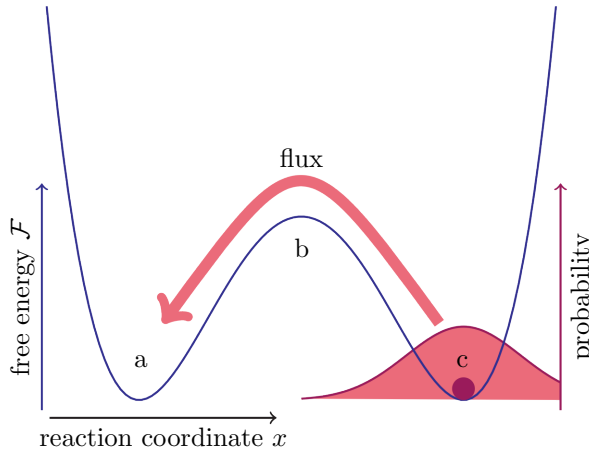


Figure 1.1: Cartoon of a free-energy barrier.

Planck equation. This choice leads to the Kramers rate equation, which we derive here following Kramers for the overdamped case [30].

We look for the rate in a one-dimensional barrier crossing problem, as depicted in Fig. 1.1. The system is imagined to consist of a particle fluctuating in a well with position x , but x can represent a more general reaction coordinate through an abstract state space. We model two meta-stable states located at positions a and c separated by a single barrier with a peak at b . Besides using a Fokker-Planck dynamics, given by Eq. 1.40, we also need to assume that the free-energy barrier is high enough such that the distribution of a particle that starts in c will approximately follow the Boltzmann distribution within the well around c . Then, we can calculate the rate for the transition from c to a using the flux-over-population method [34]. This means that we calculate the probability flux that leaves c over b , and divide it by the probability to be at c .

To find the flux, we take the definition from Eq. 1.40,

$$J(t) = -\exp(-\beta\mathcal{F}(x))D(x)\partial_x(\exp(\beta\mathcal{F}(x))p(x, t)). \quad (1.57)$$

As an initial condition, we take the particle to follow the Boltzmann distribution for $x > b$, and for the distribution to vanish for $x < b$. Since the barrier is high enough, the flux is not very large and the Boltzmann distribution is not affected much by the outgoing flux. Hence, the shape of the distribution in the well around $x = c$ is stable, and the flux J can be assumed to be independent of x . If the barrier is too low, the distribution around c changes so rapidly that a spatial gradient is formed in the flux itself, and together with the breakdown of the Boltzmann distribution around $x = c$ this would cause Kramers theory to break down. Assuming a high barrier, we can integrate Eq. 1.57 from a to c ,

$$-J(t)\int_a^c \frac{\exp(\beta\mathcal{F}(x))}{D(x)} dx = \exp(\beta\mathcal{F}(c))p(c, t). \quad (1.58)$$

and we use that $p(a, t)$ vanishes for small enough times. Next, we calculate the proba-

bility to be in the well around c , using the assumption that the shape of the distribution there remains dictated by a Boltzmann distribution,

$$p_c(t) \equiv \int_b^\infty p(x, t) dx = p(c, t) \int_b^\infty \exp(-\beta(\mathcal{F}(x) - \mathcal{F}(c))) dx. \quad (1.59)$$

Here, the normalisation constant of the distribution around $x = c$ can change, providing the time dependence in $p_c(t)$. Then, we calculate the rate with Eq. 1.58, using that the leftward flux is negative,

$$r = \frac{-J(t)}{p_c(t)} = r_0 \exp(-\beta\mathcal{F}^\ddagger), \quad (1.60)$$

with

$$r_0 = \left\{ \int_a^c \frac{\exp(\beta(\mathcal{F}(x) - \mathcal{F}(b)))}{D(x)} dx \int_b^\infty \exp(-\beta(\mathcal{F}(x) - \mathcal{F}(c))) dx \right\}^{-1} \quad (1.61)$$

and

$$\mathcal{F}^\ddagger = \mathcal{F}(b) - \mathcal{F}(c). \quad (1.62)$$

The expression for the prefactor in Eq. 1.61 is in its most general form, and can be brought to its more familiar form by applying quadratic approximations to both the peak around b and the well around c , and using Gaussian integrals to approximate both factors,

$$r_0 \approx \frac{D(b) \sqrt{-\mathcal{F}''(b) \mathcal{F}''(c)}}{2\pi k_B T}. \quad (1.63)$$

However, these quadratic approximations can be invalid, in which case the numerical integration of Eq. 1.61 still gives a prediction.

2

DIFFUSIBLE CROSS-LINKERS CAUSE SUPEREXPONENTIAL FRICTION FORCES

The friction between cytoskeletal filaments is of central importance for the formation of cellular structures such as the mitotic spindle and the cytokinetic ring. This friction is caused by passive cross-linkers, yet the underlying mechanism and the dependence on cross-linker density are poorly understood. Here, we use theory and computer simulations to study the friction between two filaments that are cross-linked by passive proteins, which can hop between discrete binding sites while physically excluding each other. The simulations reveal that filaments move via rare discrete jumps, which are associated with free-energy barrier crossings. We identify the reaction coordinate that governs the relative microtubule movement and derive an exact analytical expression for the free-energy barrier and the friction coefficient. Our analysis not only elucidates the molecular mechanism underlying cross-linker-induced filament friction, but also predicts that the friction coefficient scales superexponentially with the density of cross-linkers.

The contents of this chapter have been published in Physical Review Letters **125**, 078101 (2020) [35].

The formation of cytoskeletal structures like the mitotic spindle [36–50] and the cytokinetic ring [51–54] depends not only on motor proteins, but also on non-motor proteins that cross-link the filaments passively. Force generation is often attributed to the motor proteins, but passive cross-linkers can generate driving forces too, via their condensation to the overlap between the filaments [54, 55] or via the entropy associated with their diffusion within the overlap region [18]. Yet, in these highly dynamic systems both active and passive cross-linkers also create frictional forces, which oppose the motor, condensation, or entropic driving forces. These frictional forces are a central determinant of the mechanical properties of cytoskeletal structures [56], limit the speed and efficiency with which these structures are formed [5, 54, 57, 58], and can even be vital for their stability because motor forces need to be balanced by stabilizing passive cross-linkers [38, 41–45]. Furthermore, asymmetric friction forces can harness active filament fluctuations to generate directed motion of passive cross-linkers [59] and enhance the motion of motor proteins [60].

Friction in cellular systems has been studied theoretically. Prandtl-Tomlinson models [61], in which a particle moves over a sinusoidal potential, have been used to study how protein-filament [59, 62, 63] and filament-filament [56] friction depends on the velocity [56, 59, 62, 63] and the polarity of the filaments [56, 59, 62]. The Frenkel-Kontorova model [61], in which filaments consist of units connected via springs, has been employed to study how the contact friction depends on the overlap length between filaments [56]. Huxley-Lacker-Peskin type models, in which rigid filaments interact through cross-linkers that are modeled as harmonic springs that bind to a continuum or discrete set of binding sites [64–69] have been used to investigate force-velocity relations, and how these depend on the stiffness of the cross-linkers and the underlying substrate, and on the rates of cross-linker-filament attachment and detachment [55, 69, 70].

Yet, to understand the size of cytoskeletal structures such as the mitotic spindle and the cytokinetic ring, the speed and efficiency with they are formed, and the forces they can generate, it is vital to understand how the friction coefficient depends on the number of cross-linkers and on the overlap length between filaments [71]. Previous models either assume [42, 59, 72–74] or would predict [55, 70, 75] that the friction scales linearly with the number of cross-linkers.

Recent *in vitro* experiments have demonstrated that a protein from the Ase1/PRC1 family, which passively cross-links microtubules in the mitotic spindle, generates friction forces that do not scale linearly but rather exponentially with the number of cross-linkers in the overlap region [18]. The system exhibits generic features that are also found in other systems, such as the cytokinetic ring [54]. In particular, the filaments consist of a regular lattice of subunits that are of similar size as the cross-linkers. The cross-linkers thus bind to a discrete set of binding sites, while they are also stiff on the length scale set by the spacing between the binding sites, as discussed in more detail below. These assumptions are in marked contrast to the continuum of binding sites in the current theoretical models that predict a linear scaling of the friction with the number of cross-linkers [55, 70, 75].

Here, we present a model in which cross-linkers hop between discrete binding sites in the overlap region (Fig. 2.1). Our analysis shows that the discrete nature of the binding sites combined with the stiffness of the cross-linkers makes that the filaments can only

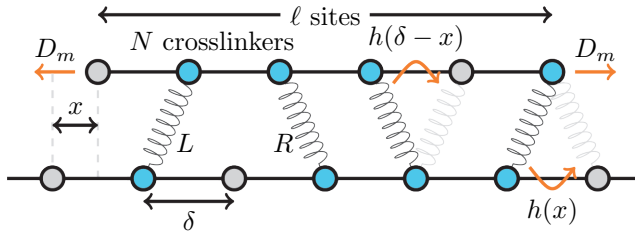


Figure 2.1: Model of the microtubule overlap. The filaments are represented as one dimensional lattices with spacing δ and are connected by cross-linking proteins, described as springs. The bottom filament is fixed, while the top filament can move in the longitudinal direction due to Brownian motion with diffusion constant D_m or the pulling of stretched cross-linkers. Cross-linkers can make a diffusive step, causing them to switch from right-pulling linkers labeled R to left-pulling linkers denoted L , or vice versa. Two of such possible transitions, together with their rates h , are indicated by orange arrows. The fixed microtubule is infinitely long and the mobile one has ℓ lattice sites. There are N cross-linkers connecting the two filaments, which stay bound indefinitely.

move if the cross-linkers reorganize collectively. This turns filament movement into an activated process with an energy barrier that scales linearly with the number of cross-linkers. It explains why the friction scales exponentially with the number of cross-linkers. At higher densities our model predicts that the friction scales superexponentially with the number of cross-linkers, because of an entropic effect caused by steric hindrance.

2.1. MODEL

OUR model is shown in Fig. 2.1. It resembles the experimental setup used to measure the filament friction generated by Ase1 cross-linkers in vitro [18]. We probe the friction through a small mobile microtubule connected via cross-linkers to a microtubule that is fixed on the bottom. The top microtubule shows one dimensional movement parallel to the bottom one, and we avoid entropic force generation by having a constant overlap length [18]. Both microtubules contain a one-dimensional lattice of binding sites with spacing $\delta = 8 \text{ nm}$ [76, 77], and cross-linkers can hop between neighboring sites while they physically exclude each other.

To allow for movement of both the microtubule and the linkers, cross-linkers can stretch as Hookean springs with spring constant k and both ends of each linker can hop to empty neighboring binding sites. The effective parameter k is estimated from experimental data by observing how the diffusion constant of cross-linkers in overlaps is reduced compared to that of proteins on a single microtubule (see Sec. 2.A). We find $k = 1.1 \times 10^5 \text{ k}_B\text{T}/\mu\text{m}^2$, which is comparable to values reported for similar proteins [68, 78–80]. This value strongly suppresses stretching more than δ , and to facilitate model analysis and speed up simulations, we choose to impose a maximum stretch of one lattice spacing.

The position of the mobile microtubule relative to the fixed one is called x , such that x modulo δ represents the misalignment of the two lattices. The requirement that the

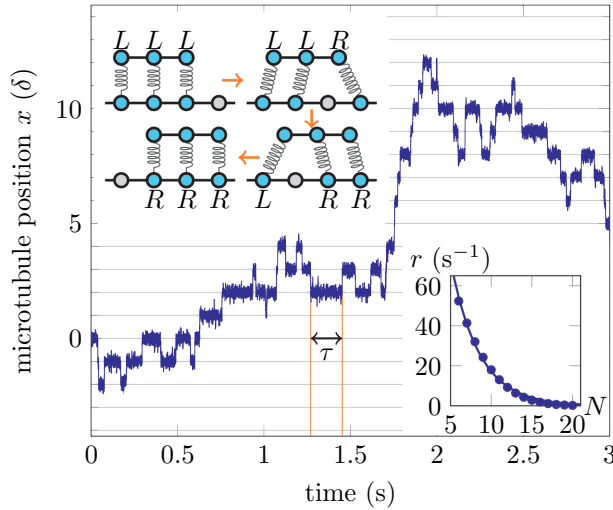


Figure 2.2: A typical time trace of the mobile microtubule position shows that it moves with sudden jumps. Horizontal lines denote positions where the microtubules are in register. The jumps occur at a fixed rate in both directions, which can be estimated from the mean waiting time in simulations, $r = 1/2\bar{T}$. (inset top-left) A typical transition, where the microtubules begin and end in register. Cross-linkers are stretched in intermediate states, which energetically suppresses transitions. (inset bottom-right) The observed rate of microtubule jumps appears to decrease exponentially with the number of cross-linkers N . Dots show simulation estimates of the rate, whereas the line shows a least square exponential fit. In the examples, $\ell = 40$, and $N = 12$ for the time trace.

cross-linking springs are extended less than one lattice spacing only allows for springs that are extended horizontally by a distance of either x or $\delta - x$. These are respectively called left- and right-pulling cross-linkers (Fig. 2.1). We model the movement of the top microtubule using Brownian dynamics with an intrinsic drag coefficient [81], and implement cross-linker hops through a kinetic Monte Carlo algorithm [82] (see Sec. 2.B).

Ase1/PRC1 (un)binding from the microtubule overlap plays no role in the *in vitro* friction experiments [18], leading us to exclude these reactions. Ignoring binding effects reduces the number of parameters, and allows us to focus on the specific dependence of the friction on the absolute number of cross-linkers in the microtubule overlap region N , and on the size of this region—the number of lattice sites on the mobile microtubule ℓ .

2.2. BARRIER CROSSINGS CAUSE MICROTUBULE JUMPS

WE visualize the dynamics of the mobile microtubule using computer simulations in Fig. 2.2. The position of the top filament makes discrete jumps between points $\{x: x \equiv 0 \pmod{\delta}\}$, where cross-linkers are energetically relaxed. The waiting time between jumps is exponentially distributed with rate $2r$ (see Sec. 2.C), which suggests that a single barrier exists between these states.

The jumping behavior causes effective Brownian motion of the microtubule with diffusion constant $D \approx \delta^2 r$ (see Sec. 2.C). We can estimate the effective friction coefficient of the cross-linked microtubule ζ using the Einstein relation Eq. 1.39 [28],

$$\zeta = \frac{k_B T}{D} = \frac{k_B T}{\delta^2 r}. \quad (2.1)$$

Hence, we can focus our attention on the jump rate r , which indirectly gives the friction coefficient via Eq. 2.1. In Sec. 2.D we show that the friction coefficient computed via Eq. 2.1 agrees with that as obtained by applying an external force on the top filament, provided the system is in the linear-response regime of low force and speed where the cross-linkers have time to re-equilibrate in between the filament jumps.

The bottom-right inset of Fig. 2.2 shows that the jump rate r decreases roughly exponentially with the number of cross-linkers in the overlap N . This indicates that the friction coefficient ζ increases exponentially with the number of cross-linkers (Eq. 2.1), whereas one would naively expect it to increase linearly with N [42, 55, 59, 70, 72, 73, 75].

To investigate the origin of the exponential decrease of the jump rate, we calculate the free-energy landscape as a function of two order parameters involved in the filament jumps. Without loss of generality, we focus on a jump to the right. As shown in the top-left inset of Fig. 2.2, a jump requires the microtubule to move one lattice spacing, and all cross-linkers need to make one net hop. The former change is captured by the microtubule position x changing from 0 to δ , and the latter change is described by the number of right-pulling cross-linkers N_R changing from 0 to N . To find the free-energy as a function of the order parameters x and N_R , we first calculate the potential energy of the system,

$$\begin{aligned} U(x, N_R) &= \frac{1}{2} k x^2 (N - N_R) + \frac{1}{2} k (\delta - x)^2 N_R \\ &= \frac{1}{2} k \delta^2 N \left[\left(\frac{x}{\delta} - \frac{N_R}{N} \right)^2 + \frac{N_R}{N} \left(1 - \frac{N_R}{N} \right) \right]. \end{aligned} \quad (2.2)$$

All potential energy is stored in the springs, and there are N_R right-pulling linkers with stretch $\delta - x$ and $N - N_R$ left-pulling linkers with stretch x . When the values of the order parameters x and N_R are set, all microstates have the same potential energy. Hence, we can make use of Boltzmann's formula $S = k_B \log \Omega$ to calculate the entropy of the system, where $\Omega(x, N_R)$ represents the number of microstates due to different permutations of the cross-linkers in the overlap. Furthermore, the number of different permutations of the L - and R -linkers is independent of the position x , meaning that $\Omega(x, N_R) = \Omega(N_R)$. The Helmholtz free-energy is thus

$$\begin{aligned} \mathcal{F}(x, N_R) &= U(x, N_R) - T S(x, N_R) \\ &= U(x, N_R) - k_B T \log \Omega(N_R). \end{aligned} \quad (2.3)$$

Surprisingly, it is possible to obtain a closed form expression for $\Omega(N_R)$ (see Sec. 2.E),

$$\Omega(N_R) = \binom{\ell - N_R}{N - N_R} \binom{\ell - N + N_R}{N_R}. \quad (2.4)$$

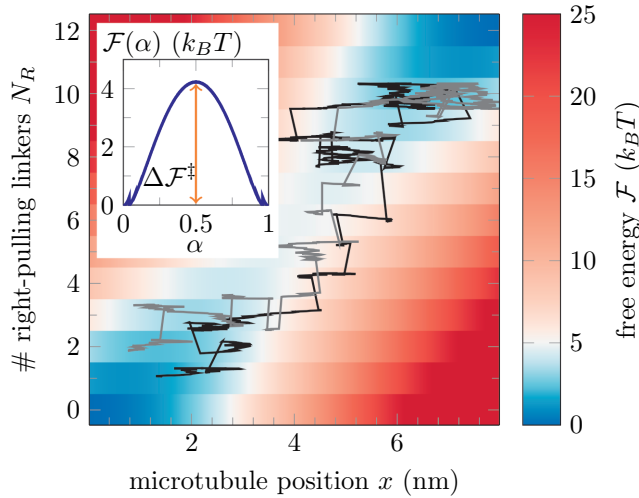


Figure 2.3: Helmholtz free-energy as a function of the position x and the number of right-pulling cross-linkers N_R . Free-energy minima exist at the bottom-left and top-right corners, where the two filaments are in register and the cross-linkers are fully relaxed. These minima are separated by a free-energy barrier, where the cross-linkers are stretched (see Fig. 2.2). A transition over the barrier is observed as a jump of the microtubule, and two transition paths are shown for illustration. N_R is a discrete parameter, and a weak sinusoidal y-offset was added to the paths to visualize their course. In this example, we use $N = 12$ and $\ell = 40$. (inset) The free-energy profile as a function of the reaction coordinate α . The height of the barrier is the difference between the Helmholtz free-energies at $\alpha = 0$ and $\alpha = 1/2$. Discontinuities occur due to the discrete nature of N_R in the definition of α .

Intuitively, the first binomial factor represents the number of ways $N - N_R$ L -linkers can be placed in an overlap with ℓ sites, when N_R of those sites are excluded by R -linkers. The second factor is simply the symmetric counterpart to the first one, and counts permutations of the R -linkers. With Eq. 2.2 and Eq. 2.4, we have arrived at an *exact* solution for the free-energy Eq. 2.3 (see Sec. 2.F). Fig. 2.3 clearly shows that a free-energy barrier exists between two minima located at $(x = 0, N_R = 0)$ and $(x = \delta, N_R = N)$, where the cross-linkers are relaxed. The energetic component of the free energy Eq. 2.2, which favours the lattices to be in register, outcompetes the entropic component Eq. 2.4, which favours the lattices to be exactly out of register. Hence, the most likely configuration of the two filaments is one where the two lattices are exactly in register, and the least likely position is one where the two lattices are offset by half the lattice spacing δ .

As can be seen in Eq. 2.2, the lowest free-energy path that connects the two minima obeys $x/\delta = N_R/N$, which corresponds to the diagonal of Fig. 2.3. As shown in Fig. 2.16 and Fig. 2.17, transition paths typically follow this diagonal, and the transition state ensemble as defined by Hummer [33] is perpendicular to it (see Sec. 2.G). Therefore, the

reaction coordinate is

$$\alpha = \frac{1}{2} \left(\frac{x}{\delta} + \frac{N_R}{N} \right), \quad (2.5)$$

which shows that the filament jumps involve a coupling between filament movement and cross-linker hops. The inset of Fig. 2.3 plots the free energy marginalized to α , revealing the effective barrier that the microtubule has to overcome every time it makes a $\delta = 8$ nm move.

According to Eq. 2.1, the friction coefficient is determined by the microtubule jump rate r , which depends on the free-energy barrier height $\Delta\mathcal{F}^\ddagger$ via [83]

$$r(N, \ell) = r_0(N, \ell) \exp\left(-\beta\Delta\mathcal{F}^\ddagger(N, \ell)\right). \quad (2.6)$$

The prefactor r_0 depends on the intrinsic drag coefficients of the top filament and cross-linkers, and, at least in principle, also on the number of cross-linkers N and the number of sites in the overlap ℓ . Yet, we find that the dependence on N and ℓ is very weak, indicating that α accurately captures the reaction coordinate (see Sec. 2.H).

2.3. JUMP RATE DECREASES SUPEREXPONENTIALLY

OUR expression for the free-energy, via Eqs. 2.2–2.4, is exact, but how it is shaped by N and ℓ remains obscure due to the discrete binomial coefficients. Therefore, we create a continuous approximation of the entropic term [84] (see Sec. 2.I). We find the following simplified analytical expression for the barrier height,

$$\beta\Delta\mathcal{F}^\ddagger \approx A + BN \exp\left(\frac{1}{4B} \frac{N}{\ell}\right). \quad (2.7)$$

Here,

$$A = \frac{1}{2} \log\left(1 + \frac{3k\delta^2}{4k_B T}\right), \quad B = \frac{k\delta^2}{8k_B T} - \log(2), \quad (2.8)$$

where B is positive since k is large relative to $k_B T/\delta^2$. Fig. 2.4 shows that this approximation is in excellent agreement with the exact result of Eqs. 2.2–2.4.

Since the parameter A has no N or ℓ dependence, we ignore it and absorb it in the kinetic prefactor r_0 in Eq. 2.6. Eq. 2.7 then shows that when the cross-linker density N/ℓ is low, the barrier height is proportional to the number of cross-linkers N . The contribution of each linker, B , has an energetic and an entropic component, which can be understood intuitively by noting that at the top of the barrier, on average, $N_R = N_L = N/2$ and each linker is stretched by a distance $\delta/2$: the average potential energy per linker is then $k\delta^2/8$ (see also Fig. 2.13), while the entropy per cross-linker is $\log(2)$. At higher cross-linker densities, however, the cross-linkers increasingly block each other's hops, and the barrier scales exponentially with the cross-linker density N/ℓ .

Combining Eqs. 2.6, 2.7 and 2.1 shows that the friction coefficient increases exponentially with N at low cross-linker density N/ℓ but superexponentially at higher densities:

$$\zeta \propto \exp\left(BN \exp\left(\frac{1}{4B} \frac{N}{\ell}\right)\right). \quad (2.9)$$

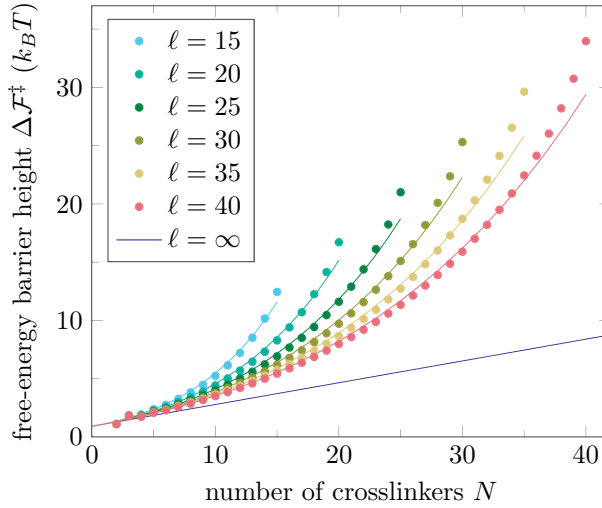


Figure 2.4: The free-energy barrier height $\Delta\mathcal{F}^\ddagger$ increases exponentially with the number of crosslinkers N . The exact values (given by Eqs. 2.2,2.4), plotted as points, are approximated well by the continuous exponential curves as given by Eq. 2.7. Notice that the number of crosslinkers cannot exceed the number of sites on the microtubule, $N \leq \ell$. Furthermore, we plot the approximated barrier height for an infinitely long mobile microtubule, which demonstrates that the barrier height increases linearly with N when the cross-linker density N/ℓ is low. Using Eqs. 2.1 and 2.6, we predict that the friction coefficient ζ increases exponentially with N at low cross-linker densities and superexponentially with N at high densities.

Hence, the crossover to superexponential scaling occurs when $N/\ell \approx 4B$, which means that the critical overlap length l^* at which this scaling sets in increases linearly with N . Yet, because ζ depends not only on N/ℓ but also on N separately, an overlap that is compressed at a high and constant N may effectively stall before the superexponential regime is reached, simply because the friction becomes prohibitive. For the parameter values of Tab. 2.1 and a force of 10 pN [85] this occurs when $N \approx 20$, corresponding to $l^* \approx 200$ nm (see Sec. 2.J). We emphasize however that ζ depends hyper-sensitively on the cross-linker stiffness k and the lattice spacing δ (Eqs. 2.8-2.9); reducing k by 10 percent increases l^* threefold. Hence, different linkers, such as the actin-binder anillin [54], or even other members from the same Ase1/PRC1 family, are expected to have markedly different l^* .

2.4. DISCUSSION

OUR work has revealed how passive cross-linkers cause friction between filaments. If the cross-linkers were to bind to a continuum of binding sites, then the friction coefficient would scale linearly with the number of cross-linkers, as predicted by previous models [42, 55, 59, 70, 72–75]. However, cytoskeletal filaments such as microtubules consist of discrete units, yielding discrete binding sites for the cross-linkers. Moreover, cross-linkers such as Ase1/PRC1 are stiff on the scale of the spacing between the binding sites ($k\delta^2 > k_B T$). These two factors together mean that the lattices of the filaments are preferentially in register, and that the filaments can only move if the cross-linkers reorganize collectively. This latter effect creates a free-energy barrier for filament movement which scales exponentially with the density of cross-linkers (Eq. 2.7). Since the friction between the filaments depends exponentially on the height of the free-energy barrier, the friction depends superexponentially on the density of cross-linkers. In Sec. 2.K we show that cooperative interactions between cross-linkers [40, 86] do not alter the fundamental mechanism for friction generation, and the friction coefficient continues to scale superlinearly with N . While we have studied here a single-protofilament model, we expect that multi-protofilaments exhibit the same scaling, because multiple protofilaments do not alter the basic mechanism that underlies the scaling: filaments jumping between positions where the cross-linker stretching energy is minimized.

The highly non-linear dependence of the friction coefficient ζ on the number of cross-linkers N and the overlap length ℓ has implications in biology, both for the formation of the mitotic spindle [36–50] and the cytokinetic ring [51–54]. Eq. 2.8 shows that the key parameters that control the scaling of ζ with N and ℓ are the lattice spacing δ and the protein stiffness k . To understand the contraction speed of the cytokinetic ring, it will be of interest to estimate k for cross-linkers like anillin [54] since it will determine how rapidly the friction rises when the ring contracts. In the mitotic spindle microtubules are pushed apart by plus-end directed motor proteins [41, 46, 48, 49, 87–90]. Our results indicate that the friction generated by proteins from the Ase1/PRC1 family is highly sensitive to the cross-linker density. As a result, a shrinking overlap region undergoes a sudden increase in the friction coefficient, which will effectively stall the microtubules. Hence, steric hindrance imposes stable overlaps not only by opposing motor stepping [48] but also by dramatically increasing the friction. The overlap length

can be fine-tuned by controlling the number of cross-linkers contained in the overlap, for example by reducing the binding affinity of PRC1 to microtubules through phosphorylation [77].

Our work yields a number of predictions that can be tested experimentally. Firstly, it predicts that cross-linked filaments move via discrete jumps, which can be tested via in vitro gliding assays using microtubules coated with quantum dots, allowing for nanometer precision [91]. Optical tweezers with sub-pN and nanometer resolution could be used to directly measure the free-energy profile [92]. But the most interesting test would be to measure the friction coefficient as a function of N and ℓ , either via the diffusion constant and the Einstein relation (Eq. 2.1) [18], or via an applied load using a stiff optical trap (see Sec. 2.D). Different filament-cross-linker systems, with different protein stiffness k and lattice spacing δ , are now accessible in vitro [18, 54], which should make it possible to test the predicted scaling of Eq. 2.9.

Cross-linker hopping rate h_0	1562.5 s^{-1}
Spring constant k	$1.1 \times 10^5 \text{ k}_B\text{T}/\mu\text{m}^2$
Diffusion constant bare microtubule D_m	$0.01 \mu\text{m}^2 \text{ s}^{-1}$
Lattice spacing binding sites δ	$0.008 \mu\text{m}$

Table 2.1: Model parameters and values. The base hopping rate h_0 was fit to the observed diffusion constant D_s of Ase1 on single microtubules, and subsequently k was fit to the observed diffusion constant D_d between two microtubules (see Sec. 2.A). D_m was estimated from previously reported experiments (see Sec. 2.B). δ approximately equals the tubulin dimer length.

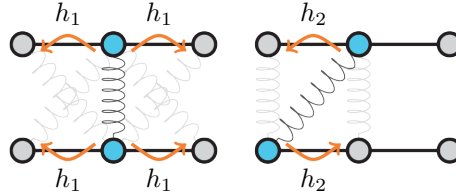


Figure 2.5: Possible transitions for a diffusing cross-linker in an overlap region. For the estimation of the diffusion constant, we assume that the two microtubules stay fixed relative to each other, and that they are perfectly aligned. Then, cross-linkers can be either in a relaxed straight (left) or stretched diagonal (right) state. When we only focus on transitions towards one direction, e.g. the left, then there are two possible transitions from the straight position, whereas there is only one possible transition from the diagonal state.

APPENDIX

2.A. ESTIMATE OF SPRING CONSTANT REVISITED

THE model parameters were previously estimated from experimental data [18]. Specifically, the spring constant was estimated by measuring the diffusion constant of linkers on a single microtubule D_s (s for singly bound), and the diffusion constant of cross-linkers in an overlap region D_d (d for doubly bound). There, measurement of the mean square displacement as a function of time gave values of $D_s = 0.085(7) \mu\text{m}^2 \text{ s}^{-1}$ and $D_d = 0.011(3) \mu\text{m}^2 \text{ s}^{-1}$. Then, the spring constant was fitted by varying it in simulations until the simulated diffusion constant roughly matched the measured one, giving a value of $k = 5 \times 10^4 \text{ k}_B\text{T}/\mu\text{m}^2$, where they used a lattice spacing of 10 nm. Here, we present an analytical expression for the spring constant in terms of the measured diffusion constants.

First, consider the diffusion of a single linker on one microtubule. We assume that the hopping rate of one head equals h_0 . Then, when the lattice spacing $\delta = 8 \text{ nm}$ is taken into account, we get the diffusion constant $D_s = h_0 \delta^2$. For consistency with previous work, we use $h_0 = 1562.5 \text{ s}^{-1}$ [18].

The diffusion of a doubly bound cross-linker in an overlap region is more complicated, as several different transitions are possible. We assume that the microtubule does

not move (much) during this diffusion, since the time scale of microtubule movement is much longer than that of individual cross-linker hopping. Then, the cross-linker can be either in a straight or in a diagonal state, as shown in Fig. 2.5. Ignoring the finite overlap length, we label the straight states with even numbers, and the diagonals with odd numbers. For example, a transition from state 0 to state 1 represents a hop of a straight linker to a diagonal on the right. Both possible diagonal configurations, which are indicated in the left illustration of Fig. 2.5, are grouped into one state. We can call this number $Z(t) \in \mathbb{Z}$, and it relates to the physical position of the center of the cross-linkers x through

$$x(t) = \frac{\delta}{2} Z(t). \quad (2.10)$$

$Z(t)$ defines a Markov chain on the integers (a two-sided birth-death process), with probabilities $p_n(t)$ to be in state n at time t . The time derivatives of these probabilities are set by the transition rate to leave a straight conformation, h_1 , and the rate to leave a diagonal conformation, h_2 . These time derivatives are different for the straight state probabilities ($n = 2m$) and diagonal state probabilities ($n = 2m + 1$),

$$\begin{aligned} \partial_t p_{2m} &= -2h_1 p_{2m} + h_2 p_{2m-1} + h_2 p_{2m+1} \\ \partial_t p_{2m+1} &= -2h_2 p_{2m+1} + h_1 p_{2m} + h_1 p_{2m+2}. \end{aligned} \quad (2.11)$$

The hopping rates equal

$$\begin{aligned} h_1 &= 2h_0 \exp\left(-\frac{1}{4} k\delta^2\right) \\ h_2 &= h_0 \exp\left(\frac{1}{4} k\delta^2\right), \end{aligned} \quad (2.12)$$

where h_0 is the rate prefactor. We can calculate the long time diffusion constant of the hopping cross-linkers from Eq. 2.11. To that end, we look at the mean square displacement and take its time derivative,

$$\begin{aligned} \partial_t \langle Z(t)^2 \rangle &= \partial_t \sum_{n=-\infty}^{\infty} n^2 p_n(t) = \sum_{m=-\infty}^{\infty} \left\{ (2m)^2 \partial_t p_{2m}(t) + (2m+1)^2 \partial_t p_{2m+1}(t) \right\} \\ &= \sum_{m=-\infty}^{\infty} \left\{ (2m)^2 [-2h_1 p_{2m} + h_2 p_{2m-1} + h_2 p_{2m+1}] \right. \\ &\quad \left. + (2m+1)^2 [-2h_2 p_{2m+1} + h_1 p_{2m} + h_1 p_{2m+2}] \right\} \\ &= \sum_{m=-\infty}^{\infty} \left\{ [-2(2m)^2 + (2m+1)^2 + (2m-1)^2] h_1 p_{2m} \right. \\ &\quad \left. + [-2(2m+1)^2 + (2m+2)^2 + (2m)^2] h_2 p_{2m+1} \right\} \\ &= 2h_1 \sum_{m=-\infty}^{\infty} p_{2m} + 2h_2 \sum_{m=-\infty}^{\infty} p_{2m+1}. \end{aligned} \quad (2.13)$$

Then, we use that in steady state, the probability to be in an even or in an odd state is

$$\begin{aligned}\sum_{m=-\infty}^{\infty} p_{2m} &= \frac{h_2}{h_1 + h_2}, \\ \sum_{m=-\infty}^{\infty} p_{2m+1} &= \frac{h_1}{h_1 + h_2}.\end{aligned}\quad (2.14)$$

Then we combine Eq. 2.13 and Eq. 2.14, together with its relation with the mean square displacement of the physical position through Eq. 2.10,

$$\partial_t \langle x(t)^2 \rangle = \delta^2 \frac{h_1 h_2}{h_1 + h_2} = 2D_d. \quad (2.15)$$

The final equality follows from the standard relation between the mean square displacement in one dimension and the diffusion constant. Then we can insert the definitions of the rates, Eq. 2.12, and solve the equation for the spring constant k . This gives us

$$k = \frac{2}{\delta^2} \left[\log(2) + 2 \operatorname{arcCosh} \left(\frac{D_s}{2\sqrt{2}D_d} \right) \right]. \quad (2.16)$$

Here, we used the simple relation $D_s = \delta^2 h_0$ to rewrite the result in terms of the diffusion constant. Evaluating this expression for the experimentally measured quantities gives $k = 1.26 \times 10^5 \text{ k}_B \text{ T} / \mu\text{m}^2 = 0.51 \text{ pN nm}^{-1}$. This value is similar to a previously reported value for a single kinesin motor, 0.3 pN nm^{-1} [78], a single myosin motor, 1.2 pN nm^{-1} [68], or tau protein, 0.25 pN nm^{-1} [80]. The value is two or three orders of magnitude lower than the spring constant related to the folding dynamics of an actin cross-linker [79]. We chose to use the value $k = 1.1 \times 10^5 \text{ k}_B \text{ T} / \mu\text{m}^2 = 0.45 \text{ pN nm}^{-1}$ in this study. A summary of the model parameters is given in Tab. 2.1.

2.B. SIMULATION DYNAMICS

Cross-linkers exert pulling forces on the microtubule, and the net force F causes it to move. We only allow the microtubule to move in one dimension, and consider the drag between the mobile microtubule and the fluid to be in the overdamped regime. Hence, we can model the time evolution of the microtubule position x using Brownian dynamics,

$$\frac{dx}{dt} = \frac{F}{\gamma_m} + \eta. \quad (2.17)$$

Here, the γ_m is the drag coefficient of the mobile microtubule when it is not linked by cross-linkers, and η is the thermal noise. The noise amplitude is set by the bare microtubule diffusion constant D_m , and is related to γ_m through the Einstein relation [28],

$$\gamma_m = \frac{k_B T}{D_m}. \quad (2.18)$$

Previously, the diffusion constant was estimated [18] from a formula for the parallel translational drag coefficient [81], which gives us $D_m = 0.01 \mu\text{m}^2 \text{ s}^{-1}$ independent of microtubule length. In simulations, we assume F to be constant during finite time steps of

size Δt , and update the microtubule position with the deterministic term and a Gaussian noise term,

$$\Delta x = \frac{D_m}{k_B T} F \Delta t + \sqrt{2D_m \Delta t} \mathcal{N}. \quad (2.19)$$

Here, \mathcal{N} denotes a Gaussian random variable with zero mean and unit standard deviation.

The net force on the microtubule F depends on the full system state, so both on the position x and on the number of right-pulling cross-linkers N_R . Furthermore, when some cross-linkers get close to their maximum stretch of δ , not all values of Δx are allowed. The maximum stretch of the cross-linkers is taken into account by placing reflective boundary conditions on η . We implement the algorithm by first updating the position using the deterministic term, since deterministic change never causes Δx to cross a boundary imposed by the cross-linkers. Then, we calculate the boundary b for the stochastic term \mathcal{N} , and if \mathcal{N} passes b , we reflect the term through

$$\mathcal{N} \rightarrow 2b - \mathcal{N}. \quad (2.20)$$

Besides the top microtubule, also the cross-linkers are dynamic. To model the Brownian motion of cross-linkers within the overlap, both ends of the linkers can hop to neighboring sites. This thermally driven process needs to obey detailed balance,

$$\frac{h(x)}{h(\delta - x)} = \exp(-\beta \Delta U(x)), \quad (2.21)$$

where $h(x)$ is the rate at which one head of a left-pulling linker hops to a right-pulling position, and $\beta = 1/k_B T$. The system is invariant under reflections where $R \leftrightarrow L$ and $x \leftrightarrow \delta - x$, so the reverse process where the head of a right-pulling linker hops occurs at the rate $h(\delta - x)$. The potential energy difference $\Delta U(x)$ between a left- and right-pulling linker is given by

$$\Delta U(x) = U_R(x) - U_L(x) = \frac{1}{2} k (\delta - x)^2 - \frac{1}{2} k x^2. \quad (2.22)$$

Notice that for this formula for potential energy to hold, we have defined the filament position x such that $x = 0$ corresponds to a position where the cross-linkers are at rest. If x' is the filament position in the frame of reference where the filaments are physically in register at $x' = 0$, and the cross-linkers have a finite rest length such that they are at rest when $x' = a$, then we redefine $x = x' - a$, such that Eq. 2.22 continues to hold.

We choose the simplest rate function $h(x)$ that obeys detailed balance and the symmetry of the system,

$$h(x) = h_0 \exp\left(-\frac{1}{2} \beta \Delta U(x)\right). \quad (2.23)$$

Here, h_0 is the hopping rate when there is no change in stretch upon a hop, i.e. for $x = \delta/2$. To estimate h_0 , we also assume that a cross-linker diffusing on a single microtubule hops with this rate.

We use a kinetic Monte Carlo algorithm to simulate the cross-linker dynamics [82]. First, we calculate the full rate

$$H(t) = \sum_i h_i(x, t). \quad (2.24)$$

To decide the next moment at which a reaction will take place, we draw a uniform random number ξ between 0 and 1, which represents a survival probability $S(t)$, for which

$$S(t) = \exp\left(-\int_0^t dt' H(t')\right). \quad (2.25)$$

We choose the time steps small enough to keep the rate $h(x, t)$ nearly constant between steps, such that we can approximate the time integral as a sum over time steps,

$$\int_0^t dt' H(t') \approx \sum_{n=1}^{t/\Delta t} H(n\Delta t) \Delta t. \quad (2.26)$$

In the simulations, we update the integral after each time step, and a hop is performed when the integrated total rate reaches a threshold value given by ξ ,

$$\sum_{n=1}^{t/\Delta t} H(n\Delta t) > -\frac{\log(\xi)}{\Delta t} \quad (2.27)$$

After the hop, a new value of ξ is drawn and the integral is reset to 0.

2.C. MICROTUBULE JUMP RATE SETS THE DIFFUSION CONSTANT

The mobile microtubule moves in a discrete fashion on macroscopic time scales, as indicated in Fig. 2.2. The filament makes jumps of size δ , which equals one tubulin dimer length, to the left or right at random points in time. We are interested in describing these jumps as a memoryless process, with a fixed rate of jumping in a random direction. In this section, we show that on average the waiting times between microtubule jumps are exponentially distributed and the directions of the jumps are split evenly, as expected for a memoryless process. However, we then show that long time correlations can persist due to the cross-linker distribution within the overlap, which causes the real diffusion constant of the system to diverge from what is expected of a memoryless process. However, these long time correlations vanish when the time between jumps becomes long enough, showing that the jumps are approximately Markovian for large free-energy barriers.

First, we check that the distribution of dwell times is exponential, which is required in a memoryless process. We measure the jump rate by tracking the position of the microtubule $X(t)$ and defining its basin of attraction $Z(t)$, where $Z(t) \in \mathbb{Z}$ labels the wells in the free-energy profile that are separated by δ . For the initial basin of attraction, we set

$$Z(0) = \left\lfloor \frac{X(0)}{\delta} + \frac{1}{2} \right\rfloor. \quad (2.28)$$

After, we check whether a jump occurred at every time step. We register a microtubule jump when

$$X(t) < (Z(t) - 1)\delta \vee X(t) > (Z(t) + 1)\delta, \quad (2.29)$$

after which we decrement or increment $Z(t)$, respectively, and we record the last waiting time T between jumps.

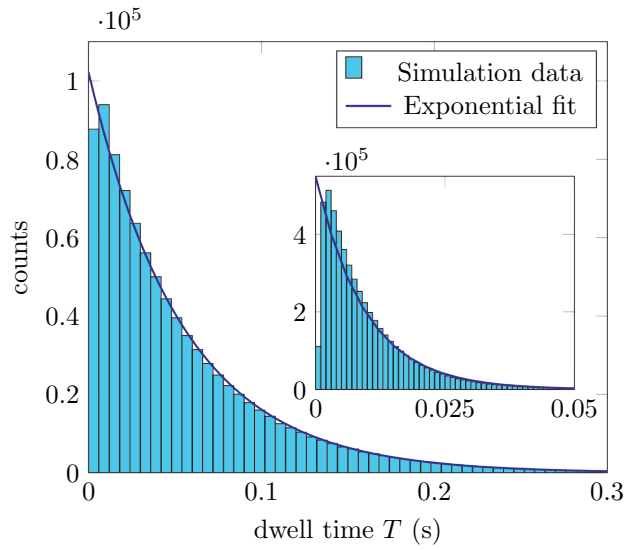


Figure 2.6: Histogram of the dwell times T at certain lattice positions, as observed for a system with $N = 12$ and $\ell = 40$. The line shows an exponential distribution with rate $2r = 1/\bar{T}$, where r is the rate to jump in one of the two directions. (inset) The same analysis, but for $N = 6$ and $\ell = 40$, showing a larger deviation from the exponential for small times.

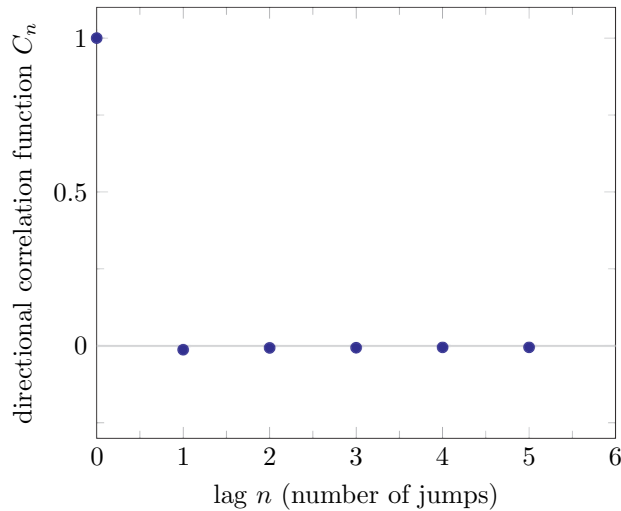


Figure 2.7: Autocorrelation function of the jump direction. The jump direction is either $+1$ or -1 , and we calculate the correlation between this random variable with its value n jumps ago, C_n . The correlation in the direction of subsequent jumps is very small.

We plot a histogram of observed dwell times in Fig. 2.6. The histogram shows an exponential distribution, as is expected for a continuous time Markov chain. We estimate the rate of jumping using the maximum likelihood estimator

$$\bar{r} = \frac{1}{2\bar{T}} = \frac{n}{2\sum_{i=1}^n T_i}, \quad (2.30)$$

where T_i are the n different samples of the waiting time between two microtubule jumps. The factor 2 in the denominator compensates for the fact that the microtubule can jump in two directions. Then, to compare the estimated exponential distribution to the histogram of dwell times, we need to calculate the expected number of counts in each bin. We call the bin width δT , which means that bin i captures values of T between $(i-1)\delta T$ and $i\delta T$. The number of expected counts in bin i is

$$n_i = n \int_{(i-1)\delta T}^{i\delta T} r e^{-rt} dt = 2 \sinh\left(\frac{r\delta T}{2}\right) e^{-(i-\frac{1}{2})r\delta T} = 2 \sinh\left(\frac{r\delta T}{2}\right) e^{-r\sigma}. \quad (2.31)$$

We call $\sigma = (i - \frac{1}{2})\delta T$ the continuous time axis of the histogram. This choice ensures that the exponential fit coincides with the centres of bins. As can be seen in Fig. 2.6, the histogram deviates little from the exponential fit when $\ell = 40$ and $N = 12$, where the barrier height $\Delta\mathcal{F}^\ddagger = 4.2k_B T$. For smaller barrier heights, e.g. for $\ell = 40$ and $N = 6$ with a barrier height of just $\Delta\mathcal{F}^\ddagger = 2.3k_B T$, there starts to be a noticeable deviation for small times, as shown in the inset of Fig. 2.6. Specifically, for low barriers the lack of events with small waiting times becomes stronger, because it takes time to cross the barrier and equilibrate in the valley. For high barriers, the typical timescale between jumps is so long that the time it takes to cross the barrier is negligible. Hence, at least for moderately high barriers, the jump times appear reasonably memoryless.

Additionally, we test for correlations in the jump directions J_i . The directions of forward and backward jumps are described by $J_i = \pm 1$, where i labels the jumps. Then, we calculate the correlation function

$$C_n = \langle J_i J_{i+n} \rangle - \langle J_i \rangle^2. \quad (2.32)$$

As shown in Fig. 2.7, the autocorrelation function does not show significant correlations between subsequent jumps.

The results from Fig. 2.6 and Fig. 2.7 combined suggest that the microtubule movement can be described by a Markov process with jump rate r as its only parameter. In that case the diffusion constant is given directly by the rate,

$$D = r\delta^2. \quad (2.33)$$

To test Eq. 2.33, we calculate the diffusion constant separately by calculating the mean squared displacement over time and fitting a linear curve. To this end, we probe the microtubule position $X(t)$ at a discrete time step Δt , such that $t_i = i\Delta t$ and i is a natural number. Then we calculate the variance of the microtubule position at some delay θ , which is a discrete number of time steps,

$$\bar{V}_\theta = \frac{1}{N-\theta-1} \sum_{i=1}^{N-\theta} \left(X(t_{i+\theta}) - X(t_i) - \bar{X}_\theta \right)^2, \quad (2.34)$$

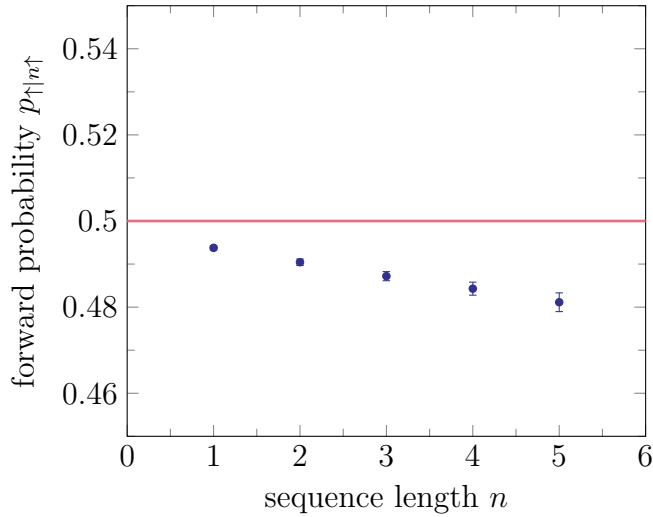


Figure 2.8: The probability that the next microtubule jump is forward (backward), given that it follows a sequence of n jumps that were all forward (backward). The first point, $p_{1\uparrow}$, equals the probability that a jump is in the same direction as the previous one. The deviation from 0.5 of this first point is linearly related to the (very small) deviation from 0 of the point at lag 1 in Fig. 2.7 through Eq. 2.50. The decreasing probability of forward jumps following a sequence in the same direction shows that long sequences of forward jumps are less likely than in a true Bernoulli process with $p = 1/2$, where points should fall on the red line, and that correlations build up depending on an extended history.

with

$$\bar{X}_\theta = \frac{1}{N-\theta} \sum_{i=1}^{N-\theta} (X(t_{i+\theta}) - X(t_i)). \quad (2.35)$$

Then, we calculate the diffusion constant by systematically varying θ and fitting the relation

$$\bar{V}_\theta = 2\bar{D}\Delta t\theta, \quad (2.36)$$

which is a simple least squares fit of the linear function in θ .

We compare the result of the diffusion constant that we obtain through this direct method with the value that we predict from the microtubule jump rate using Eq. 2.30. For $\ell = 40$ and $N = 12$, we obtain a value of

$$\bar{D} = (4.952 \pm 0.009) \times 10^{-4} \mu\text{m}^2 \text{s}^{-1} \quad (2.37)$$

using the direct method, whereas we obtain a value of

$$\bar{D} = (5.909 \pm 0.007) \times 10^{-4} \mu\text{m}^2 \text{s}^{-1} \quad (2.38)$$

using Eq. 2.33 and Eq. 2.30. These results differ significantly.

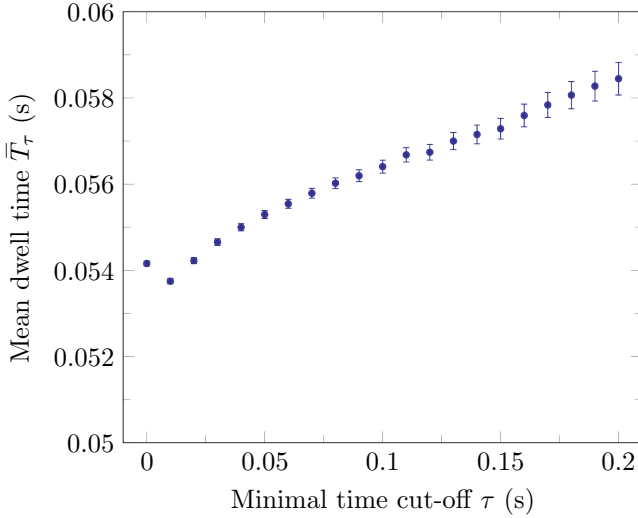


Figure 2.9: The sample mean \bar{T}_τ of all those dwell times between the jumps that are greater than τ , subtracted by the introduced bias τ , as shown in Eq. 2.39. When the distribution of dwell times is perfectly exponential, this estimate is independent of τ . Here, we use the simulation data for $\ell = 40$ and $N = 12$ to show that the dwell times shown in Fig. 2.6 are not exponentially distributed perfectly, indicating that the system retains some memory of the previous jump for times longer than the mean dwell time, since the average keeps rising even for $\tau > 3\bar{T}_0 = 0.16$ s.

To investigate the origin of this discrepancy, we focus more closely on correlations between the jump times and jump directions.

Even though Fig. 2.6 shows that the waiting time distribution between jumps differs little from an exponential distribution, we can calculate how the difference affects Eq. 2.33. First, we estimate whether the waiting time distribution differs from an exponential for small time scales. We call $\{T\}_{>\tau}$ the set of measured waiting times larger than τ , and $N_{>\tau}$ the size of this set. Then the mean waiting time can be estimated as

$$\bar{T}_\tau = \left(\frac{1}{N_{>\tau}} \sum_{t \in \{T\}_{>\tau}} t \right) - \tau. \quad (2.39)$$

This equation is only correct when the waiting time distribution is exponential, in which case \bar{T}_τ is independent of τ . However, if the distribution is not exactly exponential, the estimate of the mean time between jumps will change by changing τ . In Fig. 2.9, we plot \bar{T}_τ against τ , showing that the mean dwell time is not fully independent of the cut-off τ . For very small τ , \bar{T}_τ decreases with τ , while it increases with τ for larger values. This means that very small dwell times are underrepresented compared to an exponential distribution, whereas longer dwell times are increasingly overrepresented. The latter excess of long dwell times shows up after more than three times the average dwell time, showing that even though the memory effect is small, the system retains its memory of

the previous jump long enough to significantly break the assumption that the microtubule jumps are fully Markovian.

Since we observe that the dwell time distribution is not perfectly exponential, we test if this can cause the breakdown of Eq. 2.33. We assume that there are no correlations among the directions of the microtubule jumps, such that each jump direction follows a simple Bernoulli distribution with probability $p = 1/2$, and we assume an arbitrary waiting time distribution $f(t)$. To find a relation between the diffusion constant and this waiting time distribution, we define the probability

$$p_n(t) \equiv \mathbb{P}(Z(t) = n \mid Z(0) = 0). \quad (2.40)$$

The distribution of dwell times is related to this positional distributions via

$$p_n(t) = \delta_{0,n} \left(1 - \int_0^t f(t') dt'\right) + \int_0^t f(t') \frac{1}{2} (p_{n+1}(t-t') + p_{n-1}(t-t')) dt', \quad (2.41)$$

which makes use of the homogeneity under translations of n , and where $\delta_{0,n}$ gives the Kronecker delta. Then, we take the Laplace transform of Eq. 2.41, giving

$$\tilde{p}_n(s) = \frac{\delta_{0,n}}{s} (1 - \tilde{f}(s)) + \tilde{f}(s) \frac{1}{2} (\tilde{p}_{n+1}(s) + \tilde{p}_{n-1}(s)). \quad (2.42)$$

These equations give us relations on the Laplace transforms of the moments of $Z(t)$,

$$\langle \tilde{Z}^k(s) \rangle = \sum_{n=-\infty}^{\infty} n^k \tilde{p}_n(s). \quad (2.43)$$

Inserting Eq. 2.42 into Eq. 2.43 for $k = 1$ and $k = 2$, we find

$$\begin{aligned} \langle \tilde{Z}(s) \rangle &= \tilde{f}(s) \langle \tilde{Z}(s) \rangle, \\ \langle \tilde{Z}^2(s) \rangle &= \tilde{f}(s) \left(\langle \tilde{Z}^2(s) \rangle + \frac{1}{s} \right). \end{aligned} \quad (2.44)$$

The solution to Eq. 2.44 read

$$\begin{aligned} \langle \tilde{Z}(s) \rangle &= 0, \\ \langle \tilde{Z}^2(s) \rangle &= \frac{\tilde{f}(s)}{s(1 - \tilde{f}(s))}. \end{aligned} \quad (2.45)$$

Hence, the variance of the position can be found from the waiting time distribution if there are no correlations in the step direction. More specifically, we can make a Taylor expansion for $\tilde{f}(s)$ in s around 0, and use that the Laplace transform is the moment generating function for the waiting time T ,

$$\tilde{f}(s) = 1 - s\langle T \rangle + \mathcal{O}(s^2). \quad (2.46)$$

By inserting this in Eq. 2.45, we find

$$\langle \tilde{Z}^2(s) \rangle = \frac{1 - s\langle T \rangle + \mathcal{O}(s^2)}{s(s\langle T \rangle + \mathcal{O}(s^2))} = \frac{1}{s^2\langle T \rangle} + \mathcal{O}\left(\frac{1}{s}\right). \quad (2.47)$$

We take the inverse Laplace transform to find a relation for the diffusion constant,

$$\langle Z^2(t) \rangle = \frac{t}{\langle T \rangle} + \mathcal{O}(t^0). \quad (2.48)$$

Then, the dominant long time behaviour of the variance of $Z(t)$ leads to an expression of the diffusion constant,

$$D = \lim_{t \rightarrow \infty} \frac{\text{Var}(X(t))}{2t} = \lim_{t \rightarrow \infty} \frac{\delta^2 \text{Var}(Z(t))}{2t} = \frac{\delta^2}{2\langle T \rangle}. \quad (2.49)$$

Hence, if there are no cross-correlations between subsequent step directions and waiting times, we can calculate the diffusion constant from the average waiting time in the well. As described before, Eq. 2.49 is exactly the relation that breaks down for our system. Hence, the discrepancy between Eq. 2.37 and Eq. 2.38 cannot be explained by looking at the waiting time distribution alone, since Eq. 2.33 is true independent of the waiting time distribution when there are no dependencies between the jump directions. We conclude that the only possible explanation lies in correlations that must exist between the directions and waiting times of the microtubule jumps.

Using the simulations, we estimate the probability that the next microtubule jump is forward given that the last n jumps were all forward as well, $p_{|1|n\uparrow}$. Since the system dynamics is symmetric under reflection of the x-axis, it does not matter whether we focus on forward or on backward jumps here. If we calculate the probability that a particle jumps in the same direction as the previous jump, $p_{|1|\uparrow}$, we find a value that is slightly but significantly less than 0.5, as can be seen in the first point of Fig. 2.8. The probability of a subsequent forward jump $p_{|1|\uparrow}$ is related to the correlation function at lag 1 described in Eq. 2.32,

$$C_1 = 2p_{|1|\uparrow} - 1. \quad (2.50)$$

Hence, $p_{|1|\uparrow}$ being lower than 0.5 leads to C_1 being slightly but significantly lower than 0, which can be seen in Fig. 2.7 for the correlation at lag 1.

We hypothesize that the slight correlation in the jump directions is due to the fact that cross-linkers require time to redistribute themselves uniformly within the overlap. When there is a forward jump of the microtubule, the cross-linkers will be more likely to be in the back than in the front of the overlap region. This process would be accumulative, since the next forward jump increases the cross-linker excess in the back even more. We test this hypothesis by calculating the probability of a forward jump as a function of the number of previous jumps that were also forward. As shown in Fig. 2.8, the probability of a new forward jump indeed decreases with the sequence length, and it plateaus at some value where the diffusive forward flux of reorganizing cross-linkers equals the backward flux of cross-linkers due to the successive microtubule jumps. This indeed supports the idea that weak but significant correlations persists in the hopping of the top filament: the more steps it has made consecutively in one direction, the more likely it will be that the next step is in the opposite direction.

The net effect of these correlations lowers the diffusion constant, since the probability is higher that the microtubule moves back to where it came from. In other words, the effective diffusion constant over long time scales is lower than expected from the jump rate alone through Eq. 2.33. The probabilities to have subsequent jumps in the

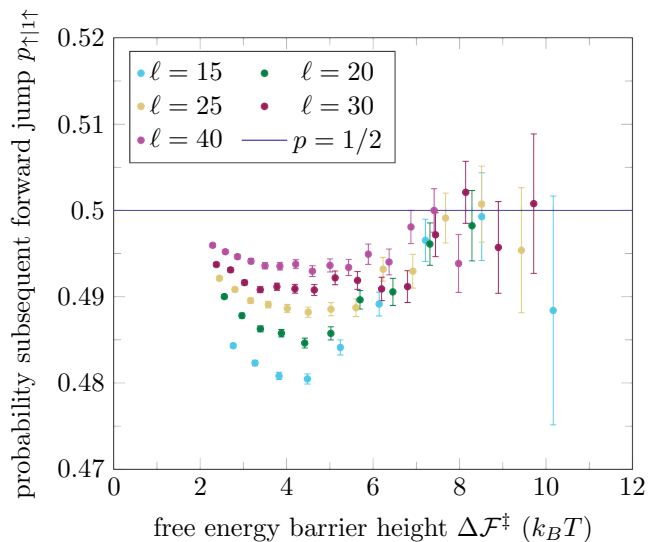


Figure 2.10: The probability that the next microtubule jump is forward (backward), given that the previous jump was also forward (backward) as a function of the free-energy barrier height. The barrier height was changed by varying the number of cross-linkers N for different overlap lengths ℓ . For high barriers, the correlation time of the bias becomes lower than the average waiting time between jumps, and the bias disappears. The statistics become worse for larger barriers since the frequency of jumps decreases.

same direction are only slightly lower than 0.5 but are persistent, causing a significantly lower diffusion constant. Hence, there is a correlation time in the jump directions that is caused by the redistribution of cross-linkers within the overlap region, causing the Markovianity assumption, which underlies Eq. 2.33, to break down.

However, the barrier height in the system for which we found the values for the diffusion constant given in Eq. 2.37 and Eq. 2.38 was relatively low, i.e. $4.2k_B T$. Fig. 2.18 shows that the waiting time between microtubule jumps increases strongly with the barrier height, and the cross-linkers redistribute themselves over the overlap during this waiting time, equilibrating the system. Thus, we expect that the bias towards reversing the jump direction will vanish when the waiting time in the well becomes longer than the timescale for equilibrating the cross-linker distribution within the overlap region.

To investigate this, we show the probability that a jump is in the same direction as the previous one, $p_{\uparrow\uparrow\uparrow}$, as a function of the free-energy barrier height in Fig. 2.10. As expected, the deviation from $p_{\uparrow\uparrow\uparrow} = 1/2$ disappears for high barriers, since the cross-linkers have enough time to reorganize themselves within the overlap between microtubule jumps. The probability also appears to come closer to $p_{\uparrow\uparrow\uparrow} = 1/2$ for low barriers, which is probably due to the low number of cross-linkers involved in these small barriers, which makes it easier to redistribute them. We conclude that we can safely use Eq. 2.33 for high barriers, and that we will underestimate the actual friction when the free-energy barrier is lower than $8k_B T$.

2.D. DEVIATIONS FROM THE EINSTEIN RELATION

Previously, we calculated the friction in the linear-response regime using the Einstein relation Eq. 2.1. This allows us to study the system in equilibrium, where we can find analytical expressions for the free-energy profile and the microtubule jump rate.

We can also measure the friction coefficient directly by applying a force on the mobile filament, and dividing the applied force by the mean observed velocity. For small forces, we expect that this friction coefficient is independent of the applied force and that it equals the reciprocal of the diffusion constant. However, for higher external forces the system does not have time to equilibrate fully in between jumps any more, leading to a deviation of the friction coefficient from its linear-response value.

We test this in simulations, where we plot the observed friction coefficient as a function of the applied force in Fig. 2.11. We see that in the linear-response regime of low external force, the friction coefficient agrees with that as computed via the diffusion constant and the Einstein relation Eq. 2.1.

Yet, for higher forces the friction coefficient deviates from that predicted by the Einstein relation, because at higher speeds the cross-linkers do not fully re-equilibrate in the overlap in between the filament jumps. More specifically, we expect that this deviation takes place when the drift velocity causes a rate of forward jumps that is comparable to the equilibrium rate of jumps in random directions r . Hence, we expect a deviation from the linear-response regime when the microtubule velocity is roughly

$$v_{\text{dev}} \approx r\delta. \quad (2.51)$$

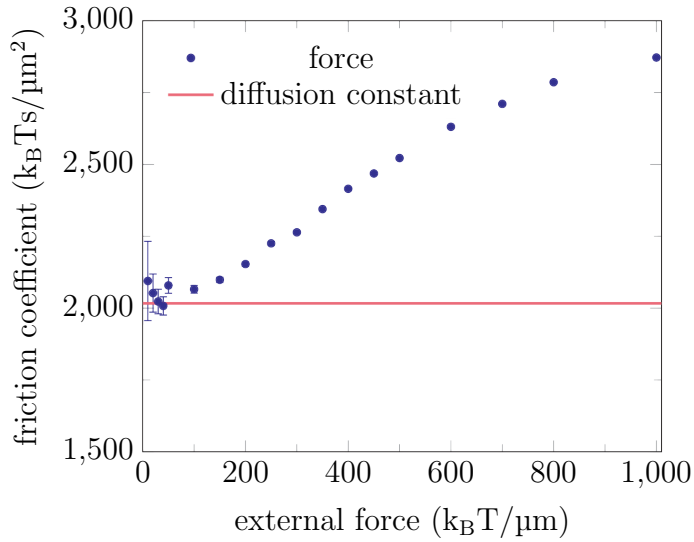


Figure 2.11: Estimating the friction of a microtubule with $N = 12$ and $\ell = 40$. We measure the friction coefficient ζ by applying an external force F and observing the mean velocity \bar{v} of the microtubule, giving $\zeta = F/\bar{v}$. Points are the result of 3×10^5 s of model dynamics in the simulations, error bars give the standard deviation of the mean. The friction coefficient is initially constant and increases for higher forces. Then, we estimate the diffusion constant and calculate the linear-response friction coefficient from it using the Einstein relation Eq. 2.1, and show the obtained value as a red line. We calculate the diffusion constant from the positional variance at zero force (Eq. 2.36), which gives the linear-response value of the friction coefficient. $1000 k_B T / \mu m$ equals roughly 4.1 pN at room temperature.

Since the friction coefficient equals

$$\zeta = \frac{k_B T}{D} = \frac{k_B T}{r \delta^2}, \quad (2.52)$$

we expect to observe non-equilibrium effects on the friction from an externally applied force of roughly

$$F_{\text{dev}} = \zeta v_{\text{dev}} \approx \frac{k_B T}{\delta} = 125 k_B T / \mu\text{m}. \quad (2.53)$$

Fig. 2.11 shows that the deviation from the friction coefficient as predicted by the Einstein relation indeed arises around the point predicted by Eq. 2.53. At higher speeds the cross-linkers do not fully redistribute themselves over the overlap in between the filaments jumps, but instead accumulate at the trailing edge of the overlap region, increasing the cross-linker density, and hence the friction coefficient.

In conclusion, the friction coefficient estimated from the force and drift velocity agrees very well with the friction coefficient estimated from the diffusion constant and the Einstein relation (Eq. 2.1) in the linear-response regime of a small external force. Moreover, as discussed in Sec. 2.C, the diffusion constant can be directly obtained from the jump rate via Eq. 2.33 provided that the barrier is high enough.

2.E. CONFIGURATION COMBINATORICS FOR ENTROPY CALCULATION

We describe a transition of the system through the change of the relative microtubule position and the number of right-pulling cross-linkers. These quantities act as our order parameters, where a transition means that the microtubule position changes by one lattice spacing δ and the number of right-pulling linkers changes by the total number of cross-linkers N . To find a description for the transition rate, we require the free-energy profile as a function of these order parameters.

In our model, the potential energy only depends on x and N_R , and is not influenced by other details of the system configuration. This lets us describe the entropy as the logarithm of the number of microstates $\Omega(x, N_R)$ at a given x and N_R . Furthermore, the number of microstates is independent of the position x , since the amount of stretch does not change the classification into left- and right-pulling linkers, as shown in Fig. 2.12. Hence,

$$S(x, N_R) = k_B \log(\Omega(N_R)). \quad (2.54)$$

To calculate $\Omega(N_R)$ we use the mapping depicted in Fig. 2.12. There, we decompose the microstate into a set of blocks that group together different sets of microtubule sites and cross-linkers. Each left-pulling linker is placed in its own box spanning a single site called an L -block, whereas all neighboring right-pulling linkers are grouped together into a single R -block. The latter is done to take into account the variable number of sites excluded by right-pulling linkers when they are alone or in contact with other diagonally placed linkers. Finally, the remaining sites are called holes and grouped into H -blocks. In Tab. 2.2, we calculate the number of blocks of each type by counting the number of sites that are occupied by each type. The numbers of R - and H -blocks are

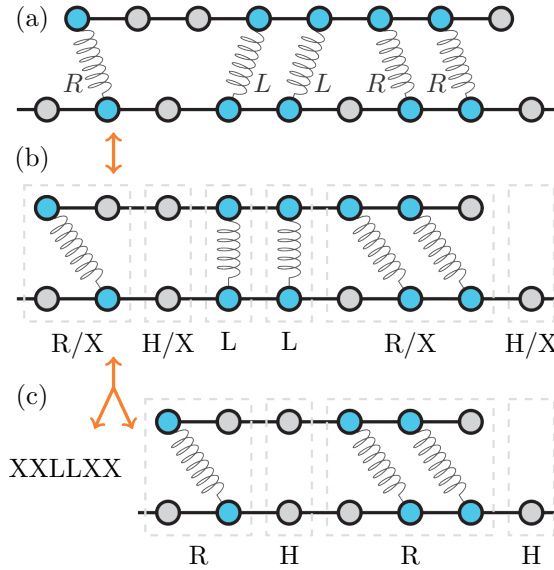


Figure 2.12: Map to calculate the number of configurations given the number of right-pulling cross-linkers N_R . Here, we show an example configuration with $\ell = 8$, $N = 5$, and $N_R = 3$. (a) The number of ways to place N_R R linkers and $N - N_R$ L linkers in the overlap does not depend on the mobile microtubule position x . Hence, for the purpose of counting configurations, we can ignore the exact alignment of the microtubules and focus on the combinatorics of linker placement. (b) In the picture where L linkers are straight, they always exclude one site on the top microtubule. However, groups of adjacent R linkers always exclude one more site. It is helpful to draw boxes around each unit, which can be an L linker (L -block), a hole (H -block), or a set of adjacent R linkers (R -block). The last block cannot be an L -block. The number of R - and H -blocks together always equals $\ell + 1 - N + N_R$, and we alternatively label those X -blocks, to contrast with L -blocks. (c) There are always $N - N_R$ L -blocks, and removing all L -blocks leaves a system with the same number of X -blocks, since none of those merge. This means that each configuration can be split into an arrangement of L - and X -blocks, and into a specific organization of the cross-linkers within the microtubule with all L -blocks removed. The arrows represent the bijective mapping between the set of linker configurations in (a) and (c).

Block type	Number of blocks	Number of excluded sites
L	$N - N_R$	$N - N_R$
R	m	$N_R + m$
H	$\ell + 1 - N - m$	$\ell + 1 - N - m$
$X = R \vee H$	$\ell + 1 - N$	$\ell + 1 - N + N_R$
all	$\ell + 1 - N_R$	$\ell + 1$

Table 2.2: The number of blocks and number of sites excluded for each type of block. The number of R blocks varies among configurations, and is called m here. The X -blocks are a name for the ensemble of R - and H -blocks, which are grouped together since their number is independent of the only variable m .

variable, but it turns out that their sum is constant. Therefore, we group these two types under a new block name, called X -blocks. Each configuration of the microtubule has a unique representation as a permutation of $\ell + 1 - N$ X -blocks and $N - N_R$ L -blocks, with $\ell + 1 - N_R$ blocks in total. Additionally, the last of these blocks always needs to be an X -block, since L -blocks cannot occupy the final site where there is no site available on the mobile microtubule. Hence, the number of ways to permute the L - and X blocks among each other is

$$\Omega_1(N_R) = \frac{(\ell + 1 - N_R - 1)!}{(\ell + 1 - N - 1)!(N - N_R)!} = \binom{\ell - N_R}{N - N_R}, \quad (2.55)$$

where the -1 terms are due to the final block always being an X .

$\Omega_1(N_R)$ captures all permutations of the left side of Fig. 2.12(c), which leaves us with calculating the number of permutations of the remaining blocks. Since removing an L block never merges two neighboring blocks together, we can remove all straight cross-linkers without changing the order of X blocks. Finally, we see that we are left with $\ell - N + N_R$ sites on the mobile microtubule with N_R linkers bound to it. Without considering the blocks, we know the number of ways these linkers can be placed,

$$\Omega_2(N_R) = \binom{\ell - N + N_R}{N_R}. \quad (2.56)$$

Each of these configurations actually constitutes a unique permutation of R - and H -blocks. This permutation is then substituted into the the X positions in the string of L - and X -blocks, such that we are left with a unique configuration of all linkers. Hence, the total number of configurations is simply the product

$$\Omega(N_R) = \Omega_1(N_R) \Omega_2(N_R) = \binom{\ell - N_R}{N - N_R} \binom{\ell - N + N_R}{N_R}. \quad (2.57)$$

This concludes our calculation of the entropy term Eq. 2.54.

To show the effect of entropy on the free-energy profile, we plot both the potential energy landscape in Fig. 2.13 and free-energy landscape in Fig. 2.14. The potential energy as a function of x and N_R is given by

$$U(x, N_R) = \frac{1}{2} k \delta^2 N \left[\left(\frac{x}{\delta} - \frac{N_R}{N} \right)^2 + \frac{N_R}{N} \left(1 - \frac{N_R}{N} \right) \right], \quad (2.58)$$

as shown in Eq. 2.2. This equation shows that the x dependence of the potential energy is given by a simple harmonic well, with a minimum at $x_{\min} = \delta N_R / N$. The value of the potential energy at the optimal x_{\min} follows a parabolic curve,

$$U(x_{\min}, N_R) = \frac{1}{2} k \delta^2 N \left[\frac{N_R}{N} \left(1 - \frac{N_R}{N} \right) \right], \quad (2.59)$$

as a function of N_R , which is proportional to $N_R(N - N_R)$, with a peak at $N_R = N/2$. The entropy only changes how the free energy depends on N_R , not how it depends on x . Furthermore, since the entropy (calculated from Eq. 2.57) has a maximum at $N_R = N/2$ as well, the barrier separating the two valleys is lowered by the entropic contribution. This also becomes evident by comparing Fig. 2.13 and Fig. 2.14.

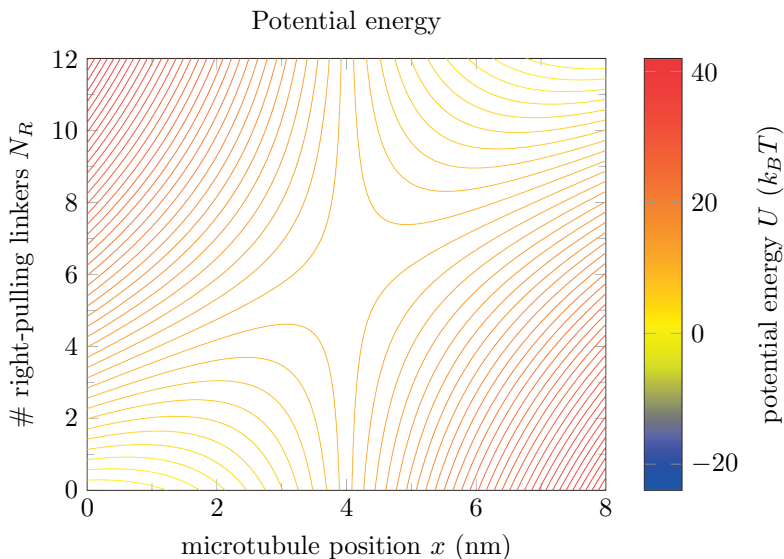


Figure 2.13: Potential energy contour plot. The discrete variable N_R is treated as a continuous variable to create smooth lines. For a given N_R , the potential energy follows a simple parabolic shape with a minimum at $x = \delta N_R / N$. Contours are spaced $1 k_B T$ apart.

2.F. NUMERICAL CONFIRMATION OF FREE-ENERGY EQUATION

We test the analytical expression for the free-energy profile by calculating it directly from numerical simulations. We obtained a two dimensional histogram of (x, N_R) positions by running simulations at $N = 12$ and $\ell = 40$ for 5×10^{10} time steps representing $\Delta t = 1 \times 10^{-8}$ s each. The barrier was crossed 9332 times during this run, which shows we have sampled the peak region to some extent. Then, we estimated the free energy by calculating $-\log(p)$, where p is the probability to be found in a particular bin, and choosing a constant offset such that the free energy vanishes at $x = 0$ and $N_R = 0$. The result is plotted in Fig. 2.15. In regions where the free energy is relatively low, including the saddle point in the barrier, the simulations confirm the exact free-energy profile. We did not sample regions with higher free energy due to the finite simulation time, thus showing a deviation from the theoretical result there. Still, these simulations confirm the agreement between simulation and theory.

2.G. DETERMINATION OF REACTION COORDINATE

Two order parameters describe the microtubule jumps. First, the microtubule position x modulo δ transitions between 0 and δ , and second, the number of right-pulling cross-linkers N_R ranges from 0 to N . As shown in Eq. 2.2, the lowest free-energy path connecting two neighbouring basins of attraction is given by the diagonal $x/\delta = N_R/N$. The reaction coordinate α is defined such that a single value groups states perpendicular to

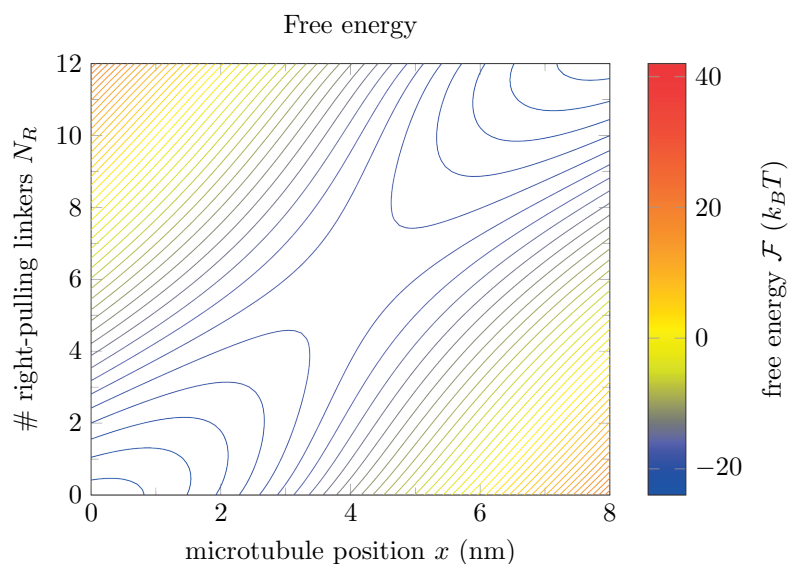


Figure 2.14: Free-energy contour plot. Comparing the figure to Fig. 2.13 it shows that the barrier is lowered by the entropic term. The entropy only depends on N_R , not on the position x . Hence, for a given N_R , the free energy follows the same parabolic curve as the potential energy, with a different base value. The colour scheme is the same as in Fig. 2.13, contours are spaced $1 k_B T$ apart.

Deviation from theory

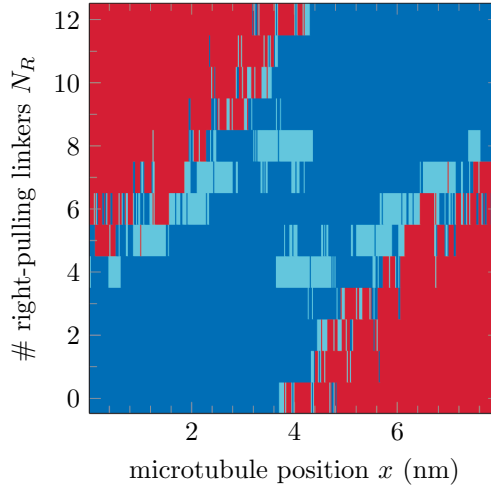


Figure 2.15: Comparison of the exact free energy and a numerical estimate. Dark blue colors represent a deviation from the theoretical value $d < 2.5\%$, light blue represent $2.5\% \leq d < 5\%$, and red represents $d > 5\%$. The numerical results confirm the validity of the equations in all regions that can be efficiently sampled. Here, $N = 12$ and $\ell = 40$, and the x axis is divided into 400 bins.

the optimal diagonal,

$$\alpha = \frac{1}{2} \left(\frac{x}{\delta} + \frac{N_R}{N} \right). \quad (2.60)$$

To study whether this gives the proper reaction coordinate, we simulated a system with $N = 12$ and $\ell = 40$ and recorded the phase space positions (x, N_R) at \mathcal{N}_{max} points in time. In this case, we used $\mathcal{N}_{max} = 5 \times 10^{10}$ time steps of $\Delta t = 1 \times 10^{-8}$ s each. Then, we created a histogram with bin dimensions $(2.5 \times 10^{-3} \delta, 1)$ that collects those points that were part of transition paths. For this, the basins of attraction are defined as squares in phase space of dimensions $(0.15 \delta, 2)$, representing the bottom-left and top-right corners of Fig. 2.16. Paths that connect separate basins of attraction are registered in the histogram, giving the number of points in each bin $\mathcal{N}_{(x, N_R)}$ and the total number of points $\mathcal{N}_{transit}$, which is given by the sum over all bins,

$$\mathcal{N}_{transit} = \sum_{\{(x, N_R)\}} \mathcal{N}_{(x, N_R)}. \quad (2.61)$$

By estimating the probability

$$\mathcal{P}(x, N_R | transit) = \frac{\mathcal{N}_{(x, N_R)}}{\mathcal{N}_{transit}}, \quad (2.62)$$

we show in Fig. 2.16 that transition paths typically follow the diagonal parameterized by α . Furthermore, we can define the transition state as the region of maximum transition

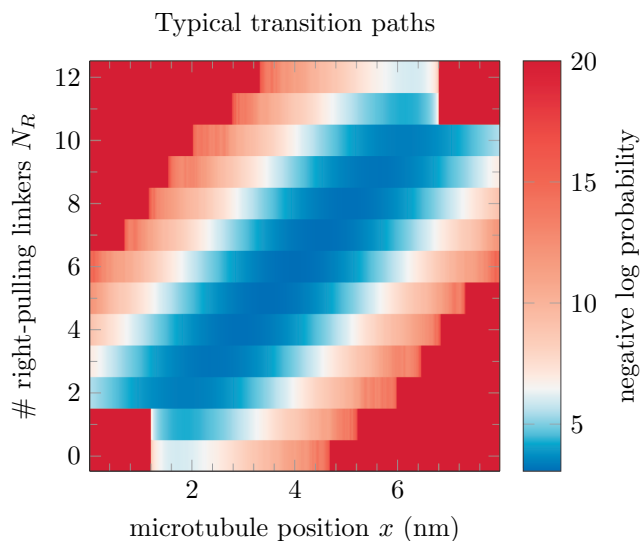


Figure 2.16: Histogram of transition paths. Two square corners of 1.2 nm wide and 2 linkers high were set as the basins of attraction. Then we estimated the probability to be at a certain coordinate, given that the system is on a transition path, $\mathcal{P}(x, N_R | \text{transit})$. This is simply a normalized histogram of all transition paths. Finally, we plot the negative natural logarithm of this probability. Most paths follow the diagonal, and it is unlikely to deviate far into the top-left or bottom-right corners, making it impossible to sample these latter regions. It is impossible to be part of a transition path in the basins of attraction, as shown by the squares in the bottom-left and top-right.

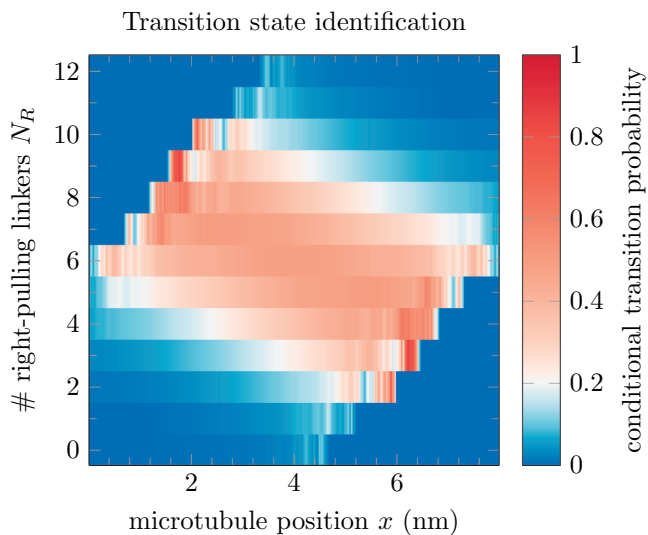


Figure 2.17: Histogram of transition path probability, $\mathcal{P}(\text{transit} | x, N_R)$. The region of largest values, where $\mathcal{P} = 1/2$, defines the transition state [33]. Value fluctuations at the edges of the sampled region are due to undersampling, whereas the top-left and bottom-right corners are not sampled at all. The transition state is roughly perpendicular to the reaction coordinate, and is approximately captured by $\alpha = 1/2$.

probability [33]. This probability is calculated using Bayes' theorem,

$$\mathcal{P}(\text{transit} | x, N_R) = \frac{\mathcal{P}(x, N_R | \text{transit}) \mathcal{P}(\text{transit})}{\mathcal{P}(x, N_R)} = \frac{\mathcal{N}(x, N_R)}{\mathcal{N}_{max} \mathcal{P}(x, N_R)}. \quad (2.63)$$

Before the estimation, \mathcal{N}_{max} is known and $\mathcal{P}(x, N_R)$ can be calculated exactly from the free energy given by Eq.2.3. To further enhance the estimation process, we make use of the invariance under reflections where both $R \leftrightarrow L$ and $x \leftrightarrow \delta - x$. Fig.2.17 shows that the transition state is approximately perpendicular to the reaction coordinate in the regions where we have sufficient statistics. This supports the view that α characterizes transitions well, and that the free-energy barrier should be calculated as a function of α .

2

2.H. MICROTUBULE JUMP RATE FOLLOWS ARRHENIUS' LAW

The height of the free-energy barrier directly influences the microtubule jump rate, and we are interested in how this rate depends on the number of cross-linkers N and the length of the mobile microtubule ℓ . We can calculate the free-energy profile as a function of α , the reaction coordinate discussed in Sec. 2.G,

$$e^{-\beta \mathcal{F}(\alpha)} = \sum_{N_R=0}^N \int_0^\delta e^{-\beta \mathcal{F}(x, N_R)} \delta(\alpha(x, N_R) - \alpha) dx, \quad (2.64)$$

where $\delta(y)$ is the Dirac delta function and $\alpha(x, N_R)$ is the function given by Eq. 2.5. As illustrated in the inset of Fig. 2.3, this free-energy profile sets the effective barrier height separating the two regions of attraction,

$$\Delta \mathcal{F}^\ddagger = \mathcal{F}(\alpha = 1/2) - \mathcal{F}(\alpha = 0). \quad (2.65)$$

We can use the free-energy barrier height to test if the reaction rate follows Arrhenius' equation [83] (see Eq. 2.6). We confirm its validity by performing prolonged kinetic Monte Carlo simulations of the model, varying ℓ between 15 and 40 sites, and varying N between 6 and, respectively, 14 ($\ell = 15$), 15 ($\ell = 20$), 18 ($\ell = 25$), and 20 ($\ell = 30$ and $\ell = 40$) linkers. We record the times T between barrier crossings and estimate the hopping rate from the mean waiting time, as illustrated in Fig. 2.2. Then, we normalized the rates by dividing by some r^* , for which we arbitrarily chose the empirically determined rate found at $\ell = 15$ and $N = 6$. We plot the logarithm of these empirically obtained rates against the analytically calculated free-energy barrier height in Fig. 2.18. This plot shows that all observed rates fall on a single master curve, which is correctly described by Eq. 2.6 with a constant prefactor.

2.I. EXPONENTIAL APPROXIMATION OF FREE-ENERGY BARRIER

We have an analytical expression for the partition sum as a function of the reaction coordinate α in Eq. 2.60,

$$\begin{aligned} \mathcal{Z}(\alpha) &= \sum_{N_R=0}^{N-1} \mathbb{1}\left(0 \leq 2\alpha - \frac{N_R}{N} \leq 1\right) \binom{\ell - N_R}{N - N_R} \binom{\ell - N + N_R}{N_R} \\ &\times \exp\left[-\frac{k\delta^2 N}{2k_B T} \left(4\left(\alpha - \frac{N_R}{N}\right)^2 + \frac{N_R}{N} \left(1 - \frac{N_R}{N}\right)\right)\right]. \end{aligned} \quad (2.66)$$

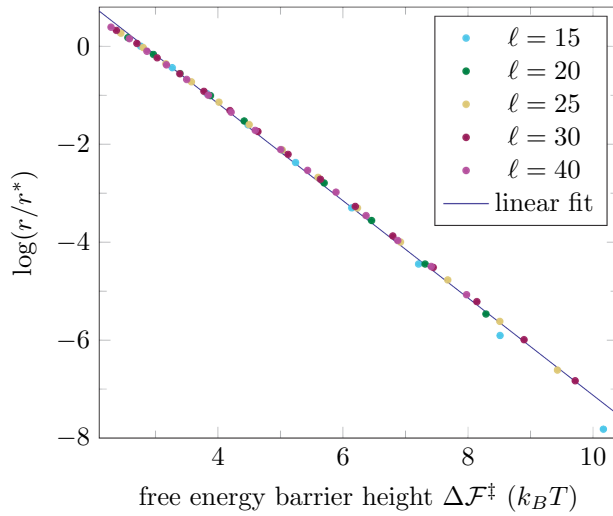


Figure 2.18: Microtubule jump rate follows Arrhenius' equation. We plot the natural logarithm of the simulated microtubule jump rate as a function of the height of the free-energy barrier separating two basins of attraction. The rate is normalized by an arbitrarily chosen rate r^* . We vary the barrier height by changing both N and ℓ , showing that all points fall on a single master curve independent of these parameters. A linear fit gives a slope of $-0.99/k_B T$, which shows that the rates are well described by Arrhenius' equation.

The indicator function $\mathbb{1}$ makes sure that the summation is only performed over those terms that represent a valid value of the position x , which should obey $0 \leq x \leq \delta$. The free-energy barrier peak is located at $\alpha = 1/2$, while the valleys are located at $\alpha = 0$ and $\alpha = 1$. Hence, the height of the barrier is given by

$$\Delta\mathcal{F}^\ddagger = -k_B T \log \left(\frac{\mathcal{Z}(\alpha = 1/2)}{\mathcal{Z}(\alpha = 0)} \right). \quad (2.67)$$

At $\alpha = 1/2$ all terms of the sum contribute to Eq. 2.66, while at $\alpha = 0$, only the $N_R = 0$ term contributes. The latter observation leads to a simple expression for the partition sum in the valley,

$$\mathcal{Z}(\alpha = 0) = \binom{\ell}{N}. \quad (2.68)$$

Then, using that

$$\frac{N_R}{N} \left(1 - \frac{N_R}{N} \right) = \frac{1}{4} - \left(\frac{N_R}{N} - \frac{1}{2} \right)^2 = \frac{1}{4} - \frac{1}{N^2} \left(N_R - \frac{N}{2} \right)^2, \quad (2.69)$$

we get

$$\begin{aligned} \frac{\mathcal{Z}(\alpha = 1/2)}{\mathcal{Z}(\alpha = 0)} &= \sum_{N_R=0}^{N-1} \binom{\ell - N_R}{N - N_R} \binom{\ell - N + N_R}{N_R} \binom{\ell}{N} \\ &\times \exp \left[-\frac{k\delta^2 N}{2k_B T} \left(\frac{3}{N^2} \left(N_R - \frac{N}{2} \right)^2 + \frac{1}{4} \right) \right]. \end{aligned} \quad (2.70)$$

This equation gives the exact value of the free-energy barrier height through Eq. 2.67.

Even though we have an exact solution for the barrier height, Eq. 2.70 does not provide any understanding on how the barrier height depends on the number of cross-linkers or on the microtubule overlap length. To acquire a better comprehension of these dependencies, we require an analytical approximation for the free-energy barrier height in terms of simple functions. Here, we make such an approximation using three conditions. First, we assume that the cross-linker density N/ℓ is small. Second, we recognize that the summand peaks at $N_R = N/2$, and that we capture the main contribution to the sum by Taylor expanding the function around this point. Third, we assume that N is large enough such that the summand does not change too strongly as a function of N_R . Under that last condition, we can replace the sum by an integral over the real line.

To start, we first rewrite the product of binomial coefficients,

$$\binom{\ell - N_R}{N - N_R} \binom{\ell - N + N_R}{N_R} \binom{\ell}{N} = \binom{N}{N_R} \frac{(\ell - N_R)! (\ell - N + N_R)!}{\ell! (\ell - N)!}. \quad (2.71)$$

The first binomial coefficient captures the main contribution of changes in N_R , while the second factor approaches unity for very low densities. Now, we will make Gaussian approximations for the binomial coefficients, following a standard approach presented e.g. by Milewski [84]. First, we reparameterize the equation using $N_R = N/2 + M/2$, or

$M = 2N_R - N$, which allows us to expand around $M = 0$. Then, we use Stirling's Approximation on all factorials in the binomial, the first factor of Eq. 2.71 becomes

$$\begin{aligned}
 \binom{N}{N_R} &= \binom{N}{\frac{N}{2} + \frac{M}{2}} = \frac{N!}{\left(\frac{N}{2} + \frac{M}{2}\right)! \left(\frac{N}{2} - \frac{M}{2}\right)!} \\
 &\approx \frac{N^{N+\frac{1}{2}}}{\sqrt{2\pi} \left(\frac{N}{2} + \frac{M}{2}\right)^{\frac{N}{2} + \frac{M}{2} + \frac{1}{2}} \left(\frac{N}{2} - \frac{M}{2}\right)^{\frac{N}{2} - \frac{M}{2} + \frac{1}{2}}} \\
 &= \frac{1}{\sqrt{2\pi}} \frac{N^{N+\frac{1}{2}}}{\left(\frac{N^2 - M^2}{4}\right)^{\frac{N}{2} + \frac{1}{2}}} \left(\frac{\frac{N}{2} - \frac{M}{2}}{\frac{N}{2} + \frac{M}{2}}\right)^{\frac{M}{2}} \\
 &= \frac{1}{\sqrt{2\pi}} \frac{N^{N+\frac{1}{2}} 2^{N+1} N^{-N-1} \left(1 - \frac{M}{N}\right)^{\frac{M}{2}}}{\left(1 - \frac{M^2}{N^2}\right)^{\frac{N}{2} + \frac{1}{2}} \left(1 + \frac{M}{N}\right)} \\
 &\approx \sqrt{\frac{2}{\pi N}} 2^N \left(1 - \frac{M^2}{N^2}\right)^{-\left(\frac{N}{2} + \frac{1}{2}\right)} \left(1 - 2\frac{M}{N} + 2\left(\frac{M}{N}\right)^2\right)^{\frac{M}{2}}. \tag{2.72}
 \end{aligned}$$

In the first line, all exponential terms from Stirling's Approximation cancel, and only one $\sqrt{2\pi}$ factor survives. Then, after rearranging the result, we apply the geometric series and keep terms that are at most quadratic in M/N . The equation can be further approximated after applying the logarithm,

$$\begin{aligned}
 \log \binom{N}{N_R} &\approx \log \left(\sqrt{\frac{2}{\pi N}} 2^N \right) - \left(\frac{N}{2} + \frac{1}{2}\right) \log \left(1 - \frac{M^2}{N^2}\right) + \frac{M}{2} \log \left(1 - 2\frac{M}{N} + 2\left(\frac{M}{N}\right)^2\right) \\
 &\approx \log \left(\sqrt{\frac{2}{\pi N}} 2^N \right) + \left(\frac{N}{2} + \frac{1}{2}\right) \frac{M^2}{N^2} - \frac{M^2}{N} \\
 &\approx \log \left(\sqrt{\frac{2}{\pi N}} 2^N \right) - \frac{M^2}{2N}. \tag{2.73}
 \end{aligned}$$

Here we used the Taylor expansion of the logarithm in M around 0, and used the assumption that M is smaller than N . We can exponentiate the result back to the desired approximation,

$$\binom{N}{N_R} \approx \sqrt{\frac{2}{\pi N}} 2^N e^{-\frac{M^2}{2N}} = \frac{2}{\sqrt{\pi N}} 2^N e^{-\frac{2}{N} \left(N_R - \frac{N}{2}\right)^2}. \tag{2.74}$$

This is the well known Gaussian approximation of the binomial distribution for $p = \frac{1}{2}$.

We use the same methods to make an approximation of the second factor in Eq. 2.71,

$$\begin{aligned}
\frac{(\ell - N_R)!(\ell - N + N_R)!}{\ell!(\ell - N)!} &\approx \frac{(\ell - N_R)^{\ell - N_R + \frac{1}{2}} (\ell - N + N_R)^{\ell - N + N_R + \frac{1}{2}}}{\ell^{\ell + \frac{1}{2}} (\ell - N)^{\ell - N + \frac{1}{2}}} \\
&= \left(\frac{\left(1 - \frac{N_R}{\ell}\right) \left(1 - \frac{N - N_R}{\ell}\right)}{\left(1 - \frac{N}{\ell}\right)} \right)^{\ell + \frac{1}{2}} \left(\frac{1 - \frac{N}{\ell}}{1 - \frac{N_R}{\ell}} \right)^{N_R} \left(\frac{1 - \frac{N}{\ell}}{1 - \frac{N - N_R}{\ell}} \right)^{N - N_R} \\
&= \left(\frac{\left(1 - \frac{N}{2\ell} - \frac{M}{2\ell}\right) \left(1 - \frac{N}{2\ell} + \frac{M}{2\ell}\right)}{\left(1 - \frac{N}{\ell}\right)} \right)^{\ell + \frac{1}{2}} \left(\frac{1 - \frac{N}{\ell}}{1 - \frac{N}{2\ell} - \frac{M}{2\ell}} \right)^{\frac{N}{2} + \frac{M}{2}} \left(\frac{1 - \frac{N}{\ell}}{1 - \frac{N}{2\ell} + \frac{M}{2\ell}} \right)^{\frac{N}{2} - \frac{M}{2}} \\
&= \left(\frac{\left(1 - \frac{N}{2\ell} - \frac{M}{2\ell}\right) \left(1 - \frac{N}{2\ell} + \frac{M}{2\ell}\right)}{\left(1 - \frac{N}{\ell}\right)} \right)^{\ell - \frac{N}{2} + \frac{1}{2}} \left(1 - \frac{N}{\ell}\right)^{\frac{N}{2}} \left(\frac{1 - \frac{N}{2\ell} + \frac{M}{2\ell}}{1 - \frac{N}{2\ell} - \frac{M}{2\ell}} \right)^{\frac{M}{2}}.
\end{aligned} \tag{2.75}$$

In the first line we applied Stirling's approximation again, after which we that both the numerator and denominator contain $(2\ell - N + 1)$ factors. This means we can divide ℓ out of them, after which we rearrange the result into three factors with different exponents. There, we also use that $N = N_R + (N - N_R)$. Then, in the third line, we substitute our definition of M , and finally regroup the results according to their new exponents.

We continue by approximating the first factor of Eq. 2.75. We apply the geometric series and only keep factors of quadratic order,

$$\begin{aligned}
\frac{\left(1 - \frac{N}{2\ell} - \frac{M}{2\ell}\right) \left(1 - \frac{N}{2\ell} + \frac{M}{2\ell}\right)}{\left(1 - \frac{N}{\ell}\right)} &\approx \left(1 - \frac{N}{\ell} + \frac{N^2}{4\ell^2} - \frac{M^2}{4\ell^2}\right) \left(1 + \frac{N}{\ell} + \frac{N^2}{\ell^2}\right) \\
&\approx 1 + \frac{N^2}{4\ell^2} - \frac{M^2}{4\ell^2}.
\end{aligned} \tag{2.76}$$

Similarly, we approximate the final factor of Eq. 2.75,

$$\begin{aligned}
\frac{1 - \frac{N}{2\ell} + \frac{M}{2\ell}}{1 - \frac{N}{2\ell} - \frac{M}{2\ell}} &\approx \left(1 - \frac{N}{2\ell} + \frac{M}{2\ell}\right) \left(1 + \frac{N}{2\ell} + \frac{M}{2\ell} + \left(\frac{N}{2\ell} + \frac{M}{2\ell}\right)^2\right) \\
&\approx 1 + \frac{M}{\ell} + 2\left(\frac{M}{2\ell}\right)^2 + 2\left(\frac{N}{2\ell}\right)\left(\frac{M}{2\ell}\right).
\end{aligned} \tag{2.77}$$

Then, we can take the logarithm of Eq. 2.75 and expand the logarithms,

$$\log\left(\frac{(\ell - N_R)!(\ell - N + N_R)!}{\ell!(\ell - N)!}\right) \approx \left(\ell - \frac{N}{2} + \frac{1}{2}\right) \log\left(1 + \frac{N^2}{4\ell^2} - \frac{M^2}{4\ell^2}\right) + \frac{N}{2} \log\left(1 - \frac{N}{\ell}\right) \quad (2.78)$$

$$\begin{aligned} &+ \frac{M}{2} \log\left(1 + \frac{M}{\ell} + 2\left(\frac{M}{2\ell}\right)^2 + 2\left(\frac{N}{2\ell}\right)\left(\frac{M}{2\ell}\right)\right) \\ &\approx \frac{N^2}{4\ell} - \frac{M^2}{4\ell} - \frac{N^2}{2\ell} + \frac{M^2}{2\ell} \\ &= -\frac{N^2}{4\ell} + \frac{M^2}{4\ell} = -\frac{N^2}{4\ell} + \frac{(N_R - \frac{N}{2})^2}{\ell}. \end{aligned} \quad (2.79)$$

After the expansion of the logarithms, we only keep terms that are at most quadratic in M and N , and that do not decay faster than $1/\ell$. By combining the results from Eq. 2.74 and Eq. 2.79, we find

$$\binom{\ell - N_R}{N - N_R} \binom{\ell - N + N_R}{N_R} / \binom{\ell}{N} \approx \sqrt{\frac{2}{\pi N}} \exp\left[N \log(2) - \frac{N^2}{4\ell} - \left(\frac{2}{N} - \frac{1}{\ell}\right) \left(N_R - \frac{N}{2}\right)^2\right]. \quad (2.80)$$

Now we have the right tools to make an approximation of the barrier probability Eq. 2.70,

$$\frac{\mathcal{Z}(\alpha = 1/2)}{\mathcal{Z}(\alpha = 0)} \approx \sqrt{\frac{2}{\pi N}} \exp\left(N \log(2) - \frac{N^2}{4\ell} - \frac{k\delta^2 N}{8k_B T}\right) \sum_{N_R=0}^{N-1} \exp\left[-\left(\frac{3k\delta^2}{2Nk_B T} + \frac{2}{N} - \frac{1}{\ell}\right) \left(N_R - \frac{N}{2}\right)^2\right]. \quad (2.81)$$

We make the variable substitution $v = N_R - N/2$ and treat it as a continuous variable, changing the sum into an integral and extending the summation region to the entire real line,

$$\begin{aligned} \frac{\mathcal{Z}(\alpha = 1/2)}{\mathcal{Z}(\alpha = 0)} &\approx \sqrt{\frac{2}{\pi N}} \exp\left(N \log(2) - \frac{N^2}{4\ell} - \frac{k\delta^2 N}{8k_B T}\right) \int_{-\infty}^{\infty} dv \exp\left[-\left(\frac{3k\delta^2}{2Nk_B T} + \frac{2}{N} - \frac{1}{\ell}\right) v^2\right] \\ &= \sqrt{\frac{2\pi}{\pi N \left(\frac{3k\delta^2}{2Nk_B T} + \frac{2}{N} - \frac{1}{\ell}\right)}} \exp\left(N \log(2) - \frac{N^2}{4\ell} - \frac{k\delta^2 N}{8k_B T}\right) \\ &\approx \frac{1}{\sqrt{1 + \frac{3k\delta^2}{4k_B T}}} \exp\left(N \log(2) - \frac{N^2}{4\ell} - \frac{k\delta^2 N}{8k_B T}\right). \end{aligned} \quad (2.82)$$

In the last line, we used that k is relatively large, and that N/ℓ is small. We find the

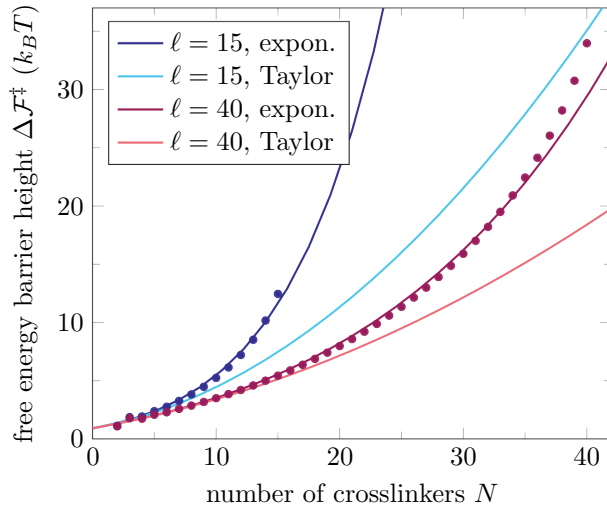


Figure 2.19: The height of the free-energy barrier $\Delta\mathcal{F}^\ddagger$ as a function of the number of crosslinkers N and two values of the mobile microtubule length ℓ . The analytical solutions as calculated through Eq. 2.67 and Eq. 2.70 are plotted as sets of points. Lighter colors show the Taylor approximation Eq. 2.83, and darker colors show the exponential approximation Eq. 2.84 as well as the exact values. The Taylor approximations break down at relatively low cross-linker densities, but they predict the required exponent very well. The exponential approximations nearly perfectly follow the true barrier heights, and only start to deviate at the highest cross-linker densities, where the true barrier height starts increasing even faster than exponentially.

approximation of the free-energy barrier height using Eq. 2.67,

$$\Delta \mathcal{F}^\ddagger \approx \frac{k_B T}{2} \log\left(1 + \frac{3k\delta^2}{4k_B T}\right) + \left(\frac{k\delta^2}{8} - k_B T \log(2)\right) N + \frac{k_B T}{4\ell} N^2 \quad (2.83)$$

$$\begin{aligned} &= \frac{k_B T}{2} \log\left(1 + \frac{3k\delta^2}{4k_B T}\right) + \left(\frac{k\delta^2}{8} - k_B T \log(2)\right) N \left(1 + \frac{1}{\frac{k\delta^2}{2k_B T} - 4\log(2)} \frac{N}{\ell}\right) \\ &\approx \frac{k_B T}{2} \log\left(1 + \frac{3k\delta^2}{4k_B T}\right) + \left(\frac{k\delta^2}{8} - k_B T \log(2)\right) N \exp\left(\frac{1}{\frac{k\delta^2}{2k_B T} - 4\log(2)} \frac{N}{\ell}\right). \end{aligned} \quad (2.84)$$

The second line rewrites the result in terms of the number of cross-linkers N and the cross-linker density N/ℓ . Then, in the final line, we exponentiate the part of the last term that depends on the density. This was done after inspection of the analytical free-energy barrier height as a function of N , of which examples are plotted as sets of points in Fig. 2.19.

The exponential version of the approximation captures the behavior of the exact function for a much larger range than the second order Taylor approximation. Furthermore, this version takes into account the variables that are intuitively important for the barrier height; for small densities, the height increases linearly with the number of cross-linkers, since a transition depends on the independent hopping of all cross-linkers. Then, at high densities, exclusion effects start playing a role. Hence, we need to include a term that depends on the cross-linker density N/ℓ , which is done by the exponential term in Eq. 2.84.

2.J. OVERLAP LENGTH RANGE FOR OBSERVING SUPEREXPONENTIAL FRICTION

One can imagine several experiments that measure the friction between two cross-linked filaments directly. For example, it is possible to measure the diffusion constant of a mobile filament cross-linked to a fixed filament, and use the Einstein relation Eq. 2.1 to estimate the friction coefficient [18]. Another possibility would be to measure the friction coefficient directly by applying a force using a stiff optical trap that causes the filaments to slide relative to each other (also see Sec. 2.D), and measure the resulting sliding velocity. These experiments would make it possible to test our principle prediction, namely that the friction coefficient scales in a highly non-linear and non-trivial manner with the number of cross-linkers N and the filament overlap length ℓ . As shown in Eq. 2.9, the friction coefficient scales exponentially with N at constant cross-linker density, while it scales superexponentially with the density at constant N .

Yet, to be able to observe the superexponential dependence of friction on the number of cross-linkers, it needs to be possible to resolve the overlap length at which we expect to find the superexponential regime, where the superexponential function deviates significantly from a simple exponential one. Furthermore, the filament needs to remain mobile enough to observe the dynamics and to measure the friction coefficient. If the number of cross-linkers is too large, the system will effectively stall before the superexponential regime can be reached.

Specifically, Eq. 2.9 shows that the crossover from exponential to an observable superexponential scaling occurs when $N/\ell \approx 4B$, which means that the critical overlap length ℓ^* at which the superexponential scaling sets in increases linearly with N ,

$$\ell^* = \frac{N}{4B}. \quad (2.85)$$

Yet, because the friction coefficient $\zeta = \zeta(N, N/\ell)$ depends not only on N/ℓ but also on N separately, an overlap that is compressed at constant N may have so many cross-linkers that it effectively stalls already before the superexponential regime becomes visible, simply because the friction becomes prohibitive. Therefore, we estimate the overlap lengths and cross-linker numbers where we expect that our prediction can be tested.

We define the velocity of stalling as $v_s \equiv 1 \text{ nm s}^{-1}$, which we assume represents the order of magnitude at which movement is not visible any more. This value is rather arbitrary, but the results depend very weakly on the exact value chosen here. Then, we take the pulling force to be $F_m \sim 10 \text{ pN}$, which approximates the force that a collection of motor proteins can produce [85]. The friction coefficient follows Eq. 2.9,

$$\zeta(N, N/\ell) = \zeta_0 \exp\left(BN \exp\left(\frac{1}{4B} \frac{N}{\ell}\right)\right). \quad (2.86)$$

From our simulations using the parameter values as listed in Tab. 2.1, we find a value for the prefactor of $\zeta_0 = 70 \text{ k}_B \text{ Ts}/\mu\text{m}^2$. Using these parameter values, we calculate the velocity at the critical density

$$v_c(N) = \frac{F_m}{\zeta(N, 4B)}. \quad (2.87)$$

By inverting the relation, we find that $v_c = v_s$ when $N = N_{\max} \approx 20$, meaning that the sliding velocity in the superexponential regime is higher than v_s when $N \leq N_{\max}$. In other words, we can only observe the dynamics at the critical density when the number of cross-linkers is not larger than 20. This corresponds to a critical overlap length of

$$l^* = \ell^* \delta \approx 200 \text{ nm}. \quad (2.88)$$

Hence, using our parameter values, we expect that experiments would have to probe filament overlaps with less than 20 cross-linkers, and they should be able to resolve filament overlaps of less than 200 nm. For a force that is 10 times higher, these values remain very stable, with $N_{\max} \approx 25$ and $l^* \approx 270 \text{ nm}$, because the friction force increases very rapidly as the number of cross-linkers rises. However, we do emphasise that these estimates depend hypersensitively on the value of B , and thus on the cross-linker stiffness k , as shown in Eq. 2.8. For example, by reducing k by 10%, such that $k = 1 \times 10^5 \text{ k}_B \text{ T}/\mu\text{m}^2$, we increase N_{\max} by 75% to $N_{\max} \approx 36$, and we more than triple l^* to $l^* \approx 700 \text{ nm}$. Hence, different cross-linkers from the Ase1/PRC family are expected to have markedly different l^* , and we expect that the superexponential friction falls in the observable regime at least for some of them. Moreover, our study, which focuses on cross-linker-generated filament friction in general, also applies to the friction between actin filaments as induced by passive cross-linkers like anillin [54]. Therefore, it would be important to estimate the spring constant of actin cross-linkers for understanding how fast the cytokinetic ring contracts and when it stalls.

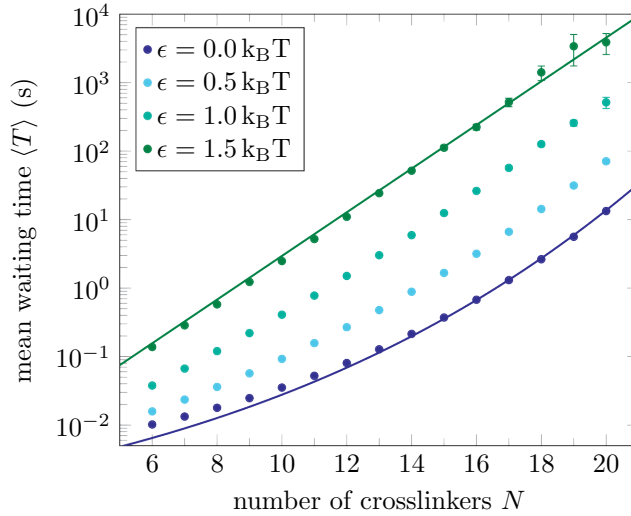


Figure 2.20: Cooperative interactions between the cross-linkers increase friction. Each head of the cross-linker has an interaction energy ϵ with each nearest neighbour head, which lowers the rate at which the head hops away from the nearest neighbour. Hence, two cross-linkers can have an interaction energy of 2ϵ when both heads of both cross-linkers interact. The mean waiting time between microtubule jumps, which is proportional to the friction, increases quicker when increasing cooperativity. We show the prediction from the superexponential function Eq. 2.9 with a fitted proportionality factor for $\epsilon = 0.0 \text{ k}_B \text{ T}$ (purple line), which increases exponentially in the logarithmic plot. Then, we show an exponential fit to the mean waiting time for $\epsilon = 1.5 \text{ k}_B \text{ T}$ (dark green line), which increases linearly on this scale. The superexponential increase is not observable for high cooperativity, since the cross-linkers cluster together creating a constant effective cross-linker density.

2.K. COOPERATIVE INTERACTIONS INCREASE FRICTION

It has been reported that Ase1/PRC1 can have cooperative interactions [40, 86]. However, other work has found no evidence for cooperative binding, finding a Hill coefficient of 1.5 for Ase1 binding to a single filament and even less evidence for cooperativity when binding between two filaments [18]. Still, it is interesting to investigate the possible effects of cooperativity on the friction coefficient in our model, since it can have an influence on how friction scales with the number of cross-linkers.

To investigate the effects of cooperativity on friction, we implement cooperative interactions in simulations by adding an interaction energy ϵ between neighboring heads of the cross-linkers. We choose to bias the rate at which one head of a cross-linker hops away from a neighboring occupied site with a factor

$$e^{-\beta\epsilon}, \quad (2.89)$$

while we leave the rate to hop towards a new neighbour unaffected. Then, we measure the mean waiting time between microtubule jumps as a function of the number

of cross-linkers for a fixed overlap length, with a mobile microtubule of $\ell = 30$ binding sites. Through Eq. 2.1, the mean waiting time is proportional to the friction coefficient of the cross-linked microtubule. The results are shown in Fig. 2.20. We vary the value of ϵ between $0.0k_B T$ and $1.5k_B T$ per head-head interaction, which corresponds to a cooperative interaction in the range of $0.0 - 3.0k_B T$ for two cross-linkers that are next to each other. This range of epsilon values would correspond to a Hill coefficient of cross-linker binding from solution between 1 and approximately 3 (data not shown).

Fig. 2.20 shows that even in the presence of cooperativity the friction continues to scale at least exponentially with the number of cross-linkers. The exponential increase of the friction with the number of cross-linkers is caused by a collective effect that gives rise to a free-energy barrier for filament hopping. Eq. 2.7 shows that the free-energy barrier increases linearly with N in the limit that the density N/ℓ goes to zero, which is caused by the fact that all left- and right pulling cross-linkers are stretched at the top of the barrier, and the combined energetic and entropic effects lead to a free-energy contribution of B per cross-linker, as seen in Eq. 2.7. Hence, the principal mechanism of friction generation, caused by the collective cross-linker dynamics which leads to microtubule jumps, does not change with cooperativity, explaining why friction still increases at least exponentially.

While the friction continues to scale superlinearly, Fig. 2.20 shows that increasing cooperativity does have two effects. With increasing ϵ , the superexponential curve (exponential in the log plot) becomes an exponential curve (linear in the log plot) when cooperativity is large enough. Furthermore, friction always increases compared to the non-cooperative case.

There are two mechanisms by which the cooperativity increases the friction between the microtubules. First, we see that Eq. 2.89 lowers the individual cross-linker hop rates, and increasing cooperative interactions will decrease the average cross-linker hop rate slightly. Since cooperative interactions increase with cross-linker density, the microtubule jump rate decreases with density, raising the friction. Still, we expect a much stronger effect from a second mechanism, which is due to an increase in exclusion effects. Since cooperativity increases the probability that two cross-linkers are next to each other, there are fewer cross-linkers that have unoccupied neighboring sites, reducing the number of options for cross-linkers to hop. This lessens the number of paths which the microtubule can take to make a jump, and increases the barrier height.

The second mechanism also explains how cooperativity changes the superexponential scaling of the friction. Eq. 2.7 shows the leading term by which cross-linker exclusion effects influence the barrier height. Without cooperative interactions, where $\epsilon = 0.0k_B T$, exclusion effects increase linearly with the cross-linker density N/ℓ , causing the superexponential increase of the friction between filaments. However, as ϵ is increased, the local increase in the density saturates for lower N . Intuitively, cooperative interactions lead to the formation of clusters of cross-linkers, and a distribution of cluster sizes can be observed when the overlap length is very large and the density of cross-linkers is fixed. However, when the filament size is limited (we choose $\ell = 30$ in the simulations of Fig. 2.20), the cross-linkers form one or at most a few large clusters. With increasing N , the clusters grow in size, but the exclusion effects do not, since the effective density inside the clusters stays roughly constant. For strong cooperative interactions, there is

thus no strong change in the effective density (set by that inside the cluster) as N increases, which means that the N/ℓ factor in Eq. 2.7 is replaced by a constant effective density that is independent of N . This explains why the superexponential increase of friction at low cooperativity changes to a (strong) exponential increase when the degree of cooperativity is high.

2

ACKNOWLEDGEMENTS

The authors thank Z. Lansky, M. Braun, and S. Diez for the fruitful collaboration, and B.M. Mulder for assessing the manuscript. This work was supported by European Research Council (ERC) Synergy Grant 609822, is part of the research programme of the Netherlands Organisation for Scientific Research (NWO), and performed at the research institute AMOLF.

3

BREAKDOWN OF SIMPLE DIFFUSION IMPAIRS KRAMERS THEORY

Passive cross-linkers induce discrete microtubule jumps, which can be described as free-energy barrier crossings. The rate of these transitions follows an Arrhenius equation, which includes a term that decreases exponentially with the free-energy barrier height multiplied by a prefactor. Here, we predict the absolute value of this prefactor using Kramers theory, but a direct comparison to simulations shows a strong discrepancy between the predicted and simulated prefactors. Furthermore, the failure of Kramers theory increases for larger densities of cross-linkers. To find the source of this breakdown, we inspect each component of the Kramers expression. We show that the small-time diffusion constant at the peak of the barrier, the free-energy profile, and the reaction coordinate are either known exactly or approximated well. We conclude that the Fokker-Planck description of the motion breaks down at small time scales due to the discrete nature of the cross-linker hops, and that exclusion effects between cross-linkers slow down the dynamics on the peak significantly, leading to a lower prefactor than predicted by Kramers theory. We conclude that transition state theory is more general than Kramers theory, since the Arrhenius equation is valid even when the system cannot be described by a continuous diffusion process.

In the previous chapter, we found that two filaments that are connected by diffusing cross-linkers move via discrete jumps, and that these events can be interpreted as free-energy barrier crossings. Then, we used the description of the free-energy barrier to show that the rate r at which the microtubule jumps over these barriers decreases exponentially with the number of cross-linkers N for low densities of cross-linkers. Moreover, if ℓ equals the number of binding sites within the overlap, we found that the rate decreases superexponentially with the fraction of occupied binding sites N/ℓ .

In Sec. 2.H we showed that r , which is the Poisson rate at which jumps occur in either direction, follows an Arrhenius equation with a prefactor r_0 ,

$$r(N, \ell) = r_0(N, \ell) \exp\left(-\Delta\mathcal{F}^\ddagger(N, \ell) / k_B T\right). \quad (3.1)$$

Furthermore, r_0 is nearly independent of the number of cross-linkers N and the overlap length ℓ . Since we were mainly interested in how the rate scales with N and ℓ , we focussed on the functional form of the height of the free-energy barrier $\Delta\mathcal{F}^\ddagger(N, \ell)$. However, we acquired not only the height of the free-energy barrier, but its full profile. Using Kramers theory [30] (see Sec. 1.5), we can utilise the full expression for the free energy to predict the prefactor r_0 . Through the Einstein relation, this would give us not only the functional dependence but also the absolute value of the friction coefficient. Moreover, we could use the expression derived from Kramers theory to investigate why the prefactor does not depend on N and ℓ , whereas Eq. 1.61 of Sec. 1.5 shows that the prefactor would normally be influenced by the shape of the free-energy profile, and therefore by the model parameters.

Here, we apply Kramers theory to the barrier crossings that dominate the movement of cross-linked microtubules. Detailed model simulations show that the prefactors predicted by Kramers theory provide the correct order of magnitude, but fail to explain how the prefactor of the jump rate changes with N or ℓ . To explain why Kramers theory breaks down, we assess the assumptions that are made in deriving it. We demonstrate that the three main ingredients of Kramers theory, namely the free-energy profile, the reaction coordinate, and the diffusion constant that governs the dynamics of the microtubules on the time scale of barrier crossings, are all reliable. Thereby, we show that the only assumptions that can break down are that the dynamics is governed by a Fokker-Planck equation on small time scales and that the system state equilibrates continuously during a transition. However, despite these basic assumptions breaking down, the Arrhenius equation explains the parameter dependence of the microtubule jump rate very well, and we discuss how the existence of a transition state provides a general explanation of the Arrhenius equation.

3.1. MICROTUBULE JUMP RATES FROM KRAMERS THEORY

FOR the cross-linked two-filament system described in Fig. 2.1, Kramers theory Eq. 1.60 estimates the prefactor of the filament jump rate as

$$r_0(N, \ell) = \left\{ \int_0^1 \frac{\exp(\beta(\mathcal{F}(\alpha) - \mathcal{F}^\ddagger))}{D(\alpha)} d\alpha \int_0^1 \exp(-\beta\mathcal{F}(\alpha)) d\alpha \right\}^{-1}. \quad (3.2)$$

As shown in Eq. 2.64, we used the exact solution for $\mathcal{F}(x, N_R)$ derived in Chap. 2 and identified the reaction coordinate α , such that the free energy marginalised to α equals

$$\mathcal{F}(\alpha) = -k_B T \log \left\{ \sum_{N_R=0}^N \mathbb{1} \left(0 \leq 2\alpha - \frac{N_R}{N} \leq 1 \right) \binom{\ell - N_R}{N - N_R} \binom{\ell - N + N_R}{N_R} \right. \\ \left. \times \exp \left[-\frac{k\delta^2 N}{2k_B T} \left(4 \left(\alpha - \frac{N_R}{N} \right)^2 + \frac{N_R}{N} \left(1 - \frac{N_R}{N} \right) \right) \right] \right\}. \quad (3.3)$$

This sum cannot be reduced analytically, except for the special values of $\alpha = 0$ and $\alpha = 1$, where the indicator function only allows for $N_R = 0$ and $N_R = N$, respectively,

$$\mathcal{F}(0) = \mathcal{F}(1) = -k_B T \log \binom{\ell}{N}. \quad (3.4)$$

Since Eq. 3.2 involves integrals over all values of α , we cannot find an analytical expression for the Kramers rate. However, we can evaluate the integrals numerically, given that we know the diffusion constant $D(\alpha)$.

3.2. THE SHORT-TIME EFFECTIVE DIFFUSION CONSTANT

The diffusion constant $D(\alpha)$ that appears in Eq. 3.2 should not be confused with the effective diffusion constant of the mobile filament that is valid on large timescales ($> 1/\tau$), and that is the result of a coarse-grained description in which barrier crossings become imperceptible. On the contrary, $D(\alpha)$ describes the short timescale fluctuations that govern the movement of the filament during barrier crossings. In this section, we find and test an expression of the short-time diffusion constant for the model described in detail in Chap. 2.

The $D(\alpha)$ that appears in the denominator of the first integrand of Eq. 3.2 could vary with the reaction coordinate α . However, we assume that these variations are low relative to the variations of the numerator, since the numerator scales exponentially with the free energy $\mathcal{F}(\alpha)$. The largest contribution to the integrand is found at the peak of the barrier, so we require an estimate for the short time diffusion constant at the position $\alpha = 1/2$. Summarising, we make the approximation

$$D(\alpha) \approx D\left(\frac{1}{2}\right) \equiv D^\ddagger. \quad (3.5)$$

To estimate this diffusion constant, we take a look at the definition of the reaction coordinate α ,

$$\alpha = \frac{1}{2} \left(\frac{x}{\delta} + \frac{N_R}{N} \right). \quad (3.6)$$

The diffusion constant Eq. 3.5 is related to the positional variance $\text{Var}(\alpha)$ of a filament that is at the peak of the barrier through

$$2D^\ddagger t = \text{Var}(\alpha) = \frac{1}{4} \left[\frac{\text{Var}(x)}{\delta^2} + \frac{2\text{Cov}(x, N_R)}{\delta N} + \frac{\text{Var}(N_R)}{N^2} \right], \quad (3.7)$$

where t is the time since the system started at the peak of the barrier. We assume that t is small enough that the shape of the barrier does not influence the diffusion yet, giving $\text{Var}(\alpha) \approx 2D^\ddagger t$.

The fluctuations at the peak are due to Brownian motion of the position x , caused by the thermal interactions between the filament and the surrounding liquid, and due to the hops of individual cross-linkers that change the number of right-pulling cross-linkers N_R . The former fluctuations happen with an intrinsic diffusion constant D_m causing a variance $2D_m t$, whereas the latter fluctuations are related to the prefactor of the hopping rate h_0 . At the peak of the barrier, $N_R \approx N/2$ on average. Furthermore, the cross-linkers are stretched $\delta/2$ on average, at which point the hopping rate is exactly h_0 according to Eq. 2.23, and each cross-linker has two heads that can hop. Hence, the average rate at which N_R increments by 1 equals Nh_0 , which also equals the rate at which N_R decrements by 1 as dictated by the symmetry of the system. Here, we assume that cross-linker exclusion plays no role, but we can include the exclusion effects up to first order by realising that a hop is forbidden if the neighbouring site of an L (R) linker is occupied by another L (R) linker. Since there are approximately $N/2$ of each spread over ℓ sites, we have that the total rate at which hops occur equals

$$h_{\text{tot}} \approx Nh_0 \left(1 - \frac{N}{2\ell}\right). \quad (3.8)$$

From this average rate at which N_R increments or decrements by 1, we calculate the variance of N_R as $2h_{\text{tot}} t$.

For the covariance term in Eq. 3.7, we assume that the random variables x and N_R fluctuate independently on small time scales, and that x only couples to N_R through the free-energy profile over large enough time scales. Hence, we ignore the correlations between x and N_R at the peak of the barrier for small times t . Combined with our approximate expressions of the variance of x and N_R , Eq. 3.7 gives

$$2D^\ddagger t = \frac{1}{4} \left[\frac{2D_m t}{\delta^2} + \frac{2Nh_0 \left(1 - \frac{N}{2\ell}\right) t}{N^2} \right]. \quad (3.9)$$

Hence, we estimate the short-time diffusion constant as

$$D^\ddagger = \frac{1}{4} \left(\frac{D_m}{\delta^2} + \frac{h_0}{N} \left(1 - \frac{N}{2\ell}\right) \right). \quad (3.10)$$

To test Eq. 3.10, we use simulations to probe the short-time diffusion constant at the peak of the free-energy barrier. We find two different estimators for the diffusion constant, namely Eq. 3.14 and Eq. 3.20 below, that are both based on a parabolic approximation of the shape of the free-energy profile at the peak. Eq. 3.3 gives an exact expression for the free energy. The peak of the free-energy barrier occurs at $\alpha = 1/2$, and we make a second order Taylor approximation

$$\mathcal{F}(\alpha) \approx \mathcal{F}\left(\frac{1}{2}\right) - \frac{1}{2}C \left(\alpha - \frac{1}{2}\right)^2, \quad (3.11)$$

where $C \equiv -\mathcal{F}''\left(\frac{1}{2}\right) > 0$, for which Eq. 3.3 gives an analytical expression that can be evaluated numerically.

The first method for estimating the diffusion constant uses the variance of the reaction coordinate. We enter Eq. 3.11 in Eq. 1.40 giving the Fokker-Planck equation for the probability density $p(\alpha, t)$ that the reaction coordinate equals α at time t given that it is at $1/2$ at time 0,

$$\partial_t p(\alpha, t) = D^\ddagger \partial_\alpha^2 p(\alpha, t) - \frac{D^\ddagger C}{k_B T} \partial_\alpha \left(\left(\alpha - \frac{1}{2} \right) p(\alpha, t) \right). \quad (3.12)$$

Because of the symmetry of the peak, we have $\langle \alpha \rangle = 1/2$, and we can apply the time derivative operator to see

$$\begin{aligned} \partial_t \text{Var}(\alpha) &\approx \int_{-\infty}^{\infty} \left(\alpha - \frac{1}{2} \right)^2 D^\ddagger \partial_\alpha^2 p(\alpha, t) - \left(\alpha - \frac{1}{2} \right)^2 \frac{D^\ddagger C}{k_B T} \partial_\alpha \left(\left(\alpha - \frac{1}{2} \right) p(\alpha, t) \right) d\alpha \\ &= \int_{-\infty}^{\infty} 2D^\ddagger p(\alpha, t) + \frac{2D^\ddagger C}{k_B T} \left(\alpha - \frac{1}{2} \right)^2 p(\alpha, t) d\alpha \\ &= 2D^\ddagger + \frac{2D^\ddagger C}{k_B T} \text{Var}(\alpha). \end{aligned} \quad (3.13)$$

In the first step, we use the definition of the variance and apply Eq. 3.12 to resolve the time derivative, and in the second step we use partial integration to resolve the derivatives to the reaction coordinate. We make the approximation that the second order polynomial free energy extends over the full real line, with the initial condition $\alpha = 1/2$. This allows us to ignore the boundary terms, since $p(\pm\infty, t) \rightarrow 0$. In the final step of Eq. 3.13, we use that the total probability is 1 and we recognise the definition of the variance again. The solution of the differential equation Eq. 3.13 is

$$\text{Var}(\alpha) \approx \frac{k_B T}{C} \left(e^{\frac{2D^\ddagger C}{k_B T} t} - 1 \right). \quad (3.14)$$

We then estimate D^\ddagger by sampling $\text{Var}(\alpha)$ for different t , where t is small enough such that the system does not leave the area where the peak is approximated well by its second order Taylor expansion, and then to fit Eq. 3.14 to the result to find D^\ddagger .

The second method measures the first passage time at two artificial boundaries $\alpha = 1/2 \pm b$, where we choose b small enough that the second order Taylor expansion approximates the barrier well in between the boundaries. We can calculate $\langle T \rangle(\alpha)$, the mean first passage time at $\frac{1}{2} \pm b$ given that the system started at $1/2 - b < \alpha < 1/2 + b$, using Eq. 1.55. The Kolmogorov backward equation corresponding to Eq. 3.12 gives

$$D^\ddagger \partial_\alpha^2 \langle T \rangle(\alpha) + \frac{D^\ddagger C}{k_B T} \left(\alpha - \frac{1}{2} \right) \partial_\alpha \langle T \rangle(\alpha) = -1. \quad (3.15)$$

A general solution for this equation exists in terms of a generalised hypergeometric function [93], but a good polynomial approximation can be found using perturbation analysis. Assuming the curvature of the parabola $\epsilon \equiv C/k_B T$ is small, $\epsilon \ll b^{-2}$, we can expand Eq. 3.15 in terms of ϵ . We define $g(\alpha) \equiv D^\ddagger \langle T \rangle(\alpha)$, which substituted into Eq. 3.15 gives

$$\partial_\alpha^2 g(\alpha) + \epsilon \left(\alpha - \frac{1}{2} \right) \partial_\alpha g(\alpha) = -1. \quad (3.16)$$

If we expand $g(\alpha) = g_0(\alpha) + \epsilon g_1(\alpha) + \mathcal{O}(\epsilon^2)$, we see that

$$[\partial_\alpha^2 g_0(\alpha) + 1] + \epsilon \left[\partial_\alpha^2 g_1(\alpha) + \left(\alpha - \frac{1}{2} \right) \partial_\alpha g_0(\alpha) \right] + \mathcal{O}(\epsilon^2) = 0. \quad (3.17)$$

Each order in ϵ has to vanish separately. This provides a second order differential equation for each order i , which determines the g_i when combined with the two absorbing boundary conditions $g_i(1/2 \pm b) = 0$. We first solve the lowest order in Eq. 3.17, yielding

$$g_0(\alpha) = \frac{1}{2} \left(b^2 - \left(\alpha - \frac{1}{2} \right)^2 \right). \quad (3.18)$$

Then, we plug this solution into the first order equation in Eq. 3.17, for which the solution reads

$$g_1(\alpha) = -\frac{1}{12} \left(b^4 - \left(\alpha - \frac{1}{2} \right)^4 \right). \quad (3.19)$$

Plugging back the previous definitions of ϵ and g into the solutions, and using that we are interested in the first passage time for a system starting at $\alpha = 1/2$, we see that

$$D^\ddagger \approx \frac{b^2}{2\langle T \rangle(\frac{1}{2})} \left(1 - \frac{Cb^2}{6k_B T} \right). \quad (3.20)$$

We use this equation to probe the diffusion constant in simulations, by setting two borders at $\alpha = 1/2 \pm b$, and measuring the time it takes to pass these borders each time the system starts at the peak.

We use both Eq. 3.14 and Eq. 3.20 to estimate the short-time diffusion constant at the peak of the barrier in the simulations. Since we try to estimate the dynamics at small time scales, we require the simulation dynamics to use time steps $\delta t = 1 \times 10^{-9}$ s, which is much smaller than the time of barrier transitions. Each time the system reaches the peak of a barrier, which we define as the region $\alpha \in (0.4999, 0.5001)$, we start sampling the positions at time intervals of $5\delta t$ for 400 time points. Hence, we track the variance of the reaction coordinate for $10\mu\text{s}$ after being on the peak, and we fit Eq. 3.14 to find the short-time diffusion constant D^\ddagger . Furthermore, we independently estimate D^\ddagger using Eq. 3.20. We set $b = 0.01$ and we record the first-passage time out of the region $\alpha \in (0.49, 0.51)$.

When we perform these steps for a system with $N = 12$ cross-linkers and $\ell = 40$ binding sites on the top microtubule, we find $D^\ddagger = 67.91(2)\text{s}^{-1}$ using the fit to the variance of α as a function of time (Eq. 3.14), while we find $D^\ddagger = 39.0(1)\text{s}^{-1}$ using the mean first-passage time (Eq. 3.20). Different values of N and ℓ lead to similar discrepancies in the estimates of D^\ddagger , while the two methods of estimating D^\ddagger do lead to consistent results when we simulate a simple diffusion process of a particle that starts from the top of a parabolic free-energy profile (data not shown). The consistency of Eq. 3.14 and Eq. 3.20 breaks down because the description of the system dynamics as a simple diffusion process fails for short times.

The reaction coordinate α changes not only through the continuous movement of the top microtubule position x , but also through the discontinuous hops of the cross-linkers that change N_R . Eq. 3.6 shows that if a cross-linker hop occurs, N_R changes by 1 and α changes by $1/(2N)$. In our simulations, N varies between 6 and 20, meaning

that the change in α upon a cross-linker hop is between 0.08 and 0.025. However, the borders are only a distance $b = 0.01$ away from the peak. Hence, the first cross-linker hop at time T will always pass the borders, and the hop will cause α to move a distance σ away from the barrier, where typically $\sigma \gg b$, so α passes the border by a significant amount. Eq. 3.20 assumes that moving α by an amount σ is the result of a continuous diffusion process with diffusion constant D^\ddagger . However, a continuous diffusion process that is at σ at time T would have been at $b < \sigma$ at time $T' < T$, whereas the process including cross-linker hops passes both b and σ at the same time T . Therefore, the mean first-passage time that we find in simulations is $\langle T \rangle$, but the mean first-passage time that appears in Eq. 3.20 should be $\langle T' \rangle < \langle T \rangle$. Hence, the simulations overestimate the first-passage time that enters Eq. 3.20, and underestimate the diffusion constant D^\ddagger .

Eq. 3.14 does give a correct estimate of D^\ddagger . As long as we sample enough events where the system reaches the peak of the barrier, the variance will properly average over the cross-linker hops and show a smooth evolution of the variance of the reaction coordinate as a function of time. Hence, we compare the theoretical expression for the diffusion constant Eq. 3.10 to the simulation results given by the variance-based estimator Eq. 3.14. We show the results of this comparison in Fig. 3.1 for different values of N and ℓ . The theoretical values slightly underestimate the true diffusion constants for small N , whereas they appear to overestimate the diffusion constant at high cross-linker densities. However, the deviations are small and the short-time diffusion constants found in the simulations generally confirm the theoretical approximation of the diffusion constant given in Eq. 3.10.

3.3. PREFACTOR OF THE FILAMENT JUMP RATE

Eq. 3.2 gives a theoretical prediction of the prefactor that appears in the expression of the Arrhenius rate (Eq. 3.1). We can also directly measure the rate at which the filaments jump in simulations, and compare it to the Kramers prediction of Eq. 3.2. We do not approximate the two integrals in Eq. 3.2 using Gaussian integrals, as is commonly done in Kramers theory [30], since the free energy contains some discontinuities as a function of α . Hence, we will evaluate Eq. 3.2 numerically.

We plot the numerical values of r_0 as given by the simulations and by Kramers theory in Fig. 3.2. Kramers theory predicts the order of magnitude of the simulated prefactors well. However, the theoretical curves seem to increase exponentially with the cross-linker density N/ℓ , whereas the simulated data points show a decrease in the prefactor r_0 with the density.

To investigate this discrepancy between the trends, we find an analytical approximation of the Kramers rate. As indicated before, the discontinuities in the free energy as a function of the reaction coordinate α prevent a good approximation of the integrals in Eq. 3.2 using Gaussian integrals. We do have two known properties of this free energy, namely that the free energy is periodic in α with period 1, and that the height of the free-energy barrier is approximated well by the analytical expression in Eq. 2.84. Using these two expressions, together with the choice $\mathcal{F}(0) = 0$, we approximate the free energy as

$$\mathcal{F}(\alpha) \approx \Delta\mathcal{F}^\ddagger \frac{1}{2} (1 - \cos(2\pi\alpha)). \quad (3.21)$$

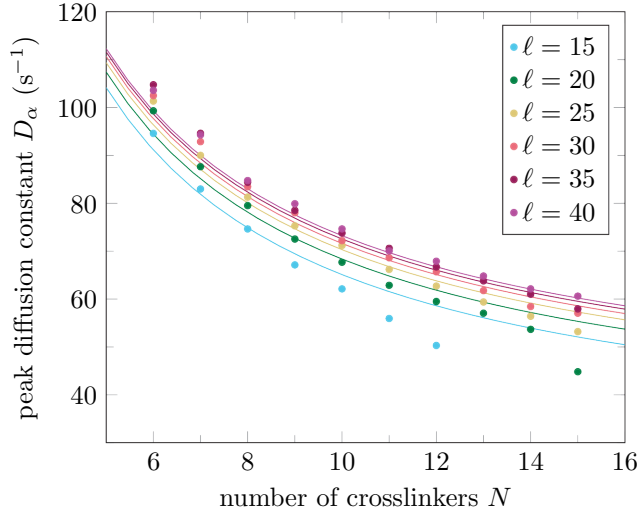


Figure 3.1: Simulated values of the diffusion constant at the peak of the free-energy barrier confirm the theoretically predicted values. The simulation points are estimated by probing the variance of the reaction coordinate as a function of time after the system propagates from an initial state at the peak of the barrier, and subsequently fitting Eq. 3.14 to find the diffusion constant. The theoretical curves are given by Eq. 3.10.

This sinusoidal function agrees well with the exact free energy, as shown in Fig. 3.3.

We then apply Kramers theory to the approximate free-energy profile Eq. 3.21,

$$\begin{aligned}
 r &= D^\ddagger \left\{ \int_0^1 \exp\left(\frac{\beta\Delta\mathcal{F}^\ddagger}{2}(1 - \cos(2\pi\alpha))\right) d\alpha \int_0^1 \exp\left(-\frac{\beta\Delta\mathcal{F}^\ddagger}{2}(1 - \cos(2\pi\alpha))\right) d\alpha \right\}^{-1} \\
 &= D^\ddagger \left\{ \int_0^1 \exp\left(\frac{-\beta\Delta\mathcal{F}^\ddagger}{2}\cos(2\pi\alpha)\right) d\alpha \int_0^1 \exp\left(\frac{\beta\Delta\mathcal{F}^\ddagger}{2}\cos(2\pi\alpha)\right) d\alpha \right\}^{-1} \\
 &= \frac{D^\ddagger}{I_0\left(\frac{\beta\Delta\mathcal{F}^\ddagger}{2}\right)^2}, \tag{3.22}
 \end{aligned}$$

where $I_0(x)$ is a modified Bessel function of the first kind. Since the free energy-barriers that we simulate are relatively high ($\Delta\mathcal{F}^\ddagger > 2k_B T$), we can use the asymptotic expansion of the Bessel function [94],

$$\begin{aligned}
 r &\approx D^\ddagger \left[\frac{\exp\left(\frac{\beta\Delta\mathcal{F}^\ddagger}{2}\right)}{\sqrt{\pi\beta\Delta\mathcal{F}^\ddagger}} \left(1 + \frac{1}{4\beta\Delta\mathcal{F}^\ddagger} + \frac{9}{32(\beta\Delta\mathcal{F}^\ddagger)^2} \right) \right]^{-2} \\
 &\approx \frac{D^\ddagger \pi \beta \Delta \mathcal{F}^\ddagger}{1 + \frac{1}{2\beta\Delta\mathcal{F}^\ddagger} + \frac{5}{8(\beta\Delta\mathcal{F}^\ddagger)^2}} \exp(-\beta\Delta\mathcal{F}^\ddagger) = r_0 \exp(-\beta\Delta\mathcal{F}^\ddagger), \tag{3.23}
 \end{aligned}$$

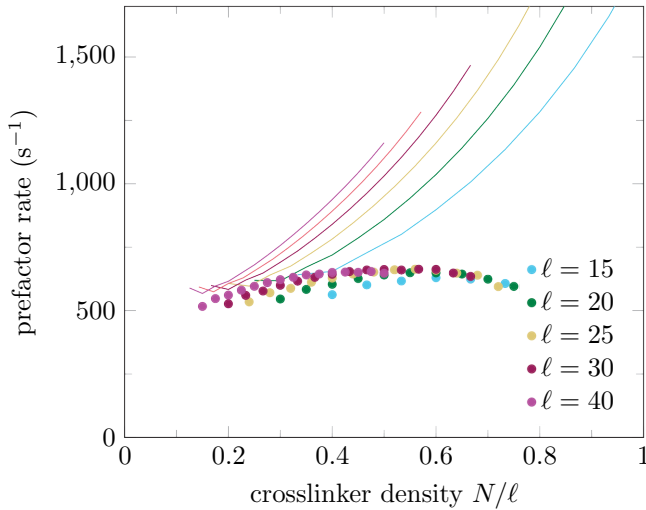


Figure 3.2: Kramers theory correctly predicts the order of magnitude of the prefactor of the microtubule jump rate. We estimate the prefactor in the simulations by estimating the full rate r as described in Chap. 2, after which we divide out the Boltzmann factor at the peak of the free-energy barrier, $r_0 = r \exp(\beta \Delta \mathcal{F}^\ddagger)$. These values are plotted as points as a function of the cross-linker density N/ℓ , since the curves for different values of the number of binding sites on the mobile microtubule ℓ seem to collapse in this representation. Kramers theory gives a numerical prediction of the prefactor through Eq. 3.2, plotted as continuous lines for the same values of ℓ . The order of magnitude of the theoretical values agree with the simulated values, but Kramers theory predicts exponentially rising trends in the prefactor while the simulations show downward trends.

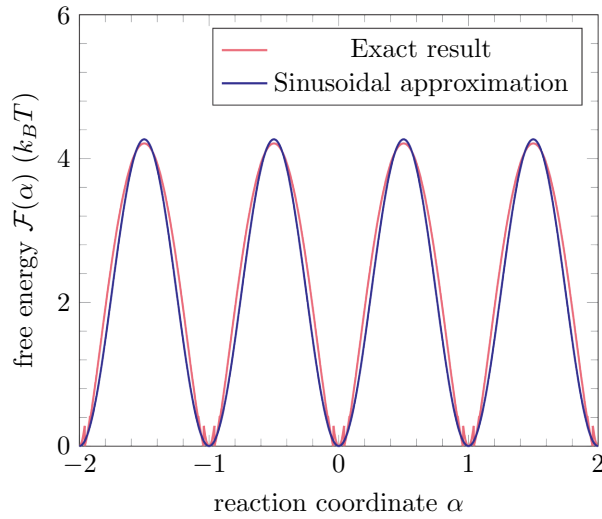


Figure 3.3: The free energy as a function of the reaction coordinate α contains discontinuities and has no simple expression in terms of elementary functions. Since we know the periodicity of the function and have analytical approximate expressions for the height of the free-energy barrier $\Delta\mathcal{F}^\ddagger$, we can approximate the free energy using a sinusoidal function with the same amplitude and periodicity. The sinusoidal function ignores the discontinuities and the approximate barrier height slightly overestimates the true barrier height, but the two functions agree well overall. The sinusoidal function can be used in combination with Kramers theory to find analytical expressions for the rate at which the microtubule jumps over the barriers. In this example, $\ell = 40$ and $N = 12$.

where we only keep terms up to the quadratic order in the expansion.

The analytical expression of the prefactor in Eq. 3.23 shows that Kramers theory predicts that the prefactor is proportional to the height of the free-energy barrier. We showed before that the height of the barrier scales exponentially with the density of cross-linkers in Eq. 2.84, so the prefactor predicted by Kramers theory also increases exponentially with the cross-linker density, as seen in Fig. 3.2.

Even though we can explain the exponential increase of the prefactor as predicted by Kramers theory, an explanation of why this predicted value deviates from the prefactor found in the simulations (see Fig. 3.2) remains lacking. The simulations show that the prefactor varies little with the number of cross-linkers N and the number of binding sites on the mobile microtubule ℓ , and it even decreases slightly with the cross-linker density, as opposed to the Kramers theory predictions. The ingredients of the prediction in Eq. 3.2 are the reaction coordinate, the free energy, and the short-time diffusion constant. Hence, we will first test whether errors in these three ingredients can explain the inaccuracy of Kramers theory.

For the short-time diffusion constant, we obtained an approximate expression in Eq. 3.10, which appears to deviate little from the values obtained from the simulations. To investigate the extent by which the diffusion constant influences the discrepancy between theory and simulations, we reverse the procedure and calculate the diffusion constant that would give rise to the correct prediction through Kramers theory. Using the approximation Eq. 3.5 that the short-time diffusion constant is independent of the reaction coordinate α , Eq. 3.2 gives

$$D^\ddagger = r_0 \int_0^1 \exp\left(\beta\left(\mathcal{F}(\alpha) - \mathcal{F}^\ddagger\right)\right) d\alpha \int_0^1 \exp(-\beta\mathcal{F}(\alpha)) d\alpha. \quad (3.24)$$

We calculate this diffusion constant for each set of N and ℓ for which we have estimated r_0 in simulations, and plot the results along with the directly sampled diffusion constants in Fig. 3.4. The required diffusion constants are significantly lower than the ones that are directly observed, showing that the approximation error of D^\ddagger using Eq. 3.10 is not the cause of the deviation, since these errors shown in Fig. 3.1 are much smaller than the errors shown in Fig. 3.4.

Another possibility is that Eq. 3.5 fails, and that the short-time diffusion constant does depend strongly on the reaction coordinate α . To investigate this, we modify Eq. 3.8 not focussing on $\alpha = 1/2$, but keeping the reaction coordinate as a variable. Then, for a given α , we assume that $N_R \approx \alpha N$, and that $x \approx \alpha\delta$. When an L -linker with stretch x hops, it becomes an R -linker with stretch $\delta - x$. Hence, Eq. 2.23 says that the rate of this single transition equals

$$h = h_0 \exp\left[-\frac{k\delta^2}{4k_B T} \left((\delta - x)^2 - x^2\right)\right]. \quad (3.25)$$

Similarly, a hop of an R -linker to an L -linker follows the same equation with a change of sign in the exponent. Then, a single cross-linker can make this transition in two ways, because both heads of the cross-linker can hop. Furthermore, an L -linker is excluded from hopping to a neighbouring site when another L -linker is directly next to it, but an R -linker cannot block the hopping of an L -linker because we do not allow cross-linkers

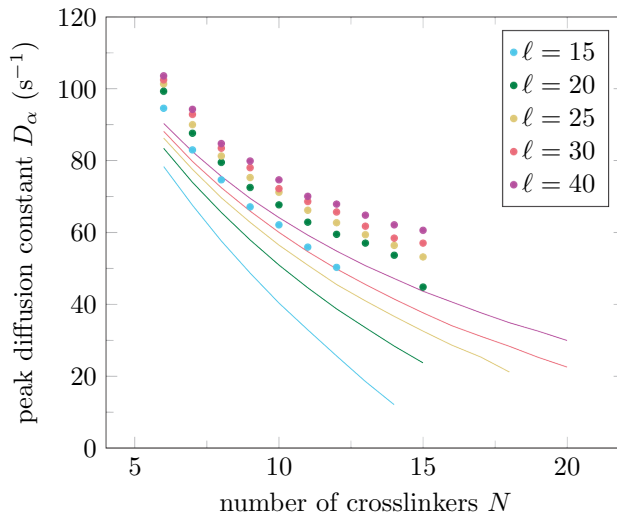


Figure 3.4: The short-time diffusion constant at the peak of the barrier D^\ddagger estimated directly in simulations (points, Eq. 3.14) compared to the diffusion constant that would lead to the correct prediction of the prefactor of the microtubule jump rate using Kramers theory (lines, Eq. 3.24). Although the trends in the two sets are similar, the difference is significant, showing that the failure of Kramers theory is not caused by inaccuracies of the theoretical diffusion constant as seen in Fig. 3.1.

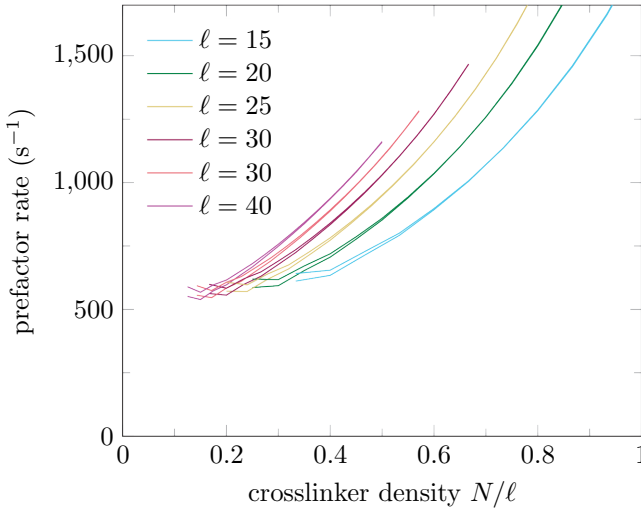


Figure 3.5: The Kramers theory predictions with a diffusion constant that varies with the reaction coordinate α according to Eq. 3.27 (lower lines) are very similar to the Kramers theory predictions that use a constant diffusion constant, which is measured at the top of the barrier and follows Eq. 3.10 (upper lines). The former prefactors are slightly lower than the latter ones for low densities, but asymptotically converge for larger densities. We thus conclude that the discrepancy between the prefactor measured in the simulations and the prefactor predicted by Kramers theory, as seen in Fig. 3.2, is not caused by our approximation that the diffusion constant does not vary with the reaction coordinate α .

to cross each other. The rates to move from N_R to $N_R + 1$ and $N_R - 1$ are not equal, and to extract the diffusion constant we take the average rate $h_{\text{tot}} = (h_{\text{tot},\uparrow} + h_{\text{tot},\downarrow})/2$. Combined, these considerations lead to an expression for the total rate of

$$h_{\text{tot}}(\alpha) \approx Nh_0 \left\{ \alpha \left(1 - \alpha \frac{N}{\ell} \right) \exp \left[-\frac{k\delta^2}{4k_B T} (\alpha^2 - (1 - \alpha)^2) \right] + (1 - \alpha) \left(1 - (1 - \alpha) \frac{N}{\ell} \right) \exp \left[\frac{k\delta^2}{4k_B T} (\alpha^2 - (1 - \alpha)^2) \right] \right\}. \quad (3.26)$$

We can confirm the validity of Eq. 3.26 by substituting $\alpha = 1/2$, in which case we retrieve Eq. 3.8. Using the total hop rate Eq. 3.26, we obtain an expression for the short-time diffusion constant that depends on α ,

$$D^\ddagger(\alpha) = \frac{1}{4} \left(\frac{D_m}{\delta^2} + \frac{h_{\text{tot}}(\alpha)}{N^2} \right). \quad (3.27)$$

Inserting Eq. 3.27 into Eq. 3.2, we retrieve new Kramers predictions of the prefactor of the microtubule jump rate as a function of the cross-linker density N/ℓ with a diffusion constant that varies over the reaction coordinate α . We compare these new results with the original ones in Fig. 3.5, where we see that the new expressions coincide nearly

perfectly with the results obtained with a non-varying diffusion constant. As shown in Fig. 3.2, these trends do not agree with the simulated prefactors. Hence, the more elaborate expression for the diffusion constant Eq. 3.27 does not provide an explanation for the failure of Kramers theory to predict the correct prefactor.

Given that the diffusion constant, which is one ingredient of Kramers theory, is sufficiently well described by Eq. 3.10, we look into the other ingredients of Kramers theory, which are the reaction coordinate and the free-energy profile. Since we have an exact expression for the free energy as a function of the microtubule position x and the number of right-pulling cross-linkers N_R , the source of the discrepancy cannot be the expression itself. However, the marginalisation to a one-dimensional free-energy profile results from the expression of α , which is an approximation of the reaction coordinate. In Fig. 2.17, we showed that the committer space is perpendicular to the reaction coordinate α for $N = 12$ and $\ell = 40$. Hence, we confirmed that α is the true reaction coordinate at the low cross-linker density $N/\ell = 0.3$, and Fig. 3.2 shows little discrepancy between the Kramers prediction and the simulated prefactor at low densities.

A possible explanation of the increased failure of Kramers theory for larger densities could be due to the changing of the reaction coordinate. To test this, we repeat the analysis shown in Fig. 2.17 for a system with $N = 7$ and $\ell = 7$, such that the mobile microtubule is fully covered. We choose this relatively low number of cross-linkers because it leads to the barrier height $\Delta\mathcal{F}^\ddagger = 5.8k_B T$ where brute force simulation of the barrier crossings remain feasible.

We show the results of the committer analysis for $N/\ell = 1$ in Fig. 3.6. Because the free energy is very high in some regions of the plot, specifically in the upper-left and bottom-right corners, the simulations strongly avoid these regions, which lowers the quality of the statistics there. Therefore, it remains largely unclear how the committer, which is the region where the probability of being on a transition path equals $1/2$ [33], is oriented in Fig. 3.6. The probability to be on a transition path seems to be higher along the diagonal $x/\delta = 1 - N_R/N$, which would indicate that α is still the reaction coordinate, but the density plot could also indicate a committer that is perpendicular to the N_R axis. Since cross-linker hops are suppressed more at high cross-linker densities because of the exclusion effects, the progress in x could become less important for crossing the free-energy barrier. Hence, we will apply Kramers theory using N_R as the reaction coordinate to investigate if a change in the reaction coordinate can explain the failure of Kramers theory for high cross-linker densities.

With the reaction coordinate N_R , the diffusion constant is given by h_{tot} in Eq. 3.8. Furthermore, the free energy needs to be marginalised along N_R , which is done by integrating out x from 0 to δ ,

$$\begin{aligned} \mathcal{F}(N_R) = & \frac{k\delta^2}{2N} N_R(N - N_R) - k_B T \log \left[\binom{\ell - N_R}{N - N_R} \binom{\ell - N + N_R}{N_R} / \binom{\ell}{N} \right] \\ & - k_B T \log \left[\left(\text{erf} \left(\sqrt{\frac{k\delta^2 N}{2k_B T}} \left(1 - \frac{N_R}{N} \right) \right) - \text{erf} \left(\sqrt{\frac{k\delta^2 N}{2k_B T}} \frac{N_R}{N} \right) \right) / \text{erf} \left(\sqrt{\frac{k\delta^2 N}{2k_B T}} \right) \right]. \quad (3.28) \end{aligned}$$

We normalised this free energy such that the zero point is at $N_R = 0$. Using this diffusion constant and free energy, we apply Kramers theory to find transition rates, treating N_R

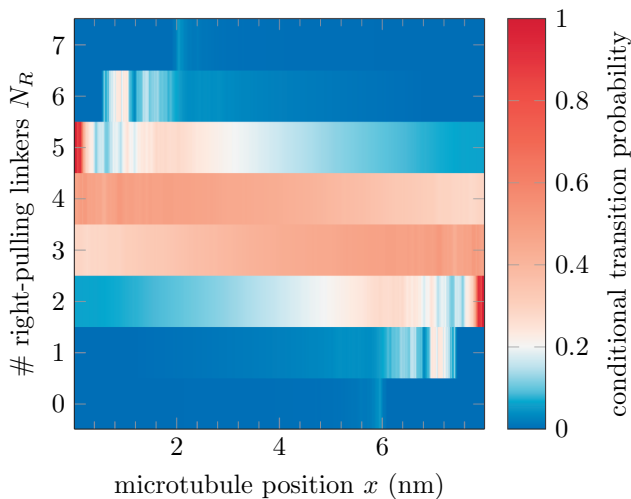


Figure 3.6: The probability that the system is on a transition path when it is at a given location x and N_R . The analysis repeats the one shown in Fig. 2.17, but for a high density system where $N = 7$ and $\ell = 7$. The committer is the space where the shown probability is roughly 0.5, and should be perpendicular to the reaction coordinate. The order parameter α , which is the reaction coordinate for a system with $N = 12$ and $\ell = 40$, runs along the diagonal from the bottom-left to the top-right in this figure. The data analysis maps all forward and backward paths to a single representation for improving the statistics, leading the histogram to be symmetric under a half rotation $((x, N_R) \rightarrow (\delta - x, N - N_R))$. The statistics is very poor in the top left and bottom right corners, obscuring whether the probability equals 0.5 there. The transition path probability does appear to rise around the top-left to bottom-right diagonal for $N_R = 6$ and $N_R = 5$, which may indicate that α still accurately captures the reaction coordinate. However, the results could also be consistent with the reaction coordinate shifting to N_R .

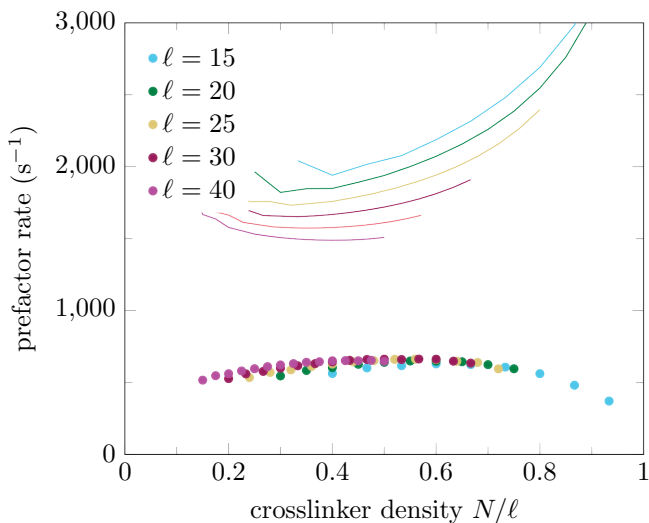


Figure 3.7: The prefactor from simulations (points) compared to the prefactor as obtained from Kramers theory with a reaction coordinate that points along N_R . Compared to the prediction shown in Fig. 3.2 that uses α as the reaction coordinate, the Kramers prefactor is much worse for small densities, and the exponential increase observed for larger densities is still observed.

as a continuous variable that runs from 0 to N . Then, we divide the obtained Kramers rates by the Boltzmann factor $\exp(-\beta\Delta\mathcal{F}^\ddagger)$, which uses α as a reaction coordinate, such that we can compare the results to the prefactors shown before. The results are shown in Fig. 3.7. Compared to Fig. 3.2, Fig. 3.7 shows that the predictions of Kramers theory using α as the reaction coordinate strongly outperform the ones using N_R , even for large densities where the predicted prefactor still shows exponential growth even with N_R as the reaction coordinate. The failure of Kramers theory can thus not be explained by a shift of the reaction coordinate towards N_R for high densities.

Summarising, the discrepancy between Kramers theory and the simulations is neither caused by the expression of the free energy, given in an exact form in Eq. 3.3, nor by the misalignment of the reaction coordinate, nor by the expression for the short-time diffusion constant at the peak, which is approximated well by Eq. 3.10, nor by the approximation in Eq. 3.5 that assumes that the diffusion constant does not vary with the reaction coordinate α . Hence, to explain the failure of Kramers theory, one of the basic assumptions of Kramers theory has to break down.

One of the assumptions of Kramers theory is that the distribution within the well always remains close to a Boltzmann distribution. It is unlikely that this assumption breaks down, since the simulated model obeys detailed balance, and the dynamics of the cross-linkers and the microtubule is intrinsically Markovian. Moreover, larger numbers of cross-linkers and higher cross-linker densities lead to larger free-energy barriers, which increases the separation of the small time scale of the equilibration within the well and the large time scale $1/2r$ of the jumps between wells. Therefore, the validity

of Kramers theory should increase with the density N/ℓ , while Fig. 3.2 shows that the validity actually decreases.

Hence, the breakdown of Kramers theory must be because the assumption breaks down that the dynamics is described well with a Fokker-Planck equation at all time scales. We saw in Sec. 3.2 that two methods of estimating the short-time diffusion constant at the peak of the barrier do not agree with each other because of the discrete nature of the cross-linker hops. It is likely that this aspect of the dynamics also causes the simulated rate of hopping to be lower than the one expected through Kramers theory.

In the theory, movement proceeds with infinitesimal diffusive steps along the reaction coordinate. In the two dimensional picture of the (x, N_R) space, true diffusion would allow the system to take transition paths that are arbitrarily close to the optimal path, where the optimal path is determined by the continuous free-energy profile on the two dimensional space. For a given N_R , the optimal position is given by minimising the potential energy (Eq. 2.2), giving $x = \delta N_R/N$. This line defines the optimal transition path which is parallel to the reaction coordinate α . Since the cross-linker hops cause an instantaneous change in α of $1/2N$, and only change N_R while leaving x invariant, the microtubule jumps cannot follow the optimal transition path as predicted by the continuous free-energy profile. Even though the reaction coordinate does capture the average direction of transition paths, the paths have to deviate from the optimal path on small time and length scales.

As an example, we imagine the system to be in a state along the optimal line $x/\delta = N_R/N$, where the potential energy equals

$$U_{\text{opt}}(N_R) = \frac{k\delta^2}{2N} N_R (N - N_R). \quad (3.29)$$

Then, a forward hop transitions $(x, N_R) \rightarrow (x, N_R + 1)$, leading to a deviation from the new optimal potential energy at $N_R + 1$,

$$U(x, N_R + 1) - U_{\text{opt}}(N_R + 1) = \frac{k\delta^2}{2N}. \quad (3.30)$$

The entropic terms are independent of x . Hence, the optimal path in the free energy equals the optimal path in the potential energy, and no paths exist that follow the optimal free-energy path exactly. Even though this can explain why Kramers theory is not exact, it cannot account for the increased failure of Kramers theory for high cross-linker densities alone, since Eq. 3.30 does not depend on the microtubule length ℓ .

As shown in Fig. 3.8, the transition paths for the highest density appear to be significantly different from the paths observed for a lower density in Fig. 2.3. Specifically, the transition paths seem to include more diffusive steps in N_R , which may be due to an increase of the time it takes to perform the transition itself. To test this, we measure the time ΔT_t that a transition path takes in the simulations, and average over 50 microtubule jumps. For a low density ($\ell = 40$ and $N = 7$) we find $\Delta T_t = 0.8$ ms, whereas for the high density simulations ($\ell = 7$ and $N = 7$) we find $\Delta T_t = 1.8$ ms. The time difference becomes more pronounced when more cross-linkers are bound, where we find $\Delta T_t = 1.0$ ms ($\ell = 40$ and $N = 12$) and $\Delta T_t = 3.8$ ms ($\ell = 12$ and $N = 12$). The longer times at which the system resides at the peak of the barrier may explain why the transitions

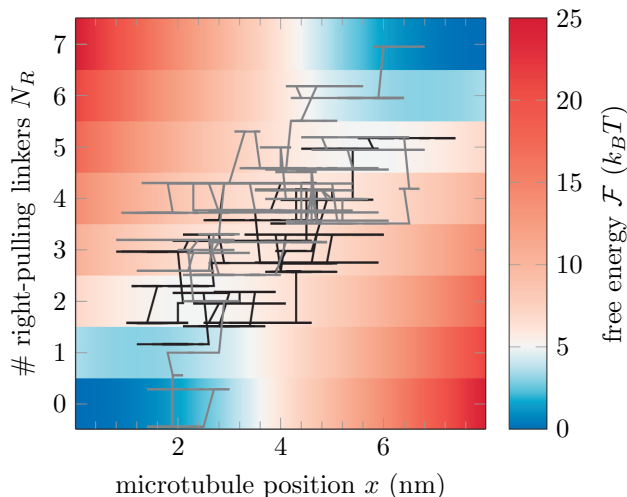


Figure 3.8: The free energy as a function of the mobile microtubule position x and the number of right-pulling cross-linkers N_R for $N = 7$ and $\ell = 7$, together with two transition paths. Compared to Fig. 2.3, the paths still roughly follow the diagonal, but seem to take more diffusive steps in both the x and the N_R directions.

become less likely with increased density. For an intuitive understanding, we define r_p as the rate at which the system moves to the peak region, and ΔT_p as the average time that the system resides around the peak of the barrier after moving to it. Then, the probability to be in the barrier region is proportional to both quantities $p_b \propto r_p \Delta T_p$. Since p_B is determined through the free energy and the Boltzmann distribution, an increase in the residence time around the peak of the barrier ΔT_p must be accompanied by a decrease of the rate at which the system moves to the peak to the barrier r_p . Furthermore, Sec. 3.2 shows that the average time to leave a small region close to the peak is lower than expected for a continuous diffusion process. We speculate that the blocking of cross-linker hops at high cross-linker densities increases the residence time at the peak of the free-energy barrier much more than expected in a continuous diffusion process. This increase of ΔT_p is accompanied by a decrease of r_p , and the rate r to jump over the barrier is limited by the rate r_p at which the system reaches the barrier. Hence, the failure of Kramers theory for higher densities of cross-linkers is likely the result of a significant slowdown of the dynamics at the peak that is not captured by the continuous diffusion constant.

3.4. DISCUSSION

We have shown that Kramers theory finds the correct order of magnitude of the prefactor of the microtubule jump rate. However, it fails at predicting how this prefactor scales with the density of cross-linkers. By examining all assumptions and ingredients

of Kramers theory, we believe that the most likely reason for its breakdown is the failure of a spatially continuous Fokker-Planck equation to describe the dynamics well enough on all time scales, specifically on the small time scales at which cross-linker hops cause significantly discrete steps in the reaction coordinate.

In Chap. 2, we chose to assume that the prefactor r_0 of the microtubule jump rate r is constant, and the success of this assumption indicates that the order parameter α generally captures the reaction coordinate well. While Kramers theory fails, the success of the Arrhenius equation shows that even in situations where the system dynamics is not described well by a simple diffusion process, the basic notion from transition state theory that the peak of the free-energy barrier constitutes the bottleneck for transitions remains valid. Hence, the expression

$$r = r_0 \exp\left(-\frac{\Delta\mathcal{F}^\ddagger}{k_B T}\right) \quad (3.31)$$

is applicable to a large class of systems with different underlying dynamics, and Kramers theory only provides an explanation for this equation for a limited subset of those systems. For a general equilibrium system, even if the dynamics is correlated and does not equilibrate within the time scale of a single transition, the assumption that the average transition rate is limited by the probability of the transition bottlenecks remains a valid one. Hence, Eq. 3.31, which by itself is true for any rate as long as there are no limitations on r_0 , becomes meaningful by stating that any variable that affects the free energy has a subexponential effect on the prefactor r_0 .

4

CONDENSATION FORCES AND ENTROPIC FORCES ON OVERLAPPING MICROTUBULES

Passive cross-linkers that bind to filaments cause the overlap length between these filaments to increase, contracting the filament-to-filament distance. This motion is caused by entropic forces when the number of cross-linkers on the filaments remains constant, and by condensation forces when the cross-linkers can bind and unbind from the filament. Since the friction between the filaments increases exponentially with the number of cross-linkers and superexponentially with the density of cross-linkers, we can predict the velocity of the filament contraction. We show that entropic forces increase the overlap length with the square root of time, while condensation forces lead to a logarithmic time dependence. Furthermore, how the overlap length depends on time does not change qualitatively if we include cooperative interactions between the cross-linkers or multiple protofilaments on the filament. We test how experimental time traces compare with these predictions, showing that the (super)exponential increase of friction can explain the shape of the time traces well.

In Chap. 2, we describe how the friction between two cross-linked microtubules scales with the number of cross-linkers and the overlap length. There, we use a geometry that is symmetric under translations of the microtubule position x by multiples of the lattice constant δ , which prevents the occurrence of entropic forces [18]. Furthermore, the cross-linkers do not bind or unbind. In this chapter, we reintroduce the original model from [18] in which the overlap length can vary, such that both entropic and condensation forces can emerge. In the context of partially overlapping filaments, an entropic force is caused by the diffusible cross-linkers that are bound within the overlap and that increase their entropy by expanding the size of the overlap while the number of cross-linkers remains constant [18]. On the other hand, a condensation force arises when the cross-linking proteins can bind from the solution, which expands the overlap by increasing the number of bound cross-linkers, lowering the free energy. Here, we investigate the effects of the asymmetric model geometry on the friction, and observe how the combination of this friction coefficient and either the entropic or the condensation force influences the speed at which the overlap expands.

Previously, it was observed computationally and confirmed experimentally that the friction between two filaments scales exponentially with the number of cross-linkers [18]. We found an explanation for this exponential scaling in Chap. 2, which shows that it persists for low densities of cross-linkers. At higher densities, we observed that exclusion effects cause the friction coefficient to scale superexponentially with the cross-linker density. However, it has been proposed that the observed exponential increase in the friction coefficient can be explained by a model in which the friction coefficient scales linearly with the number of cross-linkers for low densities, and that the exponential increase is only due to exclusion effects [74]. Here, we will investigate how the two different models for the friction coefficient influence the predicted time traces in the case of a condensation force, and compare these predicted time traces to available experiments.

Since evidence exists that the binding of microtubule cross-linking proteins such as Ase1 can be cooperative [86], we also look into the affects that cooperative binding of cross-linkers has on the entropic and condensation forces. Combined with the effects of cooperativity on the friction coefficient, as shown in Sec. 2.K, we discuss how cooperative interactions between the cross-linkers can change the dynamics of the expanding filament overlaps. Similarly, we describe how the friction coefficient and the expansion forces change when the cross-linkers bind to multiple protofilaments on each filament. Specifically, we take into account the helical offset that is found in microtubule protofilaments [95, 96], and show how this introduces extra strain on the cross-linkers, which affects the barrier crossing mechanism that caused the friction between microtubules.

4.1. FRICTION COEFFICIENT AND ENTROPIC FORCES

When two microtubules overlap partially, entropic forces can increase their overlap [18]. These forces arise when the number of cross-linkers is constant, so when the cross-linkers cannot bind or unbind, but when they can still diffuse within the overlap. In that case, the entropy associated with the number of ways to place the cross-linkers in the overlap increases if the overlap length increases, thus leading to an entropically driven force that maximises the overlap length. To investigate how the interplay between this

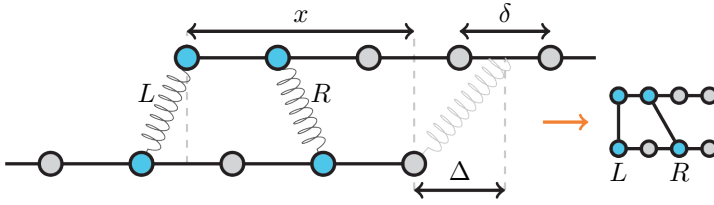


Figure 4.1: A different version of the model of Fig. 2.1, first presented in [18], that can be used to study entropic forces and condensation forces. The maximum stretch of the cross-linkers along the direction of the filaments is Δ , which we choose $\Delta = \delta$. We define the discrete overlap length ℓ as the number of binding sites on one filament that are accessible to the cross-linkers, which equals the number of sites within a length of $x + \Delta$ on either filament. In the example shown, $\ell = 4$. To count the number of microstates for a given number of right-pulling R -linkers and left-pulling L -linkers, it is convenient to ignore the offset of the two lattices. We show this simplified representation of the overlap region on the right, where L -linkers are straight lines and R -linkers are diagonal lines. The sites on the top-right and on the bottom-left cannot be occupied by an R -linker.

driving force and the opposing friction force leads to the movement of the microtubules, we revise the model of Fig. 2.1 to a situation where two long microtubules overlap partially, as shown in Fig. 4.1. In this case, we define the position x as the distance between the ends of the two microtubules, such that x increases if the top microtubule moves to the left. We define the discrete overlap length ℓ as the number of sites in the overlap that cross-linkers can access, which depends on x through

$$\ell = \left\lceil \frac{x + \Delta}{\delta} \right\rceil, \quad (4.1)$$

where Δ is the maximum stretch of the cross-linkers (set to δ) and we take the ceiling to make ℓ count the number of binding sites within the overlap.

The model shown in Fig. 4.1 gives rise to an entropic force, and also contains the same barrier crossing mechanism that makes the top microtubule move through jumps of length δ and that sets the friction coefficient, as shown in Chap. 2. We require an expression for the free energy to find both the driving force and the friction coefficient. During a jump of the microtubule from ℓ to $\ell \pm 1$, the potential energy depends on the position x similar to Eq. 2.2, but with N_R replaced by $N - N_R$ due to the change of sign of x ,

$$U(x, N_R) = \frac{1}{2} k \delta^2 N \left[\left(\frac{x}{\delta} - 1 + \frac{N_R}{N} \right)^2 + \frac{N_R}{N} \left(1 - \frac{N_R}{N} \right) \right]. \quad (4.2)$$

This potential energy is independent of the overlap length ℓ , showing that the expansion force is indeed governed by the entropic component of the free energy. Similar as in Eq. 2.4, this entropy is given by the number of permutations of N_R cross-linkers that pull the top microtubule to the right and $N - N_R$ cross-linkers that pull the top microtubule to the left. However, due to the change in geometry, the expression Eq. 2.4 needs to be

adjusted,

$$\Omega(\ell, N, N_R) = \binom{\ell - N_R}{N - N_R} \binom{\ell - N + N_R - 1}{N_R}. \quad (4.3)$$

As shown in the drawing on the right in Fig. 4.1, the right-pulling R -linkers cannot fill the rightmost site of the top microtubule in the overlap, which reduces the free space in which the R -linkers can be permuted by 1.

To investigate the origin of the entropic force, we focus on the entropy when the two filaments are in perfect register. In that case, $N_R = 0$, and the number of microstates is counted by the number of ways that N cross-linkers can be placed in an overlap of ℓ sites,

$$\Omega(\ell, N, N_R = 0) = \binom{\ell}{N}. \quad (4.4)$$

Since the potential energy is the same for all states in which the microtubules are in register, the entropy is given by the Boltzmann expression $S = k_B \log(\Omega)$, and the entropic force follows from a derivative of the free energy \mathcal{F} ,

$$F_{\text{ent}} = -\frac{d\mathcal{F}}{dx} = T \frac{dS}{dx} = k_B T \frac{d \log(\Omega)}{dx} \approx \frac{k_B T}{\delta} \log\left(\frac{\Omega(\ell)}{\Omega(\ell-1)}\right) = -\frac{k_B T}{\delta} \log\left(1 - \frac{N}{\ell}\right). \quad (4.5)$$

Here, we approximate the derivative to x by taking a finite difference δ . The final expression is strictly non-negative, showing that the entropic force can only drive the filaments to overlap more. For low densities, the expression can be approximated as

$$F_{\text{ent}} \approx \frac{k_B T}{\delta} \frac{N}{\ell} \approx \frac{N k_B T}{x}, \quad (4.6)$$

where the final form emphasises the resemblance to the ideal gas law, with F_{ent} playing the role of the pressure and the overlap length x the role of the volume [18].

The reaction coordinate α as defined in Eq. 2.5 remains largely unchanged, since the overlap length ℓ does not influence it. Only the direction of N_R changes because of the change of sign of x in our definition of the system in Fig. 4.1, leading to

$$\alpha = \frac{1}{2} \left(\frac{x}{\delta} + 1 - \frac{N_R}{N} \right). \quad (4.7)$$

Using this reaction coordinate, together with Eq. 2.2 for the potential energy and Eq. 4.3 for the entropic term, we get an expression for the free energy similar to Eq. 3.3,

$$\begin{aligned} \mathcal{F}(\alpha, \ell) = & -k_B T \log \left\{ \sum_{N_R=0}^N \mathbb{1} \left(0 \leq 2\alpha - 1 + \frac{N_R}{N} \leq 1 \right) \binom{\ell - N_R}{N - N_R} \binom{\ell - N + N_R - 1}{N_R} \right. \\ & \left. \times \exp \left[-\frac{k\delta^2 N}{2k_B T} \left(4 \left(\alpha - 1 + \frac{N_R}{N} \right)^2 + \frac{N_R}{N} \left(1 - \frac{N_R}{N} \right) \right) \right] \right\}. \quad (4.8) \end{aligned}$$

Here, $\alpha \in (0, 1]$, since $\alpha = 1$ gives the correct expression for the number of microstates when the two lattices are perfectly in register, while $\alpha = 0$ does not. We also include ℓ as a variable of the function $\mathcal{F}(\alpha, \ell)$ because it changes as the relative positions of the filaments change in Fig. 4.1.

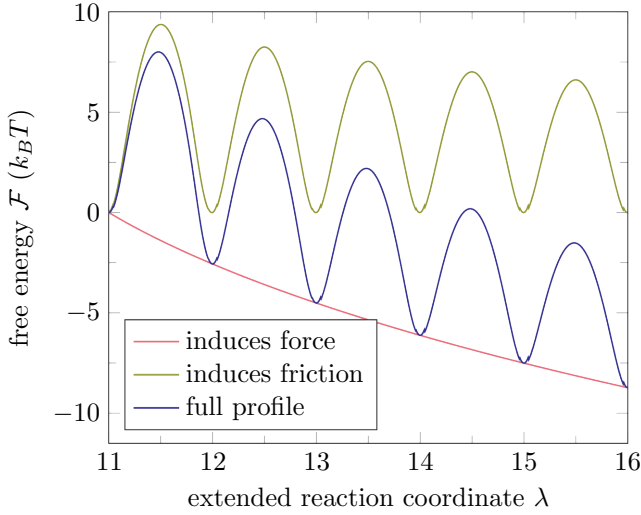


Figure 4.2: The free energy as a function of the extended reaction coordinate λ (blue line) for $N = 12$ cross-linkers. The number of sites in the overlap $\ell \geq N$, so by the construction of λ and Eq. 4.10 $\lambda > 11$. Similar to in Chap. 2, the free energy shows the barriers that make the microtubules move with jumps. Furthermore, the free energy is lowered when the overlap length increases, leading to an entropic force. The free-energy profile can be decomposed into a fine-grained barrier profile that induces an effective friction (yellow line) and a coarse-grained smooth slope that sets the entropic force (red line).

Until now, we have focussed on the dynamics within a transition between ℓ and $\ell + 1$, where $\alpha \in (0, 1]$, but to properly visualise the entropic force we need to find the free-energy profile over arbitrarily large changes in the overlap length. Therefore, we extend the reaction coordinate to the real line to represent the overlap length in units of the lattice spacing, and we call this parameter λ to distinguish it from the reaction coordinate for a single transition, which can be retrieved from λ by mapping it back to the range $(0, 1]$,

$$\alpha = 1 - \text{mod}(1 - \lambda, 1). \quad (4.9)$$

Here, $\text{mod}(x, y)$ is the modulo function that returns the remainder of x after division by y . Eq. 4.9 equals $\text{mod}(\lambda, 1)$, except that it maps λ to $(0, 1]$ instead of $[0, 1)$. Then, we link λ to the overlap length by

$$\ell = \lceil \lambda + 1 \rceil, \quad (4.10)$$

which we chose such that λ resembles x/δ in Eq. 4.1. Using Eq. 4.9 and Eq. 4.10 to define α and ℓ , Eq. 4.8 gives the free energy as a function of λ , $\mathcal{F}(\lambda) \equiv \mathcal{F}(\alpha(\lambda), \ell(\lambda))$. We plot $\mathcal{F}(\lambda)$ in Fig. 4.2, showing that the free energy consists of a periodic set of barriers that shows a downward trend due to the entropic force. We can decompose these two effects

by defining a smooth free energy that captures the large scale trend,

$$\mathcal{F}_{\text{ent}}(\lambda) = -k_B T \log \left[\binom{\lambda+1}{N} \right], \quad (4.11)$$

which uses Eq. 4.4. We approximate the overlap length $\ell \approx \lambda + 1$ as a continuous variable, because on a coarse-grained level the barriers become imperceptible and the free-energy profile appears smooth. In that coarse-grained picture, the effect of the barriers is incorporated into the effective friction coefficient. Microscopically, the barriers that cause the effective friction coefficient follow

$$\mathcal{F}_{\text{fric}}(\lambda) = \mathcal{F}(\alpha(\lambda), \ell(\lambda)) - \mathcal{F}_{\text{ent}}(\lambda). \quad (4.12)$$

Both the free energy term that induces the entropic force and the term that induces effective friction are shown in Fig. 4.2. The graph shows that the barrier height decreases as the overlap length increases, leading to a reduction in the friction coefficient according to Eq. 2.9. Simultaneously, the entropic force also decreases with the overlap length, as can be seen from the decreasing slope of the entropic force part of the free energy in Fig. 4.2. Hence, it is interesting to see how the interplay between the entropic force and the friction coefficient changes with the overlap length.

The free-energy profile obtained from Eq. 4.12 contains barriers that are nearly identical to the free-energy barriers obtained in Chap. 2. The only quantitative difference between the expressions for the free energy in the two situations comes from the new expression of the number of microstates Eq. 4.3 compared to Eq. 2.4. If we repeat the derivation of an analytical approximation of the free-energy barrier height, which is shown in Sec. 2.I for the situation without an entropic force, we realise that this small difference of the entropies does not influence the leading orders of the Taylor expansion. Hence, the approximation of the barrier heights is the same as in Eq. 2.7 and the friction coefficient follows Eq. 2.9,

$$\zeta \approx \zeta_0 \exp \left(BN \exp \left(\frac{1}{4B} \frac{N}{\ell} \right) \right), \quad (4.13)$$

with $B = k\delta^2 / (8k_B T) - \log(2)$. Using Eq. 2.37 and the Einstein relation Eq. 2.1 to estimate the friction coefficient for $N = 12$ and $\ell = 40$, we find $\zeta_0 = 71 \text{ k}_B \text{Ts} / \mu\text{m}^2 \approx 0.3 \text{ pNs} \mu\text{m}^{-1}$. The deterministic differential equation that describes the average overdamped movement of the location of the top filament $\delta\lambda$ follows from combining Eq. 4.5 and Eq. 4.13, where we replace ℓ with $\lambda + 1$ and $x \approx \lambda\delta$,

$$\frac{d\lambda}{dt} = \frac{F_{\text{ent}}(\lambda)}{\delta\zeta(\lambda)} \approx - \frac{k_B T \log \left(1 - \frac{N}{\lambda+1} \right)}{\delta^2 \zeta_0 \exp \left(BN \exp \left(\frac{1}{4B} \frac{N}{\lambda+1} \right) \right)} \approx \frac{Nk_B T}{\delta^2 \zeta_0 \exp(BN)\lambda}. \quad (4.14)$$

The expression of the first approximation is highly nonlinear, and can be solved numerically. The second approximation is valid for low cross-linker densities, so for $N/\lambda \ll 1$ and $\lambda \gg 1$, where the force approaches 0 according to Eq. 4.6 whereas the friction reaches a finite asymptotic value. This approximate differential equation has an analytical solution,

$$\lambda(t) \approx \sqrt{\lambda(0) + \frac{2Nk_B T}{\delta^2 \zeta_0 \exp(BN)} t}. \quad (4.15)$$

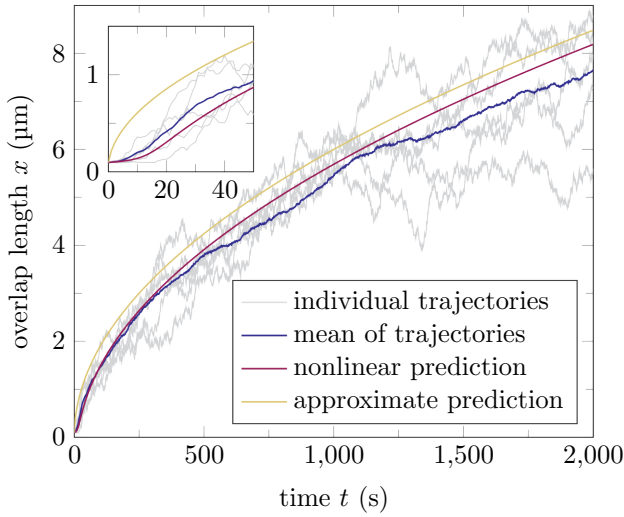


Figure 4.3: Filament overlaps expand under the influence of an entropic force. We simulate a system with $N = 12$ that starts at $\ell = 13$ and plot five trajectories (grey). Furthermore, we plot the average over 50 such trajectories (blue). We compare the results to the numerical solution to the nonlinear differential equation Eq. 4.14 (red), and the analytical solution that is valid for low cross-linker densities (yellow). For larger times, the solutions converge, leaving a finite difference, and the average simulated trajectory confirms their validity. (inset) For small times, the movement of the microtubules speeds up nonlinearly, which is caused by the superexponential decrease of the friction given in Eq. 4.13.

In Fig. 4.3, we plot the numerical solution of the nonlinear differential equation given by Eq. 4.14 together with the approximate analytical solution Eq. 4.15. We set $N = 12$ and use $\lambda = N = 12$ as the initial boundary condition ($\ell \approx \lambda + 1 = 13$), corresponding to a highly compressed system with an initial overlap length $x \approx \lambda\delta$. The approximate solution is very similar to the numerical solution for larger times, where the overlap length is large and the density of cross-linkers is low. For small times, the numerical solution shows that the microtubules move much slower. Because the initial density of cross-linkers N/ℓ is close to 1 and the friction coefficient scales superexponentially with this density, the high entropic force still leads to a slow initial expansion.

We compare the solutions of the differential equations to several simulated trajectories. We show five of these simulation time traces together with an average over 50 trajectories, showing both the relative thermal diffusion of the microtubules and confirming that the average trend indeed resembles the numerical solution to Eq. 4.14 well. The inset of Fig. 4.3 focusses on time scales up to 30s, confirming that the movement of the microtubule overlap is initially very slow. After the overlap starts to expand, the density of cross-linkers decreases, leading to a strong nonlinear decrease of the friction and speeding up the relative movement of the microtubules. Hence, an experimental setup with sufficient spatiotemporal resolution may directly observe the superexponential in-

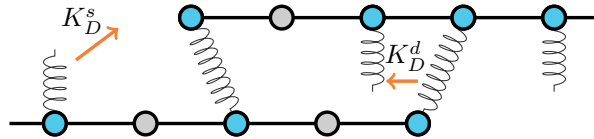


Figure 4.4: The same model as in Fig. 4.1, but including cross-linker binding dynamics. Cross-linkers can be in the solution, singly bound at any binding site, or doubly bound between a site on the top microtubule and a site on the bottom microtubule that are within reach of each other. We define the dissociation constant K_D^s for unbinding from the singly bound state to the solution and K_D^d for unbinding from the doubly bound to the singly bound state.

4

crease in friction by studying the short time movement of highly condensed microtubule overlaps with fixed numbers of cross-linkers.

4.2. FRICTION COEFFICIENT AND CONDENSATION FORCES

So far, we analysed the model shown in Fig. 4.1 for a situation where no cross-linkers are present in the solution, and the cross-linkers in the overlap cannot unbind. However, the dynamics of the model changes significantly when the cross-linkers display binding dynamics. To analyse the effects of binding, we change the model by including the options for cross-linkers to be partially bound, as shown in Fig. 4.4.

When (un)binding is allowed, we assume that the concentration of cross-linkers in the solution $[X]$ is constant, and we set the binding affinity of the cross-linkers to each site on the microtubules by defining the dissociation constant K_D^s . Once the cross-linker is partially bound to one of the microtubules, it can create a full connection to a site on the opposing microtubule when that site is within a distance Δ , which sets the maximum stretch of the cross-linkers (see Fig. 4.1). The dissociation constant K_D^d quantifies the affinity of a partially bound cross-linker that is within the overlap region to bind to a site on the opposite filament. Then, the likelihood that a specific site is occupied by a singly or doubly bound cross-linker is set by the Boltzmann factors $q_s = [X]/K_D^s$ and $q_d = [X]/(K_D^d K_D^s)$, respectively, where we define the Boltzmann factor for the unbound state to equal 1.

Because the cross-linkers can bind partially everywhere along both filaments, but can only bind fully when they are within the overlap region, the number of possible microstates increases if the overlap length increases. This effect creates a force that is driven by the binding, or condensation, of cross-linkers in the overlap region, and is therefore called a condensation force [18]. Using the definitions of the Boltzmann factors q_s and q_d , we find a partition function for the system shown in Fig. 4.4 which will give us an expression for this condensation force. We focus on a situation where the two lattices with an overlap ℓ are in perfect register, because Sec. 4.1 shows that the shape of the free-energy profile along a transition can be coarse-grained such that it only affects the effective friction coefficient. Then, if we assume that both microtubules have a finite length and L binding sites, then each microtubule contains $L - \ell$ sites that are not within the overlap. Those sites can be unoccupied (Boltzmann factor 1) or occupied by a dan-

gling cross-linker (q_s). Within the overlap, there are ℓ pairs of binding sites. There is one configuration in which both sites are free (Boltzmann factor 1), two configurations in which one of the two is occupied by a dangling cross-linker ($2q_s$), one configuration in which both sites are occupied by two different dangling cross-linkers (q_s^2), and finally one configuration in which a single cross-linker connects both binding sites (q_d). Hence, the full partition function for two microtubules that overlap with ℓ sites equals

$$\mathcal{Z}(\ell) = [1 + q_s]^{2(L-\ell)} [1 + 2q_s + q_s^2 + q_d]^\ell = [1 + q_s]^{2L} \left[1 + \frac{q_d}{(1 + q_s)^2} \right]^\ell. \quad (4.16)$$

The condensation force that drives the overlap expansion is found by taking the derivative of the free energy to the overlap length $x \approx (\ell - 1)\delta$,

$$F_{\text{cond}} = -\frac{d\mathcal{F}}{dx} = k_B T \frac{d \log(\mathcal{Z})}{dx} \approx \frac{k_B T}{\delta} \log\left(\frac{\mathcal{Z}(\ell)}{\mathcal{Z}(\ell-1)}\right) = \frac{k_B T}{\delta} \log\left(1 + \frac{q_d}{(1 + q_s)^2}\right). \quad (4.17)$$

Substituting back the definitions of q_s and q_d , we find how the force depends on the concentration of cross-linkers,

$$F_{\text{cond}} = \frac{k_B T}{\delta} \log\left(1 + \frac{K_D^s [X]}{K_D^d (K_D^s + [X])^2}\right). \quad (4.18)$$

This condensation force vanishes both in the limits of low and high cross-linker concentrations, because the force is generated by the binding of doubly connected cross-linkers within the overlap, which is impossible when $[X] \rightarrow 0$ and which get outcompeted by the binding of singly connected cross-linkers when $[X] \rightarrow \infty$. The force is always positive otherwise, and reaches a maximum for $[X] = K_D^s$,

$$F_{\text{cond,max}} = \frac{k_B T}{\delta} \log\left(1 + \frac{1}{4K_D^d}\right). \quad (4.19)$$

Hence, the condensation force is maximal when half of the binding sites are occupied by dangling cross-linkers ($[X] = K_D^s$), such that the overlap has exactly the right amount of empty sites and sites filled with cross-linkers to create full connections. Then, the force is simply increased by increasing the affinity of the cross-linkers to form fully bound cross-linkers, since $1/K_D^d = q_d/q_s$ shows that $1/K_D^d$ quantifies the likelihood of a doubly bound state compared to a singly bound one.

The condensation force interacts in a different way with the friction coefficient than the entropic force shown in Eq. 4.5. Unlike the entropic force, the condensation force does not decrease as the overlap length increases, but remains constant. Furthermore, the friction coefficient remains roughly constant during entropic expansion as given by Eq. 4.13, but in the case of a condensation force the friction coefficient increases because of the binding of new cross-linkers as the overlap expands.

To see how the friction coefficient depends on the overlap length when cross-linkers bind and unbind, we use Eq. 4.13 as a basis,

$$\zeta = (\zeta_0 \exp(-A)) \exp(\beta \Delta \mathcal{F}^\ddagger). \quad (4.20)$$

Here, we use that $\beta\Delta\mathcal{F}^\ddagger = A + BN \exp(N/(4B\ell))$ and that the constant term A was absorbed into the prefactor ζ_0 . According to Eq. 2.67, the barrier height is related to the ratio of the partition function at the peak of the barrier ($\alpha = 1/2$) to the partition function in the valley ($\alpha = 0$). The ratio of partition functions is approximately given by the exponential barrier height Eq. 2.84,

$$\frac{\mathcal{Z}(\alpha = \frac{1}{2})}{\mathcal{Z}(\alpha = 0)} \approx \exp(-\beta\Delta\mathcal{F}^\ddagger). \quad (4.21)$$

Furthermore, $\mathcal{Z}(\alpha = 0)$ equals a simple binomial coefficient, as shown in Eq. 2.68. The expressions for these partition functions are valid for a fixed number of cross-linkers N , and the expressions at a fixed chemical potential follow by summing over N ,

4

$$Q\left(\alpha = \frac{1}{2}\right) = \sum_{N=0}^{\ell} \mathcal{Z}\left(\alpha = \frac{1}{2}\right) q^N \approx \sum_{N=0}^{\ell} \binom{\ell}{N} \exp\left[-A - BN \exp\left(\frac{1}{4B} \frac{N}{\ell}\right)\right] q^N. \quad (4.22)$$

Here, q gives the Boltzmann factor for a fully bound cross-linker compared to all states that are not fully bound,

$$q = \frac{q_d}{(1 + q_s)^2}. \quad (4.23)$$

We cannot find a closed form expression of Eq. 4.22 because of the factor that depends superexponentially on the cross-linker density N/ℓ . Therefore, we replace N/ℓ by the mean density ρ_d there. Moreover, Eq. 4.22 depends superexponentially on the density of cross-linkers because of exclusion effects that prohibit cross-linker hops during barrier crossings. In the case of cross-linker condensation, a part of the microtubule is covered in partially bound cross-linkers that also prohibit these hops, and which are ignored in the current expression. Therefore, we also include the density of singly-bound cross-linkers on one of the microtubules ρ_s . The cross-linker densities can be expressed in terms of the Boltzmann factors q_s and q_d ,

$$\rho_s = \frac{q_s + q_s^2}{(1 + q_s)^2 + q_d}, \quad \rho_d = \frac{q_d}{(1 + q_s)^2 + q_d} = \frac{q}{1 + q}. \quad (4.24)$$

Replacing N/ℓ with $\rho_s + \rho_d$, we find a closed form expression for the partition function at the peak of the barrier,

$$\begin{aligned} Q\left(\alpha = \frac{1}{2}\right) &\approx \sum_{N=0}^{\ell} \binom{\ell}{N} \exp\left[-A - BN \exp\left(\frac{\rho_d + \rho_s}{4B}\right)\right] q^N \\ &= \exp(-A) \left\{1 + q \exp\left[-B \exp\left(\frac{\rho_d + \rho_s}{4B}\right)\right]\right\}^{\ell}. \end{aligned} \quad (4.25)$$

Similarly, in the valleys of the free-energy profile, the partition function is given by

$$Q(\alpha = 0) = \sum_{N=0}^{\ell} \binom{\ell}{N} q^N = \{1 + q\}^{\ell}. \quad (4.26)$$

The expression for the free-energy barrier height in the case of cross-linker binding follows from combining Eq. 4.25 with Eq. 4.26,

$$\beta\Delta\mathcal{F}_q^\ddagger = A + \ell \log \left\{ \frac{1+q}{1+q \exp[-B \exp(\frac{\rho_d + \rho_s}{4B})]} \right\}. \quad (4.27)$$

Then, the friction coefficient follows

$$\zeta(\ell) = \zeta_0 \left\{ \frac{1+q}{1+q \exp[-B \exp(\frac{\rho_d + \rho_s}{4B})]} \right\}^\ell. \quad (4.28)$$

Using that the condensation force is independent of the overlap length ℓ , and replacing $\ell \approx \lambda + 1$ again, Eq. 4.28 sets an ordinary differential equation for the overlap dynamics due to a condensation force,

$$\frac{d\lambda}{dt} \approx a \exp(-b\lambda), \quad (4.29)$$

with

$$a = \frac{F_{\text{cond}}}{\delta\zeta_0 \exp(b)}, \quad b = \log \left\{ \frac{1+q}{1+q \exp[-B \exp(\frac{\rho_d + \rho_s}{4B})]} \right\}. \quad (4.30)$$

The solution to Eq. 4.29 together with the boundary condition $\lambda(0)$ reads

$$\lambda(t) \approx \frac{1}{b} \log[\exp(b\lambda(0)) + abt]. \quad (4.31)$$

Compared to an entropic force, which causes the overlap length to follow a power law $t^{1/2}$, a condensation force leads to a slower logarithmic increase of the overlap length.

To test how well the deterministic solution Eq. 4.31 predicts the stochastic movement of the overlap length, we simulate trajectories of a microtubule overlap that expands due to a condensation force. We use the parameter values listed in [18] to set the additional (un)binding rates. We label an unbound cross-linker with 0, a partially bound cross-linker with 1, and a fully bound cross-linker with 2, and call $r_{i,j}$ the (un)binding rate from state i to state j . Because state 1 consists of two sub-states (partially bound to the top or bottom filament), the total rates to and from state 1 are $r_{0,1}^{\text{tot}} = 2r_{0,1}$, $r_{1,0}^{\text{tot}} = r_{1,0}$, $r_{1,2}^{\text{tot}} = r_{1,2}$, and $r_{2,1}^{\text{tot}} = 2r_{2,1}$. We use the values given in [18],

$$r_{0,1} = 0.001 \text{ s}^{-1}, \quad r_{1,0} = 0.1 \text{ s}^{-1}, \quad r_{1,2} = 0.5 \text{ s}^{-1}, \quad r_{2,1} = 0.025 \text{ s}^{-1}. \quad (4.32)$$

We can relate these simulation parameters to the affinities q_s and q_d with the local detailed balance relation Eq. 1.23,

$$q_s = \frac{r_{0,1}}{r_{1,0}}, \quad q_d = \frac{r_{0,1}r_{1,2}}{r_{1,0}r_{2,1}}. \quad (4.33)$$

Using Eq. 4.17, we find a condensation force of $F_{\text{cond}} = 0.05 \text{ pN}$. As shown in Fig. 4.5, the average overlap length of 50 simulated trajectories initially grows much faster than predicted by Eq. 4.31, but then appears to stall.

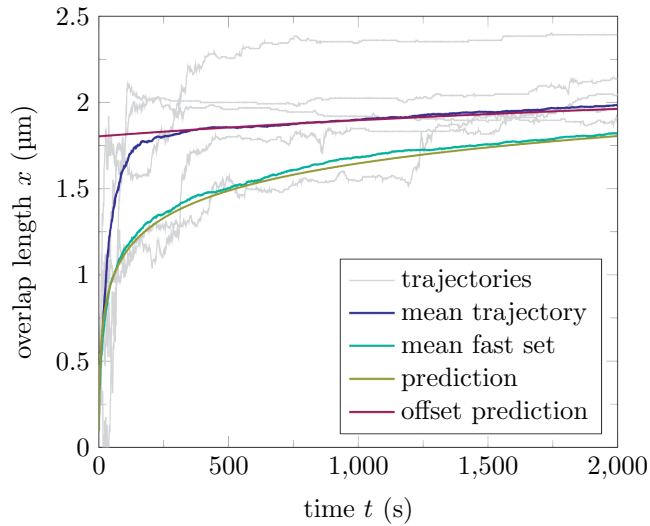


Figure 4.5: We simulate a system where cross-linkers bind with the (un)binding rates given in Eq. 4.32. The resulting trajectories of the overlap length, of which five are shown in grey, start at $\ell = 13$ and propagate due to the condensation force. Then, we compare the average over 50 such trajectories (blue) to the results to the exact deterministic solution Eq. 4.31 (yellow). The simulated trajectories appear to stall after an initial period of fast movement. The average overlap length (blue) initially expands faster than predicted, because the number of cross-linkers cannot equilibrate when the expansion is too fast. Hence, the number of cross-linkers is lower than expected based on the overlap length alone. Using the faster (un)binding rates given in Eq. 4.34, the mean of 50 trajectories follows the predicted overlap length nearly perfectly. Furthermore, the original mean trajectory does follow the predicted logarithmic scaling after $t_0 = 500$ s, as given by Eq. 4.35, at which time the filaments have slowed down and the cross-linkers can equilibrate.

A possible explanation for the breakdown of the logarithmic scaling Eq. 4.31 is that the (un)binding rates are not fast enough on the time scale of the overlap movement, such that there is no equilibration of the number of cross-linkers. To test this, we repeat the simulations where we change the set of binding parameters. We call Eq. 4.32 the slow parameter set, and add a fast parameter set

$$r_{0,1} = 1 \text{ s}^{-1}, \quad r_{1,0} = 100 \text{ s}^{-1}, \quad r_{1,2} = 50 \text{ s}^{-1}, \quad r_{2,1} = 2.5 \text{ s}^{-1}. \quad (4.34)$$

Both parameter sets have the same affinities q_s and q_d as given by Eq. 4.33, but the number of cross-linkers can equilibrate quicker in the fast set. We also show the mean of 50 simulated trajectories for the fast parameter set in Fig. 4.5, which leads to a slower expansion of the microtubule overlap than the slow parameter set and coincides nearly perfectly with the predicted logarithmic overlap expansion without any parameter fitting.

In the slow parameter set, the microtubule overlap initially expands rapidly due to the diffusion of the cross-linkers, which cannot be followed directly by an increase of the number of cross-linkers N because the binding rate is too low. However, N does eventually increase, increasing the friction coefficient and slowing down movement. Then, even the slow rates of (un)binding allow for the equilibration of the cross-linker number on the time scale of filament jumps. Hence, we expect the dynamics to follow the predicted scaling again after some time t_0 ,

$$\lambda(t) \approx \frac{1}{b} \log[\exp(b\lambda(t_0)) + ab(t - t_0)], \quad (4.35)$$

where we choose $t_0 = 500 \text{ s}$ as the offset after which we assume the cross-linker number to remain equilibrated and insert the $\lambda(t_0)$ as obtained from the simulations. The resulting curve is shown in Fig. 4.5, confirming that the system moves slow enough after t_0 such that even the slow parameter set leads to the equilibration of N .

Using the hypothesis that the friction force increases exponentially with the number of cross-linkers, we obtained the predicted logarithmic motion of the microtubule overlap in Eq. 4.31. On the other hand, it has been proposed that the friction coefficient scales linearly with the number of cross-linkers [74], and therefore with the overlap length,

$$\zeta(\lambda) = c_1 + c_2 \lambda. \quad (4.36)$$

Using the linear friction coefficient and a constant condensation force, we find that the overlap length scales like a square root with time,

$$\lambda(t) = c_3 + \sqrt{(\lambda(0) - c_3)^2 + c_4 t}. \quad (4.37)$$

Here, the c_i represent unknown fit parameters, and c_3 and c_4 can be expressed in terms of c_1 , c_2 , and the condensation force. The basic assumption that friction is proportional to the number of cross-linkers would set $c_1 = 0$ in Eq. 4.36, leading to $c_3 = 0$ in Eq. 4.37. However, we choose to include two parameters, such that we can more easily compare the equation with Eq. 4.31, which also has two parameters.

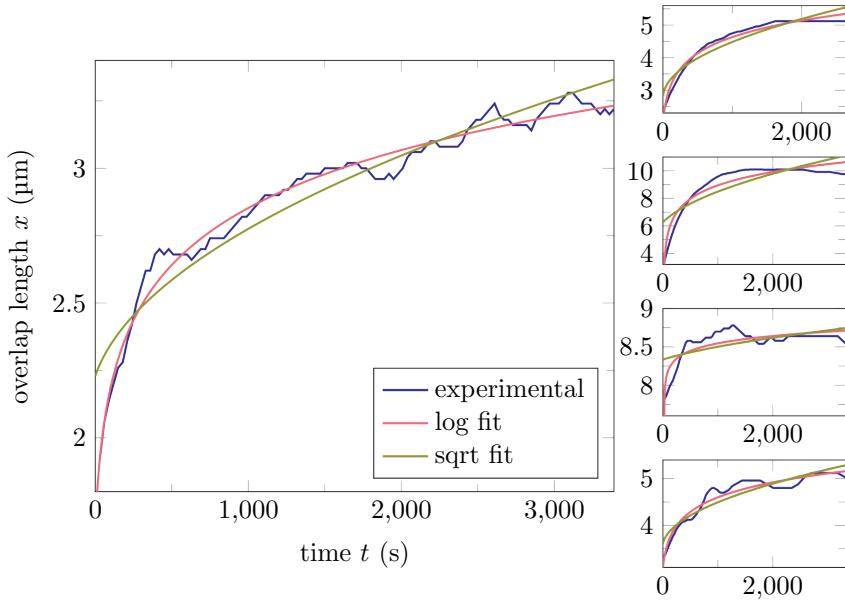


Figure 4.6: Experimental time traces of microtubules driven by condensation forces show that the friction most likely scales exponentially with the number of cross-linkers. These results were obtained with permission from [18]. In the experiments, a microtubule was connected to glass and a second microtubule was cross-linked to the first using the diffusive cross-linking protein Ase1. Then, total internal reflection fluorescence microscopy was used to image the overlap length as a function of time with Ase1 present in the solution. We plot the overlap length as a function of time in blue, and show all five experimental trajectories that were taken at a cross-linker concentration of $[X] \approx 1 \text{ nM}$ (out of fifteen trajectories taken at different concentrations). We fit the logarithmic prediction Eq. 4.31 that assumes a constant condensation force and a friction coefficient that scales exponentially with the number of cross-linkers in red, showing good agreement each time. We also fit the square root prediction Eq. 4.37 that follows from a friction coefficient that scales linearly with the number of cross-linkers to each experimental time trace in yellow, showing that the logarithmic fit outperforms the square root one in each of the five cases.

Previous experiments have confirmed the computational prediction that the friction coefficient scales exponentially with the number of cross-linkers [18]. However, these experiments were performed at a fixed number of cross-linkers per overlap, and the cross-linker density N/ℓ was not controlled. Therefore, the observed exponential dependence could possibly be explained by a friction coefficient that scales linearly with N at a constant density, but exponentially with the density N/ℓ due to exclusion effects. To further test whether the friction scales exponentially with the number of cross-linkers at a constant density, we compare which prediction, Eq. 4.31 or Eq. 4.37, best fits to experimental time traces of microtubules that expand their overlap length under condensation forces. Because the cross-linker (un)binding constantly equilibrates their density in the overlap, the effect of exclusion effects does not change with the overlap length.

Such experiments were performed in [18], of which we show five time traces in Fig. 4.6. We perform least squares fits of Eq. 4.31 and Eq. 4.37 to each time trace, where we demand $a > 0$ and $b > 0$ in each case, showing that the logarithmic scaling is superior to the square root scaling in explaining the trends. Hence, the motion caused by the binding of cross-linkers to microtubule overlaps appears to confirm that the friction coefficient scales exponentially with the number of cross-linkers when the cross-linker densities are low.

4.3. COOPERATIVE INTERACTIONS REDUCE THE ENTROPIC FORCE

The entropic expansion force that drives two partially overlapping microtubules to slide together is caused by cross-linkers that diffuse within the overlap and stay bound. One such a cross-linker is the yeast protein Ase1 [18, 43, 86], which was observed to interact cooperatively [86], although these interactions were absent in other experiments [18]. Here, we calculate how cooperativity affects the entropic expansion force. Again, we assume that N cross-linkers are bound within an overlap length with ℓ binding sites on each microtubule, and we introduce a Boltzmann factor of ω for each pair of neighbouring cross-linkers. If we assume that there are i such neighbouring pairs, the Boltzmann factor appearing in the partition function equals ω^i . Furthermore, the number of neighbouring pairs is maximal when $N = \ell$, in which case $i = N - 1$. Since each microstate has a certain number of interactions i , we can expand the partition function as a polynomial in ω ,

$$\mathcal{Z}(\ell, N, \omega) = \sum_{i=0}^{\max(N-1, 0)} \Omega(\ell, N, i) \omega^i. \quad (4.38)$$

Here, $\Omega(\ell, N, i)$ counts the number of microstates in which i out of N cross-linkers are found next to each other in an overlap of ℓ sites. The sum always includes the term $i = 0$, even when $N = 0$, because there is always one state of the overlap in which $N = 0$ and also $i = 0$. To calculate $\Omega(\ell, N, i)$, we first look at an example where $i = 2$, giving a Boltzmann factor ω^2 . This factor can be the result of two pairs of neighbouring cross-linkers and $N - 4$ lone cross-linkers, or of one group of three neighbouring cross-linkers with $N - 3$ lone cross-linkers that are separated by empty sites. Hence, if we let a lone cross-linker define a group of size one, the total number of groups equals $N - 2$ in each case. In general, if we group together all neighbouring cross-linkers, we see that for $i = 0$ the number of groups equals N , and each time the number of connections i increments by

one the number of groups shrinks by 1. When i is constant, cross-linkers can move from one group to the other, leaving the number of groups unchanged. Hence, the number of groups of neighbouring cross-linkers equals $N - i$, and the number of empty sites that separates these groups equals $\ell - N$. There has to be at least one empty site between each pair of adjacent groups, otherwise they simply form a single larger group. Hence, we already know the location of $N - i - 1$ empty sites, so there are $\ell - 2N + i + 1$ empty sites that can be freely mixed with the groups of cross-linkers. The number of ways to mix $N - i$ groups and $\ell - 2N + i + 1$ empty sites equals

$$\binom{\ell - N + 1}{N - i}. \quad (4.39)$$

4

Then, we still require the individual sizes of each group to completely specify the microstate. Hence, we have to calculate the number of ways to distribute N cross-linkers over $N - i$ groups, where each group has a size of at least one and the order of the groups matters. This is known as a stars and bars problem, in which in general n items are distributed over k distinguishable groups with at least one item in each group. We can first place one item into each group to make them non-empty, after which we still have to distribute $n - k$ items (or stars) over the k groups. Between the groups, there are $k - 1$ borders (or bars), and any permutation of the borders and the $n - k$ items specifies how many items each group receives. Hence, the number of ways to place n items in k groups is given by

$$\binom{n - 1}{k - 1} = \binom{n - 1}{n - k}. \quad (4.40)$$

Using that we have to partition N cross-linkers into $N - i$ groups, and multiplying the resulting binomial coefficient with Eq. 4.39, we find the number of microstates with i cross-linkers that have a cooperative interaction,

$$\Omega(\ell, N, i) = \binom{\ell - N + 1}{N - i} \binom{N - 1}{i}. \quad (4.41)$$

Hence, combined with Eq. 4.38 we have an exact expression for the full partition function with a fixed number of cross-linkers N and cooperative interactions between them,

$$\mathcal{Z}(\ell, N, \omega) = \sum_{i=0}^{\max(N-1, 0)} \binom{\ell - N + 1}{N - i} \binom{N - 1}{i} \omega^i. \quad (4.42)$$

To confirm the validity of Eq. 4.42, we also provide a recursive expression for the partition function and test whether Eq. 4.42 solves the recursive relation. We split the equation for $\mathcal{Z}(\ell, N, \omega)$ into two parts, depending on whether the first site is occupied or not,

$$\mathcal{Z}(\ell, N, \omega) = \mathcal{Z}_0(\ell, N, \omega) + \mathcal{Z}_1(\ell, N, \omega). \quad (4.43)$$

When the first site is empty, the N particles have to be distributed over the other $\ell - 1$ sites, such that

$$\mathcal{Z}_0(\ell, N, \omega) = \mathcal{Z}(\ell - 1, N, \omega). \quad (4.44)$$

If the first site is occupied, then the second site is also important, because a cooperative interaction can occur between them. Hence, we also split the expression for the partition function with the first site occupied,

$$\mathcal{Z}_1(\ell, N, \omega) = \mathcal{Z}_0(\ell - 1, N - 1, \omega) + \omega \mathcal{Z}_1(\ell - 1, N - 1, \omega), \quad (4.45)$$

where an interaction between the first two occupied sites gives a Boltzmann factor ω . Furthermore, rearranging Eq. 4.43 gives

$$\mathcal{Z}_1(\ell - 1, N - 1, \omega) = \mathcal{Z}(\ell - 1, N - 1, \omega) - \mathcal{Z}_0(\ell - 1, N - 1, \omega). \quad (4.46)$$

Combining Eqs. 4.43–4.46, we find a recursive relation for the partition function,

$$\begin{aligned} \mathcal{Z}(\ell, N, \omega) &= \mathcal{Z}(\ell - 1, N, \omega) + \mathcal{Z}(\ell - 2, N - 1, \omega) \\ &\quad + \omega [\mathcal{Z}(\ell - 1, N - 1, \omega) - \mathcal{Z}(\ell - 2, N - 1, \omega)]. \end{aligned} \quad (4.47)$$

Together with the two boundary conditions

$$\mathcal{Z}(\ell, 0, \omega) = 1, \quad \mathcal{Z}(\ell, \ell, \omega) = \omega^{\ell-1}, \quad (4.48)$$

Eq. 4.47 fully determines $\mathcal{Z}(\ell, N, \omega)$.

To confirm that Eq. 4.42 solves the recursive Eq. 4.47, we make repeated use of Pascal's rule

$$\binom{n}{k} = \binom{n-1}{k} + \binom{n-1}{k-1}. \quad (4.49)$$

First, we see that

$$\begin{aligned} &\mathcal{Z}(\ell - 1, N - 1, \omega) - \mathcal{Z}(\ell - 2, N - 1, \omega) \\ &= \sum_i \left[\binom{\ell - N + 1}{N - i - 1} - \binom{\ell - N}{N - i - 1} \right] \binom{N - 2}{i} \omega^i = \sum_i \binom{\ell - N}{N - i - 2} \binom{N - 2}{i} \omega^i. \end{aligned} \quad (4.50)$$

Multiplying this equation by ω and changing the variable $i \rightarrow i - 1$, we again apply Eq. 4.49 to see that

$$\begin{aligned} &\mathcal{Z}(\ell - 2, N - 1, \omega) + \omega [\mathcal{Z}(\ell - 1, N - 1, \omega) - \mathcal{Z}(\ell - 2, N - 1, \omega)] \\ &= \sum_i \binom{\ell - N}{N - i - 1} \left[\binom{N - 2}{i} + \binom{N - 2}{i - 1} \right] \omega^i = \sum_i \binom{\ell - N}{N - i - 1} \binom{N - 1}{i} \omega^i. \end{aligned} \quad (4.51)$$

Finally, we see that the full relation equals

$$\begin{aligned} &\mathcal{Z}(\ell - 1, N, \omega) + \mathcal{Z}(\ell - 2, N - 1, \omega) + \omega [\mathcal{Z}(\ell - 1, N - 1, \omega) - \mathcal{Z}(\ell - 2, N - 1, \omega)] \\ &= \sum_i \left[\binom{\ell - N}{N - i} + \binom{\ell - N}{N - i - 1} \right] \binom{N - 1}{i} \omega^i = \sum_i \binom{\ell - N + 1}{N - i} \binom{N - 1}{i} \omega^i. \end{aligned} \quad (4.52)$$

The final expression equals the expression for $\mathcal{Z}(\ell, N, \omega)$, confirming that Eq. 4.42 solves Eq. 4.47.

Additionally, by the Chu-Vandermonde identity

$$\binom{i+j}{k} = \sum_l \binom{i}{l} \binom{j}{k-l}, \quad (4.53)$$

we have

$$\mathcal{Z}(\ell, N, \omega = 1) = \sum_{i=0}^{\max(N-1,0)} \binom{\ell-N+1}{N-i} \binom{N-1}{i} = \binom{\ell}{N}. \quad (4.54)$$

Hence, we retrieve the partition function given in Eq. 4.4 when there are no cooperative interactions ($\omega = 1$).

We can use Eq. 4.42 to find an expression for the entropic force when the cross-linkers interact cooperatively. To calculate the entropic force, we repeat the calculation of Eq. 4.5 to find

$$F_{\text{ent}} \approx \frac{k_B T}{\delta} \log \left[\frac{\sum_{i=0}^{\max(N-1,0)} \frac{\ell-N+1}{\ell-2N+i+1} \binom{\ell-N}{N-i} \binom{N-1}{i} \omega^i}{\sum_{i=0}^{\max(N-1,0)} \binom{\ell-N}{N-i} \binom{N-1}{i} \omega^i} \right] \equiv \frac{k_B T}{\delta} \log \left\langle \frac{\ell-N+1}{\ell-2N+i+1} \right\rangle_{i,\omega}. \quad (4.55)$$

We define $\langle \dots \rangle_{i,\omega}$ as the average of what is inside the brackets over i , with the weights given by the terms of the partition function, as shown in Eq. 4.55. We know from Eq. 4.54 and Eq. 4.55 that for $\omega = 1$

$$\left\langle \frac{\ell-N+1}{\ell-2N+i+1} \right\rangle_{i,\omega=1} = \frac{\ell}{\ell-N}. \quad (4.56)$$

Furthermore, we see that $\omega > 1$ biases the average towards the terms with larger i , and because the fraction within the average decreases with i , we have

$$\left\langle \frac{\ell-N+1}{\ell-2N+i+1} \right\rangle_{i,\omega>1} < \frac{\ell}{\ell-N}. \quad (4.57)$$

Similarly, for $\omega < 1$,

$$\left\langle \frac{\ell-N+1}{\ell-2N+i+1} \right\rangle_{i,\omega<1} > \frac{\ell}{\ell-N}. \quad (4.58)$$

Hence, the entropic force Eq. 4.55 decreases when the cooperativity between cross-linkers increases, such that $\omega > 1$, and oppositely the entropic force increases when the cross-linkers repel each other, $\omega < 1$. In Sec. 2.K, we showed that the friction coefficient increases with cooperativity while it still depends exponentially on the number of cross-linkers. Combined with a reduced entropic force, this shows that the expansion of the overlap length will be significantly hindered by cooperative interactions between the cross-linkers. Intuitively, we can think of cooperativity clustering the cross-linkers together, reducing their pressure to expand the overlap length. On the other hand, anti-cooperative interactions push the cross-linkers apart, increasing their pressure on the microtubule overlap.

4.4. COOPERATIVE INTERACTIONS INCREASE THE CONDENSATION FORCE

To describe how the condensation force changes when cross-linkers bind cooperatively, we require the partition function in the grand canonical ensemble. Using the partition function for a fixed number of cross-linkers N , as given by Eq. 4.38, we could find the one in the grand canonical ensemble by the relation

$$Q(\ell, q, \omega) = \sum_{N=0}^{\ell} \mathcal{Z}(\ell, N, \omega) q^N = \sum_{N=0}^{\ell} \sum_{i=0}^{N-1} \binom{\ell-N+1}{N-i} \binom{N-1}{i} \omega^i q^N. \quad (4.59)$$

Here, we assume that the cooperative factor ω only arises when two fully bound cross-linkers neighbour each other, and we ignore the possibility of partially bound cross-linkers cooperatively interacting with each other and with the fully bound cross-linkers. Hence, the factor q is given by Eq. 4.23.

Although Eq. 4.59 is correct, a different form allows us to map the problem to solving the one-dimensional Ising model. We use the labels $n_i \in \{0, 1\}$ to denote the number of cross-linkers occupying the i -th site, such that the full partition function equals

$$Q(\ell, q, \omega) = \sum_{n_1=0}^1 \sum_{n_2=0}^1 \dots \sum_{n_{\ell}=0}^1 q^{n_1/2} \left(\prod_{i=1}^{\ell-1} q^{(n_i+n_{i+1})/2} \omega^{n_i n_{i+1}} \right) q^{n_{\ell}/2}. \quad (4.60)$$

We can solve this partition function by defining the matrix \mathbf{A} with elements

$$A_{i,j} = q^{(i+j)/2} \omega^{ij}, \quad (4.61)$$

and the vector \mathbf{b} with elements

$$b_i = q^{i/2}. \quad (4.62)$$

The matrix \mathbf{A} has the eigenvalues

$$\begin{aligned} \lambda_1 &= \frac{\omega q + 1}{2} + \sqrt{\left(\frac{\omega q - 1}{2}\right)^2 + q} \\ \lambda_2 &= \frac{\omega q + 1}{2} - \sqrt{\left(\frac{\omega q - 1}{2}\right)^2 + q}, \end{aligned} \quad (4.63)$$

where $\lambda_1 > 0$, $\lambda_2 > 0$ if $\omega > 1$ ($\lambda_2 < 0$ if $\omega < 1$), and $\lambda_1 > |\lambda_2|$. The corresponding normalised orthogonal eigenvectors \mathbf{v}^i with $i \in \{1, 2\}$ are

$$\mathbf{v}^i = \frac{1}{\sqrt{q + (\lambda_i - 1)^2}} \begin{pmatrix} \sqrt{q} \\ \lambda_i - 1 \end{pmatrix}. \quad (4.64)$$

If we define the orthogonal matrix \mathbf{P} by its elements $P_{i,j} = v_i^j$, the matrix \mathbf{A} can be diag-

onalised by $\mathbf{P}^T \mathbf{A} \mathbf{P}$, leading to

$$\begin{aligned}
 Q(\ell, q, \omega) &= \mathbf{b}^T \mathbf{A}^{\ell-1} \mathbf{b} \\
 &= \mathbf{b}^T \mathbf{P} [\mathbf{P}^T \mathbf{A} \mathbf{P}]^{\ell-1} \mathbf{P}^T \mathbf{b} \\
 &= \mathbf{b}^T \mathbf{P} \begin{pmatrix} \lambda_1^{\ell-1} & 0 \\ 0 & \lambda_2^{\ell-1} \end{pmatrix} \mathbf{P}^T \mathbf{b} \\
 &= \lambda_1^{\ell-1} (\mathbf{v}^1 \cdot \mathbf{b})^2 + \lambda_2^{\ell-1} (\mathbf{v}^2 \cdot \mathbf{b})^2.
 \end{aligned} \tag{4.65}$$

Together with Eq. 4.62 and Eq. 4.64, this gives the answer

$$Q(\ell, q, \omega) = \frac{q \lambda_1^{\ell+1}}{q + (\lambda_1 - 1)^2} + \frac{q \lambda_2^{\ell+1}}{q + (\lambda_2 - 1)^2}. \tag{4.66}$$

For $\omega = 1$, we have $\lambda_1 = q + 1$ and $\lambda_2 = 0$, and we retrieve Eq. 4.26. In general, when the overlap length ℓ is large enough, the largest eigenvalue λ_1 dominates the expression, and the condensation force becomes roughly

$$F_{\text{cond}} \approx \frac{k_B T}{\delta} \log(\lambda_1). \tag{4.67}$$

To see how the cooperative interactions affect the condensation force, we see how λ_1 changes with ω ,

$$\frac{d\lambda_1}{d\omega} = \frac{q}{2} \left(1 + \frac{\left(\frac{\omega q - 1}{2}\right)}{\sqrt{\left(\frac{\omega q - 1}{2}\right)^2 + q}} \right) > 0, \tag{4.68}$$

where the final inequality follows from $q > 0$. Hence, λ_1 grows monotonically with ω , and we have that F_{cond} is monotonically increasing itself.

For large $\omega \gg 1/q$, the largest eigenvalue $\lambda_1 \approx \omega q$. Both increasing q and ω lead to a higher binding affinity of cross-linkers for the microtubule overlap region, and hence increase the condensation force in a similar way. However, the increase of the force is accompanied by an increase of the friction coefficient, which still increases exponentially with the number of cross-linkers as shown in Sec. 2.K. Hence, the velocity of the microtubules driven by condensation forces will be reduced by increasing the cooperativity for large values of ω .

Even though cooperative interactions between the cross-linkers influence the movement of the overlap length quantitatively, we expect that the functional dependence given by Eq. 4.31 remains unchanged. When the binding and unbinding of cross-linkers is fast compared to the jump rate of the filaments, the cross-linker density is independent of the overlap length. Hence, the condensation force remains constant when the overlap expands, while the friction coefficient increases exponentially with the overlap length, leading to an exponential decrease of the overlap velocity with time. This results in the logarithmic scaling of the overlap length with time that was found without considering cooperative interactions.

4.5. EFFECTS OF MULTIPLE PROTOFILAMENTS

Another effect that may influence the dynamics of microtubule overlaps is the three dimensional structure of the microtubules. In our model, filaments are represented as one dimensional lattices of binding sites. The microtubules typically consist of 13 protofilaments that are parallel to axis of the microtubule, and in which neighbouring protofilaments are offset such that the lateral contacts between tubulin dimers follow a left-handed three-start helix in which one turn leads to an offset of three monomers [95, 96]. Because each tubulin dimer provides a single binding site for Ase1 [77], the longitudinal offset between the lattices of two neighbouring protofilaments equals roughly $\theta = ((3/2)/13)$. Using a tubulin dimer length of $\delta = 8\text{ nm}$, we find a longitudinal offset of $\theta \times \delta \approx 0.9\text{ nm}$ between neighbouring protofilaments [97].

In Chap. 2, we showed that if only a single protofilament is involved on each microtubule, the filaments are forced into register by the collective harmonic potential of the spring-like cross-linkers. The filaments can then only jump between these basins of attraction that are separated by free-energy barriers and are spaced at a distance δ . However, if the cross-linking of two microtubules involves several protofilaments on each filament, then the microtubules can only have one pair of protofilaments in register at the same time, since the other protofilaments are offset by θ . Furthermore, the structure of the microtubule dictates that if two pairs of protofilaments face each other, the first pair being in register leads to the second pair having an offset of 2θ . This offset introduces a strain on the cross-linkers in the second pair that makes it less likely that one of the pairs of protofilaments is in register. Furthermore, since the left-handed helix of neighbouring tubulin dimers does not depend on the orientation of the microtubule, this offset is the same for parallel and anti-parallel microtubule overlaps.

Even though the involvement of multiple protofilaments makes it impossible for all pairs to be in register simultaneously, the fact that all protofilaments share the same periodicity δ in their lattice of binding sites still results in a barrier profile with a periodicity of δ . In Fig. 4.7, the red line shows the free-energy profile $\mathcal{F}(\lambda, N, \ell)$ for a single protofilament model of a small microtubule that fully overlaps with a long microtubule, where we use $N = 20$ and $\ell = 40$. Here, λ is the extended reaction coordinate introduced in Eq. 4.9. To find the free energy when two protofilaments are involved, we split the cross-linkers evenly over the two protofilaments, resulting in twice the free energy for $N = 10$ and $\ell = 40$. Furthermore, we account for the protofilament offset 2θ by translating the reaction coordinates in each profile such that the free-energy minima are still found at integer values of λ ,

$$\mathcal{F}_2(\lambda, N, \ell) = \mathcal{F}(\lambda - \theta, N/2, \ell) + \mathcal{F}(\lambda + \theta, N/2, \ell). \quad (4.69)$$

We plot the resulting free-energy profile in blue in Fig. 4.7, which shows that the barriers are shallower when two protofilaments are involved. However, because the terms in Eq. 4.69 are periodic in δ and scale linearly with the number of cross-linkers N for low densities N/ℓ , their sum $\mathcal{F}_2(\lambda, N, \ell)$ does too. Hence, we still have optimal positions for the microtubules that form a lattice with a spacing δ , and the superexponential scaling of the friction coefficient as shown in Eq. 2.9 remains.

Even though the barrier profile of $\mathcal{F}_2(\lambda, N, \ell)$ shown in Fig. 4.7 shows that the free-energy barriers become lower the more protofilaments are involved, there are two con-

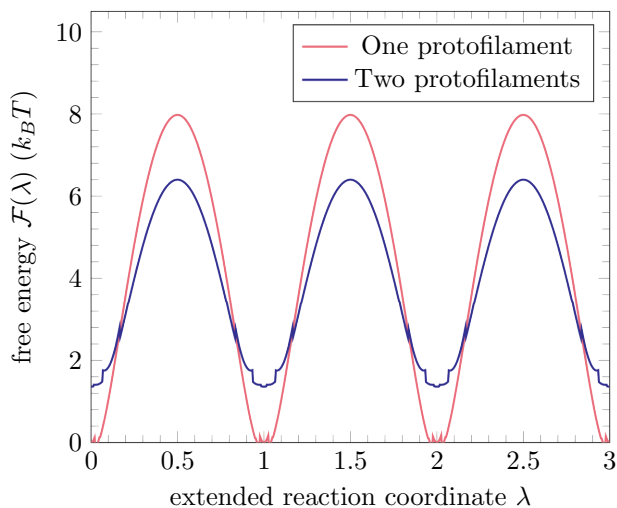


Figure 4.7: Possible effect of multiple protofilaments on the free-energy profile. We plot the free energy for the symmetric system introduced in Fig. 2.1 that lacks entropic or condensation forces. The microtubule overlap contains $\ell = 40$ sites per protofilament, and there are either $N = 20$ cross-linkers on a single protofilament or 2×10 cross-linkers on two protofilaments. If two pairs of protofilaments are cross-linked, the geometry of the microtubules dictates that the free-energy profiles are shifted by 2θ relative to each other, after which they are superimposed resulting in the full free-energy profile shown. Evidently, including two protofilaments lowers the height of the barrier, but a significant free-energy barrier remains.

cerns that alleviate the impact of the flatter barrier profile. First, we estimated the value of the spring constant k assuming the single protofilament model. As shown in Sec. 2.A, we compared the experimentally observed diffusion constant of Ase1 cross-linkers that are bound to a single microtubule to the diffusion constant of Ase1 proteins that are bound in the overlap between two microtubules. We assumed that the diffusion is reduced in the overlap because the spring constant makes it difficult for cross-linkers to hop from a relaxed to an unfavourable position, providing a relation that sets the value of the spring constant. However, when multiple protofilaments are involved and there is always strain on the cross-linkers, the change in potential energy after a hop is smaller. Hence, the spring constant has to be larger than currently estimated to explain the same reduction in the diffusion constant that was observed experimentally, and a larger spring constant would increase the barrier heights of $\mathcal{F}_2(\lambda, N, \ell)$.

The second reason why the involvement of multiple pairs of protofilaments does not reduce the barrier as much as Fig. 4.7 seems to suggest, is that the stiff cross-linkers actually favour binding to a single protofilament. If the cross-linkers can not only hop between binding sites on the same protofilament, but can also move to neighbouring protofilaments, then the free energy is minimised for a set of cross-linkers that binds almost exclusively to a single pair of protofilaments. Beside showing that the barrier profile is shallower when two protofilaments are involved, Fig. 4.7 also shows that the two-protofilament free-energy is always higher than the wells in the one-protofilament model. Therefore, the cross-linkers would mostly remain on a single protofilament, or, if the inter-protofilament dynamics of the cross-linkers is fast enough, the microtubules would move between the wells in the one-protofilament free energy, crossing peaks given by the two-protofilament free energy. The latter mechanism would lead to microtubule jumps that span $\theta \times \delta \approx 0.9 \text{ nm}$, accompanied by a rotation of the microtubule by $1/13$ of a full circle. Due to the left-handed helical shape of the microtubules [96], both parallelly and anti-parallelly cross-linked microtubules would perform a left-handed rotation around each other and around their own axis. However, the helical pitch of this rotation would be around $3 \times 4 = 12 \text{ nm}$, which is significantly smaller than the right-handed helical pitch of $\sim 1 \mu\text{m}$ observed for kinesin-14 [98]. Still, whether the microtubule jumps between binding sites along a single protofilament or between binding sites on different protofilaments, the free-energy barriers are higher than the blue line in Fig. 4.7 indicates.

If the cross-linkers bind to multiple pairs of protofilaments, the entropic or condensation forces are also affected. In contrast with the friction coefficient, which depends on a collective effect of all cross-linkers, these forces are expected to scale in a simple way as a function of the number of protofilaments m . The entropic force $F_{\text{ent},m}(N, \ell)$, which occurs in partially overlapping filaments with a fixed number of cross-linkers N and with m protofilaments that participate in the binding per microtubule, is a superposition of the entropic forces caused by each pair of cross-linked protofilaments. Assuming that the entropic force per protofilament $F_{\text{ent}}(N, \ell)$ is not affected by the offset of the lattices and the cross-linkers are evenly distributed among the protofilaments, the total entropic force is approximately given by

$$F_{\text{ent},m}(N, \ell) \approx mF_{\text{ent}}(N/m, \ell). \quad (4.70)$$

For low densities of cross-linkers, the dependence on m disappears, as shown in Eq. 4.6. Combined with a lowering of the friction coefficient by having fewer exclusion effects and a lower barrier, the overlap length would expand quicker. The functional dependence of the overlap length as given by Eq. 4.15 would not change though, since the friction still becomes asymptotically constant and the entropic force scales with the inverse of the overlap length for large overlap lengths.

For condensation forces caused by the (un)binding of cross-linkers, an increase of the number of protofilaments also increases the number of binding sites. Hence, the density of cross-linkers would be the same on each protofilament, and the condensation force becomes a superposition of the condensation forces caused by each pair of cross-linked protofilaments. If we assume that the value of the condensation force per protofilament is not impacted by the offset between protofilaments in the microtubule lattice, we find

$$F_{\text{cond},m}(N, \ell) = mF_{\text{cond}}(N, \ell). \quad (4.71)$$

Then, the effects of multiple protofilaments on the friction coefficient are more subtle compared to the case when N is constant, since the barrier height decreases due to the protofilament offsets while it increases due to the larger number of cross-linkers. Still, the condensation force is independent of the overlap length, and the friction coefficient scales exponentially with the overlap length. Therefore, the functional dependence of the overlap length as given by Eq. 4.31 remains invariant.

4.6. DISCUSSION

In this chapter, we have shown how the exponential scaling of the cross-linker induced friction influences the motion of two filaments that partially overlap. When the number of cross-linkers is constant, the overlap expands due to the increase of the number of microstates of the cross-linkers, causing an entropic force. The cross-linker density decreases as the overlap expands, slowly decreasing the force and leading to an overlap length that increases with the square root of time for large times. Furthermore, if the cross-linkers interact cooperatively, the entropic force will decrease while the friction coefficient increases, leading to a significant slowdown of the overlap length expansion. On the other hand, the friction coefficient is lowered if the cross-linkers bind to multiple protofilaments on each filament, because the offset between protofilaments makes the barrier profile shallower and because the exclusion effects between the cross-linkers are lowered by increasing the number of binding sites. Since the entropic force is not affected strongly by the involvement of multiple protofilaments, this would increase the speed at which the overlap expands.

If binding and unbinding of the cross-linkers is allowed, the overlap expansion is driven by the increased affinity of the cross-linkers for the filament overlap. Cross-linkers bind to, or condense in, the overlap region, causing a condensation force. Because the constant binding and unbinding equilibrates the density of cross-linkers on the filaments with the concentration of cross-linkers in the solution, the condensation force does not depend on the overlap length. However, the speed at which the overlap expands still decreases with time because the friction coefficient increases as more cross-linkers bind. These effects combine to an overlap length that increases logarithmically with

time. Additionally, how the overlap length depends on time remains qualitatively the same even when cooperative effects increase both the condensation force and the friction coefficient. Similarly, we showed that the logarithmic scaling of the overlap length with time is unchanged when multiple protofilaments are involved.

Since the predicted temporal dependence of the overlap length expanding under condensation forces remains invariant under the introduction of either cooperative binding or multiple protofilaments, it is a good candidate for experimentally verifying that the friction coefficient scales exponentially with the number of cross-linkers. Because the (un)binding of cross-linkers keeps their concentration in the overlap constant, the superexponential density effect is independent of the overlap length. Competing models that claim a linear dependence of the friction coefficient with the number of cross-linkers [74] would predict that the overlap length scales with the square root of time. We showed five experimental time traces that each contain a diffusive component [18], whereas the predicted overlap expansion only considers the mean movement and ignores the diffusive motion of the filaments. To systematically test the friction models, we would require many experimental time traces of microtubules expanding their overlap under the influence of condensation forces. Furthermore, all would have to be taken at the same concentration of cross-linkers, such that we could reliably estimate their mean trajectory and compare it to the logarithmic (Eq. 4.31) and square root (Eq. 4.37) functions. Still, the currently available data shows that the logarithmic prediction that follows from an exponentially increasing friction coefficient fits better than the square root prediction to all five experimental time traces (see Fig. 4.6). Even if the microtubules do not jump in a longitudinal direction to positions that are 8 nm apart, but between the protofilaments that require a longitudinal motion of 0.9 nm and a lateral motion of roughly 6 nm, we have shown that the functional form of the friction coefficient remains unaffected. Hence, the friction between microtubules that are cross-linked by Ase1 proteins likely follows the superexponential scaling of the friction coefficient shown in Chap. 2.

5

PASSIVE CROSS-LINKERS DRIVE ACTIN TRANSPORT BY GROWING MICROTUBULES

CELINE ALKEMADE and HARMEN WIERENGA

Cell migration depends on a polarised organisation of the actin cytoskeleton, with a protrusive actin network at the front. Microtubules are known to play a key role in the spatial control of actin network remodelling, but the underlying mechanisms of the interactions remain largely elusive. One potential mechanism for the remodelling of actin is the transport of single actin filaments by growing microtubule plus ends, and here we study the mechanism of this transport by in vitro reconstitution, computer simulations, and a minimal theoretical model. We show that microtubules can transport actin filaments over large (micrometer-range) distances, and find that this transport results from two antagonistic forces arising from the binding of cross-linkers to the overlap between the actin and microtubule filaments. The cross-linkers attempt to maximise the overlap between the actin and the tip of the growing microtubules, creating a forward condensation force, and simultaneously creating a competing friction force. We predict and verify experimentally how the average transport time depends on the actin filament length and the microtubule growth velocity, confirming the competition between a forward condensation force and a backward friction force. In addition, we theoretically predict and experimentally verify the condensation force is of the order of 0.1 pN. Thus, our results reveal a new mechanism for local actin remodelling by growing microtubules.

This chapter was written by Celine Alkemade (experiments) and Harmen Wierenga (theory and simulations) as shared first authors, together with Vladimir A. Volkov, Magdalena Preciado-López, Anna Akhmanova, Pieter Rein ten Wolde, Marileen Dogterom, and Gijsje H. Koenderink.

Migrating cells need to be responsive to environmental cues such as chemotactic stimuli and mechanical gradients [99, 100], while stably maintaining cell polarity with a leading edge at the front. Examples are found in epidermal migration [101] and in neuronal growth cones [102]. Interactions between microtubules and actin filaments play an important role in establishing and maintaining polarity in migrating cells [4, 6, 103, 104]. Different mechanisms of microtubule/actin crosstalk have been identified, including filament co-alignment mediated by motor proteins and passive cross-linkers, and co-regulation of the two cytoskeletal systems by biochemical signalling via RhoGTPases [105, 106].

So far, the emphasis in studies of microtubule/actin crosstalk has been on the effect of actin filaments on microtubules. It has been shown that actin bundles can guide microtubule growth via various cross-linking proteins, including ACF7 and tau, to target microtubule plus ends to focal adhesions where they regulate adhesion turnover [101, 107–110]. Less is known about the converse effect of microtubules on actin filaments. There is evidence that microtubules stimulate actin growth via signalling [105] and by local actin nucleation at the growing microtubule plus end [111, 112], and that microtubules help stabilise actin filaments in neurons [113, 114]. Using a biochemical reconstitution approach, it was previously showed that growing microtubules can also actively transport actin filaments [107]. Such transport has not yet been directly observed in cells, but there is recent direct evidence of actin filament association with microtubule plus ends [111, 112, 115]. Thus, this work raises the intriguing possibility that microtubules may locally remodel actin at the leading edge by exerting directional forces without the need for motor proteins. However, the required conditions for actin transport by growing microtubules are obscured by the lack of a mechanism that explains the transport of actin filaments without motor proteins.

Here, we investigate the conditions necessary for microtubule-mediated actin transport and identify the mechanism by combining biochemical reconstitution experiments with coarse-grained computer simulations and a minimal theoretical model. We show that in the presence of passive cross-linkers, microtubules can transport actin filaments over large (micrometer-range) distances in events that last up to several minutes. We propose and test a new mechanism to explain this movement, in which actin transport is the result of a competition between a forward condensation force that tends to maximise the overlap of the actin filament with the plus end of a growing microtubule and a backward force caused by the friction between the actin and microtubule filaments. These two antagonistic forces are both caused by the binding of cross-linkers. Previously, condensation forces [18] have been shown to be responsible for the movement of intracellular cargoes [116–119] or for the contraction of filament bundles [18, 54, 55, 120] in various biological contexts (see Chap. 4). However, the combination of a processive transport of cargo by a cross-linker driven condensation force that is simultaneously hindered by a friction force caused by the same cross-linkers has not been studied. Furthermore, the active transport by the moving microtubule plus end provides a new minimal mechanism by which two cytoskeletal systems can interact, which is distinct from cytoskeletal crosstalk that is driven by motor proteins [121–125]. Our findings reveal that interactions at microtubule plus ends enable local and dynamic actin remodelling, which provides a novel mechanism to steer cell migration.

5.1. GROWING MICROTUBULES PLUS ENDS CAN TRANSPORT ACTIN FILAMENTS

TO study actin filament transport by growing microtubule plus ends, we use the engineered cross-linking protein TipAct (see Sec. 5.A) that contains both a domain that specifically binds actin filaments and a domain that recognises end-binding (EB) proteins to target it to the growing ends of microtubules (Fig. 5.6) [107]. Dynamic microtubules are grown from surface-immobilised seeds stabilised with the nucleotide analogue GMPCPP and incubated with fluorescently labelled tubulin (see Sec. 5.B). The microtubules grow in the presence of TipAct, EB3, and freely diffusible stabilised actin filaments and are imaged by total internal reflection fluorescence (TIRF) microscopy (Fig. 5.1A). We observe a $54\mu\text{m} \times 54\mu\text{m}$ sized region of interest, which typically contains in the order of 30 microtubules (Fig. 5.7), and we look for instances where growing microtubules interact with actin filaments (see Sec. 5.D for criteria). Figure 5.1B shows a typical example of an encounter of a growing microtubule with an actin filament. Once the microtubule starts growing, an EB3-TipAct complex localises at its growing end (yellow arrow). After several seconds, an actin filament binds and co-localises to this tip-tracking complex (blue arrows) and is transported over a distance of several micrometers, before finally unbinding while the microtubule continues growing (white arrows).

To analyse the transport rate and duration, we construct a kymograph, i.e. a space-time plot along the length of the microtubule (Fig. 5.2A). This particular example clearly visualises the recruitment of the actin filament shortly after the microtubule starts growing, and its unbinding before the microtubule undergoes a catastrophe. For each event, we measure the transport time from the moment when the actin filament begins to move along with the growing microtubule tip region until this directed motion stops. In addition, we can extract the microtubule growth velocity from the microtubule tip position as a function of time. In the example kymograph in Fig. 5.2A, actin transport does not affect the growth velocity. This finding is confirmed by an analysis of 265 transport events (Fig. 5.8A).

We observe long-range actin filament transport (Fig. 5.9A) for actin filaments with a wide range of lengths from around $0.5\mu\text{m}$ to $8\mu\text{m}$ (Fig. 5.9B). In the example of Fig. 5.2A, the actin filament is only $0.6\mu\text{m}$ long, which is of the same order as the length of the microtubule tip region where EB3 preferentially binds. Actin filaments that are longer than the tip length sometimes land behind the microtubule tip and immediately start following it (Fig. 5.2B), while others land with part of the filament in front of the tip (Fig. 5.2C). In the latter situation, we observe that actin transport only starts once the microtubule tip has caught up with the front of the actin filament. Upon analysing 265 actin transport events, we observe a broad distribution of transport times with a median transport time of 48 s and a long tail that extends up to several minutes (Fig. 5.2E, left in grey).

The kymographs in figures 5.2A–C additionally demonstrate several mechanisms by which actin transport can end: the actin filament unbinds (21% of events), the microtubule undergoes a catastrophe (58%), or the actin filament falls behind the growing microtubule tip region, leaving the filament bound to the microtubule lattice, which is the microtubule region behind the tip (19%). A summary of the distribution of events is shown in Fig. 5.2D (see Fig. 5.10 for more details). Irrespective of whether we include

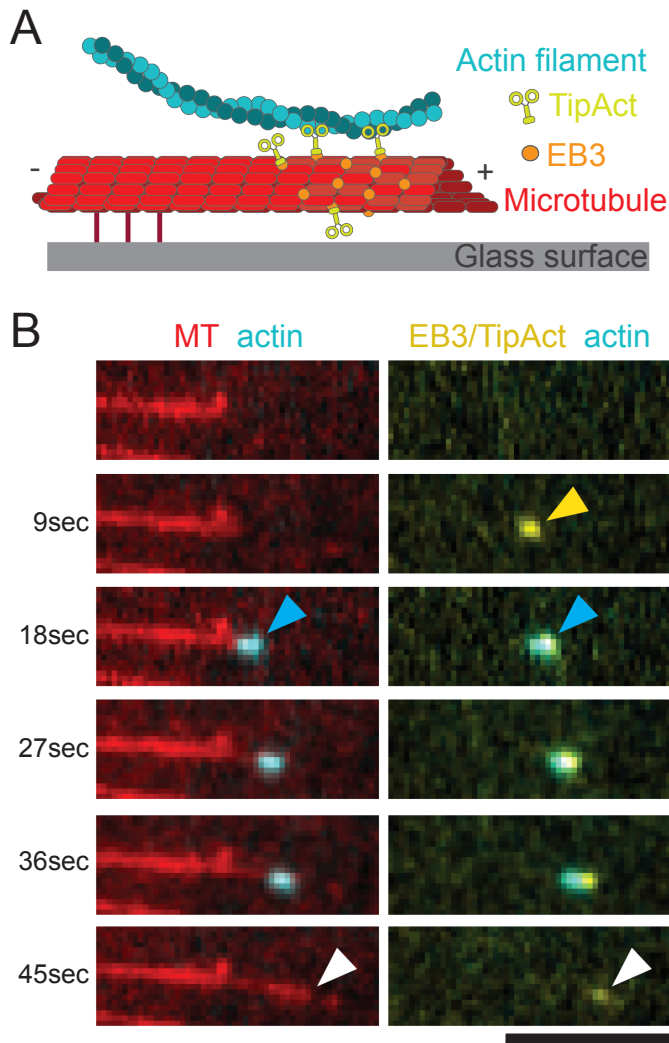


Figure 5.1: Actin transport by growing microtubule plus ends. (A) Schematic of the experimental assay for observing microtubule-mediated actin transport, showing a stabilised actin filament (cyan), the engineered cross-linker TipAct (green-yellow), and the microtubule end-binding protein EB3 (orange) moving freely in solution, while the growing microtubule (red) is anchored to the surface of a functionalised and passivated glass slide. (B) Time series of the growing plus end of a microtubule that recruits and transports an actin filament via EB3/TipAct complexes. Arrowheads show the localisation of the EB3/TipAct-complex (yellow), the binding of a short actin filament (cyan), and the unbinding of this actin filament while the microtubule continues to grow (white). Scale bar: 5 μ m.

all transport events in the distributions or only subsets, the distributions of microtubule growth velocities and of the actin transport times remain similar (Fig. 5.2E). Specifically, the distribution of transport times excluding those events that end by microtubule catastrophe is indistinguishable from the distribution including all events, in line with the assumption that the three mechanisms of ending the actin transport are independent and Markovian processes (see Sec. 5.F).

5.2. SIMULATIONS REPRODUCE MICROTUBULE-MEDIATED ACTIN TRANSPORT

WE hypothesise that the actin transport is driven by a condensation force that originates from the binding free energy of the TipAct proteins that cross-link the filaments and act to maximise the overlap between the actin filament and the microtubule tip region. Similar forces have been identified in several other biological contexts [18, 54, 55, 116–120]. However, in contrast with these other systems, the force driving actin transport results from the difference in cross-linker binding affinity between the microtubule lattice and tip regions, which arises from the different chemical modification states of the monomers in the microtubule tip and lattice [126–128], and the force vanishes when this affinity difference is not present. Furthermore, the binding of cross-linkers not only provides an affinity driven force but presumably also causes a friction force that hinders actin transport, leading to an interesting competition that results in the transient but processive transport of actin filaments.

To test the hypothesis that actin transport is the result of a competition between cross-linker induced forces, we perform kinetic Monte Carlo simulations of the simple model presented in Fig. 5.3A. The simulations are based on a modified version of the algorithm described in Sec. 2.1. We model the microtubule and the actin filament as one dimensional lattices of binding sites, where the actin filament can move along its long axis. In contrast with Chapter 2, the exact values of the lattice spacings between the binding sites of both filaments are insignificant, since the cross-linkers are relatively flexible and a cross-linker bound to a specific microtubule binding site can probe a range of different binding sites on the actin filament. To reduce the complexity of the simulated model, we assume the same lattice spacing δ between the binding sites on both filaments (see Sec. 5.I).

Microtubule growth is modelled through the addition of new binding sites with a fixed rate r_g . We assume that the microtubule contains a chemically different microtubule tip region of $l_t = 200$ nm long. To maintain the size of the tip region, we transform the oldest site in the tip region to a lattice site upon each addition of a new tip site, as indicated in Fig. 5.3A. We treat TipAct and EB3 proteins as a single complex that can bind to and unbind from the microtubule, where EB3 enhances the affinity of the cross-linking complex for the microtubule tip compared to the microtubule lattice region by about 20-fold (Fig. 5.13). Since we observe in experiments that TipAct strongly localises to microtubules, but barely to single actin filaments away from microtubules (Fig. 5.6), we assume that the cross-linkers always bind to the microtubule first and can then bind to the actin filament. We include the microscopic reverse reactions for all binding reactions, such that microtubule growth is the only process that breaks detailed balance. The

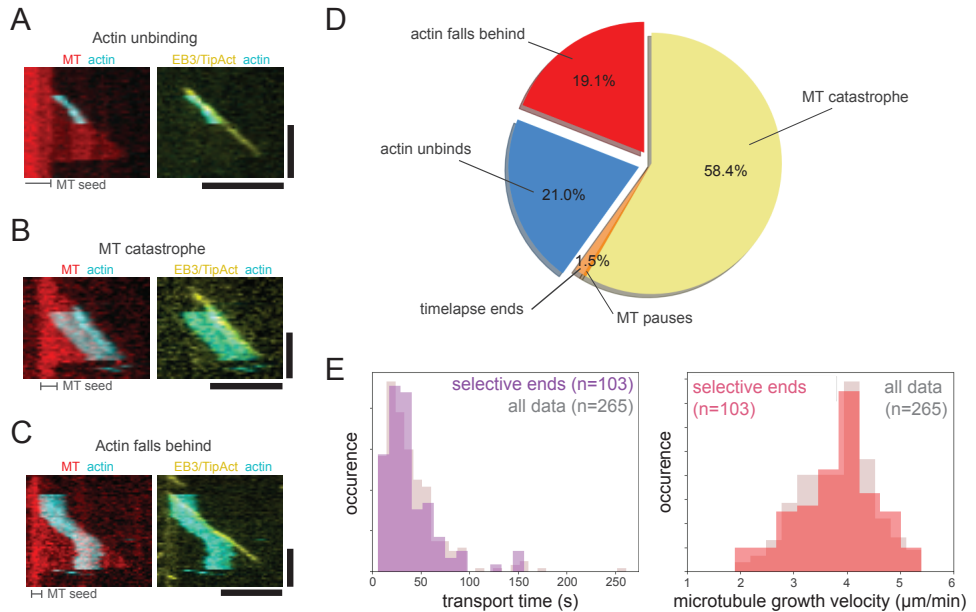


Figure 5.2: Mechanisms limiting the actin transport time. (A) Kymograph of the actin transport event depicted in Fig. 5.1B, showing that the event ends by the unbinding of the actin filament while the microtubule continues growing for a while. (B) Kymograph of a typical transport event that ends upon a microtubule catastrophe. (C) Kymograph of a typical transport event that ends by loss of contact of the actin filament with the tip resulting in the actin filament falling behind and lingering on the MT lattice. (D) Categories of termination events together with their observed frequency ($n=265$). The events that end with microtubule catastrophe contain two subsets: one where the actin filament unbinds upon catastrophe (as is shown in B), and one set where the shrinking microtubule pulls the actin filament along (as is shown in Fig. 5.10B). Fig. 5.10A further subdivides the catastrophes into these two categories. A small fraction of events corresponded to truncated events ending with the end of the time-lapse movie or to MT pauses (as is shown in Fig. 5.10B). (E) Distributions for the transport times (left) and microtubule growth velocities (right) are indistinguishable when we consider the complete dataset ($n=265$) or just a subset of transport events that end by actin filament unbinding (i.e., both the 'actin unbinds' and 'actin falls behind' events). Scale bars: $5\mu\text{m}$ (horizontal) and 60s (vertical).

actin filament moves with an intrinsic diffusion constant D_a when it is not cross-linked, and D_a is limited by viscous interactions with the solution. When the actin filament is connected to the microtubule, movement is limited mainly by the transient cross-linker binding events, strongly reducing the effective diffusion constant of the actin filament.

The diffusive movement of the actin filament is modelled using Brownian Dynamics with a fixed time-step. Cross-linkers can pull on the actin filament in its longitudinal direction with a simple harmonic force given by the spring constant k . We model the (un)binding of cross-linkers and the addition of new subunits to the microtubule tip as continuous-time Markov processes, which are described by the reaction rates shown in Fig. 5.3A. We simulate these reactions using a kinetic Monte Carlo algorithm, as described in Sec. 2.B. We simulate both the actin unbinding and the actin falling behind the microtubule tip region (see Fig. 5.1C). We omit the microtubule catastrophes from the computational model, since these occur at a constant Markovian rate, as indicated in Fig. 5.8.

We use experimental observations to estimate all parameters shown in Fig. 5.3A (see Sec. 5.I). Among these observations are actin diffusion on the microtubule lattice, fluorescence recovery after photobleaching (FRAP) experiments on fluorescently labelled TipAct proteins unbinding from microtubules, and the order of magnitude of the actin transport time for a specific combination of an actin length and a growth velocity ($4\ \mu\text{m}$ and $3\ \mu\text{m min}^{-1}$, respectively).

Simulations using this parameter set systematically show that the actin filament follows the growing microtubule tip region, as shown in Fig. 5.3B. In the example, the actin filament initially overlaps partially with the microtubule tip, but eventually loses its interaction with the tip and performs random diffusion on the microtubule lattice. We observe some instances (black arrow in Fig. 5.3B) where the actin filament transiently falls behind the tip, but then catches up again through a diffusion event. We observe the same transient diffusion events in our experiments, as shown in Fig. 5.11. Hence, the transition from transport to diffusion occurs when the actin filament loses its interaction with the microtubule tip and does not rebind to the microtubule tip before the microtubule grows away.

5.3. THE ACTIN FILAMENT DISPLAYS EFFECTIVE DIFFUSION AND DRIFT

TO identify the requirements for actin transport by growing microtubules, we develop a general theory for actin transport based on two key assumptions shown in Fig. 5.3C. First, the stochastic motion of the actin filament can be described as diffusion on time scales longer than the time in which cross-linkers remodel, such that the positional distribution of the actin filament follows a Fokker-Planck equation with a diffusion constant D_{eff} . Second, the condensation force is constant and is directed such that the overlap between the actin filament and the microtubule tip increases, leading to a drift term in this Fokker-Planck equation.

In the simulations, the motion of the actin filament is influenced by its viscous interactions with the solution and its stochastic interactions with the cross-linkers. To find a coarse grained description of this movement, we define the actin position x in a ref-

erence frame that is comoving with the growing microtubule, as indicated in Fig. 5.3C. Hence, an actin filament moving along with the growing microtubule tip remains at a constant position x .

The effective diffusion constant of the actin filament decreases with an increasing average number of connections between the actin filament and the microtubule [35, 55, 70, 75]. In turn, this average number of connections depends on the length of the overlap between the actin filament and the microtubule lattice region y_ℓ and between the actin filament and the microtubule tip region y_t . As indicated in Fig. 5.3C, we have $y_\ell = l_a - x$ when the actin position $x > 0$ and the actin filament has length l_a . When $x < 0$, $y_\ell = l_a$, since the actin filament is fully within the microtubule lattice region. Furthermore, with a microtubule tip length of l_t , $y_t = 0$ when $x < 0$, $y_t = x$ when $0 \leq x \leq l_t$, and $y_t = l_t$ when $x > l_t$. We recognise that short actin filaments can be in states where no cross-linkers connect the actin to the microtubule. In that case, the diffusion constant is set by the viscosity of the solution to $D_a = 1 \mu\text{m}^2 \text{s}^{-1}$ (see Sec. 5.I). However, when the actin filament is bound to the microtubule, its diffusion constant is mainly limited by the binding dynamics of the cross-linkers. The effective diffusion constant is related to the friction coefficient of the bound actin filament $\zeta_{\text{bound}}(y_t, y_\ell)$ through the Einstein relation, $D_{\text{bound}} = k_B T / \zeta_{\text{bound}}$ [28]. Defining the probability $p_0(y_t, y_\ell)$ that the actin filament is unbound, the effective diffusion constant is the average over the unbound and bound states of the actin filament,

$$D(y_t, y_\ell) = p_0(y_t, y_\ell) D_a + (1 - p_0(y_t, y_\ell)) \frac{k_B T}{\zeta_{\text{bound}}(y_t, y_\ell)}. \quad (5.1)$$

In Sec. 5.L, we derive that the probability that no cross-linkers connect to the actin filament is given by

$$p_0(y_t, y_\ell) = e^{-y_t/\lambda_t} e^{-y_\ell/\lambda_\ell}. \quad (5.2)$$

The length scales λ_t and λ_ℓ are expressed in terms of the (un)binding rates and the spring constant in Sec. 5.L, completely specifying $p_0(y_t, y_\ell)$. Because the cross-linker density is higher on the microtubule tip than on the microtubule lattice, the probability to have no cross-linkers connected to the actin decays faster with the length of the overlap with the tip region than with the lattice overlap length, $\lambda_t < \lambda_\ell$. To calculate the diffusion constant, Eq. 5.1 requires an expression for the friction coefficient when the actin filament is bound to the microtubule. Contrary to Chap. 2, we assume that this friction coefficient scales linearly with the actin overlap lengths,

$$\zeta_{\text{bound}}(y_t, y_\ell) = \zeta_t y_t + \zeta_\ell y_\ell, \quad (5.3)$$

since the average number of cross-linkers is proportional to the overlap lengths y_t and y_ℓ , and friction scales linearly with the number of cross-linkers when the spring constant is low enough and exclusion effects between the cross-linkers are insignificant [55, 70, 75]. To find the proportionality constants ζ_t and ζ_ℓ , we perform two separate sets of simulations where we keep y_ℓ or y_t at 0 and vary the other one, and then measure the diffusion constant of the actin filament. In Fig. 5.3D, we fit Eq. 5.1 to the simulated diffusion constants, using ζ_t and ζ_ℓ as the fitting parameter for the curve varying the actin length y_t or y_ℓ , respectively. For both $y \in \{y_t, y_\ell\}$, the effective diffusion constant has

an exponential regime for small y due to Eq. 5.2, and then a linearly decreasing regime for large y due to Eq. 5.3. Since Eq. 5.1 assumes a simple diffusion process and Fig. 5.3D shows that Eq. 5.1 fits the diffusion constants in the simulations remarkably well over the whole range of y , we confirm that the motion of the actin filament is well described by an effective diffusion process.

Then, a forward pointing condensation force F_f provides a drift term to this diffusion process when the actin filament overlaps with the microtubule tip region but does not fully cover it, $0 < x < l_t$, increasing this overlap. Furthermore, when the actin filament extends in front of the microtubule tip region, $x > l_t$, a negative, backward condensation force F_b attempts to increase the overlap between the actin filament and the microtubule lattice region. We derive analytical expressions for these forces in Sec. 5.J, yielding estimated force values of $F_f = 0.10$ pN and $F_b = -4.6$ fN using the parameter set given in Table 5.1.

Using these forces and Eq. 5.1, we can describe the effective drift of the actin filament observed in the comoving frame x . The effective force $F_{\text{eff}}(x)$ that acts on the actin filament is a combination of the condensation forces with an opposing force due to the coordinate transformation to a comoving frame in overdamped dynamics. This pseudo force equals the friction force at drift velocity v_g , leading to

$$F_{\text{eff}}(x) = F_f \mathbb{1}(0 \leq x < l_t) + F_b \mathbb{1}(x > l_t) - \frac{k_B T}{D(x)} v_g. \quad (5.4)$$

Here, $\mathbb{1}(c)$ is the indicator function returning 1 if the condition c is true and 0 otherwise. The diffusion constant $D(x) = D(y_t(x), y_\ell(x))$, where the x dependence of the overlap lengths y is given in Fig. 5.3C, and the diffusion constant follows Eq. 5.1. The comoving frame adds a backward drift to the actin filament, which is captured by the negative term in the effective force in an overdamped system. This term does not always equal the full friction force on the actin filament, since the velocity of the filament can stochastically differ from v_g . The comoving frame of reference is special because it is the only frame of reference in which time is not an explicit parameter of Eq. 5.4.

5.4. ACTIN TRANSPORT IS A META-STABLE STATE

ACTIN transport is a non-equilibrium process, and hence cannot be described by an equilibrium free energy. However, since we know the Fokker-Planck equation that governs the motion of the actin position x in the comoving frame of reference, and because we assume that the dynamics is within the linear response regime giving rise to the Einstein relation [28], we can define a generalised free energy that is consistent with this Fokker-Planck equation.

We integrate the effective force from Eq. 5.4 to find the emergent generalised free energy $\mathcal{F}(x)$ shown in Fig. 5.3E. The free energy shows three regimes, corresponding to the three situations indicated in the bottom of Fig. 5.3C. For $x < 0$, there is no condensation force since the actin filament does not interact with the microtubule tip region. The negative slope is caused by the effective backward drift of the actin filament in the comoving frame. For $0 \leq x \leq l_t$, the condensation force acts to maximise the overlap region, causing a drop in the free energy for an increasing overlap length. For $x > l_t$, the overlap

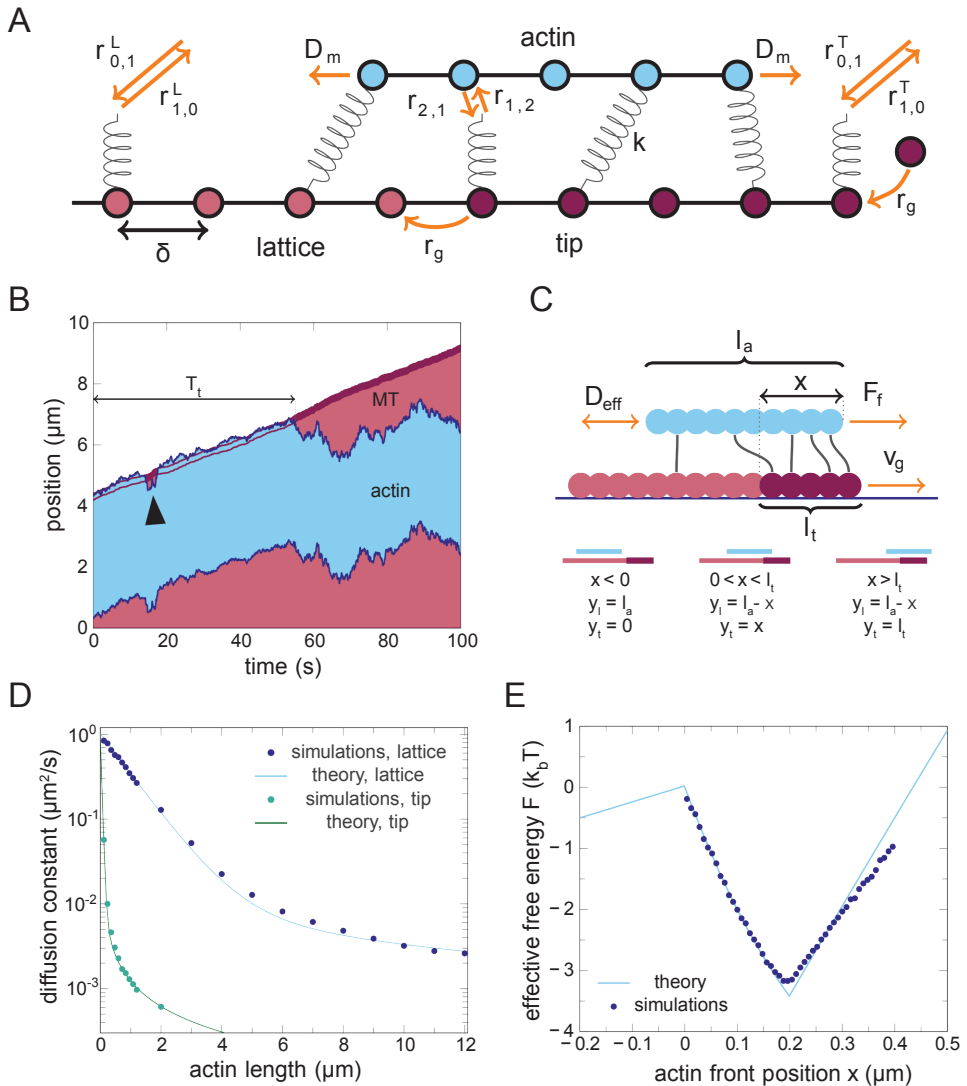


Figure 5.3: Computer simulations and analytical theory of a mechanism for actin transport by growing microtubules (MTs). (A) The model used for simulating the interaction between an actin filament (blue, top) cross-linked to a growing MT (red, bottom). Both filaments are modelled as one dimensional inflexible chains of binding sites with lattice constant δ . Cross-linkers are modelled as springs with spring constant k that can first bind to the MT and from there to the actin filament. These cross-linkers represent a complex of TipAct and EB3, which has a higher affinity for the tip region of the MT (dark red, right) compared to the lattice region (light red, left). The distance between the filaments remains fixed, so the actin filament can only move forward and backward. Viscous interactions with the solution result in a diffusion constant D_a for the actin filament, while the longitudinal components of the pulling forces from the cross-linkers provide additional movement of the actin filament. (caption continues on the next page)

between the actin filament and the microtubule tip region can no longer increase, so the forward condensation force disappears. A very small negative force remains, since the actin filament loses overlap with the microtubule lattice as x increases. However, the largest contribution of the upward slope for $x > l_t$ is again caused by the effective backward motion in the comoving frame. The combination of these three regimes creates the well in the free-energy landscape shown in Fig. 5.3E, showing that actin transport is a meta-stable state. Interestingly, we can compare this theoretical free-energy profile to the negative log probability of actin positions x sampled in the simulations. The generalised free-energy profile obtained from the simulations closely agrees with the theoretical prediction without any adjustable parameters, validating our hypotheses that actin transport is in the linear response regime where the Einstein relation holds, and that it is driven by a condensation force.

5.5. SIMULATIONS AND THEORY PREDICT CORRECT TRENDS IN TRANSPORT TIMES

THE simulations and the analytical theory make predictions about actin transport that can be directly tested against the experimental data. Specifically, we study how the mean duration of transport $\langle T_t \rangle$, where T_t is defined in Fig. 5.3B, changes with the microtubule growth velocity and actin filament length. We observed in Fig. 5.1C that actin transport ends by microtubule catastrophes, actin unbinding, or actin falling behind the tip region of the microtubule.

Actin unbinding events rarely occur when the overlap between the actin filament and the microtubule tip region is long, $x \gg 0$, since the density of cross-linkers is large on the

(B) A typical time trace of the MT and the actin filament. Compare to Fig. 5.1C. The actin filament is transported when it interacts with the MT tip region (dark red, front of MT), and can recover from quick detachments from this tip region through diffusion (black arrow). However, after a stochastic transport time T_t , the actin filament falls behind the tip region and then performs random diffusion on the MT lattice. (C) Parameter definitions for an analytical theory in a comoving frame. We define x as the position of the front of the actin filament compared to the back of the MT tip region. Since the tip region advances upon MT growth, this constitutes a comoving frame of reference. The theory describes the dynamics of x using the cross-linker induced effective diffusion constant of the actin filament $D_{\text{eff}}(x)$, the MT growth velocity v_g and the effective forward condensation force F_f . The actin filament has a length l_a , the microtubule tip region has a length l_t , and the microtubule lattice region is assumed to extend leftward. The overlap lengths between the actin filament and the microtubule tip and lattice regions are denoted y_t and y_ℓ , respectively, and the bottom schematics show the relations between these overlap lengths and the other parameters in three regimes. (D) The effective actin diffusion constant $D_{\text{eff}}(x)$ decreases with the overlap between the actin filament and MT lattice region y_ℓ (blue) and the MT tip region y_t (green). Simulations give the proportionality constants of the actin friction coefficients ζ_t and ζ_ℓ by fitting Eq. 5.1 (lines) to the simulation results (points). (E) Using an analytical expression for the condensation force and the fits from (D), the theory predicts a free-energy well (blue line), where a comoving actin position $x > 0$ within the well represents meta-stable transport, whereas a barrier crossing at $x = 0$ and the subsequent slide towards $x < 0$ represents the actin falling behind the MT tip. Direct sampling of the positional distribution of x in simulations (blue points) confirms the validity of the theoretical prediction.

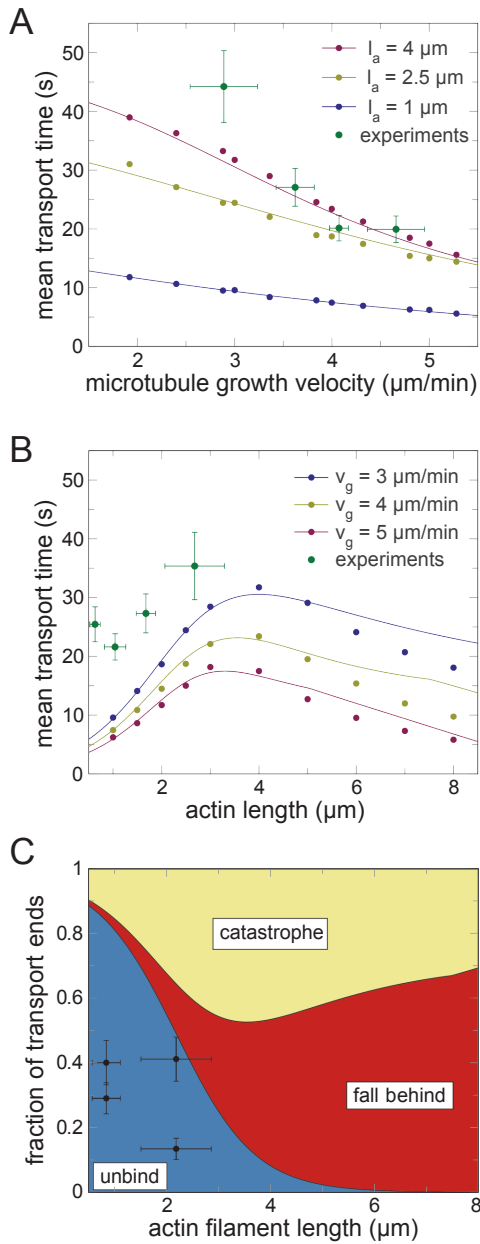


Figure 5.4: Comparing experimental, simulation, and theoretical results for the mean transport times. The transport time T_i is defined in Fig. 5.3B. (caption continuous on the next page)

microtubule tip and the actin filament cannot unbind when a cross-linker connects it to the microtubule. On the other hand, if there is no overlap, and the actin filament is behind the tip region such that $x < 0$, then the transport event will not end via the direct unbinding of the filament either, because the event most likely ends by the actin filament falling further behind the tip. Hence, the rate at which actin unbinding from the microtubule tip region ends actin transport is limited by the probability that the actin filament position x (defined in Fig. 5.3C) is close to 0, and this probability can be calculated using the effective free-energy profile. In Sec. 5.N, we show that the probability that $x \approx 0$ scales exponentially with the growth velocity v_g . Once the actin filament has climbed up the barrier and lost all connections with the microtubule tip region, the actual unbinding requires the filament to lose all connections to the microtubule lattice too. Using Eq. 5.2, which we derive in Sec. 5.L, we can calculate how the probability to be disconnected changes with the actin length l_a ,

$$r_u = r_u^0 e^{-l_a/\lambda_\ell} e^{v_g/\gamma}. \quad (5.5)$$

Here, λ_ℓ is the same as in Eq. 5.2, and γ follows from the free energy and measures how fast the barrier height changes with the microtubule growth velocity v_g . Analytical expressions for λ_ℓ and γ are given Sec. 5.N. Only the prefactor r_u^0 remains unknown, so we fit it once to the complete set of simulated average transport times that is shown in Fig. 5.4AB, after which we keep this single value of r_u^0 fixed.

(A) Mean actin transport time plotted against the growth velocity. Simulations and theoretical predictions shown for three different actin filament lengths. Experimental data is sorted according to the growth velocity and grouped into four sets with 63 or 64 data points each. The error bars represent $(\bar{v}_{g,i} \pm SD_i, \bar{T}_{t,i} \pm SEM_i)$, where i labels the four groups, a bar on a random variable represents the sample mean, SD is the standard deviation of the distribution of growth velocities, and the SEM is the standard error of the mean of the transport times over that group. The experimental data samples over a distribution of actin lengths $\bar{l}_a = 1.5 \pm 0.8 \mu\text{m}$ (mean \pm SD). The theory correctly predicts both the order of magnitude and the declining trend of the mean transport times. (B) Mean actin transport time plotted against the actin length. Simulations and theoretical predictions shown for three different microtubule growth velocities. The same experimental data as in A is sorted according to the actin length and divided into four equally sized groups of 63 or 64 data points each, with $v_g = 3.8 \pm 0.7 \mu\text{m min}^{-1}$ (mean \pm SD). The experimental data confirms the order of magnitude and the trends of the theoretical predictions. There is insufficient experimental data to test the declining transport times due to increased friction for $l_a > 4 \mu\text{m}$. However, for $l_a < 4 \mu\text{m}$, the experimental data confirms that the transport time increases due to an increase of the actin binding times when the actin length increases. (C) Fractions of transport events that end by microtubule catastrophes, actin falling behind the microtubule tip region, or actin unbinding from the tip region as a function of actin filament length. The fractions calculated from theoretical values of the catastrophe rate r_c , rate of falling behind r_e , and unbinding rate r_u are plotted as the indicated coloured regions. We group the experimental data into two bins of equal size, because the four data bins used in (B) provide insufficient statistics per bin to calculate two numbers per bin. We calculate the mean actin length (horizontal error bars are the SD) and the fractions at which each mechanism ends the transport events in both bins. We report the borders between these three regions (vertical error bars are the SEM). Microtubule catastrophes either lead to backward actin transport or to actin unbinding, but are always counted as catastrophes in these fractions. The theory overestimates the fraction of events that unbinds, but it correctly shows that unbinding events become less important with an increasing actin length.

To compute the rate at which the actin filament falls behind the tip region, $x < 0$, we note that the filament has to cross a free-energy barrier to leave the tip region, as shown in Fig. 5.3E. Hence, we can employ Kramers theory [30] (see Sec. 1.5) to calculate the rate r_e at which the actin filament escapes from the free-energy well,

$$r_e = \left[\int_{-\infty}^{l_t} \frac{e^{\mathcal{F}(x)/k_B T}}{D(x)} dx \int_0^{\infty} e^{-\mathcal{F}(x)/k_B T} dx \right]^{-1}. \quad (5.6)$$

Finally, we treat microtubule catastrophes as an independent process that occurs at a fixed rate r_c . The total rate at which transport ends is given by $r_t = r_u + r_e + r_c$, and the average transport time is simply the inverse of this rate, $\langle T_t \rangle = 1/r_t$.

We calculate $\langle T_t \rangle$ using this theoretical description, and additionally sample T_t in computer simulations as a function of the microtubule growth velocity v_g and the actin length l_a . As shown in Fig. 5.4, the theory successfully describes the simulation data, showing that the coarse-grained analytical theory is valid for all regimes probed in the simulations. Only the single parameter r_u^0 was directly fitted once to the complete set of lines in Fig. 5.4, otherwise all parameters in the theory are based on analytically calculable expressions or on ζ_ℓ and ζ_t , which are separately fitted to the diffusion constants in Fig. 5.3D. The curves in Fig. 5.4A show that higher growth velocities lead to shorter transport times, because the friction force between the filaments increases while the condensation force remains unchanged, lowering the free-energy barrier. The friction also increases with the actin length, which explains why the theory predicts a decrease of the transport time as the actin length increases for large actin lengths, as shown in Fig. 5.4B. However, for short actin filaments, transport ends predominantly through actin unbinding, strongly limiting the transport time. The competition between these two effects explains the two regimes observed in Fig. 5.4B.

Experimentally, we observe a set of transport events, each characterised by a microtubule growth velocity v_g , actin length l_a , and transport time T_t . Since both v_g and l_a vary stochastically in the experiments, we sort the experimental data according to the microtubule growth velocity (actin length), and group the data into four sets with an equal number of data points each. Then, we calculate the mean \bar{v}_g (\bar{l}_a) and the mean \bar{T}_t for each set, giving the four green data points in Fig. 5.4A (Fig. 5.4B). Hence, the experimental data points in Fig. 5.4 are not varied at fixed l_a or v_g , but always contain a range of different values for these variables, in contrast with the theoretical data sets.

In Fig. 5.4AB, the experimental data shows decreasing transport times for increasing growth velocities (also see Fig. 5.14A), and increasing transport times for increasing filament length (also see Fig. 5.14B). These trends were confirmed by calculations of Spearman correlation coefficients, both for the experimental data and for the simulations (Table 5.2). As shown in Fig. 5.4A, the experiments (with $\bar{l}_a = 1.5 \mu\text{m}$, see Fig. 5.9B) confirm the predicted theoretical order of magnitude and trends with varying the growth velocity. Moreover, Fig. 5.4B shows that the experimental data (with $\bar{v}_g = 3.8 \mu\text{m min}^{-1}$, see Fig. 5.8A) confirm the order of magnitude and the trends of the transport time with varying the actin length predicted by the theory in the small actin length regime. The experimentally observed actin filaments are not long enough to also probe the regime $l_a > 4 \mu\text{m}$ where the transport time is predicted to decline again due to increased filament friction. The direct unbinding of short actin filaments from the microtubule tip

region ends a significant fraction of the transport events, as shown in Fig. 5.15B. Using the theoretically calculated rates for microtubule catastrophes, actin falling behind, and actin unbinding, we predict the fractions each of the three categories of events, and compare these fractions to the experimentally determined fractions as a function of the microtubule growth velocity in Fig. 5.4C (Fig. 5.14C shows the fractions as a function of the actin length). We observe that the model parameters overestimate the direct unbinding rate of the actin filaments, but the experiments do confirm that the fraction of unbinding events decreases strongly with the actin filament length.

5.6. CROSS-LINKER BINDING CREATES A SIGNIFICANT CONDENSATION FORCE

WE calculate the condensation force for the model presented in Fig. 5.3A by focusing on the binding sites on the microtubule. Each site on the microtubule tip can have three binding states; unbound, bound by a cross-linker that dangles in the solution, or bound by a cross-linker that is also bound to the actin filament. We assume that the filaments are far enough apart such that the free-energies of the unbound and the partially bound states are unaffected by the presence or absence of the actin filament. Then, increasing the overlap length between the actin filament and the microtubule tip region always reduces the free energy, since the fully cross-linked state is only available when the filaments overlap. We can calculate the condensation force using the model shown in Fig. 5.16 using an analytical approximation that is described in Sec. 5.J. We find a condensation force of $F_f = 0.10$ pN in the simulation model, which is part of the effective force in Eq. 5.4.

As a direct test of the existence of the condensation force, we use optical tweezer measurements in a simplified geometry where TipAct is attached to a bead in the absence of actin filaments (Fig. 5.5A). Each experiment starts with placing such a TipAct-coated bead in front of a growing microtubule end with the trap. Successful binding of the bead to the microtubule tip region is evident from its movement towards a microtubule (Fig. 5.17A). The bead then gradually returns to the centre of the trap under the assisting force of the trap (Fig. 5.5A,B). We take the first positive displacement of the bead against the opposing force until the smoothed bead trajectory crosses the zero displacement again as the force signal for further analysis shown in Fig. 5.17B. The magnitude of the force on the beads is expected to be different from the force on actin in the transport experiments. As shown in Eq. 5.25, we find an analytical expression for the condensation force in this simplified geometry where the TipAct-coated bead replaces the actin filament. Using order of magnitude estimates of the relevant parameters, we predict the growing microtubule to exert a condensation force of roughly 0.2 pN on the bead.

From typical force signals as shown in Fig. 5.5C, we measure forces with a mean of 0.12 pN (± 0.07 , SD) for the same conditions as the previously described actin transport experiments (Fig. 5.17C), which is less than the predicted 0.2 pN, but confirms its order of magnitude. We also observe that the force magnitudes decrease when we lower the cross-linker affinity for the microtubule by raising the salt concentration, consistent with Eq. 5.25. This confirms the predictive power of our theoretical model, and further supports the hypothesis that actin transport is driven by a condensation force that competes

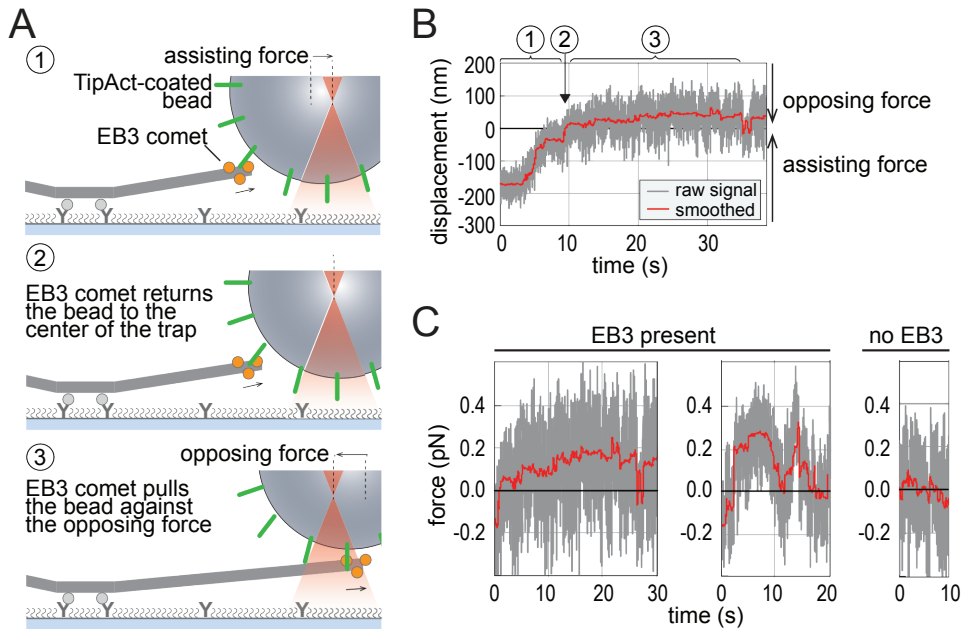


Figure 5.5: Optical tweezer measurement of the force developed by cargo-bound TipAct at the growing microtubule plus end. (A) Schematic diagram of the experimental setup. A TipAct-coated bead is initially attached to a growing microtubule carrying an EB3 comet. The bead moves back to the centre of the trap under the assisting force (1). After having arrived in the trap center (2), the bead is pulled by the EB3 comet against the opposing force from the trap (3). (B) A typical recording of a bead moving against the opposing trap force with experimental steps numbered according to (A). (C) Examples of forces exerted by growing microtubule ends through the TipAct coupling in presence or absence of EB3.

with a cross-linker induced friction.

5.7. DISCUSSION

IN this study, we have reconstituted transport of actin filaments by growing microtubule plus ends in the presence of transiently binding cross-linkers. We have shown that this transport is governed by a condensation force and a competing friction force that are both caused by the cross-linkers. Microtubule growth leads to the net motion of the chemically distinct microtubule tip region, but the microtubule performs no mechanical movement. The actin filament recognises the microtubule tip region through cross-linking proteins that bind more strongly to the tip region compared to the lattice region, creating a force that tries to maximise the overlap between the actin filament and the microtubule tip region. However, the resulting mechanical movement of the actin filament is opposed by a friction force with the motionless microtubule, and actin movement is only possible if the cross-linkers remodel their binding positions on the

actin filament through (un)binding dynamics. Hence, increasing the condensation force by increasing the cross-linker density does not necessarily lead to longer-range actin transport, since the cross-linker induced friction force between the filaments is also increased.

In recent years, it is becoming increasingly clear that, in addition to motor-driven and (de)polymerisation-driven forces, passive cross-linkers can also generate active forces. One mechanism for passive cross-linkers to generate active forces is via entropic expansion [18] (see Sec. 4.1), where the overlap region between two filaments is maximised to increase the entropy of a fixed number of diffusible cross-linkers, as was shown for Ase1 cross-linkers that connect anti-parallel microtubules in the mitotic spindle [18]. A second mechanism to generate active forces by passive cross-linkers is via their binding affinity for overlap regions when the cross-linkers are present in the solution. This mechanism can result in bundle contractions, as was shown for FtsZ filaments in bacteria [120] and for actin filaments [54, 55], it can lead to the deformation of elastic structures, such as lipid membranes [119], and it can cause processive movement, as for the proposed transport by a shrinking microtubule in a sleeve [116] and for the actin transport described here.

The mechanism that we describe is similar to a previously proposed mechanism for cargo transport by shrinking microtubules binding in a sleeve, originally introduced as a mechanism for chromosome transport via kinetochores [116]. Also in that case, the force that drives the transport is simultaneously countered by a friction force between the sleeve and the microtubule. However, previous theoretical analysis of chromosome transport focused on finding the meta-stable distribution of microtubule positions within the sleeve [116] equivalent to finding the generalised free-energy profile we present in Fig. 5.3E. In contrast, we focus on the transport time distribution that results from this meta-stable state, which can be compared to the experimental measurements. Furthermore, actin transport differs from the sleeve mechanism since it is only driven by the higher attractive interaction of the actin filament with the microtubule tip region compared to the chemically different lattice region, whereas the sleeve transport follows a depolymerising microtubule.

Another example of condensation forces that result in processivity is a recent experimental study on pulling of membrane-tubes by growing microtubules [119]. Similar to the transport of actin filaments, the forward force on the membrane tubes is driven by the affinity of the membrane for the growing microtubule plus-end. However, the membrane is also pulled over the microtubule lattice, whereas actin transport stops when the actin filament is no longer interacting with the microtubule tip region. Moreover, the actin filament slides relative to the microtubule, causing a friction force, whereas the fluid nature of the membrane means that the pulled tubes can spread over the microtubule like a continuous track.

Actin transport by growing microtubule plus ends results in much lower forces and velocities than are measured for microtubule motor proteins (0.10 pN and $1\text{--}10\ \mu\text{m min}^{-1}$ for microtubule growth compared to $1\text{--}10\ \text{pN}$ and $0.1\text{--}1\ \mu\text{m s}^{-1}$ for single motors or collectives of motor proteins) [85, 129]. In direct competition, motor forces would therefore likely dominate over the condensation forces. However, these forces can remodel actin filaments specifically at the growing microtubule plus end, whereas motor-driven forces

mainly remodel actin filaments along the microtubule lattice, or at depolymerising microtubule ends [121, 130]. In addition, Tip-localised transport could be useful in cells for relocating newly nucleated actin filaments towards the leading edge of migrating cells. Recent studies uncovered two distinct pathways to specifically nucleate new actin filaments at the growing microtubule plus end [111, 112]. The transport mechanism identified in our study could rapidly relocate those filaments to the leading edge of the cell, where they influence the formation of new actin-based protrusions.

The microtubule tip region is chemically different from the microtubule lattice region, which is recognised by microtubule end-binding (EB) proteins [126–128]. As the microtubule grows, the GTP bound to the subunits of the microtubule tip are hydrolysed, creating new lattice units. The condensation force adopts this wave of chemical modification on the mechanically still microtubule to generate mechanical motion of the actin filament. This transport mechanism might also be used to transport other cytoskeletal filaments, such as intermediate filaments [131–134]. Furthermore, we speculate that the theoretical description can be applied not only to filament transport, but also to transport by propagating reaction-diffusion patterns on membranes, such as the transport of plasmids by ParA [135–137].

APPENDIX

5.A. PROTEIN ISOLATION AND PREPARATION

Engineered cross-linking protein TipAct (composed of an N-terminal eGFP followed by the actin binding domain and EB-binding domain of full-length MACF1, separated by the coiled-coiled linker of Cortexillin I) was expressed in *E. coli* T7 cells and purified using a His-tag affinity column, as was previously described [107, 138]. Lyophilized porcine brain tubulin was obtained from Cytoskeleton (Denver, CO, USA), resuspended at 50–100 μM MRB80 buffer [80 mM piperazine-*N,N'*-bis(2-ethanesulfonic acid) (Pipes), pH 6.8 with KOH, supplemented with 4 mM MgCl_2 and 1 mM EGTA], snap-frozen and stored at -80°C until use. G-actin was purified from rabbit skeletal muscle acetone powder as previously described [139], filtered on a Superdex 200 10/60 size-exclusion column (GE Healthcare, Waukesha, WI, USA) to remove any oligomers and stored at -80°C in G-buffer [5 mM tris(hydroxymethyl)aminomethane (Tris), pH 7.8 with HCl, 0.1 mM CaCl_2 , 0.2 mM ATP, 1 mM dithiothreitol (DTT)]. Fluorescent actin was prepared by labelling monomers with Alexa Fluor 649 carboxylic acid succinimidyl ester (Molecular Probes, Life Technologies, Carlsbad, CA, USA). Before use, G-actin was thawed overnight at 4°C and spun for 15 min at 149,000 g to remove any aggregates, and stored at 4°C for no longer than 2 weeks. 6xHis-tagged recombinant human GFP-EB3 and mCherry-EB3 were expressed and purified as described before [140].

5.B. DYNAMIC MICROTUBULE ASSAY

Microscope flow cells were constructed as previously described [138]. In brief, flow channels of 10–15 μl , assembled from base-piranha cleaned glass cover slips and slides and Parafilm spacers, were functionalised by sequential incubation with 0.1 mgml^{-1} PLL-PEG-Biotin (PLL(20)-g[3.5]-PEG(2)/PEG(3.4)-Biotin(20%), SuSos AG, Dübendorf, Switzerland) for 30–60 min, 0.25 mgml^{-1} streptavidin (Thermo Scientific Pierce Protein Biology Products, Rockford, IL, USA) for 10 min, 0.5 mgml^{-1} κ -casein for 10 min and 1 % (w/v) Pluronic F-127 for 10 min, all solutions in MRB80, and including 40–70 μl rinses with MRB80 in between incubation steps.

Actin filaments were pre-polymerized at 7.5 μM G-actin concentration (15 mol % labelled and 85 mol % unlabelled premixed monomers) in MRB80 for 30–90 min at room temperature, before adding phalloidin (Sigma-Aldrich) in 1:1 molar ratio to stabilise the filaments. Dynamic microtubules were nucleated from guanylyl-(α,β)-methylene-diphosphate (GMPCPP) stabilised microtubule seeds, which were bound to the biotinylated surface and prepared according to standard double-cycling protocols [16, 138]. Any non-attached seeds were rinsed off with MRB80 before adding the final imaging mix. The core imaging buffer consisted of MRB80 supplemented with 0.5 mgml^{-1} κ -casein, 0.2% (v/v) methyl cellulose (M0512, Sigma-Aldrich Chemie B.V., the Netherlands), 75 mM KCl, 1 mM guanosine triphosphate(GTP), 0.2 mM Mg-ATP and an oxygen scavenging system [4 mM dithiothreitol (DTT), 2 mM protocatechuic acid (PCA) and 100 nM protocatechuate-3,4-dioxygenase (PCD)]. This solution further contained tubulin concentrations ranging from 20–30 μM (6 mol % Rhodamine labeled), 7.5–10 nM F-actin, 133 nM EB3 (mCherry

or GFP labeled), and 50 nM TipAct (GFP).

5.C. MICROSCOPY

Imaging of *in vitro* actin transport by growing microtubule plus ends was performed using a Nikon Eclipse Ti-E inverted microscope (Nikon Corporation, Tokyo, Japan) equipped with an Apo TIRF 100x/1.49 numerical aperture oil objective, a QuantEM:512SC EM-CCD camera (Photometrics, Roper Scientific), a motorized stage, Perfect Focus System, and a motorised TIRF illuminator (Roper Scientific, Tucson, AZ, USA). For excitation, we used a 561 nm (50 mW) Jive (Cobolt, Solna, Sweden), a 488 nm (40 mW) Calypso (Cobolt) diode-pumped solid-state laser and a 635 nm (28 mW) Melles Griot laser (CVI Laser Optics & Melles Griot, Didam, Netherlands). A custom-built objective heater was used to maintain the sample at 30 °C. Triple-colour images were acquired for 10–20 min with 3 s intervals and 100–200 ms exposure times.

5.D. IMAGE AND DATA ANALYSIS

Image processing and analysis were performed using plug-ins for Fiji [141] or ImageJ and custom-written programs in Python, MATLAB and Mathematica. Time-lapse series of TIRF images were drift-corrected using a custom-written Matlab program. Kymographs of microtubule growth were created using the reslice tool in Fiji [141]. Plus and minus ends were distinguished based on their growth rates: faster-growing ends were identified as the plus ends and the slower-growing ends as the minus ends. The parameters characterising actin transport and microtubule dynamics were determined from these time-lapses and kymographs.

A microtubule/actin interaction event was classified as transport and included in further analysis when (1) an actin filament colocalised with an EB3/TipAct-complex at the growing microtubule plus end, (2) moved for at least 0.5 μm (3 pixels) and for 9 s (3 time steps) along with the microtubule tip, and (3) was not interacting with other actin filaments or microtubules. The actin filament length and tracking time were obtained from manual fits on the kymographs. From the original time lapse image series, the binding states of the actin filament before and after the transport event were determined.

The microtubule dynamics were characterised as previously described [142]. In brief, growth velocities were obtained from manual fits to the growth phases, and the average velocity was taken as the average over all events weighted with the duration of the individual events. The error is the weighted standard deviation. Catastrophe rates were calculated as the number of catastrophe events divided by the total time microtubules spent growing. The error is given by the rate divided by the square-root of the number of events.

5.E. OPTICAL TWEEZERS

Silica beads (1 μm in diameter) functionalised with carboxy groups (Bangs Laboratories) were conjugated PLL-PEG-Biotin (PLL(20)-g[3.5]-PEG(2)/PEG(3.4)-Biotin(10%), SuSoS AG, Switzerland) as described in [143]. 10 μl of PLL-PEG-coated beads (ca 0.2% w/v) were washed in washing buffer (80 mM K-Pipes pH 6.9 with 1 mM EGTA, 4 mM MgCl_2 ,

1 mM DTT and 0.5 mg ml⁻¹ casein) by centrifugation for 1 min at 16000 g, then resuspended in 20 μ l of 8 μ M Neutravidin (Thermo Scientific) in the same buffer. After 30 min incubation at 23 °C with frequent mixing, the beads were washed twice in 100 μ l of the washing buffer, resuspended in 20 μ l of 0.2 μ M biotinylated anti-GFP IgG (Rockland) and further incubated for 30 min at 23 °C with frequent mixing. After two more washes in the washing buffer, the beads were resuspended in 20 μ l 120 nM GFP-TipAct and incubated for 1 h on ice with frequent mixing. Finally, the beads were washed three times and resuspended in 50 μ l of the washing buffer.

To attach microtubule seeds to glass, we used digoxigenin (DIG)-labelled tubulin to prevent interactions with the biotinylated beads. Briefly, tubulin was purified from porcine brain [144] and chemically labelled with NHS-DIG [145]. GMPCPP stabilised microtubule seeds were prepared using 30% DIG-labelled tubulin and according standard double-cycling protocols [16].

Optical trapping was performed as described previously [119]. Slides and cover slips were silanised using Plus-One Repel Silane (GE Life Sciences), then assembled into flow chambers using double-sided tape and functionalised with 0.2 μ M anti-DIG IgG (Roche), then passivated with 1% Pluronic F-127 in MRB80, before DIG-labelled seeds were introduced. The reaction mix (80 mM K-Pipes pH 6.9, 50 or 75 mM KCl, 1 mM EGTA, 4 mM MgCl₂, 1 mM GTP, 1 mg ml⁻¹ κ -casein, 4 mM DTT, 0.2 mg ml⁻¹ catalase, 0.4 mg ml⁻¹ glucose oxidase, 20 mM glucose and either 25 mM unlabelled tubulin with addition of 133 nM EB3, or 10 mM unlabelled tubulin in the absence of EB3) was centrifuged at 30 psi for 5 min. TipAct-coated beads were added to the supernatant at a ratio of 1:33-1:50. This final mix was then introduced into the flow chamber, and experiments were carried out at 25 °C.

DIC microscopy and optical trapping were performed as described previously [143]. Measurements were performed at nominal trap power of 0.2 W (the lowest setting of our instrument), and then the trap stiffness was additionally softened down to 4×10^{-3} – 6×10^{-3} pN nm⁻¹ using a circular polarising filter placed in the wave path of the trapping laser. The QPD signal was recorded at 10 kHz.

5.F. MICROTUBULE CATASTROPHES AFFECT THE TRANSPORT TIME DISTRIBUTION

As shown in Fig. 5.2A–C, transport events typically end in one of three ways. Actin can fall behind the growing microtubule tip and escape to the microtubule lattice, actin can unbind directly from the microtubule tip and escape to the solution, or a microtubule catastrophe occurs. The stochastic times at which these events happen are called T_e , T_u , and T_c , respectively. Our description assumes that these three random variables are independent, and the shortest time decides which event actually occurs. In this section, we discuss a framework to separate the events of interest, i.e., the actin falling behind the tip or unbinding, from simple catastrophe events. Hence, we group the former two event types, $T_i \equiv \min(T_e, T_u)$, and refer to them as events of interest. In case of a microtubule catastrophe, the actin filament either unbinds from the microtubule or it is transported back by the shrinking microtubule (see Fig. 5.10), but we consider the microtubule catastrophe itself to be responsible for terminating transport in both cases,

since we only focus on forward transport. We call $r_i = r_e + r_u$ the rate at which the events of interest occur, and we call the rate of microtubule catastrophes r_c . Then, the experimentally measurable rate r_t at which the transport events end is given by

$$r_t = r_i + r_c. \quad (5.7)$$

We next consider how the distribution of observed transport times depends on whether we only select the events of interest or if we combine them with the catastrophe events.

The transport time T_t obeys

$$T_t = \min(T_i, T_c). \quad (5.8)$$

Since both types of events are independent and exponentially distributed, we have

$$\mathbb{P}(T_t > t) = \mathbb{P}(T_i > t \wedge T_c > t) = \exp[-(r_i + r_c)t], \quad (5.9)$$

which agrees with Eq. 5.7.

To better isolate the two event types, we can analyse how the transport times of the events of interest are distributed. If we cut out the events that end in catastrophes, we observe the transport time distribution

$$\mathbb{P}(T_t > t \mid T_i < T_c) = \frac{\mathbb{P}(T_i > t \wedge T_i < T_c)}{\mathbb{P}(T_i < T_c)}, \quad (5.10)$$

where we rewrite the first probability using Bayes' theorem and Eq. 5.8. We can calculate the probability density of T_c happening at time t' , and integrate over all possible t' ,

$$\begin{aligned} \mathbb{P}(T_i > t \wedge T_i < T_c) &= \int_0^\infty \mathbb{P}(t < T_i < t') r_c \exp[-r_c t'] dt' \\ &= \int_t^\infty (\exp[-r_i t] - \exp[-r_i t']) r_c \exp[-r_c t'] dt' \\ &= \frac{r_i}{r_i + r_c} \exp[-(r_i + r_c)t]. \end{aligned} \quad (5.11)$$

In a similar fashion, one can show that

$$\mathbb{P}(T_i < T_c) = \frac{r_i}{r_i + r_c}. \quad (5.12)$$

Hence, Eq. 5.10 gives

$$\mathbb{P}(T_t > t \mid T_i < T_c) = \exp[-(r_i + r_c)t] = \exp[-r_t t] = \mathbb{P}(T_t > t). \quad (5.13)$$

The cumulative distribution function (CDF) we look for is simply $\mathbb{P}(T_t \leq t \mid T_i < T_c) = 1 - \mathbb{P}(T_t > t \mid T_i < T_c)$, and Eq. 5.13 shows that this distribution equals the CDF $\mathbb{P}(T_t \leq t)$. Naively, one may expect that removing the catastrophe data and looking only at the events of interest would lead to measuring the CDF $\mathbb{P}(T_i \leq t)$, the distribution that is measured when catastrophes never occur. To get an intuitive understanding why the distribution Eq. 5.13 is biased compared to $\exp[-r_i t]$ when we remove the events that end in microtubule catastrophes, it is helpful to estimate the likelihood that an event ends in

a catastrophe when the event time T_i is short ($T_i < 1/r_c$) or when it is long ($T_i > 1/r_c$). When T_i is short, and catastrophes do occur, it is likely that the catastrophe takes place after the actin filament escapes, or $T_i < T_c$. When the events that end in catastrophe are then discarded, it is likely that the short T_i is still observed. However, when T_i is long, the catastrophe is more likely to happen before the event of interest, and usually $T_i > T_c$. The selection then discards these events more often. Hence, short T_i are selected more often than long T_i , which introduces a negative bias in the distribution of transport times of those events that do not end in a microtubule catastrophe. Eq. 5.13 shows that the CDF for the selected transport times $\mathbb{P}(T_t \leq t \mid T_i < T_c)$ equals the CDF of the complete data set of transport times $\mathbb{P}(T_t \leq t)$, and is biased compared to the desired CDF $\mathbb{P}(T_i \leq t)$. Hence, we proceed by simply measuring the mean transport time using all events T_t , and then separately measure the microtubule catastrophe rate in order to identify the contribution of r_i to r_t .

5.G. DETAILS OF THE SIMULATED MODEL

The simulation model (see Fig. 5.3A) is based on the model developed in Chap. 2 to describe cross-linked microtubules. The simulation uses discrete time step dynamics for the movement of the actin filament, while using a kinetic Monte Carlo algorithm for simulating the Markovian reactions that take place with time-varying rates. Below, we list several details of the simulation model that are not described Sec. 5.2.

First, we describe the experimentally observed binding properties of TipAct, and then how we choose to model them. TipAct has a binding site that can bind to actin directly [107]. In the presence of EB3, TipAct has a higher binding affinity for microtubules than for actin filaments. TipAct forms a complex with EB3, which in turn has a high affinity for the microtubule tip region and a low affinity for the microtubule lattice region. In the model, we make the simplifying assumption that there is a single cross-linker that represents the complex of TipAct and EB3, but could also represent states where TipAct binds to microtubules and actin on its own. We will refer to this single cross-linker as TipAct, except when we need to specifically distinguish between internal binding states.

To form a cross-link between a microtubule and an actin filament, there are two different pathways. TipAct can first bind to the microtubule or first to the actin filament, after which it can bind to the opposite filament. All these binding transitions are reversible, leading to are eight (un)binding rates; two for the transition between the unbound and actin-bound states, two between the unbound and microtubule-bound states, two between the actin-bound and fully bound states, and two between the microtubule-bound and fully bound states. Detailed balance reduces this to a set of seven different rates. In vitro experiments showed that the binding of TipAct to single actin filaments is negligible compared to the binding to single microtubules [146] (Fig. 5.15), meaning that we can remove one of the pathways, and we are left with four (un)binding rates per pair of binding sites on the microtubule and actin filament, as shown in Fig. 5.3A. These are the two rates for the transition between a fully unbound state and a state where TipAct is solely bound to the microtubule, and two rates for the transition from this dangling cross-linker state to the state where the cross-linker binds both the microtubule and the actin filament.

Since TipAct binds strongly to the microtubule tip region through EB3, but also has a low but significant affinity for the microtubule lattice, we use two separate sets of (un)binding rates for TipAct binding from the solution to the microtubule lattice and tip regions. However, we assume that the rates to bind to or unbind from the actin filament are the same for dangling TipAct cross-linkers bound to the microtubule tip or lattice. For convenience, we label the unbound state as 0, the state with a dangling cross-linker bound to the microtubule 1, and the fully bound state where the cross-linker also binds to the actin filament 2, and we distinguish between the microtubule lattice region L and the microtubule tip region T . As Fig. 5.3A shows, this gives us the rates $r_{0,1}^T, r_{1,0}^T, r_{0,1}^L, r_{1,0}^L, r_{1,2}^0$, and $r_{2,1}^0$. Here, a rate $r_{i,j}$ corresponds to the transition from state i to state j , and the 0 in the superscript indicates that the rate will depend on the amount that the linker has to stretch,

$$r_{1,2}(d) = r_{1,2}^0 \exp\left[-\frac{U(d)}{2k_B T}\right], \quad (5.14)$$

where d is the amount by which the linker is stretched after the transition, and $U(d)$ gives the potential energy for a cross-linker with extension d . The same equation holds for the reverse rate $r_{2,1}(d)$ if we change the sign of the potential energy. Detailed balance sets a Boltzmann factor for the ratio between the forward and backward rates, but not for the rates individually. We make the model choice to distribute this factor evenly between the forward and backward reactions, explaining the factor 1/2 in the exponent. This choice ensures that the binding rate to a site that requires a cross-linker stretch d decreases with d , and the corresponding unbinding rate increases with d .

Even though there are typically multiple cross-linkers connecting the actin filament to the microtubule, the filaments can occasionally disconnect due to stochastic nature of the (un)binding dynamics of the cross-linkers. However, upon the unbinding of the last cross-linker, the filaments are still in close enough proximity such that new cross-linkers can bind. Hence, cross-linker rebinding can keep the filaments connected. To simulate this rebinding dynamics, we introduce a time scale τ_a and end a simulation when there are no connections between the two filaments for longer than τ_a . This time scale simulates the time it takes the actin filament to diffuse over a distance corresponding roughly to the size of a cross-linker, such that the probability of rebinding becomes negligible [147].

Since we keep the distance between the filaments fixed in the simulations, we only have to describe the longitudinal component of the stretch of the cross-linkers d , and we assume that the potential energy obeys a simple harmonic function $U(d) = kd^2/2$. This potential provides forces on the actin filament and also influences the (un)binding rates through Eq. 5.14. When a cross-linker is bound to the microtubule and dangling, there are many binding sites on the actin filament that the cross-linker could bind to, but the harmonic potential sets very low rates for binding to the ones that require the cross-linker to stretch far. Hence, we improve the efficiency of the simulations by setting a maximum stretch for the cross-linkers, such that the simulations do not check binding positions that are unrealistically far away. We set this maximum stretch to 4δ , where δ is the spacing between binding sites on either filament. Using the parameter values from Table 5.1, the springs store a potential energy of $10.4k_B T$ at a stretch of 4δ . Hence, thermal fluctuations are unlikely to cause a stretch that large, justifying the simulation

choice. For consistency, we also disallow the actin filament to change its position in a way that would stretch linkers more than 4δ .

We made the model choice that the density of microtubule tip sites follows a step function, such that the tip is a well-defined region on the microtubule of length l_t . This simple structure simplifies calculations and expresses our ignorance about the precise structure of the microtubule tip region where EB3 binds, which remains under discussion [148–150]. To confirm that the proposed mechanism of tip tracking also works with different microtubule tip region structures, we performed simulations where the density of tip sites decreases exponentially with the distance from the front of the microtubule. Leaving the other parameter values as they are listed in Table 5.1, we still observed actin transport, as shown in Fig. 5.18. Hence, the mechanism of a condensation force caused by transiently binding cross-linkers works independent of the exact shape of the tip region.

To calculate the statistics of the transport times, we make use of Welford's online algorithm, as described in Sec. 5.O.

5.H. ACTIN DIFFUSION MEASUREMENTS

5

We experimentally observed that actin filaments occasionally land on the microtubule lattice and perform one-dimensional diffusion while remaining bound via TipAct. By raising the tubulin concentration to $30\ \mu\text{M}$, we obtained longer microtubules that allowed us to measure the diffusive motion of the actin filaments on the microtubule lattice, away from the tip region. The estimation of the diffusion constant is complicated by thermal fluctuations of the apparent actin filament length. We quantify this apparent length by manually measuring the positions of the beginning and the end of the actin filament, called x_b and x_e , respectively, as a function of time with time steps of $\delta t = 3\text{ s}$. Two kymographs of diffusing actin are shown in Fig. 5.12AB, along with the trajectories of x_b and x_e and the apparent actin length $l_a = x_e - x_b$. Besides small fluctuations around a constant length, Fig. 5.12AB also shows large transient deviations of the actin length that occur at the beginning of the time traces, as shown in the bottom panels of Fig. 5.12AB. These length fluctuations are probably caused by the binding process of the actin filaments. To estimate the length of the part of the actin filament that interacts with the microtubule, we remove the initial part of the time traces and take the mean value of l_a over the cropped time trace, as shown in Fig. 5.12AB. Then, we define the actin position x as the centre point of the actin filament, $x = (x_b + x_e)/2$, and estimate the diffusion constant from the time trace of x in the cropped window.

Since the recorded data for x is noisy and contains a finite number of time points, it is difficult to find a reliable estimate of the diffusion constant from a single time trace [151]. The data set consists of $N + 1$ time points x_i , which are acquired at $t_i = i\delta t$ and $i = \{0, 1, \dots, N\}$. For the diffusion constant, we use a family of estimators based on the time-averaged square displacement [152],

$$\bar{D}_\Delta = \frac{1}{2\Delta(N - \Delta + 1)\delta t} \sum_{i=0}^{N-\Delta} (x_{i+\Delta} - x_i)^2, \quad (5.15)$$

which depends on a choice of the number of time steps $\Delta \in \mathbb{N}$ over which we probe the

fluctuations. The movement of the actin filament is likely correlated for small times, and when Δ is smaller than the largest correlation time, the estimate of the diffusion constant will be influenced by these correlations. Furthermore, measurement noise and thermal length fluctuations have a larger influence on \bar{D}_Δ when Δ is small, because the actin steps ($x_{i+\Delta} - x_i$) are typically smaller. However, when Δ is too large, the number of time points $N - \Delta$ decreases, and the uncertainty in the estimate grows. As shown in Fig. 5.12D, the time traces last for only 30 s to 950 s before cropping, giving between 9 and 291 data points after cropping. We focus on the two time traces that are longer than 500 s to obtain reliable estimates of the actin diffusion constants.

We show the results of Eq. 5.15 as a function of the time gap $\Delta\delta t$ for the two long time traces in Fig. 5.12C. These two time traces are obtained from actin filaments with lengths $l_a = 6.6\mu\text{m}$ and $l_a = 7.1\mu\text{m}$, and after cropping the time traces to a total duration of 873 s and 762 s, respectively. For small times, the estimate \bar{D}_Δ decreases strongly with Δ and reaches a plateau value after roughly 150 s. We believe that the strong bias in \bar{D}_Δ contains contributions from actin filament length fluctuations and external measurement noise. Furthermore, actin movement is different for time scales shorter than the time scales over which cross-linker remodelling occurs, and we expect that these effects also contribute to the bias in \bar{D}_Δ . We estimate the true diffusion constant as the sample mean of \bar{D}_Δ over a window between 150 s and 450 s, and report the standard deviation of the mean over this window as the error in our estimate. This results in the values $\bar{D} = 0.014(3)\mu\text{m}^2\text{s}^{-1}$ ($l_a = 6.6\mu\text{m}$) and $\bar{D} = 0.009(3)\mu\text{m}^2\text{s}^{-1}$ ($l_a = 7.1\mu\text{m}$).

5.1. SIMULATION PARAMETER VALUE ESTIMATION

The simulation model presented in Fig. 5.3A contains many parameters, which are listed in Table 5.1. We constrain these parameters by combining several experimental observations.

First, for model simplicity, we chose to have a single lattice spacing between cross-linker binding sites both on the microtubule and on the actin filaments. We take this lattice spacing to be equal to the distance between subunits of the microtubule, which is $\delta = 8\text{ nm}$ [76]. The actual distance between binding sites on the actin filament is around 5 nm [153, 154]. However, the actin binding domain of TipAct consists of a tandem of CH domains and TipAct forms a dimer [107], making it likely that TipAct typically fills two neighbouring binding sites. Moreover, due to the helical twist of the actin filament [155], it is unclear how many binding sites are available on average. Hence, we can only find an approximate value for the lattice spacing between binding sites on the actin filament. Importantly, our model results do not depend qualitatively on the values of the lattice spacings on the microtubule and the actin filament.

Another parameter that can be estimated relatively easily from experiments is the size of the microtubule tip region. In our model, the tip region is a deterministic step function. In experiments, the EB3-TipAct comet fills roughly a single pixel of the camera, which has a size of $0.2\mu\text{m}$. Therefore, we take the length of this tip region $l_t = 0.2\mu\text{m}$ as a rough estimate, which sets the number of tip sites to 25 using the previously introduced choice for lattice spacing δ .

Next, the longitudinal friction coefficient of F-actin due to its viscous interactions

with the solution can be calculated theoretically for a thin rod [156–158],

$$\zeta_{\parallel} = \frac{2\pi\eta l_a}{\log(l_a/d) + \gamma_{\parallel}}. \quad (5.16)$$

Here, the correction parameter $\gamma_{\parallel} = -0.114$, as confirmed experimentally for actin filaments [158], and the actin diameter $d = 9 \times 10^{-9}$ m [155]. Furthermore, the viscosity is taken to be that of water, $\eta = 1 \times 10^{-3}$ Pa s, and we use a filament length of $l_a = 3 \mu\text{m}$ here, which falls within the experimental length distribution shown in Fig. 5.10C. Using the Einstein relation [28] and $k_B T = 4.1 \times 10^{-21}$ J, this gives us $D_a \approx 1 \mu\text{m}^2 \text{s}^{-1}$. For simplicity, we will not vary the value of D_a with the actin length, which is justified by the fact that the cross-linkers limit the motion of the actin filament much more strongly than the viscous drag by the solvent.

Another parameter in our model is τ_a , the time it takes for the actin filament to diffuse far enough away from the microtubule such that it is unlikely to be recaptured. To estimate this time scale, we use the time it takes diffusion of the actin filament to produce a standard deviation of $0.1 \mu\text{m}$ in the perpendicular position. This is roughly three times the length of the TipAct-EB3 complex [146], and also accounts for the possibility that the actin filament could slightly bend. Using an equation for the friction coefficient ζ_{\perp} similar to Eq. 5.16 [158], we arrive at

$$\tau_a \approx 5 \times 10^{-3} \text{ s}. \quad (5.17)$$

As Fig. 5.3A shows, we have to constrain the rates $r_{0,1}^T$, $r_{1,0}^T$, $r_{0,1}^L$, $r_{1,0}^L$, $r_{1,2}^0$, and $r_{2,1}^0$, and also the spring constant k . Since these parameters are difficult to access directly, we estimate them based on a comparison between experimental observations and simulation results. Firstly, we use the observed diffusion constants of actin filaments on the lattice. Secondly, we measure the duration of actin diffusion on the microtubule lattice before unbinding as a function of the actin length. Thirdly, we fit our parameter set to the order of magnitude of the duration of actin transport events. Fourthly, we label TipAct and EB with the same fluorescent tag, and measure the difference in the fluorescence signal between the microtubule lattice and tip regions as a read-out of the binding affinity of the complex. Lastly, we use several specific observations on the (un)binding rates obtained by fluorescence recovery after photobleaching (FRAP) measurements. We explain all these experimental sources in detail below.

We discussed above that the actin diffusion constant is roughly $D_{\text{eff}} = 0.01 \mu\text{m}^2 \text{s}^{-1}$ at $l_a = 7 \mu\text{m}$, as shown in Fig. 5.12. This diffusion constant is affected by the average number of cross-linkers that bind to the actin filament. If there are many cross-linkers, the diffusion on the lattice slows down. The number of bound linkers is set by all binding rates on the lattice, $r_{0,1}^L$, $r_{1,0}^L$, $r_{1,2}^0$, and $r_{2,1}^0$. The parameter $r_{2,1}^0$ is also important for actin movement in another way, since movement is limited by how fast the cross-linkers can remodel. Hence, a higher $r_{2,1}^0$ will quickly increase the effective diffusion constant of actin on the microtubule lattice by reducing the number of cross-linkers and by increasing the rate of cross-linker remodelling. Additionally, the actin diffusion constant decreases by lowering the spring constant k , since it increases the numbers of bound cross-linkers by increasing the accessibility of the actin binding sites.

Another experimental observation that constrains the binding rates is the average duration of actin diffusion on the microtubule lattice. Fig. 5.12D shows that this duration depends exponentially on the actin length, since it becomes exponentially more likely that at least one cross-linker binds to the actin filament when more binding sites are available. The experimentally observed duration is strongly stochastic, and since we only have 19 events where actin simply diffuses on the lattice, we can only make an order of magnitude estimate of the average time of being bound for a diffusing actin filament of a certain length. The experiments show that the actin stays on the microtubule lattice for roughly 40s at $l_a = 4\mu\text{m}$, so we fit the order of magnitude of the actin binding time in our simulations to this value. Specifically, we perform simulations in which a $4\mu\text{m}$ long actin filament is transported by the microtubule, and then record both the time until the actin falls behind the tip and the time until the actin unbinds from the microtubule lattice. Several parameters influence the duration of lattice diffusion in the simulations. Increasing the average number of cross-linkers on the lattice by changing $r_{0,1}^L$, $r_{1,0}^L$, $r_{1,2}^0$ or $r_{2,1}^0$ makes this binding time larger. Additionally, the actin binding time can be increased by reducing the time scale of cross-linker remodelling, so by increasing both $r_{1,2}^0$ and $r_{2,1}^0$ while keeping the number of cross-linkers fixed. The actin unbinds when no cross-linkers connect the filaments for a duration of τ_a , and rebinding events often rescue the actin filament from unbinding if the cross-linkers remodel quickly.

Then, we use a rough estimate of the average time an actin filament is transported by a growing microtubule tip in cases where microtubule catastrophes and actin unbinding play no role. We used preliminary data sets that are part of the data presented in Fig. 5.14AB and Fig. 5.8 together with Eq. 5.7 to estimate the average time $T_e \approx 80\text{s}$ for an actin filament of $l_a = 4\mu\text{m}$ and a microtubule growth velocity of $v_g = 3\mu\text{min}^{-1}$. We hence excluded simulation parameter sets that showed order of magnitude deviations from this value of T_e .

All binding parameters have an influence on the transport time T_e . Increasing the condensation force leads to longer transport times, and a larger condensation force can be created by increasing the binding affinity on the tip compared to the lattice. This can be seen in Eq. 5.23, where changing k , $r_{0,1}^T$, $r_{1,0}^T$, $r_{0,1}^L$ or $r_{1,0}^L$ changes the condensation force. Increasing the number of cross-linkers by altering $r_{1,2}^0$ and $r_{2,1}^0$ also increases the force, since the stronger interaction between the actin filament and the microtubule amplifies the effect of the stronger affinity for the lattice as set by $r_{0,1}^T$ and $r_{1,0}^T$. However, simply increasing the force by increasing the number of cross-linkers is not generally favourable, since it also increases friction between the moving actin filament and the fixed microtubule.

Another set of experiments shows that TipAct has a significant affinity for the microtubule lattice, which we can directly compare to the affinity for the microtubule tip. Specifically, we observe that the intensity of TipAct and EB3 is roughly $R = 20$ times higher on the tip than on the lattice when no actin is present, as shown in Fig. 5.13. This ratio is set by the rates $r_{0,1}^T$, $r_{1,0}^T$, $r_{0,1}^L$ and $r_{1,0}^L$,

$$R = \left(\frac{K_{0,1}^t}{1 + K_{0,1}^t} \right) / \left(\frac{K_{0,1}^\ell}{1 + K_{0,1}^\ell} \right), \quad (5.18)$$

where the equilibrium constants $K_{0,1}^t$ and $K_{0,1}^\ell$ are defined in Eq. 5.20. These same parameters also influence the condensation force, as seen in Eq. 5.23. Hence, the ratio R sets a limit on the condensation force in the limit where $K_{1,2} \rightarrow \infty$,

$$F_{f,max} = \frac{k_B T}{\delta} \log[R] \approx 1.5 \text{ pN}. \quad (5.19)$$

The true force $F_f = 0.10 \text{ pN}$ is more than an order of magnitude lower, since $K_{1,2}$ is far from ∞ using our final parameter set. So far, we have only talked about the effects of the ratios $K_{0,1}$, but we do not have data on the specific rates $r_{0,1}^L$ or $r_{1,0}^L$. Hence, we make a choice that makes $r_{0,1}^L < r_{0,1}^T$ and $r_{1,0}^L > r_{1,0}^T$, but the specific choice has little effect as long as the factors $K_{0,1}$ stay the same.

To gain insight into the rate $r_{2,1}^0$ at which TipAct unbinds from the actin while it remains connected to the microtubule, we use in vitro TIRF measurements of the TipAct fluorescence signal on single actin filaments, as shown in Fig. 5.15A. We find that TipAct barely binds to actin filaments when no microtubule is present, and the binding events that do happen are quickly followed by unbinding events. From measurements with an inter-frame duration of $\Delta T = 33 \text{ ms}$, a mean binding time of $\bar{T} = 111 \text{ ms}$ is deduced (Fig. 5.15A), giving an off-rate of $r_{\text{off}} \approx 9 \text{ s}^{-1}$ from actin without a microtubule present. However, the rate $r_{2,1}^0$ used in the simulations does not simply equal r_{off} . In the simulations, TipAct unbinds from the actin filament but remains bound to a microtubule that is very close. Furthermore, in the experiments shown in Fig. 5.15A, unbinding means that the cross-linker has not only detached but also that it has diffused away, since it is no longer in the proximity of the actin filament. In the simulations, what is required is only a short moment where the cross-linker is not bound, and we consider a quick rebinding to a neighbouring location to be a new binding event. Hence, the binding and unbinding rates in our model will be higher than the r_{off} observed in full (un)binding experiments.

The (un)binding rates for the TipAct on the microtubule tip also require some interpretation. Since the protein is assumed to bind in a complex with EB3, TipAct and EB3 could in principle unbind individually. In the simulations, we consider only a single cross-linker, ignoring the possibility of the complex dissociating. To estimate the (un)binding rates $r_{0,1}^T$ and $r_{1,0}^T$, kinetic data is available on EB1 [148], and on TipAct and EB3 on microtubule tips as shown in Fig. 5.15BC. The binding rate of EB1 to the microtubule tip is $0.15 (\text{nM})^{-1} \text{ s}^{-1}$ [148]. With an EB concentration of 100 nM , we would get a binding rate of 15 s^{-1} . However, we assume that the concentration of the complex equals the (limiting) TipAct concentration, which is 25 nM in our experiments.

For the unbinding rate of the complex from the microtubule tip $r_{1,0}^t$, Fig. 5.15BC shows that we found unbinding rates of 1.8 s^{-1} for EB3 on microtubule tips, 0.8 s^{-1} on microtubule tips associated with actin bundles, 3.1 s^{-1} for TipAct on microtubule tips, and 0.7 s^{-1} for TipAct cross-linked between microtubules and actin bundles. The reported unbinding rate of EB1 from microtubule tips equals 3.4 s^{-1} [148]. We need to assume a higher unbinding rate $r_{1,0}^t$, since a rate of 3.4 s^{-1} makes partial binding very likely and makes it impossible for sites not to be bound. We justify this choice by seeing that this rate is an effective parameter that combines the unbinding of EB3 from the microtubule and of TipAct from EB3. Furthermore, the floppiness of the actin makes the binding of cross-linkers less likely because the actin is occasionally at a distance,

but this flexibility is completely ignored in our model. Hence, we overestimate the likelihood of the fully bound state of the cross-linkers due to our inflexible actin filament, which we can compensate for by increasing $r_{1,0}^t$. Moreover, we have that the rate of 3.4s^{-1} obtained by FRAP measures the effective unbinding rate after possible rebinding events [148], whereas we consider the short-time unbinding events to be separate events, again showing that $r_{1,0}^t > 3.4\text{s}^{-1}$.

The value for the spring constant is also not easily accessible by direct measurements. We choose a value of $2 \times 10^4 \text{ k}_B\text{T}/\mu\text{m}^2$, which is lower than the range of previously reported spring constants $6 \times 10^4 - 3 \times 10^5 \text{ k}_B\text{T}/\mu\text{m}^2$ for other cytoskeletal cross-linking proteins [68, 78, 80] (see Sec. 2.A). This low value accounts for the flexibility of a complex of EB3 dimers and TipAct dimers, and for the floppiness of actin. We chose several values of k going down from $1 \times 10^5 \text{ k}_B\text{T}/\mu\text{m}^2$ (similar to the value obtained for Ase1 in Sec. 2.A) to $1 \times 10^4 \text{ k}_B\text{T}/\mu\text{m}^2$, then varying the binding rates until we find parameter sets that roughly comply with all considerations listed in this section. The value of $k = 2 \times 10^4 \text{ k}_B\text{T}/\mu\text{m}^2$ leads to a parameter set where the effective diffusion constant of the cross-linked actin filament is consistent with the experimental measurements. Lowering the spring constant even more leads to frequent events where the actin filament stochastically moves to $x \sim 1\mu\text{m}$ in the comoving reference, where $x = 0$ is at the front of the growing microtubule tip. An actin filament that sticks so far past the front of the microtubule should be observable in TIRF microscopy. Since we do not observe such events experimentally, we do not lower the spring constant further.

We finally arrive at a set of a parameters that accounts for all the experimental observations, listed in Table 5.1. We find an actin diffusion constant on the microtubule lattice of $D_{\text{eff}} = 0.006\mu\text{m}^2\text{s}^{-1}$ for an actin length of $7\mu\text{m}$, comparable with the experimental values of $0.014(3)\mu\text{m}^2\text{s}^{-1}$ ($l_a = 6.6\mu\text{m}$) and $\bar{D} = 0.009(3)\mu\text{m}^2\text{s}^{-1}$ ($l_a = 7.1\mu\text{m}$). The average transport duration is 90s in simulations for a microtubule growth velocity of $3\mu\text{m}\text{min}^{-1}$ and an actin length of $4\mu\text{m}$, consistent with the experimental value of 80s. With the final parameter set, an actin filament of $4\mu\text{m}$ unbinds from the microtubule roughly 44s after it loses its interaction with the microtubule tip in the simulations, close to the experimental value of 40s observed in the actin diffusion experiments. Finally, our parameter set leads to a factor $R = 26.1$ from Eq. 5.18, which is very similar to the factor 20 measured experimentally.

5.J. ANALYTICAL EXPRESSION FOR CONDENSATION FORCE

The magnitude of the condensation force that drives actin transport by microtubule tips depends on the strength of the interaction between the cross-linkers and the filaments and on the density of binding sites in the overlap between the actin filament and the microtubule tip region. Here we derive an analytical expression for this force.

Because the model does not allow cross-linkers that are only bound to the actin filament, we focus on the binding sites on the microtubule and classify the sites according to their cross-linker binding state, as shown in Fig. 5.16. The state is denoted by 0 if the site is free, 1 if the microtubule site is occupied by a cross-linker that is dangling and not connected to the actin, and 2 if the site is occupied by a cross-linker that is also bound to the actin. We use $r_{i,j}$ for the transition rate from state i to state j , as shown in Fig. 5.3A.

We define the equilibrium constants $K_{i,j}$ between the states through the local detailed balance relation,

$$\begin{aligned} K_{0,1}^\alpha &= \exp(-(\mathcal{F}_1^\alpha - \mathcal{F}_0)/k_B T) = \frac{r_{0,1}^\alpha}{r_{1,0}^\alpha}, \\ K_{1,2} &= \exp(-(\mathcal{F}_2^\alpha - \mathcal{F}_1^\alpha)/k_B T) = \frac{r_{1,2}^0}{r_{2,1}^0} \sqrt{\frac{2\pi k_B T}{k\delta^2}}, \end{aligned} \quad (5.20)$$

where $\alpha \in \{t, \ell\}$ represents the microtubule tip or lattice region, respectively. The equilibrium constants are ratios of partition functions, and are thus related to differences between the free energies \mathcal{F}_i of different binding states i . The process to create a cross-linker in the dangling state 1, where it is bound to the microtubule but not to the actin, depends on the microtubule region α that the cross-linker is binding to. Cross-linkers bind faster and unbind slower from the microtubule tip than from the lattice. However, we assume that the rate to bind to the actin filament is the same for all dangling cross-linkers, independent of the microtubule region they are bound to. Hence, the equilibrium constant $K_{1,2}$ does not depend on α . The rate $r_{0,1}^\alpha$, and hence $K_{0,1}^\alpha$, is proportional to the TipAct concentration in the solution, but we keep this dependence implicit since we do not vary the concentration. Since the cross-linkers act as harmonic springs, a cross-linker bound to a specific binding site on the microtubule can bind to multiple binding sites on the actin filament. We group all these possible binding states into a single state 2. Therefore, the expression for $K_{1,2}$ is a sum over all possible cross-linker binding positions on the actin filament, and we approximate the sum by assuming that there are no interactions between the cross-linkers and that the actin filament is infinitely long,

$$K_{1,2} \approx \sum_{i=-\infty}^{\infty} \frac{r_{1,2}^0}{r_{2,1}^0} \exp\left(-\frac{k(i\delta)^2}{2k_B T}\right) \approx \int_{-\infty}^{\infty} \frac{1}{\delta} \frac{r_{1,2}^0}{r_{2,1}^0} \exp\left(-\frac{kx^2}{2k_B T}\right) dx = \frac{r_{1,2}^0}{r_{2,1}^0} \sqrt{\frac{2\pi k_B T}{k\delta^2}}. \quad (5.21)$$

Here, we make use of our model assumption that the actin filament has lattice spacing δ .

To calculate the condensation force, we consider the case where an actin filament overlaps with both the microtubule lattice and tip regions, such that the front of the actin filament is behind the front of the microtubule, as shown in Fig. 5.16. We assume that there are n_ℓ microtubule lattice sites and n_t microtubule tip sites overlapping with the actin filament, such that the actin filament contains $\ell_a = n_\ell + n_t$ sites. Furthermore, the microtubule has ℓ_ℓ lattice sites and ℓ_t tip sites. For the calculation of the force, we also assume that the cross-linker binding states of different microtubule binding sites are independent, such that the partition function describing the binding state of the full system can be expressed as the product of the local partition functions for each site on the microtubule. The microtubule sites can always be in states 0 and 1, but state 2 is only available when the actin filament overlaps with that site. The local partition function for each microtubule binding site is a sum over the possible binding states of the Boltzmann factors. These factors contain the free energies \mathcal{F}_i , and we make the choice to set the free energy $\mathcal{F}_0 \equiv 0$, giving a Boltzmann factor of 1 for state 0. Using Eq. 5.20, we see that the Boltzmann factors for binding states 1 and 2 are simply products of the equilibrium

constants. Hence, the full partition sum for the system shown in Fig. 5.16 is

$$\mathcal{Z}(n_\ell, n_t) = \left[1 + K_{0,1}^\ell\right]^{\ell_\ell - n_\ell} \left[1 + K_{0,1}^\ell + K_{0,1}^\ell K_{1,2}^\ell\right]^{n_\ell} \left[1 + K_{0,1}^t + K_{0,1}^t K_{1,2}^t\right]^{n_t} \left[1 + K_{0,1}^t\right]^{\ell_t - n_t}. \quad (5.22)$$

The four factors correspond to the $(\ell_\ell - n_\ell)$ lattice sites outside of the actin overlap, the n_ℓ lattice sites within the actin overlap, the n_t tip sites within the actin overlap, and the $(\ell_t - n_t)$ tip sites outside of the actin overlap, as shown in Fig. 5.16A. The condensation force can be calculated as a positional derivative of the free energy $\mathcal{F}(n_\ell, n_t) = -k_B T \log[\mathcal{Z}(n_\ell, n_t)]$, given by Eq. 5.22. The actin filament position x is defined in Fig. 5.3C as the difference between the front of the actin filament and the location on the microtubule where the lattice region turns into the tip region, and Fig. 5.16A shows that this region contains n_t sites that are spaced δ apart. Hence, $n_t = x/\delta$, and since the number of sites on the actin filament ℓ_a is constant, $n_\ell = \ell_a - n_t = \ell_a - x/\delta$. The forward pointing condensation force can thus be calculated as

$$F_f = -\frac{d\mathcal{F}(\ell_a - x/\delta, x/\delta)}{dx} = \frac{k_B T}{\delta} \log \left[\frac{1 + K_{0,1}^\ell}{1 + K_{0,1}^\ell + K_{0,1}^\ell K_{1,2}^\ell} \frac{1 + K_{0,1}^t + K_{0,1}^t K_{1,2}^t}{1 + K_{0,1}^t} \right]. \quad (5.23)$$

We see that the condensation force does not depend on the position of the actin filament x as long as there is a partial overlap with the microtubule tip region. The situation changes when $x > l_t = \ell_t \delta$, such that the actin fully covers the microtubule tip region and sticks out in front of the microtubule. Then, the *forward* pointing condensation force disappears because it is no longer possible for the actin filament to gain binding free energy by increasing the overlap with the microtubule tip. Further forward motion of the actin filament now leads to a loss of the number of binding sites on the microtubule lattice, which comes with a free energy cost. Hence, while the number of tip sites overlapping with the actin filament $n_t = \ell_t$ remains constant, n_ℓ still depends on x as before, and Eq. 5.22 shows that there will be a *backward* pointing condensation force due to the loss of overlap with the microtubule lattice,

$$F_b = -\frac{d\mathcal{F}(\ell_a - x/\delta, \ell_t)}{dx} = \frac{k_B T}{\delta} \log \left[\frac{1 + K_{0,1}^\ell}{1 + K_{0,1}^\ell + K_{0,1}^\ell K_{1,2}^\ell} \right]. \quad (5.24)$$

F_b is negative because all equilibrium constants K are positive. Since the binding affinity of cross-linkers for the microtubule lattice is much lower than for the microtubule tip, $K_{0,1}^\ell \ll K_{0,1}^t$, we have that $|F_b| \ll |F_f|$. Using the parameter values of Table 5.1, we find the values $F_f = 0.10$ pN and $F_b = -4.6$ fN, showing that the backward force is typically irrelevant. The condensation force is plotted as a function of the actin position in Fig. 5.16B. The backward force is only able to move the actin filament when the microtubule is depolymerising, an effect that we confirmed experimentally (see Fig. 5.10B). Depolymerising microtubules have no tip region where EB3 binds strongly, leading to a low number of cross-linkers and thus to a low cross-linker induced friction force. A force in the femtonewton range can easily overcome the viscous friction between the actin filament and the solution, since F_f applied to an actin filament with a diffusion constant of $1 \mu\text{m}^2 \text{s}^{-1}$ would lead to a drift velocity of $-1.1 \mu\text{m} \text{s}^{-1}$.

5.K. CONDENSATION FORCE IN THE OPTICAL TWEezer EXPERIMENTS

In the optical tweezer experiments, the bead plays the role of the actin filament that is transported by the growing microtubule tip region in the actin transport experiments. Below, we theoretically estimate the condensation force associated with the geometry of the optical tweezer experiment. Because TipAct (in complex with EB3) has a much higher affinity for microtubules than for actin filaments, we assume in the simulations of actin transport that TipAct never binds to the actin filament directly, but that it first binds to the microtubule before it can bind to the actin filament. By contrast, TipAct is irreversibly bound to the bead in the optical tweezer experiments, and there is no TipAct in solution. Hence, the only possible binding path is from the dangling state on the bead to a fully connected state between the bead and the microtubule. The two regions of the microtubule then lead to two equilibrium constants describing the affinity for the microtubule, K_t and K_ℓ . A third and final parameter for the system is the density of bound cross-linkers on the bead ρ .

Calculating the free energies relative to the dangling state, such that this state has the Boltzmann factor 1, we derive the force on the bead using a similar method as used to derive Eq. 5.23,

$$F_{f,\text{bead}} = k_B T \rho \log \left[\frac{1 + K_t}{1 + K_\ell} \right]. \quad (5.25)$$

We do not have data to estimate these parameters properly, but we can make an order of magnitude estimate. First, we estimate the density of cross-linkers on the bead ρ . This density represents the number of cross-linkers that is conformationally capable to bind per micrometer of microtubule length. We make the order of magnitude estimate that ρ equals 10% of a fully covered microtubule, $\rho \approx 0.1/\delta$.

To find the equilibrium constants K_t and K_ℓ , we recognise that TipAct binds much more strongly to microtubules than to single actin filaments, since single microtubule tips show a strong fluorescent TipAct signal while single actin filaments do not (see Fig. 5.7). This was previously quantified, reporting dissociation constants of $K_D^t = 67 \text{ nM}$ for the binding between TipAct and microtubule tip regions, and $K_D^a = 5.2 \mu\text{M}$ for the binding between TipAct and actin [146]. We note that K_D^a was probably underestimated in the experiments, because TipAct forms dimers that have two actin binding sites, which likely caused actin filaments to bundle and lead to a higher measured affinity than should be expected for the binding of TipAct to single actin filaments. To find a relation for the parameters K_t and K_ℓ , we use that the equilibrium constant K_t describes the transition to bind from the bead (representing the actin filament) to the microtubule, and $K_{1,2}$ represents the transition to bind from the microtubule to the actin filament. The experimental values set $K_t/K_{1,2} \approx K_D^a/K_D^t = 78$, giving us the order of magnitude $K_t = 100K_{1,2}$ in the simulations. This is likely an underestimation due to the described bias in the value of K_D^a .

Finally, to find K_ℓ , we use that the difference in affinity between the microtubule tip and lattice regions should be the same for the optical tweezer experiments and the actin transport experiments, $K_t/K_\ell = K_{0,1}^t/K_{0,1}^\ell$. Using Table 5.1, we find the force

$$F_{f,\text{bead}} \approx 0.17 \text{ pN}. \quad (5.26)$$

This is the force on the bead when the bead is behind the front of the microtubule and still overlapping with the microtubule tip region. However, when the bead and the microtubule first come into contact, the bead is in front of the microtubule. Then, the condensation force caused by the increasing overlap with the microtubule tip region equals

$$F_{b,\text{bead}} = -k_B T \rho \log[1 + K_t] \approx -0.21 \text{ pN}, \quad (5.27)$$

using the same parameters as before. As shown in Fig. 5.17, we experimentally find a forward force of $F_{f,\text{bead}} \approx 0.2 \text{ pN}$ and a backward force of $F_{b,\text{bead}} \approx -0.7 \text{ pN}$. Hence, we correctly estimate the order of magnitude for these forces, but the ratio between these forces is not well predicted. This may be due to an overestimation of the ratio K_t/K_ℓ , which is in turn due to an overestimation of $K_{0,1}^t/K_{0,1}^\ell$.

5.L. BINDING PROBABILITY SCALES EXPONENTIALLY WITH ACTIN LENGTH

5

In our simulations, we consider the actin filament to be bound to the microtubule as long as there is at least a single cross-linker binding the two filaments together. Here, we obtain an approximate expression for this binding probability using similar expressions as in the derivation of the condensation forces. The probability of having no cross-linkers connecting an actin filament that overlaps with the microtubule tip region over a length y_t and overlaps with the microtubule lattice region over a length y_ℓ , $p_0(y_t, y_\ell)$ defined in Eq. 5.2, equals

$$p_0(y_t, y_\ell) = \left[\frac{1 + K_{0,1}^t}{1 + K_{0,1}^t + K_{0,1}^t K_{1,2}} \right]^{y_t/\delta} \left[\frac{1 + K_{0,1}^\ell}{1 + K_{0,1}^\ell + K_{0,1}^\ell K_{1,2}} \right]^{y_\ell/\delta} = e^{-y_t/\lambda_t} e^{-y_\ell/\lambda_\ell}. \quad (5.28)$$

Here, the discrete numbers of binding sites that overlap with the microtubule tip region and lattice region are approximated as $n_t = y_t/\delta$ and $n_\ell = y_\ell/\delta$, respectively. We recognise that the probability decreases exponentially with both overlap lengths, which allows us to define the length scales λ_t and λ_ℓ ,

$$\lambda_\alpha = \frac{\delta}{\log[1 + K_{0,1}^\alpha + K_{0,1}^\alpha K_{1,2}] - \log[1 + K_{0,1}^\alpha]}, \quad (5.29)$$

with $\alpha \in \{t, \ell\}$ representing the microtubule region again. Using the parameters listed in Table 5.1, we calculate $\lambda_t = 0.038 \mu\text{m}$ and $\lambda_\ell = 0.89 \mu\text{m}$. Since there is a higher density of bound cross-linkers on the microtubule tip than on the lattice, as shown in Fig. 5.13, the probability to have no cross-linkers decays much more rapidly with the overlap length with the tip region than with the overlap length with the lattice region. This explains why the length scale λ_t is much shorter than λ_ℓ .

5.M. KRAMERS THEORY

In Fig. 5.3E we identify that the actin filament needs to cross a free-energy barrier to fall behind the microtubule tip region. Given that we know the free-energy profile and the diffusion constant, we can calculate the rate of these transitions using Kramers theory.

As shown in Fig. 5.3C, x is the position of the front of the actin filament relative to the point on the microtubule where the lattice region ends and the tip region begins. Since the latter point moves with the growing microtubule tip, x constitutes a comoving frame of reference. We call $D(x)$ the effective diffusion constant of the actin filament, and we obtain $D(x)$ by calculating how the overlaps between the actin filament and the microtubule lattice region y_ℓ and between the actin filament and the microtubule tip region y_t change with x . As shown in Fig. 5.3C,

$$\begin{aligned} y_t(x) &= x \mathbb{1}(0 \leq x < l_t) + l_t \mathbb{1}(x \geq l_t), \\ y_\ell(x) &= l_a - x \mathbb{1}(x \geq 0), \end{aligned} \quad (5.30)$$

where we assume that $l_a \gg l_t, x$. Then, we enter these expressions into Eq. 5.2 and Eq. 5.3 to find $D(x) = D(y_t(x), y_\ell(x))$, which is given in Eq. 5.1.

Next, we call $F_{\text{eff}}(x)$ the forward pointing force on the actin filament, given by Eq. 5.4. We integrate this effective force to find the generalised free energy

$$\mathcal{F}(x) = - \int_0^x F_{\text{eff}}(x') dx'. \quad (5.31)$$

The function $\mathcal{F}(x)$ behaves exactly like an equilibrium free energy, even though it describes the non-equilibrium process of microtubule growth and actin transport. This is the result of the comoving frame, in which the free-energy profile loses its time dependence.

Combining the expressions for the diffusion constant and the generalised free energy, and assuming the Einstein relation [28], we find a Fokker-Planck equation for $f_a(x, t)$, the probability density of the actin position x ,

$$\partial_t f_a(x, t) = \partial_x \left[D(x) e^{-\mathcal{F}(x)/k_B T} \partial_x \left(e^{\mathcal{F}(x)/k_B T} f_a(x, t) \right) \right]. \quad (5.32)$$

As shown in Eqs. 5.1–5.4, the free energy is determined by the parameters $D_a, \lambda_t, \lambda_\ell, \zeta_t, \zeta_\ell, F_f$, and F_b . D_a is a parameter in the simulations as well, and we have analytical approximations to the length scales λ_t and λ_ℓ in Eq. 5.29, and for the condensation forward and backward forces F_f and F_b in Eq. 5.23 and Eq. 5.23, respectively. The only fitting parameters are the two proportionality factors ζ_t and ζ_ℓ that show how the friction coefficient scales with the actin length on the microtubule tip and lattice. Direct measurements of the diffusion constant in simulations, shown in Fig. 5.3D, give the values $\zeta_t = 810 \text{ k}_B \text{ Ts}/\mu\text{m}^3$ and $\zeta_\ell = 30.2 \text{ k}_B \text{ Ts}/\mu\text{m}^3$. We emphasise that this set of simulations is independent of the set of simulations in which we estimate the free-energy profile and transport times, which means that we can make independent theoretical predictions on the generalised free-energy profile and on the functional behaviour of the actin transport time. We obtain the rate of actin falling behind the tip using Kramers theory [30] (see Sec. 1.5) based on Eq. 5.32, and the resulting rate is given in Eq. 5.6.

5.N. RATE OF ACTIN UNBINDING

One of the processes by which actin transport ends is by the direct unbinding of the actin filament from the microtubule when it is still in contact with the microtubule tip

region. Here, we develop a theoretical explanation of the unbinding rate observed in the simulations. If the actin filament is at a position $x < 0$, transport will most likely end when the filament falls behind the tip, which we treat as an independent process. Hence, we consider the scenario $x > 0$ for the unbinding rate, such that the actin filament overlaps both with the microtubule lattice region and with the tip region.

The actin filament can only unbind when there are no cross-linkers binding the actin filament. First, the actin filament needs to loose all connections with the microtubule lattice region. Second, the cross-linkers bind very strongly to the microtubule tip region, so the actin can only unbind when the overlap between the actin filament and the tip region almost vanishes, $x \approx 0$. Then, we assume that the rate of unbinding is limited by the probability that both these events happen,

$$r_u \propto \mathbb{P}[\text{no connections lattice} \wedge x \approx 0] = \mathbb{P}[\text{no connections lattice}] \mathbb{P}[x \approx 0 \mid \text{no connections lattice}] \quad (5.33)$$

Here, we use the definition of conditional probability to rewrite the proportionality into two factors, and we will discuss each factor separately.

First, we calculate the probability that no cross-linkers are bound between the actin filament and the microtubule lattice using Eq. 5.28. This probability limits the rate at which the actin filament can unbind in Eq. 5.33, so the unbinding rate decreases exponentially with the actin filament length,

$$r_u \propto e^{-l_a/\lambda_\ell}. \quad (5.34)$$

We only focus on how the unbinding rate is shaped by the actin length l_a and the microtubule growth velocity v_g , since these are the variables we use to compare the transport time between simulations and experiments, and absorb all other effects into the proportionality constant. We use the length scale λ_ℓ here, since elongating a filament at fixed position x only increases the overlap with the microtubule lattice region, not with the tip region.

Then, we require the probability that $x \approx 0$ given that the actin filament has lost its connections with the microtubule lattice region. This probability follows from the free-energy profile $\mathcal{F}(x)$ shown in Fig. 5.3E. Specifically, the peak of the barrier is always located at $x = 0$, while the valley is at $x = l_t$, where l_t is the length of the microtubule tip region. Hence, the probability to find the actin filament close to the peak is given by the free-energy barrier height $\Delta\mathcal{F}^\ddagger = \mathcal{F}(0) - \mathcal{F}(l_t)$,

$$r_u \propto e^{-\Delta\mathcal{F}^\ddagger/k_B T}. \quad (5.35)$$

Eq. 5.31 shows that this free-energy barrier requires integrating the effective force defined in Eq. 5.4. The only term that depends on v_g or l_a is the friction term,

$$F_{\text{eff}}(x) = -\zeta(x) v_g + \dots \quad (5.36)$$

Given that there are no cross-linkers connecting the actin filament to the microtubule lattice, only the overlap with the microtubule tip provides a significant friction coefficient ζ for the actin filament,

$$\zeta(x) \approx \zeta_t x. \quad (5.37)$$

Now, integrating Eq. 5.36 gives us

$$\Delta \mathcal{F}^\ddagger = \frac{1}{2} \zeta_t l_t^2 v_g + \dots \quad (5.38)$$

By combining Eq. 5.34, Eq. 5.35, and Eq. 5.38, we find the actin unbinding rate

$$r_u(v_g, l_a) = r_u^0 e^{-l_a / \lambda_\ell} e^{v_g l \gamma}, \quad (5.39)$$

where the velocity γ is defined as

$$\gamma = \frac{2k_B T}{\zeta_t l_t^2}. \quad (5.40)$$

5.O. ALGORITHMS

WE often need to estimate the mean and variance of a random variable, for example to measure the drift and diffusion constant of the position of the actin filament. For this, we could make use of the simple textbook formulas,

$$\begin{aligned} \bar{x}_{a,b} &= \frac{1}{b-a+1} \sum_{i=a}^b x_i, \\ \bar{V}_{a,b} &= \frac{1}{b-a} \sum_{i=a}^b (x_i - \bar{x}_{a,b})^2, \end{aligned} \quad (5.41)$$

for a set of n data points $\{x_i\}$. The estimate of the mean over all data points with labels between a and b is denoted by $\bar{x}_{a,b}$, and similarly the estimate of the sample variance over those data points is denoted by $\bar{V}_{a,b}$. However, these formulas require all data to be stored, and the calculations of the moments requires to loop through the data twice, once to estimate the mean and once to estimate the variance. Another simple algorithm would be to calculate the sum $\sum_i x_i$ and the sum of squares $\sum_i x_i^2$ in a single loop, after which the square of the sum is subtracted from the sum of squares to find the variance. However, this algorithm is very unstable due to catastrophic cancellation of the floating point precision [159].

To avoid these problems, we use Welford's online algorithm [160], in which we keep track of the quantities

$$\begin{aligned} \bar{x}_{a,b} &= \frac{1}{b-a+1} \sum_{i=a}^b x_i, \\ S_{a,b} &= \sum_{i=a}^b (x_i - \bar{x}_{a,b})^2. \end{aligned} \quad (5.42)$$

Then, given that we receive samples one by one, we use the following rule to update the mean,

$$\bar{x}_{a,b} = \frac{1}{b-a+1} \sum_{i=a}^{b-1} x_i + \frac{1}{b-a+1} x_b = \bar{x}_{a,b-1} + \frac{x_b - \bar{x}_{a,b-1}}{b-a+1}. \quad (5.43)$$

This step uses the old mean $\bar{x}_{a,b-1}$ and the new value x_b to update the estimate of the mean. For a similar update rule for the quantity S , we first make note that Eq. 5.43 implies

$$(x_b - \bar{x}_{a,b}) = x_b - \bar{x}_{a,b-1} - \frac{x_b - \bar{x}_{a,b-1}}{b - a + 1} = \frac{b - a}{b - a + 1} (x_b - \bar{x}_{a,b-1}). \quad (5.44)$$

Then we see

$$\begin{aligned} S_{a,b} &= \sum_{i=a}^{b-1} (x_i - \bar{x}_{a,b})^2 + (x_b - \bar{x}_{a,b})^2 \\ &= \sum_{i=a}^{b-1} \left(x_i - \bar{x}_{a,b-1} - \frac{x_b - \bar{x}_{a,b-1}}{b - a + 1} \right)^2 + (x_b - \bar{x}_{a,b})^2 \\ &= \sum_{i=a}^{b-1} (x_i - \bar{x}_{a,b-1})^2 - 2 \frac{x_b - \bar{x}_{a,b-1}}{b - a + 1} \sum_{i=a}^{b-1} (x_i - \bar{x}_{a,b-1}) \\ &\quad + (b - a) \left(\frac{x_b - \bar{x}_{a,b-1}}{b - a + 1} \right)^2 + (x_b - \bar{x}_{a,b})^2 \\ &= S_{a,b-1} + \frac{1}{b - a + 1} (x_b - \bar{x}_{a,b-1}) (x_b - \bar{x}_{a,b}) \\ &\quad + \frac{b - a}{b - a + 1} (x_b - \bar{x}_{a,b-1}) (x_b - \bar{x}_{a,b}) \\ &= S_{a,b-1} + (x_b - \bar{x}_{a,b-1}) (x_b - \bar{x}_{a,b}). \end{aligned} \quad (5.45)$$

In the third line, we observe that the second sum vanishes by definition of $\bar{x}_{a,b-1}$, and we apply Eq. 5.44 to one factor in both square terms on the fourth line. Hence, we can now update the quantity $S_{a,b}$ as we receive data as well, without having to store all data. We get an estimate of the variance using

$$\bar{V}_{a,b} = \frac{S_{a,b}}{b - a}. \quad (5.46)$$

When running, we sometimes wish to combine data from multiple parts that run concurrently to get a better estimate of the mean and variance. We can use Welford's algorithm as described above for each of those individual parts, but we need a rule for how to combine this data in the end. If we divide the data labelled $\{a, a + 1, \dots, b, b + 1, \dots, c\}$ in two such that we have $b - a + 1$ points in the first set and $c - b$ points in the second set, we can use the following combination rules [159],

$$\begin{aligned} \bar{x}_{a,c} &= \frac{(b - a + 1) \bar{x}_{a,b} + (c - b) \bar{x}_{b+1,c}}{c - a + 1}, \\ S_{a,c} &= S_{a,b} + S_{b+1,c} + \frac{(b - a + 1)(c - b)}{c - a + 1} (\bar{x}_{b+1,c} - \bar{x}_{a,b})^2. \end{aligned} \quad (5.47)$$

The latter update rule can be derived in a similar fashion as Eq. 5.45. In the derivation, we use that

$$\begin{aligned} \bar{x}_{a,c} &= \bar{x}_{a,b} + \frac{c - b}{c - a + 1} (\bar{x}_{b+1,c} - \bar{x}_{a,b}) \\ \bar{x}_{a,c} &= \bar{x}_{b+1,c} - \frac{b - a + 1}{c - a + 1} (\bar{x}_{b+1,c} - \bar{x}_{a,b}). \end{aligned} \quad (5.48)$$

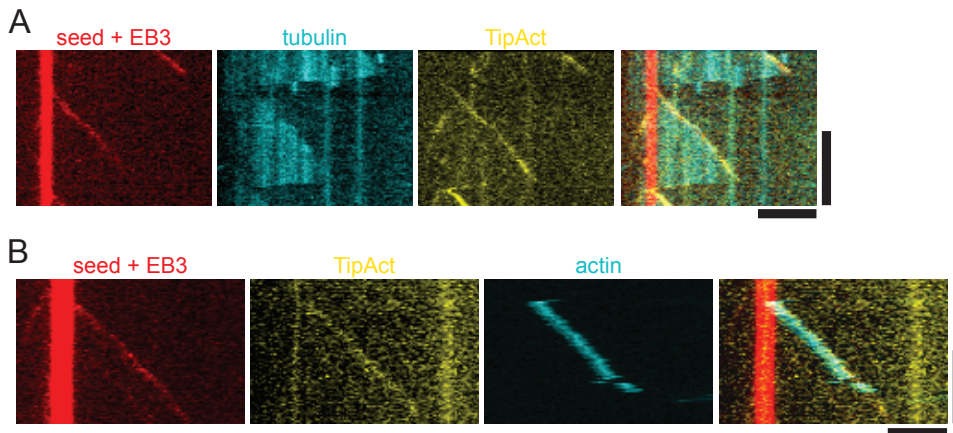


Figure 5.6: TipAct tip-tracks growing microtubule plus ends in the presence of EB3. (A) TipAct in the absence of actin filaments tracks the growing microtubule plus end. Images (left to right) show microtubule seeds and EB3 in red, tubulin in cyan, TipAct in yellow, and the merged image. (B) TipAct is present at the growing microtubule plus end during actin transport events. Images (left to right) show microtubule seeds and EB3 in red, TipAct in yellow, actin filaments in cyan, and the merged image. Note that in this experiment, tubulin is not labelled. Scale bars: $5\ \mu\text{m}$ (horizontal) and 2 min (vertical).

We use these algorithms for estimating the diffusion constant and drift of the actin filament as a function of its position.

ACKNOWLEDGEMENTS

We thank Jeffrey den Haan and Marjolein Vinkenoog for actin purification, and Andrea Martorana for TipAct purification. We thank Michel Steinmetz for the gift of EB3's. We thank Maurits Kok for help with image analysis. We thank Michele Monti for performing an early theoretical analysis. This work was supported by the European Research Council (Synergy grant 609822 to M.D. and A.A.). CA, HW, VAV, PRtW, MD and GHK designed research; HW performed simulations and theoretical analysis; CA performed experiments; MPL performed exploratory and FRAP experiments; VAV performed optical tweezer experiments; CA, HW and VAV analysed experimental data; and CA, HW, VAV, MPL, AA, PRtW, MD and GHK wrote the text.

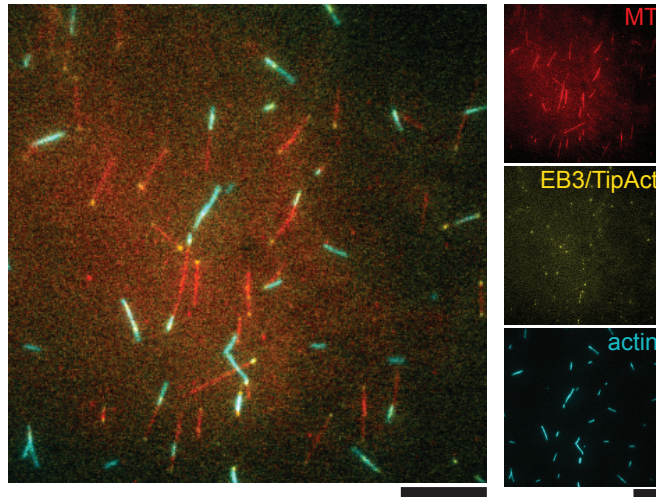
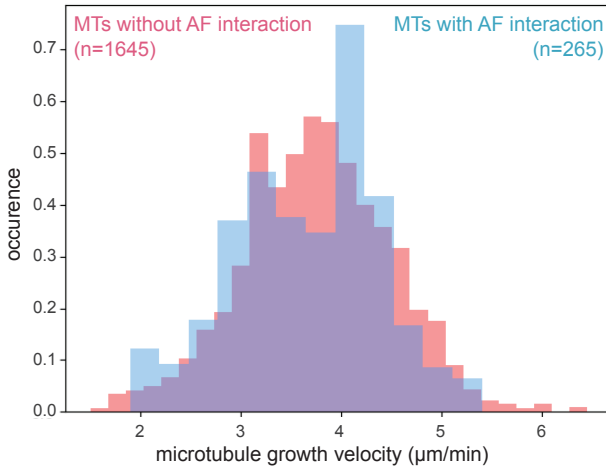


Figure 5.7: Experimental field of view. Typical cropped region that was used for analysis, including microtubules/tubulin (red), EB3 (yellow), TipAct (yellow), and stabilised actin filaments (cyan). We imaged $80\ \mu\text{m}$ by $80\ \mu\text{m}$ regions, and analysed a $54\ \mu\text{m}$ by $54\ \mu\text{m}$ crop in the centre where the illumination is homogeneous. The EB3/TipAct signal is much stronger on the microtubule tip regions than on the actin filaments, justifying our model simplification that TipAct does not bind to actin filaments when no microtubules are present. Left: merged image. Right: the three separate channels, as labelled. Scale bars: $10\ \mu\text{m}$.

A



B

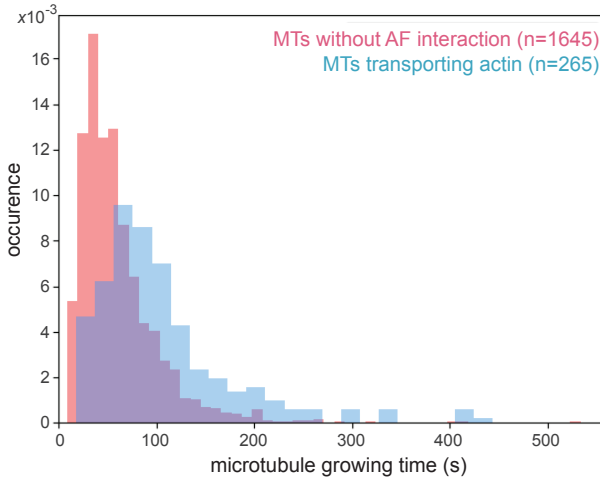


Figure 5.8: Microtubule dynamics. (A) Normalised distribution of microtubule growth velocities for growth events where the microtubule does not interact with actin filaments (red) and for microtubules that transport an actin filament (blue). The average growth velocities are $3.5 \pm 0.6 \mu\text{m min}^{-1}$ and $3.7 \pm 0.7 \mu\text{m min}^{-1}$ for non-interacting and interacting events, respectively. (B) Normalised distribution of microtubule growing times for growth events where the microtubule does not interact with actin filaments (red) and for growth events where microtubules transport an actin filament (blue). Average catastrophe rates of $1.00 \pm 0.03 \text{ min}^{-1}$ and $0.57 \pm 0.03 \text{ min}^{-1}$ for non-interacting MTs and actin-transporting MTs, respectively. Microtubules that quickly undergo a catastrophe have had less time to bind an actin filament, so selecting for microtubules that interact with actin introduces an observation bias, showing only long lived microtubules. This bias can fully explain the difference between the red and blue distributions (data not shown). Number of measured growth events indicated in figure.

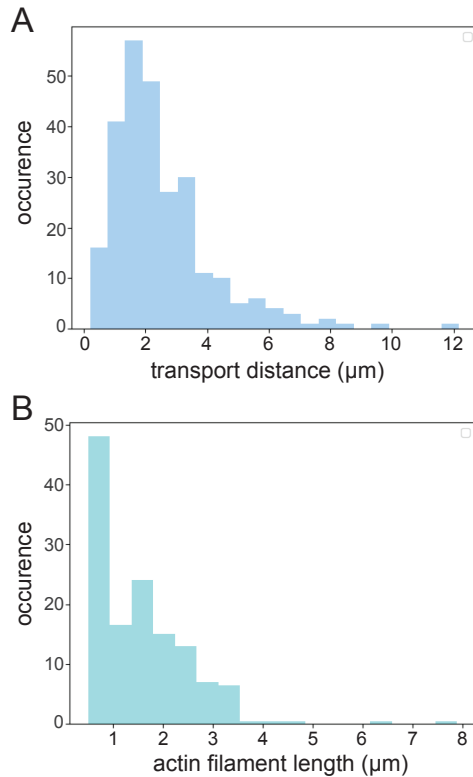


Figure 5.9: Distributions of transport parameters. (A) Distribution of transport distances for actin filaments transported by growing microtubule plus end. Median distance of 2.1 μm (and mean of 2.5 μm) and range of 0.2–12.2 μm . (B) Length distribution of transported actin filaments. Median length of 1.4 μm (and mean of 1.6 μm) and length range of 0.5–7.9 μm long filaments. Note that all filaments shorter than 0.5 μm are binned as 0.5 μm because of the diffraction limit. The maximal length is limited by the tendency of longer filaments to form bundles, which are excluded from further analysis.

Parameter	Value	Sources
Lattice spacing binding sites δ	0.008 μm	literature [76, 107, 153–155]
Microtubule tip size l_t	0.2 μm	imaging
Binding rate to microtubule tip $r_{0,1}^T$	3 s^{-1}	literature [146, 148], transport
Unbinding rate from microtubule tip $r_{1,0}^T$	4 s^{-1}	FRAP, literature [146, 148], transport
Binding rate to microtubule lattice $r_{0,1}^L$	1 s^{-1}	fluorescence, diffusion, transport, unbinding
Unbinding rate from microtubule lattice $r_{1,0}^L$	60 s^{-1}	fluorescence, diffusion, transport, unbinding
Basic binding rate to actin filament $r_{1,2}^0$	75 s^{-1}	diffusion, transport, unbinding
Basic unbinding rate from actin filament $r_{2,1}^0$	300 s^{-1}	diffusion, transport, unbinding
Effective spring constant k	$2 \times 10^4 \text{ k}_B\text{T}/\mu\text{m}^2$	literature [35, 68, 78, 80], diffusion, transport, unbinding
Diffusion constant bare actin filament D_a	1 $\mu\text{m}^2 \text{ s}^{-1}$	viscosity, literature [155–158]
Actin unbinding time τ_a	$5 \times 10^{-3} \text{ s}$	viscosity

Table 5.1: Model parameters, their values used in the simulations, and the sources used for determining the parameter values. As explained in the Sec. 5.I, we use a combination of experimental observations to fit the model parameters, and most of these observables are influenced by multiple parameters. Hence, we manually varied the parameters and searched for a parameter set that is consistent with all experimental observations. The sources that influenced each parameter value are previously published data (literature), direct microscopy observations (imaging), the order of magnitude of the duration of actin transport without the effects of actin unbinding or microtubule catastrophe (transport), fluorescence recovery after photobleaching experiments determining effective unbinding rates (FRAP), experimental observations of the actin diffusion constant (diffusion) or binding duration (unbinding) on the microtubule lattice, and calculations of the viscous drag of the solution on an actin filament (viscosity).

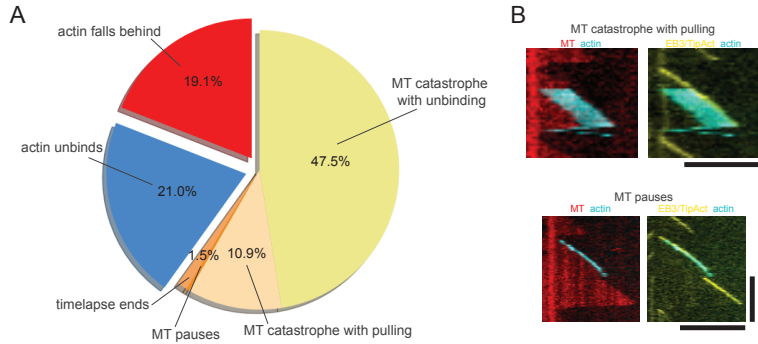


Figure 5.10: Termination of actin transport events at growing microtubule plus end. (A) Categories of termination events together with their frequency ($n=265$). Examples for these events are shown for actin unbinding in Fig. 5.2A, for actin falling behind in Fig. 5.2C, and for the microtubule undergoing a catastrophe in Fig. 5.2B. microtubule catastrophe where the shrinking microtubule pulls the actin filament along in Fig. 5.10B (top), and actin transport ending by microtubule pausing in Fig. 5.10C(bottom). (B) Kymographs showing examples of a shrinking microtubule that pulls an actin filament backwards after the catastrophe (top), and of a microtubule that pauses, upon which the EB3/TipAct comet disappears and the actin unbinds (bottom). Scale bars: $5\ \mu\text{m}$ (horizontal) and $60\ \text{s}$ (vertical).

5

	v_g, T_t		l_a, T_t	
	Corr.	Perm.	Corr.	Perm.
Experiments ($n=265$)	-0.15	0.00 ± 0.06	0.17	0.00 ± 0.06
Selected experiments ($n=103$)	-0.23	-0.01 ± 0.10	0.33	-0.01 ± 0.09
Simulations ($n=60\ 000$)	-0.252	0.000 ± 0.004	0.113	0.000 ± 0.004

Table 5.2: Spearman correlation coefficients show that the transport time decreases with the microtubule growth velocity while it increases with the actin length. By making 100 random permutations of the transport times linked to the growth velocities or the actin lengths, we find the range of Spearman coefficients that can be expected for an uncorrelated data set (mean \pm SD), showing that the measured correlation coefficients are significantly outside of this range. By selecting only those events that end by actin falling behind the microtubule tip region, we find similar correlation coefficients. Finally, we perform the same analysis on the two data sets shown in Fig. 5.4AB. Each data point in those figures is the result of simulating 2000 events, giving 66000 events for the set varying the growth velocity and 60000 events for the set varying the actin length. The correlation coefficient between the transport time and the growth velocity obtained in the simulations is comparable to the correlation coefficient found in experiments, while the correlation coefficient between the transport time and the actin length agrees in the sign, but is lower in magnitude for the simulations than for the experiments. The reason for this discrepancy is that the simulation data extends to larger actin lengths where the transport time decreases again.

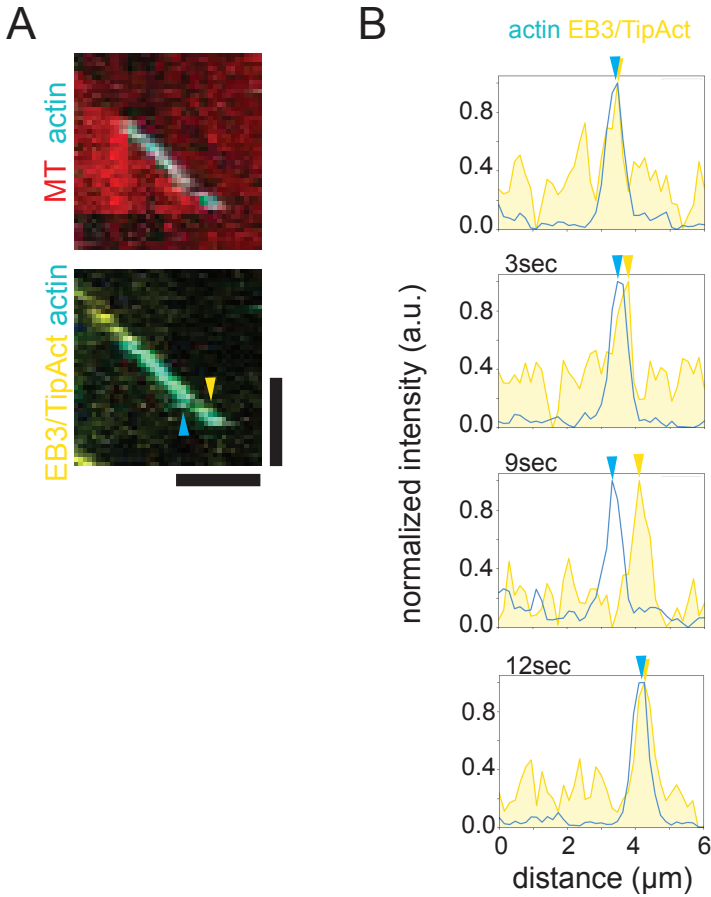


Figure 5.11: Catching-up of actin filament to tip-tracking-complex. (A) Kymograph showing a growing microtubule (red), the tip-tracking-complex consisting of EB3 and TipAct (yellow), and a transported actin filament (cyan). At one point, the actin filament (cyan arrow) falls behind the tip (yellow arrow), but remains at the microtubule lattice and quickly catches up with the tip-tracking-complex again to continue transport. (B) Line profiles along the kymograph in (A), showing an actin filament catching up with the tip-tracking-complex. Arrows indicate the locations of the actin filament (cyan) and of the tip-tracking-complex (yellow). Scale bars: $3\ \mu\text{m}$ (horizontal) and 60 s (vertical).

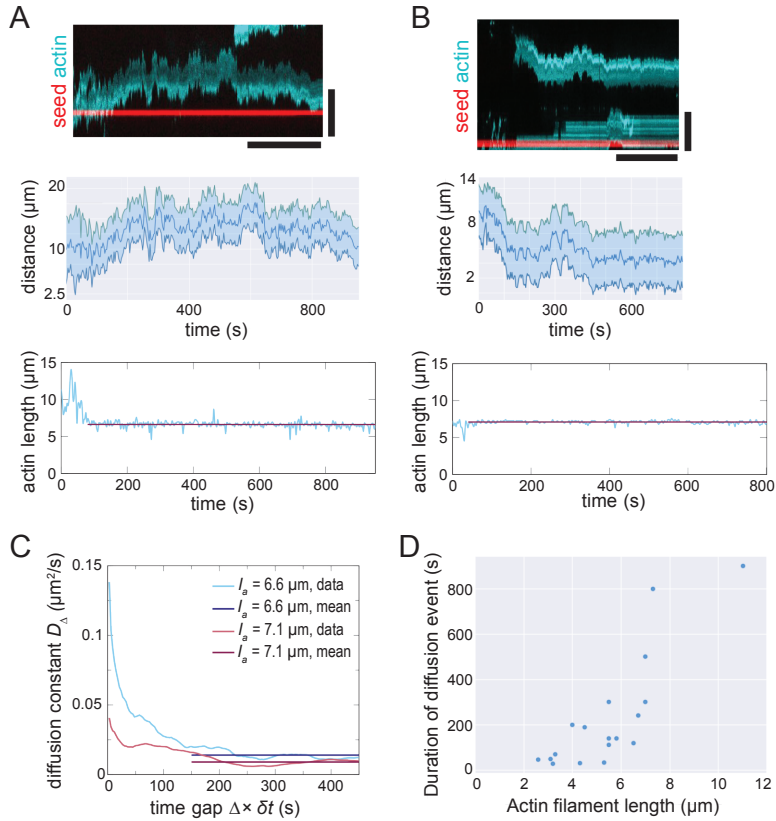


Figure 5.12: Diffusion of actin filaments along the microtubule lattice. (A) Diffusion of 7.1 μm long actin filament along the microtubule lattice in a kymograph (top), corresponding time trace of the filament front and rear end positions (middle), and the filament length fluctuations used to determine the actin length (bottom). (B) Another example, showing diffusion of a 6.6 μm long actin filament. (C) Diffusion constant estimates given by Eq. 5.15. For small time scales, the observed actin position fluctuations are influenced by external noise and length fluctuations, so we can only extract the diffusion constant at large time scales. We take the sample mean of the estimator over the window between 150 s and 450 s, yielding $\bar{D} = 0.014(3) \mu\text{m}^2 \text{s}^{-1}$ ($l_a = 6.6 \mu\text{m}$) and $\bar{D} = 0.009(3) \mu\text{m}^2 \text{s}^{-1}$ ($l_a = 7.1 \mu\text{m}$). (D) The typical duration of diffusion events increases with the actin filament length, since the rate at which the actin filament unbinds from the microtubule lattice region decreases with the number of cross-linkers that connect the two filaments. Scale bars: 5 min (horizontal), 10 μm (vertical).

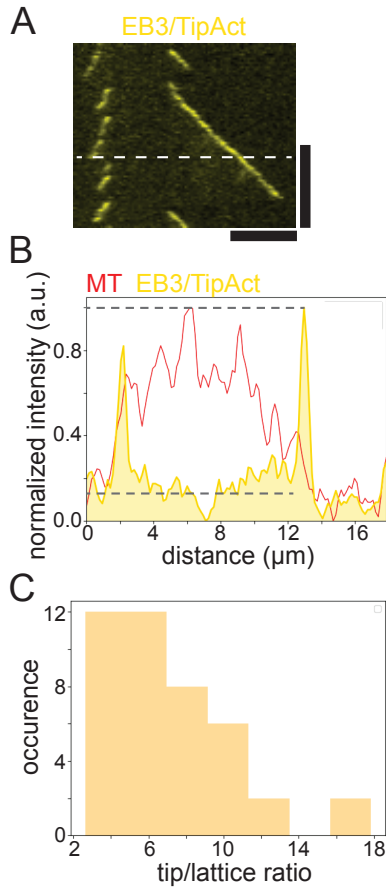


Figure 5.13: Ratio between the fluorescence signal of EB3 and TipAct on the microtubule tip and on the lattice. (A) Example kymograph showing the GFP signal of EB3 and TipAct, from which tip/lattice-ratios can be calculated. The dashed line was used to produce an intensity profile. (B) Intensity profile showing the lattice (red) and plus end intensity of EB3 and TipAct (yellow). Dashed lines on the profile, showing the maximum value and the mean value along the microtubule lattice for GFP, were used to estimate the 1:10 lattice:tip ratio of the EB3/TipAct-complex. (C) Distribution of ratios for 40 analysed profiles of EB3/TipAct intensity while transporting an actin filament. Scale bars: 5 μm (horizontal) and 2 min (vertical).

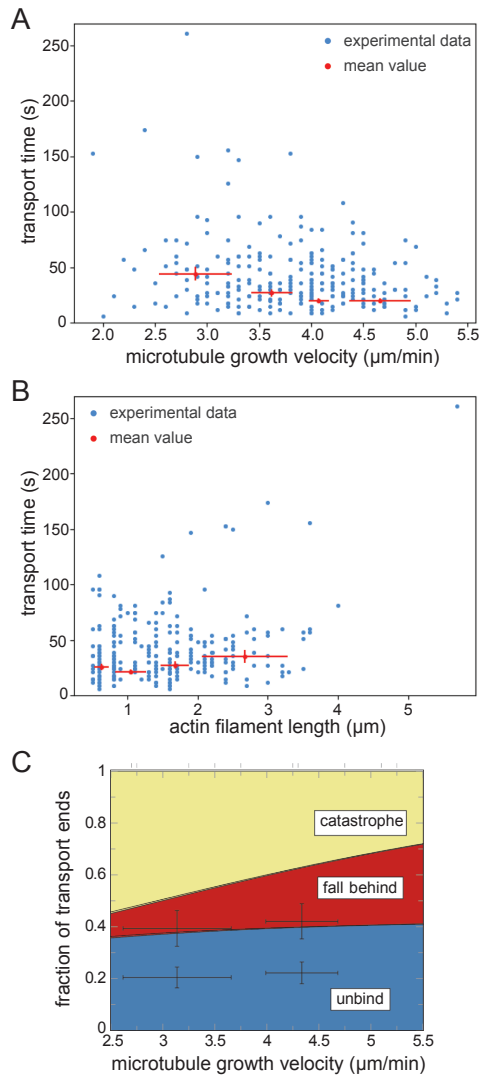


Figure 5.14: Raw and binned data for actin transport. (A) The transport time versus the microtubule growth velocity and (B) the transport time versus the actin filament length. Single data points are shown in blue; binned experimental means (when distributing data in 4 bins of equal size) are shown in red. Horizontal error bars represent the standard deviation of the growth velocities or the actin filament length within the bin, and vertical error bars represent the standard deviation of the mean transport time. (C) The fractions of the categories of transport ends as a function of the microtubule growth velocity. The fractions were calculated from theoretical values of the catastrophe rate (constant r_c), falling behind rate (Eq. 5.6) and unbinding rate (Eq. 5.5). Experimental data was binned into two bins of equal size, shown as points with errors. Transport events ending by microtubule catastrophes include both events where actin is pulled back with the depolymerising microtubule and events where the actin unbinds upon a catastrophe. The horizontal error bars show the weighted standard deviation of the microtubule growth velocity and of the actin filament length, and the vertical error bars show the standard error of the estimated mean ratio. Since we have to estimate two data points per bin with sufficient statistics, we only divided the growth velocities and actin lengths into two bins.

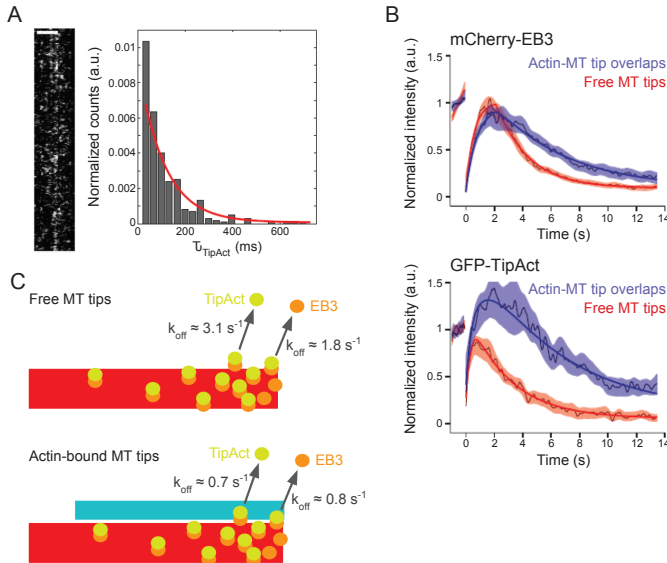


Figure 5.15: Binding dynamics of the tip-tracking complex. (A) TipAct single-molecule dwell times on actin filaments. High temporal resolution kymograph (33 ms/frame) of TipAct molecules showing multiple binding and unbinding events at a surface-bound actin filament, and a normalised distribution of TipAct dwell times (right), including single-exponential fit (red curve) which yielded an average dwell time of (111 ± 6) ms ($n=301$). (B) FRAP experiments to probe protein off-rates at microtubule plus-ends. We analyse the recovery curves for mCherry-EB3 (top) and GFP-TipAct (bottom) at both free (red) and actin-bound (blue) microtubule tips. The solid lines show fits, and the thin coloured lines and shaded areas show the average curves and SEM for $n=19$ (free) and $n=13$ (actin-bound) recovery profiles for mCherry-EB3, and $n=7$ (free) and $n=6$ (actin-bound) recovery profiles for GFP-TipAct, respectively. Note that the maximum recovery intensity of GFP-TipAct at actin-bound microtubule tips reaches values larger than one due to the variable amount of GFP-TipAct that can localise to the F-actin bundles independently of microtubules. (C) Schematics to interpret the FRAP experiments. Top, showing the unbinding rates for EB3 and TipAct at free microtubule plus ends. Bottom, showing the unbinding rates for EB3 and TipAct at actin-bound microtubule plus ends.

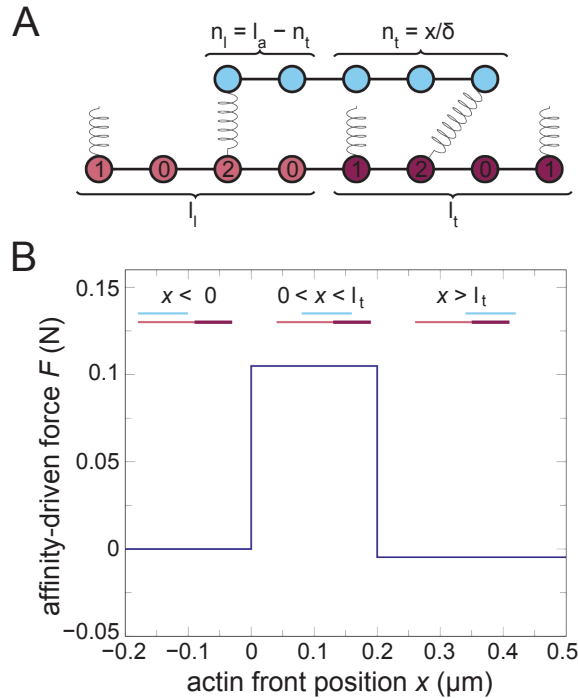


Figure 5.16: (A) Parameter definitions for analytically calculating the condensation force. ℓ_ℓ is the number of binding sites in the microtubule lattice region, and ℓ_t is the number of binding sites in the microtubule tip region. The actin filament contains ℓ_a binding sites, which are split into n_ℓ sites that overlap with the microtubule lattice and n_t sites that overlap with the microtubule tip. The actin position x , defined as the distance between the front of the actin filament and the back of the microtubule tip region (see Fig. 5.3C), equals $n_t \times \delta$, where δ is the lattice spacing between binding sites. We describe the full configuration of all cross-linkers by labelling each microtubule binding site with its binding state: no cross-linker is bound (0), a dangling cross-linker is bound (1), or a cross-linker is bound that connects with the actin (2). To calculate the condensation force, we take into account all possible extents to which the cross-linker can stretch. (B) The condensation forces for the parameters given in Table 5.1. No condensation force exists when the actin filament is fully behind the microtubule tip region, but a forward force is generated when the filament overlaps partially with the microtubule tip region. When the front of the actin filament passes the front of the microtubule, the forward force disappears, but a small negative condensation force still exists, because the actin filament loses its overlap with the microtubule lattice region.

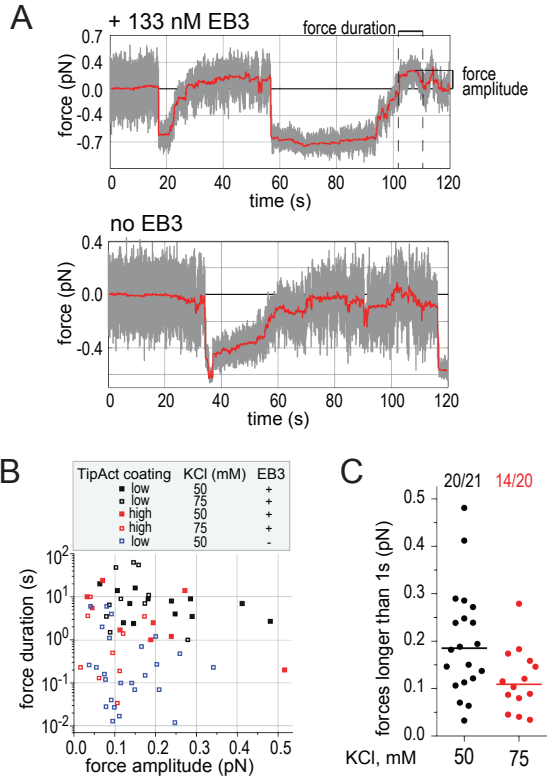


Figure 5.17: Additional force measurements. (A) Examples of full recordings of TipAct-coated beads interacting with growing microtubule ends in presence or absence of EB3. (B) Distributions of the duration and amplitude of forces obtained in conditions indicated in the legend. In absence of EB3, most forward force events last shorter than 1 s. (C) Distribution of force amplitudes for signals longer than 1 s, comparing two different salt concentrations, with (0.20 ± 0.11) pN for 50 mM and with (0.12 ± 0.07) pN for 75 mM (mean \pm SD). For the transport assays, we used 75 mM KCl. Straight line is the median (0.19 pN for 50 mM KCl and 0.11 pN for 75 mM KCl). The numbers above the bins indicate the fraction of force signals included in the distribution out of all signals regardless of their duration.

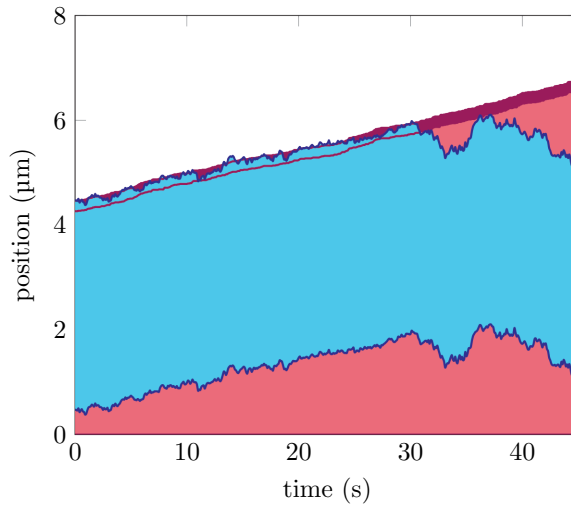


Figure 5.18: Actin transport also occurs when tip sites hydrolyse stochastically, resulting in an exponentially decaying density of tip sites. New sites are added with a rate of 6.25 s^{-1} (microtubule growth velocity of $v_g = 3\text{ }\mu\text{m min}^{-1}$) and all tip sites decay to lattice sites with a rate of 0.25 s^{-1} . These values lead to a density of tip sites that decays exponentially with a length scale of $0.2\text{ }\mu\text{m}$. The other parameter values are listed in Table 5.1.

6

ENERGETIC CONSTRAINTS ON FILAMENT MEDIATED MEMBRANE POLARISATION

Cell polarisation is an essential process for the function and development of many cell types and organisms, for example for the unicellular organisms budding yeast and fission yeast. These cells utilise cytoskeletal structures to transport proteins to one location on the membrane and create a high density spot of membrane-bound proteins. We investigate if active transport alone can establish a polarised protein distribution on the membrane, and quantify the free-energy cost of creating this non-equilibrium steady state. Using a minimal model, we find that next to active transport, detailed balance can also be broken by the shuttling of proteins between the filament, membrane, and cytosol, and the model predicts that this driven binding dynamics dissipates orders of magnitude less free-energy than active transport to create the same membrane spot. Active transport along filaments may be sufficient to create a polarised distribution of membrane-bound proteins, but an additional chemical modification cycle of the proteins themselves is more efficient and less sensitive to the physical exclusion of proteins on the transporting filaments, providing insight in the design principles of the Pom1/Tea1/Tea4 system in fission yeast and the Cdc42 system in budding yeast.

Cell polarisation is a common motif for establishing different cellular functions and for cell development, in which a cell generates a distinct front and back. For example, cells that perform unidirectional movement need to polarise along a single axis [161]. Lophotrichous bacteria require the placement of multiple flagella on one side of the cell, and crawling eukaryotic cells need to polarise their cytoskeleton to create a protrusive leading edge on one side and a contractile trailing edge on the opposite side of the cell [105, 162]. Moreover, epithelial cells are polarised to distinguish the apical and basal sides [161, 162], and asymmetric cell division requires cell polarisation along the division axis to create different fates for the daughter cells [161, 163]. For instance, budding yeast requires the formation of a bud on one spot on its cell membrane [20]. Similarly, fission yeast remains polar after cell division, primarily growing at the old pole initially [20].

Because cell polarisation is an essential cellular feature, many different biological processes exist that induce cell polarisation [164]. A large class of such processes involves the cytoskeletal filaments [165], because both microtubules and actin filaments have an intrinsically polar structure by which they can act as tracks for the directional transport of cargoes by motor proteins. Because the cytoskeleton itself is often asymmetrically organised, for example in the mitotic spindle, these structures can be used to guide other proteins into a polarised state [162]. For example, motor proteins that walk on central spindle microtubules can transport proteins such as the RHO activator ECT2 [105] towards the membrane, where they can promote the formation of the cytokinetic ring. In budding yeast, the small GTPase of the Rho family Cdc42 is bound to the membranes of vesicles that are delivered to the membrane along actin cables [20, 166], which may produce cell polarisation. Furthermore, fission yeast uses microtubule based transport to place the proteins Tea4 and Tea1 at the membrane, where Tea4 forms a complex with Dis2 and dephosphorylates the DYRK family kinase Pom1, which subsequently binds to the membrane [19, 20]. Once Pom1 is on the membrane, it autophosphorylates and unbinds again, leaving a steady state distribution of Pom1 on the membrane in the neighbourhood of the microtubule tips [19].

The transport of vesicle-bound Cdc42 in budding yeast shows that active transport can play a role in creating a high density of proteins in one spot on the membrane [20, 166]. In contrast, the organism fission yeast does not directly transport Pom1, but it uses (de)phosphorylation to drive the protein through a chemical modification cycle where it binds to the membrane preferably near the positions of the microtubule tips where Dis2 is present [19, 20]. Here, we investigate which of these two mechanisms, active transport along a filament or the chemical driving of a binding cycle catalysed by the cytoskeleton, is more efficient in creating a polarised distribution of proteins on the membrane. Because a polarised state corresponds to a non-equilibrium distribution of the protein, the maintenance of this distribution requires the constant dissipation of chemical free energy, usually in the form of NTP hydrolysis. To assess the efficiency of both active transport and driven chemical modification in creating a polarised protein distribution, we take into account the chemical free-energy dissipation of each process. Such energetic constraints are typically excluded when discussing cellular pattern formation, but they are important because they provide a quantitative measure by which we can compare different mechanisms for polarising a cell. Using a minimal model in which both transport along a filament and non-equilibrium binding can lead to cell polarisation, we

will show that transport alone can be sufficient for creating a polarised spot on the membrane, but that a chemical modification cycle of the protein itself can dissipate orders of magnitude less free energy to achieve the same quality of polarisation. This may explain why many cell polarisation systems, including the Cdc42 system in budding yeast and the Pom1 system in fission yeast, contain a chemical modification cycle.

6.1. MINIMAL MODEL FOR MEMBRANE SPOT FORMATION

Inspired by the cell polarisation systems in fission yeast and budding yeast, we create an analytically solvable minimal model in which a filament can transport proteins and where the proteins bind to a membrane patch at the end of the filament. We consider a single stable filament that is perpendicular to the cell membrane, as shown in Fig. 6.1. All model parameters are shown and explained in Fig. 6.1. We do not model the entire cell, but only a finite volume around the filament, because diffusion will smooth out the protein distributions sufficiently far from the filament. By choosing a cylindrical shape for this volume, we can find analytical solutions for the probability densities in each part of the system. The membrane patch is located on one side of the cylinder, so the proteins can be on the membrane, on the filament, or in the cytosol (bulk). Crucially, the particles are transported along the filament towards the membrane, and because the filament is in direct contact with the membrane, particles can transition between the membrane and the filament. Additionally, we include transitions between bulk and the filament and between the bulk and the membrane. Hence, a particle flux can exist that moves from the bulk along the filament to the membrane, and from there back to the bulk. The transition pathways between the three system parts are memoryless, and we include the microscopic reverse reaction for each transition such that the free-energy dissipation in the system remains finite. These transitions can be out of equilibrium by coupling the chemical reactions to a non-equilibrium NTP bath, such that the binding rates alone break detailed balance and cause a flux of proteins from the bulk to the filament, to the membrane, and back to the bulk again. This mechanism can act independently from and concurrently with active transport to create a polarised distribution of membrane-bound proteins. In the following sections, we will first keep the binding reactions in equilibrium to assess how efficiently the non-equilibrium distribution on the membrane is maintained by active transport along the filament. Subsequently, we will also take into account the effects of a non-equilibrium binding cycle.

We use cylindrical coordinates (s, z) , where the radial distance s runs from the filament radius r to the container radius R , and the longitudinal coordinate z runs from 0 to the filament length L . Because the system is rotationally symmetric, the resulting concentration profiles will be too, and we do not require the azimuth. Having a finite microtubule radius eases the mathematics of membrane-filament transitions compared to a one dimensional microtubule, by avoiding unphysical divergences of the protein densities. We model the dynamics of the system in time t by a set of coupled Fokker-Plank equations for the protein densities $f(z, t)$, $m(s, t)$ and $b(z, s, t)$, which cover the filament, the membrane and the bulk, respectively.

To make the equations analytically tractable, we first consider a system with a large bulk diffusion constant $D_B \rightarrow \infty$, which smears out density fluctuations and turns the

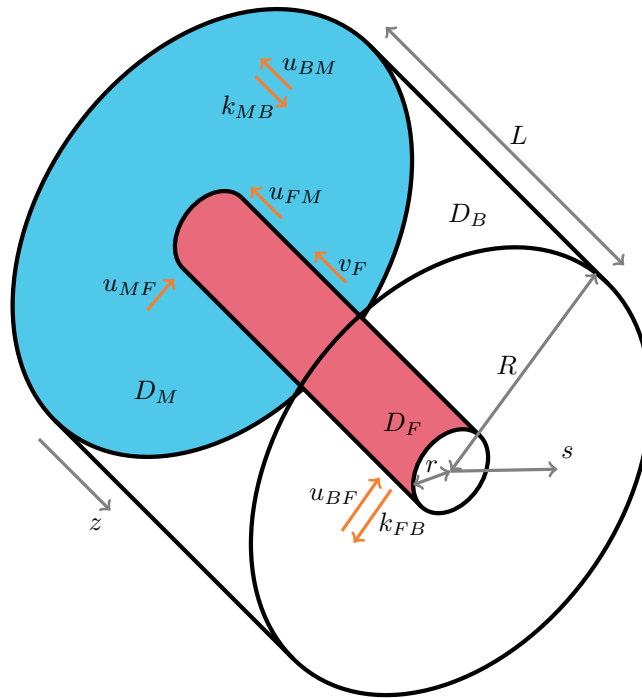


Figure 6.1: Minimal model to investigate how protein transport along a filament can create a polarised distribution of membrane bound proteins. We consider a subvolume of a cell in the shape of a closed cylinder with radius R , with a circular patch of the membrane on one side (blue). A finite filament (red) with a radius r and a length L is located in the centre of the cylinder, perpendicular to the membrane. We consider a single protein species that can be membrane bound (M), dissolved in the bulk (B), or connected to the filament by motor proteins (F). In each of these parts, the particles diffuse with diffusion constants D_M , D_B , and D_F , respectively, and on the filament the motor proteins provide an average drift velocity v_F towards the membrane. The particles can unbind from the membrane and the filament with the Markovian rates k_{MB} and k_{FB} . The corresponding reverse binding transitions can occur when a particle that is dissolved in the bulk is in contact with the membrane or the filament, and the transition rates u_{BM} and u_{BF} have the dimensions of a velocity, not of a rate. Finally, a particle that is bound to the filament and in contact with the membrane can transition to the membrane with a rate u_{FM} that is possibly different from u_{BM} , and similarly the particle can bind from the membrane to the filament with a rate u_{MF} that can be different from u_{BF} . We define a coordinate system with z longitudinal to the filament, such that the membrane is at $z = 0$, and with s as the radial distance, with the microtubule surface at $s = r$.

bulk field into a single concentration,

$$b(z, s, t) = b(t). \quad (6.1)$$

The partial differential equations for the protein concentrations read

$$\partial_t f(z, t) = D_F \partial_z^2 f(z, t) + v_F \partial_z f(z, t) - k_{FB} f(z, t) + 2\pi r u_{BF} b(t), \quad (6.2)$$

$$\partial_t m(s, t) = D_M \frac{1}{s} \partial_s (s \partial_s m(s, t)) - k_{MB} m(s, t) + u_{BM} b(t), \quad (6.3)$$

$$\begin{aligned} V \partial_t b(t) = & \int_0^L [k_{FB} f(z, t) - 2\pi r u_{BF} b(t)] dz \\ & + \int_r^R 2\pi s [k_{MB} m(s, t) - u_{BM} b(t)] ds, \end{aligned} \quad (6.4)$$

where we define volume of the bulk V ,

$$V = \pi (R^2 - r^2) L. \quad (6.5)$$

Here, the filament density $f(z, t)$ represents the protein concentration per unit length along the filament, which is the density per unit surface area of the filament multiplied by the angular factor $2\pi r$. Hence, we will use units μm^{-1} for f , μm^{-2} for m , and μm^{-3} for b . The boundary conditions of the partial differential equations are set by the conservation of the number of particles and by the transition rates between the filament and the membrane, which provide relations for the fluxes on the filament and on the membrane at their edges,

$$[D_F \partial_z f(z, t) + v_F f(z, t)]_{z=0} = u_{FM} f(0, t) - 2\pi r u_{MF} m(r, t), \quad (6.6)$$

$$[D_F \partial_z f(z, t) + v_F f(z, t)]_{z=L} = 0, \quad (6.7)$$

$$[D_M 2\pi s \partial_s m(s, t)]_{s=r} = -u_{FM} f(0, t) + 2\pi r u_{MF} m(r, t), \quad (6.8)$$

$$[D_M 2\pi s \partial_s m(s, t)]_{s=R} = 0. \quad (6.9)$$

The system is greatly simplified by studying it in steady state, setting all time derivatives in Eqs. 6.2, 6.3, and 6.4 to zero and eliminating t as a variable. In steady state, integrating over Eqs. 6.2 and 6.3 and applying the boundary conditions shows that Eq. 6.4 becomes linearly dependent on Eqs. 6.2 and Eq. 6.3. The linear dependence is a consequence of the conservation of particles, which imposes that steady state fluxes have to loop back to their origin. Hence, we omit Eq. 6.4 from the steady state equations. Additionally, it is helpful to make the equations non-dimensional by defining the following dimensionless variables,

$$\begin{aligned} \alpha &= \frac{v_F}{\sqrt{D_F k_{FB}}}, & \beta &= \frac{u_{FM}}{\sqrt{D_F k_{FB}}}, & \gamma &= \frac{u_{MF}}{\sqrt{D_M k_{MB}}}, \\ \delta &= \frac{u_{MF} k_{FB} u_{BM}}{u_{FM} u_{BF} k_{MB}}, & \lambda &= \sqrt{\frac{k_{FB}}{D_F}} z, & \Lambda &= \sqrt{\frac{k_{FB}}{D_F}} L, \\ \sigma &= \sqrt{\frac{k_{MB}}{D_M}} s, & \rho &= \sqrt{\frac{k_{MB}}{D_M}} r, & P &= \sqrt{\frac{k_{MB}}{D_M}} R. \end{aligned} \quad (6.10)$$

We also rescale the density fields to make them dimensionless,

$$\begin{aligned}\varphi(\lambda) &= \frac{k_{FB}}{2\pi r u_{BF} b} f\left(\sqrt{\frac{D_F}{k_{FB}}}\lambda\right), \\ \mu(\sigma) &= \frac{k_{MB}}{u_{BM} b} m\left(\sqrt{\frac{D_M}{k_{MB}}}\sigma\right).\end{aligned}\quad (6.11)$$

Using these definitions and the steady state condition, Eq. 6.2 and Eq. 6.3 become

$$\partial_\lambda^2 \varphi(\lambda) + \alpha \partial_\lambda \varphi(\lambda) - \varphi(\lambda) + 1 = 0, \quad (6.12)$$

$$\frac{1}{\sigma} \partial_\sigma (\sigma \partial_\sigma) \mu(\sigma) - \mu(\sigma) + 1 = 0. \quad (6.13)$$

Using the dimensionless variables, the boundary conditions become

$$[\partial_\lambda \varphi(\lambda)]_{\lambda=0} + \alpha \varphi(0) = \beta (\varphi(0) - \delta \mu(\rho)), \quad (6.14)$$

$$[\partial_\lambda \varphi(\lambda)]_{\lambda=\Lambda} + \alpha \varphi(\Lambda) = 0, \quad (6.15)$$

$$[\partial_\sigma \mu(\sigma)]_{\sigma=\rho} = -\frac{\gamma}{\delta} (\varphi(0) - \delta \mu(\rho)), \quad (6.16)$$

$$[\partial_\sigma \mu(\sigma)]_{\sigma=P} = 0. \quad (6.17)$$

6

The general solutions of the ordinary differential equations Eq. 6.12 and Eq. 6.13 are found by solving the homogeneous equations, and adding the particular solutions $\varphi(\lambda) = 1$ and $\mu(\sigma) = 1$. The full solutions read

$$\varphi(\lambda) = 1 + C_1 \exp\left[-\frac{\lambda}{2}(\sqrt{4 + \alpha^2} + \alpha)\right] + C_2 \exp\left[\frac{\lambda}{2}(\sqrt{4 + \alpha^2} - \alpha)\right], \quad (6.18)$$

$$\mu(\sigma) = 1 + C_3 K_0(\sigma) + C_4 I_0(\sigma). \quad (6.19)$$

Here, $I_0(\sigma)$ and $K_0(\sigma)$ are the modified Bessel functions of the first and second kind, respectively. The integration constants C_1 , C_2 , C_3 , and C_4 are determined by Eq. 6.14–6.17, and are listed in Sec. 6.A. We can simply recover the protein density fields in the dimensionful representation by using the dimensionless exact solutions and substituting back the expressions listed in Eq. 6.10, providing exact solutions for the protein densities and for the protein flux in the case of $D_B \rightarrow \infty$.

Instead of the fourteen parameters of the full model, the dimensionless model with fast bulk diffusion only contains seven independent parameters. Three of those parameters set the system size (ρ , P , and Λ), and the four remaining independent parameters (α , β , γ , and δ) set the system dynamics. Of these, β and γ determine how fast the particles transition between the membrane and the filament.

The parameters α and δ describe the non-equilibrium nature of the system. When $\alpha = 0$ and $\delta = 1$, we find that $C_1 = C_2 = C_3 = C_4 = 0$, and the particle densities reach their equilibrium values

$$\varphi_{\text{eq}}(\lambda) = 1, \quad (6.20)$$

$$\mu_{\text{eq}}(\sigma) = 1. \quad (6.21)$$

When the system is out of equilibrium, a steady-state flux can exist that on average brings particles from the bulk to the filament, from the filament to the membrane, and from the membrane back to the bulk. Eqs. 6.14–6.16 show that this flux is proportional to

$$J_{ss} \propto \varphi(0) - \delta \mu(\rho). \quad (6.22)$$

Using the exact solution, it can be shown that this flux vanishes if and only if $\alpha = 0$ and $\delta = 1$, so these parameters determine whether detailed balance holds. Because α and δ can be varied independently, the model contains two essential processes by which detailed balance can be broken. Firstly, a positive value of α represents a drift velocity on the filament, as shown in Eq. 6.10. Here, motor proteins on the filament drive the particles and create a flux through the system, where particles bind from the bulk to the filament, are driven towards the membrane to which they bind, diffuse on the membrane moving away from the filament, and finally fall off into the bulk again. Secondly, the value of δ , defined in Eq. 6.10, describes the extent to which membrane and filament binding are in or out of equilibrium. The particle itself can undergo a chemical modification step along the cycle filament-membrane-bulk-filament, which is driven by the dissipation of chemical free energy and leads to a value $\delta < 1$. For example, a protein may exist in several phosphorylation states, such as fission yeast Pom1 which has a high affinity for the membrane when it is dephosphorylated at microtubule tips, but quickly unbinds from the membrane when it is rephosphorylated there [19]. If an NTP molecule is hydrolysed at any step in the forward direction of the filament-membrane-bulk-filament cycle, the model shows that a membrane spot is formed independent of whether particles are actively transported along the filament. There are thus two distinct mechanisms that can act independently to create a polarised distribution of membrane proteins.

The parameter α describes how fast the particles are driven on the filament,

$$\alpha = \frac{v_F}{k_{FB}} / \sqrt{\frac{D_F}{k_{FB}}} = l_v / l_D. \quad (6.23)$$

Here, l_v is the average distance that a particle travels on the filament before it unbinds when it moves with a drift velocity v_F , and l_D sets a length scale over which diffusion smooths out the profile of the particle density on the filament $f(z)$. Hence, α measures how much the particle density is shaped by the drift velocity. In Fig. 6.2, we show that the particle distribution on the filament is reshaped more strongly when α increases. Particles are transported from the right to the left, where the membrane is located at $\lambda = 0$. In the centre of the filament, the rate at which particles bind from the bulk equals the rate at which particles unbind from the filament, and transport of particles coming in from the right equals the transport out to the left. Hence, the particle density is simply the equilibrium density there. However, within a distance λ_{binding} from the end of the filament ($\lambda = \Lambda$), the particle density decreases because no particles can be transported from beyond Λ while particles are still transported towards the left. Similarly, within a distance $\lambda_{\text{crowding}}$ from the membrane ($\lambda = 0$), the particle density peaks because transport brings in particles from the right while they cannot be transported further to the left. As shown in Eq. 6.18, the two dimensionless length scales are given by

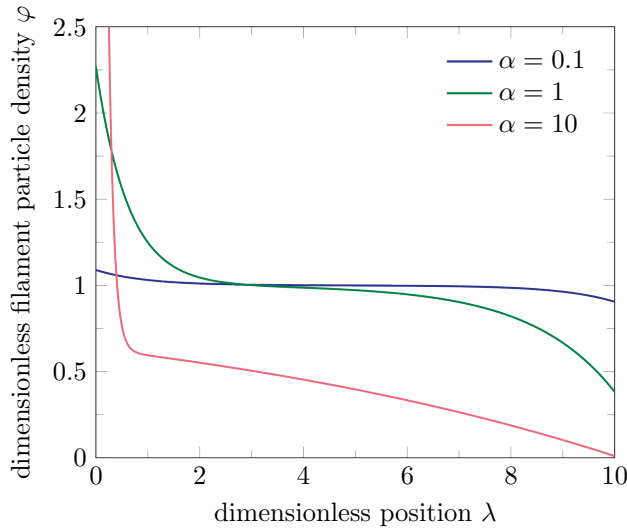


Figure 6.2: The dimensionless particle density along the filament $\phi(\lambda)$ is shaped by the dimensionless drift velocity $\alpha = v_F / \sqrt{D_F k_{FB}}$. The driving force moves particles away from the right border at $\lambda = \Lambda$ towards the membrane at $\lambda = 0$, lowering the particle density close to $\lambda = \Lambda$. Due to this reduced density on the right, the binding of new particles exceeds the unbinding as the particles move to the left, and the binding and unbinding balance out after a length scale λ_{binding} . On the opposite side, particles are crowded against the membrane, which leads to a peak in the distribution with a size of $\lambda_{\text{crowding}}$. For low drift velocities ($\alpha = 0.1$), the distribution is close to the equilibrium shape $\phi(\lambda) = 1$, but for larger values ($\alpha = 1$) the shape becomes more pronounced. When the drift velocity increases even more ($\alpha = 10$), the amplitudes of the density deformations increase further, but are now accompanied by a decrease of the length scale $\lambda_{\text{crowding}}$ and an increase of the length scale λ_{binding} . For $\alpha \approx \Lambda$, the full filament acts as an antenna for the adsorption of particles from the bulk, and roughly all those particles reach the membrane. If $\alpha < \Lambda$, many particles fall off the filament before they reach the membrane. We use the parameter values listed in Table 6.2, except for α and $\Lambda = 10$.

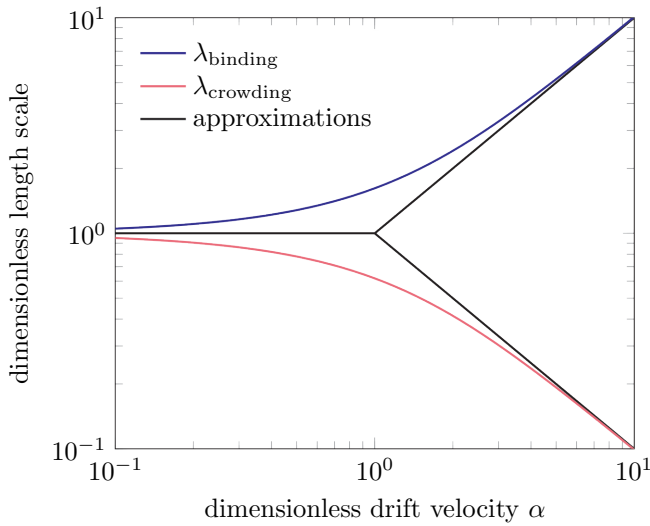


Figure 6.3: The dimensionless length scales λ_{binding} and $\lambda_{\text{crowding}}$ are roughly equal for $\alpha < 1$, but when the driving velocity increases ($\alpha > 1$) the particles can be transported for longer distances, which increases $\lambda_{\text{binding}} \approx \alpha$. Furthermore, particles are pushed against the membrane more strongly, decreasing $\lambda_{\text{crowding}} \approx 1/\alpha$. The exact expressions are given in Eq. 6.24 and Eq. 6.25, while the approximations are given in Eqs. 6.26–6.29.

$$\lambda_{\text{binding}} = \frac{2}{\sqrt{4 + \alpha^2} - \alpha}, \quad (6.24)$$

$$\lambda_{\text{crowding}} = \frac{2}{\sqrt{4 + \alpha^2} + \alpha}. \quad (6.25)$$

These length scales can be approximated in both the small and large limits of α , showing that up to leading order

$$\lambda_{\text{binding}} \xrightarrow{\alpha \ll 1} 1, \quad (6.26)$$

$$\lambda_{\text{crowding}} \xrightarrow{\alpha \ll 1} 1, \quad (6.27)$$

$$\lambda_{\text{binding}} \xrightarrow{\alpha \gg 1} \alpha, \quad (6.28)$$

$$\lambda_{\text{crowding}} \xrightarrow{\alpha \gg 1} \frac{1}{\alpha}. \quad (6.29)$$

These approximations are plotted in Fig. 6.3 along with the exact length scales from Eq. 6.24 and Eq. 6.25. The figure shows that for $\alpha < 1$, the length scales λ_{binding} and $\lambda_{\text{crowding}}$ barely change with α , and increasing the driving velocity only increases the absolute slopes of the particle densities at both ends of the filament, as seen in Fig. 6.2. But when $\alpha > 1$, the larger drift velocity crowds the proteins tighter against the membrane, creating a peak with a small $\lambda_{\text{crowding}}$ close to $\lambda = 0$. Furthermore, the slope at the back of the filament becomes longer as the average distance that particles travel before they unbind increases. This is known as the antenna effect [167, 168], since the microtubule acts as an antenna that transports particles over a distance that equals the motor protein processivity length l_v (see Eq. 6.23). Hence, protein transport to the membrane is the most efficient when the length of the filament equals the antenna length, $\Lambda = \lambda_{\text{binding}}$. If the filament is shorter, the protein concentration at the membrane will decrease. However, if the filament is longer, then many proteins will fall off the filament before they arrive at the membrane, wasting the chemical energy that was spent on driving them forward.

Because the motor drift on the filament creates a high protein density on the filament end that is close to the membrane, the interaction between the membrane and the filament will also lead to a higher protein density on the membrane. As shown in Fig. 6.4, this leads to the formation of a high density spot on the membrane close to the filament. The density of the spot increases with α , as the steady state particle flux around the cycle increases, but the size of the spot l_s is set by the unbinding rate and the diffusion constant,

$$l_s = \sqrt{\frac{D_M}{k_{MB}}}. \quad (6.30)$$

Hence, the size of the spot is roughly constant, and the dimensionless density on the membrane close to the filament $\mu(\rho)$ fully measures how pronounced the membrane spot is. If there is no spot, $\mu(\rho) = 1$, and a value larger than unity shows how much higher the protein density is in the membrane spot compared to the density on the membrane far away from the filament, which is set by the equilibrium dynamics between the bulk and the membrane. Therefore, we will use $\mu(\rho)$ to assess the quality of polarisation, which allows us to measure the impact that different parameters have on cell polarisation.

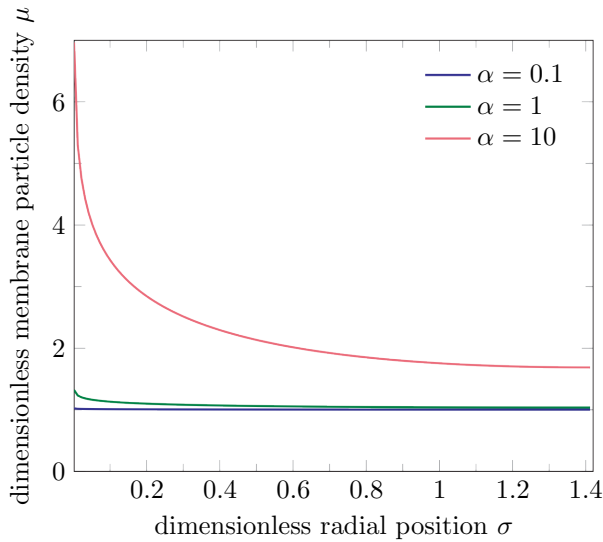


Figure 6.4: The dimensionless particle density on the membrane $\mu(\sigma)$ becomes more peaked when the dimensionless drift velocity α increases. There is a peak in the particle density on the filament as shown in Fig. 6.2, which is connected to the membrane at $\sigma = \rho \approx 1.8 \times 10^{-3}$. Some of these particles are deposited on the membrane, after which they diffuse away and finally unbind to the bulk. This diffusion and unbinding sets a length scale that equals 1 in the dimensionless representation. If the particles are driven along the filament to the membrane faster (increasing α), the height of the particle density on the membrane increases, but the width of the high density spot does not change. This width equals $\sqrt{D_M/k_{MB}}$, or 1 in the dimensionless system. The parameters are the same as in Fig. 6.2.

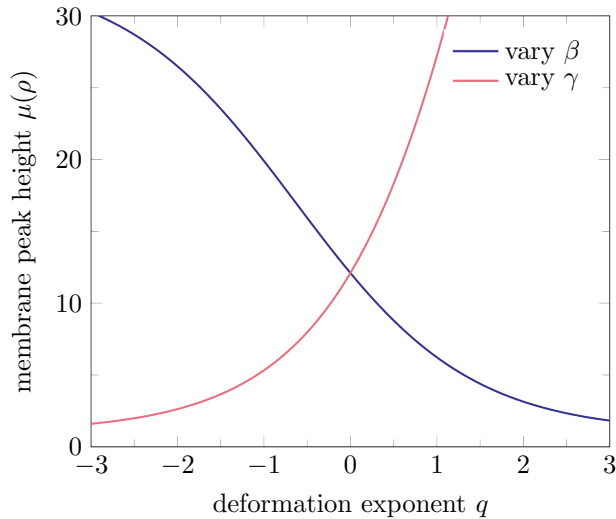


Figure 6.5: The measure for the height of the membrane spot, $\mu(\rho)$, changes when varying the dimensionless parameters β and γ , which describe the rate of hopping from the filament to the membrane and vice versa, respectively. Here we vary these parameters and keep $\delta = 1$, such that there is no free-energy drop associated with the binding and unbinding around the full cycle filament-membrane-bulk-filament, and detailed balance is only broken by active transport ($\alpha \approx 11$). We vary either $\beta = \beta_0 \exp(q)$ and $\gamma = \gamma_0$ (dark blue), or $\beta = \beta_0$ and $\gamma = \gamma_0 \exp(q)$ (light red), where β_0 and γ_0 are the values shown in Table 6.2. We see that if we increase the rate β to move from the filament to the membrane while keeping $\delta = 1$, the height of the spot decreases. Similarly, if we increase the rate γ to move back from the membrane to the filament while keeping $\delta = 1$, the polarisation of the membrane distribution improves. Hence, when binding is in equilibrium, the affinity for the membrane should be low compared to the affinity for the microtubule, such that the particles that are deposited on the membrane by the microtubule have a large impact on the membrane distribution.

The dimensionless parameter β quantifies how fast the particles move from the microtubule tip to the membrane, and the parameter γ quantifies the speed of the reverse transition. In Fig. 6.5, we show that the height of the membrane spot decreases if we increase the rate of binding from the filament to the membrane or decrease the reverse rate, while keeping $\delta = 1$. This counter-intuitive result holds true precisely because $\delta = 1$, such that there is no net free-energy drop along the cycle filament-membrane-bulk-filament. Increasing β or decreasing γ increases the affinity for the membrane relative to that for the filament, but the constraint that there is no free-energy drop around the cycle means that this must be accompanied by a decrease of the relative affinity for the filament compared to the bulk or by an increase of the relative affinity for the membrane compared to the bulk. In the former case, the density of particles at the tip of the filament decreases, which reduces the height of the membrane spot because the flux from the filament tip to the membrane is decreased. In the latter case, the equilibrium density on the membrane increases, reducing the contrast between the membrane spot and the density far away. The absolute equilibrium probability that the particle is found in the bulk does not influence the relative likelihoods of finding the particle on the membrane or on the filament when the binding cycle is in equilibrium, explaining why the details of the transition rates to and from the bulk become irrelevant in the non-dimensional representation. Hence, increasing β and decreasing γ decreases $\mu(\rho)$ because the binding affinity for the filament should be high compared to the binding affinity for the membrane to create a polarised membrane spot.

Finally, we focus on how δ affects the formation of a steady state membrane spot. If $\delta < 1$, then there is a free-energy drop each time a particle moves from the bulk to the filament, from the filament to the membrane, and from the membrane back to the bulk. The protein density in the membrane spot depends on the flux that runs through this cycle, so we expect $\mu(\rho)$ to increase when δ decreases. Fig. 6.6 shows that the height of the membrane spot indeed increases when $\delta < 1$. Furthermore, the shape of the density profile on the filament barely changes, only slightly reducing the size of the density peak $\varphi(0)$ when $\delta < 1$ (data not shown). Hence, breaking detailed balance through a chemical modification cycle in the binding cycle filament-membrane-bulk-filament has a strong effect on the formation of a polarised protein distribution on the membrane.

6.2. BIOLOGICALLY RELEVANT PARAMETER VALUES

The dimensionful model presented in Sec. 6.1 contains fourteen parameters, including one that sets the average concentration b . To focus the model analysis, we find a set of biologically relevant parameter values, which also provide values for the dimensionless parameter set. Then, we vary individual parameters to investigate how they influence the polarisation of the membrane and the free-energy dissipation.

Because microtubules are roughly 25 nm in diameter [12], we choose a filament radius $r = 12.5$ nm. Furthermore, we choose a filament length of $L = 10 \mu\text{m}$, which is a typical microtubule length. For the container radius, we choose a value of $R = 10.0125 \mu\text{m}$, which will be large enough to show the full membrane spots that are created by a single microtubule, and which ensures that $R - r = 10 \mu\text{m}$, simplifying the creation of histograms that cover the entire radial space of the membrane. This leads to a container

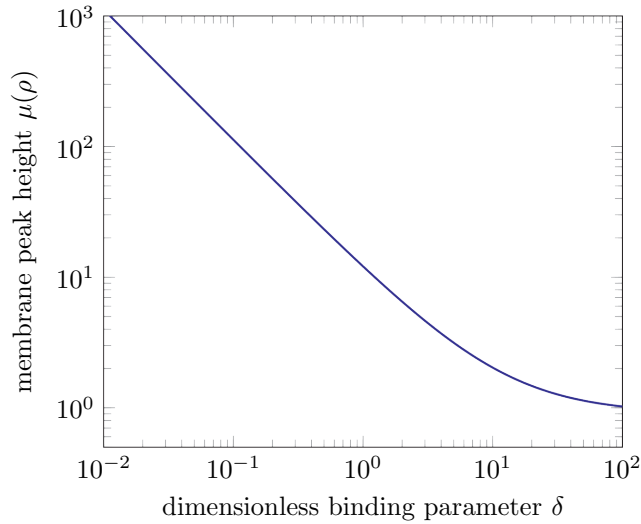


Figure 6.6: The measure for the height of the membrane spot relative to the equilibrium density on the membrane, $\mu(\rho)$, decreases when δ increases while the driving velocity remains constant ($\alpha \approx 11$). If the binding cycle filament-membrane-bulk-filament is coupled to the dissipation of chemical free energy, for example by performing an NTP hydrolysis each time the particle moves through the cycle, then $\delta < 1$ and the steady state flux through the cycle increases. Increasing this flux has a positive effect on the protein density in the membrane spot, and increases the polarisation independent of the driving velocity on the filament α . Apart from δ , the parameter values are given in Table 6.2.

that is large compared to the typical size of a fission yeast cell, which is roughly $10\mu\text{m}$ long [169]. However, the exact size of the spot, and thus the required container size, does not influence the conclusions of this chapter. Furthermore, we will discuss in the following paragraphs that we expect that the diffusion constant of proteins on the membrane is effectively lower *in vivo* compared to *in vitro*, creating a smaller spot that would fit on a yeast cell.

The dynamical parameters on the filament describe how a cargo moves on a microtubule under the influence of motor proteins. Single kinesin motors can move between 0.01 microm/s and $1\mu\text{m s}^{-1}$ depending on the ATP concentration, the load, and the kind of kinesin protein [129, 170]. Since we consider low load single protein cargoes, we set the average drift velocity to $v_F = 0.5\mu\text{m s}^{-1}$. The dynamics on the filament is defined by this drift velocity in combination with the diffusion constant of kinesin motors running along a microtubule, which has been measured to be roughly between $0.002\mu\text{m}^2\text{ s}^{-1}$ [171] and $0.005\mu\text{m}^2\text{ s}^{-1}$ [172]. Hence, we set $D_F = 0.004\mu\text{m}^2\text{ s}^{-1}$.

The diffusion constant on the membrane depends on the diffusing protein and the type of lipid bilayer. For a simple membrane *in vitro*, the diffusion constant of proteins with a radius of roughly 2 nm equals around $8\mu\text{m}^2\text{ s}^{-1}$ [173]. Because we employ a minimal model, we ignore the compartmentalisation of the membrane [174], and choose a diffusion constant on the membrane of $D_M = 5\mu\text{m}^2\text{ s}^{-1}$. In the bulk, we require the diffusion constant of proteins in the cytosol, which was measured to be on average $D_B = 60\mu\text{m}^2\text{ s}^{-1}$ [175].

We assume that the rate at which the cargo unbinds from the microtubule is limited by the unbinding rate of kinesin, which is roughly $k_{FB} = 0.5\text{ s}^{-1}$ when no external force pulls on the motor [176]. For the rate at which the particles unbind from the membrane, we use the experimental off-rate that was measured for the Rho-GTPase Cdc42, which sets a value of $k_{MB} = 0.1\text{ s}^{-1}$ [177]. Together with the membrane diffusion constant D_M , this rate sets a typical length scale for the membrane spot size of

$$l_M = \sqrt{\frac{D_M}{k_{MB}}} \approx 7\mu\text{m}. \quad (6.31)$$

The same experiments also provide an order of magnitude for the binding rate of particles from the bulk to the membrane by observing the Cdc42 association with liposomes. In equilibrium, the total binding rate from the solution equals

$$k_{\text{on}} = u_{BM}Ab, \quad (6.32)$$

where A is the area of the membrane on spherical liposomes. Taking a concentration of $b = 50\text{ nM}$, a liposome radius of $0.5\mu\text{m}$ (giving $A \approx 3.1\mu\text{m}^2$), and a $k_{\text{on}} = 1\text{ s}^{-1}$ [177], we find $u_{BM} \approx 0.01\mu\text{m s}^{-1}$.

The binding rate of cargo proteins from the cytosol to the filament is affected by the binding rate of motor proteins to the microtubule and the binding rate of the cargo to motor proteins. We assume that this binding is relatively strong, such that the equilibrium affinity for the microtubule is much higher than for the membrane, which allows the driving on the microtubule to have a pronounced effect on the membrane concentration. Because the rate of unbinding from the filament to the bulk is larger than that

from the membrane to the bulk, $k_{FB} = 5k_{MB}$, this means that u_{BF} must be several orders of magnitude larger than u_{BM} to guarantee a higher equilibrium affinity for the filament. Furthermore, because the area of the microtubule is much smaller than the area of the membrane, the affinity for the microtubule needs to be very large to find a significant fraction of particles on the filament. Hence, we choose $u_{BF} = 100\mu\text{ms}^{-1}$. We can compare our values of k_{FB} and u_{BF} to the reported dissociation constant $K_{D,BF}$ of a kinesin subunit binding to microtubules, which was found to be lower than $K_{D,BF} < 50\text{nM} \approx 30\mu\text{m}^{-3}$ [178]. This dissociation constant should equal

$$K_{D,BF} = \frac{k_{FB}}{u_{BF}A_{\text{tub}}}, \quad (6.33)$$

where A_{tub} is the surface area of a single tubulin dimer on the microtubule, which we take to be roughly 50nm^2 . Using the previously mentioned values of k_{FB} and u_{BF} , we find $K_{D,BF} \approx 100\mu\text{m}^{-3}$. Hence, the experimental value of the dissociation constant suggests that we slightly underestimate the binding to the microtubule, but our value is of the right order of magnitude.

Once the particles are driven to the tip of the filament, and are in contact with the membrane, the rate to bind to the membrane u_{FM} is related to the rate u_{BM} . If the mechanism of binding from the filament is the same as from the bulk, then we assume $u_{FM} = u_{BM} = 0.01\mu\text{ms}^{-1}$. However, the cell may implement a different mechanism for transporting the cargo from the tip of a microtubule to the membrane, in which case this value could be larger. Hence, it will be interesting to see how the prominence of the membrane spot changes with u_{FM} .

Finally, detailed balance provides a relation for the reverse rate u_{MF} at which particles that are on the membrane and close to the filament bind to the filament. If the binding and unbinding is in equilibrium, we have

$$\delta = \frac{u_{MF}k_{FB}u_{BM}}{u_{FM}u_{BF}k_{MB}} = 1. \quad (6.34)$$

Using the previously mentioned values for all other (un)binding rates, we find $u_{MF} = 1\mu\text{ms}^{-1}$. In Table 6.3, we give an overview of all parameter values, and in Table 6.2 we list the values that the dimensionless parameters take in the biologically relevant regime.

6.3. A FINITE BULK DIFFUSION CONSTANT IS BENEFICIAL FOR CELL POLARISATION

In steady state, Eqs. 6.2–6.4 provide a set of ordinary differential equations that can be solved analytically, as shown in Eq. 6.18–6.19. However, these equations are valid when the diffusion constant in the bulk is very large, $D_B \rightarrow \infty$. When D_B is finite, we could modify the steady state differential equations and the corresponding boundary conditions, leading to a set of coupled partial differential equations for $f(z)$, $m(s)$ and $b(z, s)$ that cannot be solved analytically. To find numerical solutions for the steady state density profiles, we perform simple time step based Monte Carlo simulations of a single particle moving through the system. We do not require multiple particles since we model an "ideal gas" of proteins that never interact.

Because of the radial symmetry of the system, we only keep track of the longitudinal position z and the radial distance s . To model the particle diffusion, we implement a discrete time random walk in which particles move by a stochastic longitudinal step δz or radial step δs each time step δt . On the filament, δz follows a Gaussian distribution with mean $-v_F \delta t$ and standard deviation $\sqrt{2D_F \delta t}$, while in the bulk the mean of δz vanishes and the standard deviation equals $\sqrt{2D_B \delta t}$. For the diffusion in the radial direction, we draw two Gaussian random numbers δx and δy with zero mean and standard deviation $\sqrt{2D_M \delta t}$ (membrane) or $\sqrt{2D_B \delta t}$ (bulk). Then, we calculate $(s + \delta s)^2 = (s + \delta x)^2 + \delta y^2$, where we use that the x -axis can always be chosen to point in the radial direction. When either δz or δs brings the particle outside of the container, we reflect the particle position back across the boundary. The algorithm to reflect the particles in a flat or circular surface without breaking detailed balance is described in Sec. 6.B.

To simulate the particle transitions between the three system parts, we use the same kinetic Monte Carlo algorithm that we used for implementing cross-linker hopping as explained in Eq. 2.27. In summary, we integrate the transition rates until a stochastically chosen threshold is passed upon which we perform a reaction [82]. Since the binding rates u_{BF} , u_{FM} , u_{MF} , and u_{BM} contain a spatial dimension as well, we define the reaction length scales l_{long} and l_{rad} . When a particle is in the bulk and within a distance l_{long} from the membrane, it can bind to the membrane with a transition rate

$$k_{BM} = \frac{u_{BM}}{l_{\text{long}}}. \quad (6.35)$$

This definition ensures that if the bulk concentration is roughly constant within the reaction volume, then the flux is modelled correctly, $k_{BM} l_{\text{long}} b \approx u_{BM} b$. Hence, this equation is only valid when l_{long} is much smaller than the size of typical density fluctuations. Similarly, we have

$$k_{FM} = \frac{u_{FM}}{l_{\text{long}}}. \quad (6.36)$$

In the radial direction close to the filament, the reaction volume has a tubular form, and we must have that $k_{BF} \pi ((r + l_{\text{rad}})^2 - r^2) b \approx 2\pi r u_{BF} b$. Therefore, we choose

$$k_{BF} = \frac{u_{BF}}{l_{\text{rad}} + l_{\text{rad}}^2/2r} \quad (6.37)$$

and

$$k_{MF} = \frac{u_{MF}}{l_{\text{rad}} + l_{\text{rad}}^2/2r}. \quad (6.38)$$

When a reverse reaction occurs, we place the particle uniformly within the reaction volume. For example, when a particle unbinds from the filament to the bulk, it will be placed at a radial position $r < s < r + l_{\text{rad}}$, which is uniformly distributed over the area $\pi ((r + l_{\text{rad}})^2 - r^2)$. This mechanism ensures that detailed balance holds when $\alpha = 0$ and $\delta = 1$.

We show the simulated protein concentration profiles on the filament and on the membrane in Fig. 6.7 and Fig. 6.8, respectively, and compare them to the exact solutions for $f(z)$ and $m(s)$ that are valid at $D_B \rightarrow \infty$. We use the biologically relevant parameters listed in Table 6.3, and the figures show that the simulations with $D_B = 60 \mu\text{m}^2 \text{s}^{-1}$ agree

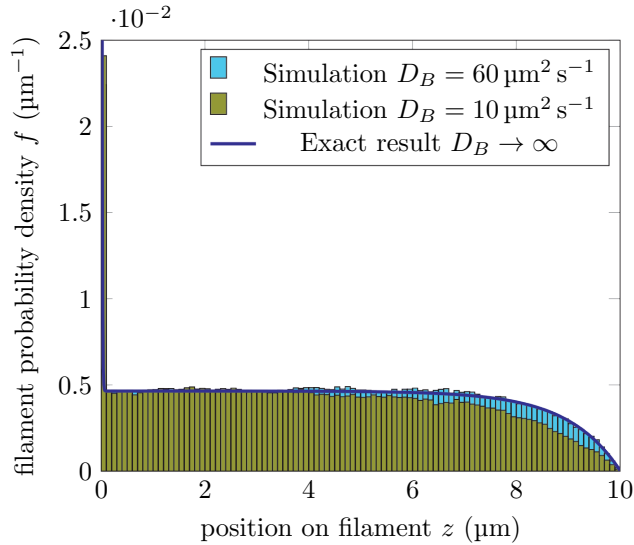


Figure 6.7: The probability density $f(z)$ that a particle is at position z on the filament, where the membrane is located at $z = 0$ and motor proteins drive the particles from the right to the left. We use the biologically relevant parameters of Table 6.1. The dark blue line gives the exact result for $D_B \rightarrow \infty$, showing that the filament acts as an antenna over a length $l_{\text{binding}} \approx 1.0 \mu\text{m}$. After this distance, the unbinding of particles balances out the binding of new particles. When the particles reach the membrane, they are crowded over a length scale $l_{\text{crowding}} \approx 8 \text{ nm}$. In light blue, we show a histogram of the particle density in simulations using the parameters of Table 6.3, in which the bulk diffusion constant $D_B = 60 \mu\text{m}^2 \text{s}^{-1}$, which nearly perfectly coincides with the theoretical result. Simulations with a lower bulk diffusion constant $D_B = 10 \mu\text{m}^2 \text{s}^{-1}$ are shown in yellow, revealing that the antenna effect acts over a longer length scale when the bulk diffusion constant is lower. The lower diffusion constant allows some particles that unbind from the filament to rapidly rebind to the filament, increasing the effective distance over which the particles can be transported. The density peak in the leftmost bin is predicted to be $2.1 \times 10^{-2} \mu\text{m}^{-1}$ ($D_B \rightarrow \infty$), and the simulations find $2.2 \times 10^{-2} \mu\text{m}^{-1}$ ($D_B = 60 \mu\text{m}^2 \text{s}^{-1}$) and $2.4 \times 10^{-2} \mu\text{m}^{-1}$ ($D_B = 10 \mu\text{m}^2 \text{s}^{-1}$), indicating that the particle density at the filament tip increases when the bulk diffusion constant decreases.

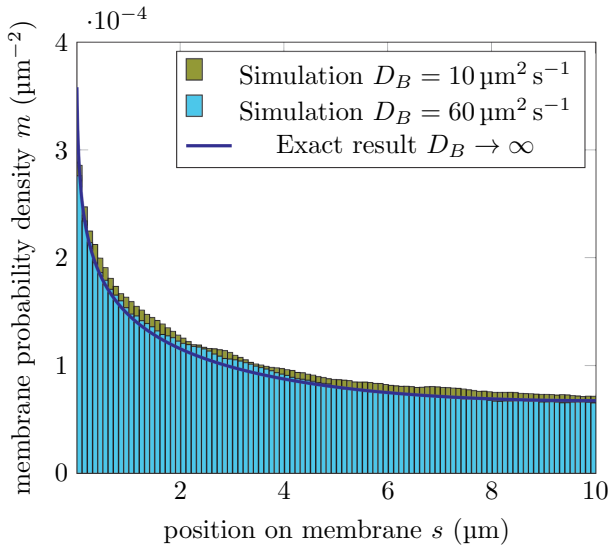


Figure 6.8: The probability density $m(s)$ that a particle is at a radial position s on the membrane, where the filament is located at $s = r = 0.0125\mu\text{m}$. We use the same parameters and simulation as in Fig. 6.7. The dark blue line gives the exact result for $D_B \rightarrow \infty$, which predicts a spot size of $\sqrt{D_M/k_{MB}} = 7.1\mu\text{m}$. The difference between the simulations with a high bulk diffusion constant ($D_B = 60\mu\text{m}^2\text{s}^{-1}$) and the exact solution are likely caused by insufficient sampling. The particle density in the leftmost bin is predicted to be $2.7 \times 10^{-4}\mu\text{m}^{-2}$ ($D_B \rightarrow \infty$), and the simulations find $2.8 \times 10^{-4}\mu\text{m}^{-2}$ ($D_B = 60\mu\text{m}^2\text{s}^{-1}$) and $2.9 \times 10^{-4}\mu\text{m}^{-1}$ ($D_B = 10\mu\text{m}^2\text{s}^{-1}$). The higher density for the lower bulk diffusion constant persists inside the whole membrane spot (yellow bins), showing that a lower bulk diffusion constant can slightly improve cell polarisation.

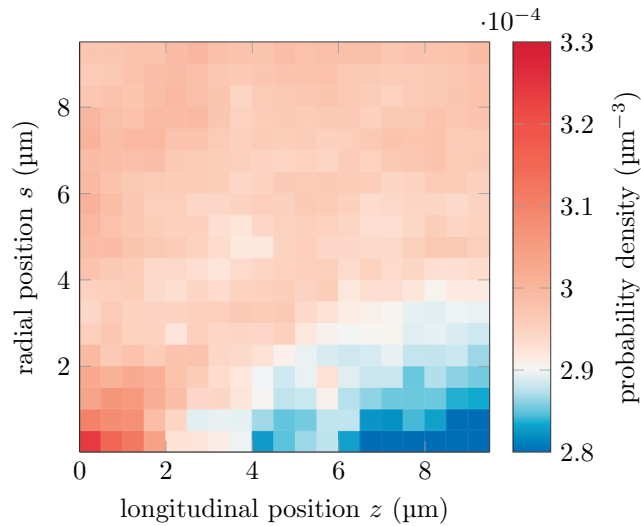


Figure 6.9: The probability density $b(z, s)$ that a particle is at a longitudinal position z and a radial position s in the bulk, where the membrane is located at $z = 0$ and the filament is located at $s = r = 0.0125 \mu\text{m}$. We show the histogram produced by simulations with a lower diffusion constant in the bulk, $D_B = 10 \mu\text{m}^2 \text{s}^{-1}$, because $D_B = 60 \mu\text{m}^2 \text{s}^{-1}$ results in a nearly flat density profile. Otherwise, all parameters are the same as listed in Tab. 6.1. With a lower diffusion constant, the density profile on the filament shown in Fig. 6.7 persists for some distance into the bulk, improving the effects of active transport on the polarised particle distribution.

6

with the analytical solutions. In contrast, additional simulations with a bulk diffusion constant $D_B = 10 \mu\text{m}^2 \text{s}^{-1}$ do display significant deviations from the predicted behaviour for $D_B \rightarrow \infty$. Specifically, it appears that the length scale l_{binding} on the filament increases, improving the antenna effect caused by the motor proteins. Furthermore, the density peak on the filament close to $z = 0$ is higher when the bulk diffusion constant is lower. This subsequently causes a larger flux of particles to be deposited on the membrane, leading to a slight increase of the particle density in the membrane spot as shown in Fig. 6.8.

The steady state particle density in the bulk $b(z, s)$ is almost homogenous when $D_B = 60 \mu\text{m}^2 \text{s}^{-1}$ (data not shown), explaining why the exact solution for $D_B \rightarrow \infty$ is nearly identical to the simulation results. To visualise the effects of a lower bulk diffusion constant, we plot how the proteins are distributed in the cytosol for $D_B = 10 \mu\text{m}^2 \text{s}^{-1}$ in Fig. 6.9. Close to the filament, which is located at $s = r$, the bulk density profile resembles the shape of the density on the filament shown in Fig. 6.7. The transport along the filament removes particles from the back of the container, lowering the protein density in a region that extends several microns into the bulk. Furthermore, Fig. 6.9 shows that the particles are concentrated more densely close to $z = 0$ and $s = r$, which is close to the density peak on the filament and on the membrane. Since a finite diffusion constant does not smear out the protein distributions instantly, lowering the diffusion constant in

the bulk is beneficial for the formation of a strongly polarised non-equilibrium distribution on the membrane.

6.4. FREE-ENERGY IS DISSIPATED TO FORM A MEMBRANE SPOT

Using the exact solutions of the protein densities on the filament and the membrane in Eqs. 6.18–6.19, we saw that the flux through the system vanishes if and only if $\delta = 1$ and $\alpha = 0$. The parameter δ can break detailed balance when the particles undergo a driven chemical modification cycle when they revolve through the filament, membrane, and bulk. On the other hand, a non-zero value for the parameter α is caused by motor proteins driving the movement of the particles along the filament. Both processes dissipate free energy, and we can find lower bounds for the free-energy dissipation caused by each process.

On the filament, the particles have a drift velocity v_F and a diffusion constant D_F . Using the Einstein relation [28] (see Eq. 1.39), these two parameters define the average drift force F_F that acts on particles bound to the filament,

$$F_F = k_B T \frac{v_F}{D_F}. \quad (6.39)$$

We can calculate the work performed on a particle by multiplying this force with the net distance that the particle travels on the filament.

For the binding reactions, we make use of the local detailed balance relation Eq. 1.23. Because the individual transitions can also involve the changing of dimensions, for example from the bulk to the membrane, it is nonsensical to assign free-energy differences between particle states on the membrane or in the bulk,

$$\Delta \mathcal{F}_{BM} \neq k_B T \log \left[\frac{u_{BM}}{k_{MB}} \right]. \quad (6.40)$$

In this expression, we would take the logarithm of a factor that has a dimension of length. Still, because a particle that moves through a loop has to pass the dimensional transitions along the z - and s -axis in both directions, these length scales have to cancel in the ratio δ . Only a multiplicative constant c may survive because the length scales of the transitions from the filament to the membrane and from the bulk to the membrane, or the length scales in the transitions from the membrane to the filament and from the bulk to the filament could differ. Hence,

$$\Delta \mathcal{F}_{FMB} = k_B T \log \left[\frac{u_{FM} k_{MB} u_{BF}}{u_{MF} u_{BM} k_{FB}} \right] + k_B T \log [c] = -k_B T \log [\delta] + k_B T \log [c]. \quad (6.41)$$

Here, we take the dissipated free energy to be positive, such that a positive free-energy drop around the loop $\Delta \mathcal{F}_{FMB}$ drives a flux through the loop filament-membrane-bulk-filament. Because we have shown that detailed balance holds if and only if $\delta = 1$, and we require $\Delta \mathcal{F}_{FMB} = 0$ in that case, we see that the length scale $c = 1$, showing that

$$\Delta \mathcal{F}_{FMB} = -k_B T \log [\delta]. \quad (6.42)$$

We can use Eq. 6.39 and Eq. 6.42 to define free-energy differences, but to compare the two we require the average dissipated power per particle. In the simulations, we can

keep track of the net distance travelled on the filament d_{net} , which increases if motor proteins drive the particle towards $z = 0$, but decreases again if the diffusion with diffusion constant D_F increases z . Hence, we take into account that motor proteins that hydrolyse ATP have a small chance of moving back, reattaching a phosphate group to an ADP molecule. Similarly, we record the net number of times the particle moves forward in the transition filament-membrane N_{FM} . We run the simulations for a time t , after which the total average dissipated power P_{sim} equals

$$P_{\text{sim}} = \frac{F_F d_{\text{net}} + N_{FM} \Delta \mathcal{F}_{FMB}}{t}. \quad (6.43)$$

If the simulated time t is long enough, we will find a reliable measurement of the power.

Using the steady state versions of Eq. 6.2–6.9 and their analytical solutions, we can also calculate the exact dissipated power per particle for $D_B \rightarrow \infty$. First, we see that the steady state flux that moves through the filament-membrane-bulk-filament cycle equals

$$J_{ss} = u_{FM} f(0) - 2\pi r u_{MF} m(r). \quad (6.44)$$

Then, the power dissipated by the binding dynamics equals

$$P_{\text{exact},FMB} = J_{ss} \Delta \mathcal{F}_{FMB}. \quad (6.45)$$

Then, the power dissipated by the driving on the filaments follows from the flux along the filament,

$$P_{\text{exact},F} = \int_0^L (D_F \partial_z f(z) + v_F f(z)) F_F dz, \quad (6.46)$$

where the diffusive term includes the free energy that is returned if a motor protein makes a backward step. By integrating over the differential equations Eq. 6.2–6.4, we can find expressions for the number of particles in each part of the system,

$$\begin{aligned} N_F &= \int_0^L f(z) dz = \frac{1}{k_{FB}} (2\pi r L u_{BF} b - J_{ss}), \\ N_M &= \int_r^R m(s) 2\pi s ds = \frac{1}{k_{MB}} (\pi (R^2 - r^2) u_{BM} b + J_{ss}), \\ N_B &= \int_0^L \int_r^R b 2\pi s ds dz = \pi (R^2 - r^2) L b, \\ N_{\text{tot}} &= N_F + N_M + N_B. \end{aligned} \quad (6.47)$$

Using these definitions, we find the power per particle to equal

$$P_{\text{exact}} = \frac{D_F (f(L) - f(0)) + v_F N_F}{N_{\text{tot}}} F_F + \frac{J_{ss}}{N_{\text{tot}}} \Delta \mathcal{F}_{FMB}. \quad (6.48)$$

This solution is exact, but only valid when the diffusion constant in the bulk is very large, $D_B \rightarrow \infty$.

In Sec. 6.3, we showed that lowering the bulk diffusion constant slightly improves the quality of polarisation, but we also expect that it improves its efficiency. Particles that

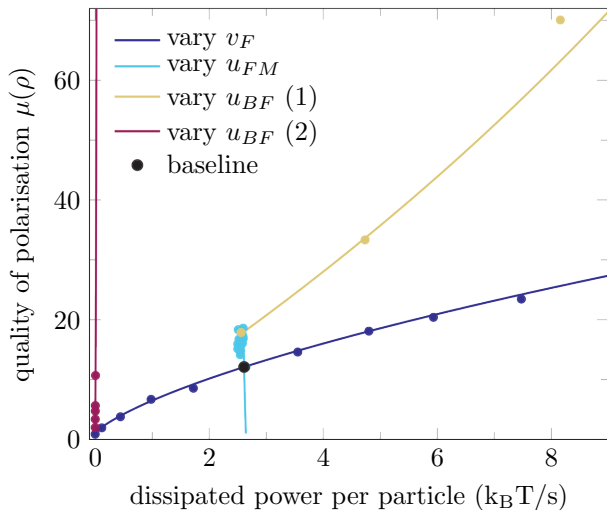
are transported along the filament and fall off before they reach the membrane instantly diffuse away when $D_B \rightarrow \infty$. Hence, the free energy that is dissipated in transporting these particles is wasted as soon as they fall off the filament. However, a lower bulk diffusion constant allows the particles to rebind to the filament, reducing the number of wastefully transported particles. For the parameter values listed in Table 6.1, we predict that the power of active transport equals $2.61 k_B T/s$ for $D_B \rightarrow \infty$, and we find a power of $2.6 k_B T/s$ in simulations with $D_B = 60 \mu m^2 s^{-1}$ and a power of $2.4 k_B T/s$ in simulations with $D_B = 10 \mu m^2 s^{-1}$. Hence, simulations show that lowering the bulk diffusion constant can indeed improve the efficiency of active transport by increasing the quality of polarisation and decreasing wasteful free-energy dissipation.

6.5. DRIVEN BINDING KINETICS IS MORE EFFICIENT THAN MOTOR TRANSPORT

Using the results of Sec. 6.4, we can quantify both the dissipated power by the motor proteins and by the binding kinetics of the cargo proteins. Furthermore, we showed in Sec. 6.1 that the quality of the polarised protein distribution on the membrane can be quantified by $\mu(\rho)$, which compares the protein density in the centre of the membrane spot to the density on the periphery of the membrane. Starting from the biologically relevant set of parameter values listed in Table 6.1, we investigate how varying some parameters influences the membrane spot.

First, we vary the drift velocity on the filament v_F between 0 and $1 \mu m s^{-1}$, and calculate both the dissipated power P_{exact} (see Eq. 6.48) and the quality of the membrane spot $\mu(\rho)$ for each value of v_F . The results of the exact solutions are plotted in Fig. 6.10 (dark blue line) together with the values obtained in simulations with $D_B = 60 \mu m^2 s^{-1}$ (dark blue dots). We see that the membrane spot becomes more pronounced if we increase v_F , but that the dissipation per particle also increases strongly. Combined, the quality of the membrane spot appears to increase with the dissipated power as a power law when it is only driven by active transport.

Instead of increasing the drift velocity, the system may also break detailed balance in the binding cycle filament-membrane-bulk-filament, lowering the value of the non-dimensional parameter $\delta < 1$. In Sec. 6.2, we noted that the rate to bind from the filament to the membrane u_{FM} may be different from the rate to bind from the bulk to the membrane u_{BM} . For example, the motor proteins that transport the particles on the filament may also provide a mechanism to deliver them to the membrane. Furthermore, the chemical state of the proteins may be different when they are on the filament, for example by strongly favouring the binding of (de)phosphorylated particles to the motor proteins, or by packing the proteins on a vesicle before transport. Hence, we vary the rate u_{FM} while maintaining the driving velocity $v_F = 0.5 \mu m s^{-1}$, and calculate both $\mu(\rho)$ and P_{exact} . Fig. 6.10 (light blue line and dots) shows that increasing u_{FM} improves the quality of the polarised spot, but it does not cost more free energy. In fact, the power per particle caused by the binding cycle $P_{\text{exact},FMB}$ becomes non-zero and remains small, but increasing u_{FM} also reduces the time that particles spend on the filament, which reduces the probability that a particle unbinds from the filament to the bulk and wastes the free energy that was spent in transporting it. Hence, the power per particle caused by



6

Figure 6.10: The quality of polarisation, given by the protein density at the centre of the spot relative to the equilibrium density on the membrane, $\mu(\rho)$, as a function of the dissipated power in the system. The black point corresponds to the biologically relevant parameter values shown in Table 6.1, providing a baseline from where to change parameters. We vary the drift velocity on the filament v_F between 0 and $1 \mu\text{m s}^{-1}$, where the baseline value is given by $v_F = 0.5 \mu\text{m s}^{-1}$, and we keep the binding in equilibrium (dark blue line, power law). We also vary the binding rate from the filament to the membrane u_{FM} between $7 \times 10^{-5} \mu\text{m s}^{-1}$ and $1.5 \mu\text{m s}^{-1}$ (baseline $u_{FM} = 0.01 \mu\text{m s}^{-1}$, light blue vertical line). This binding lowers the highly crowded density at the front of the filament, improving polarisation while slightly saving on dissipated power. However, increasing u_{FM} past v_F does not influence the polarisation. Hence, we keep the optimal value $u_{FM} = 0.5 \mu\text{m s}^{-1}$ and increase the power dissipated through binding by increasing the rate to bind to the filament u_{BF} from the baseline value $100 \mu\text{m s}^{-1}$ to $425 \mu\text{m s}^{-1}$ (yellow exponential line, 1), or set $v_F = 0$ and vary u_{BF} between $100 \mu\text{m s}^{-1}$ and $5250 \mu\text{m s}^{-1}$ (red vertical line, 2). All theoretical curves are compared to simulations with a bulk diffusion constant $D_B = 60 \mu\text{m}^2 \text{s}^{-1}$ (points), confirming the agreement with the assumption $D_B \rightarrow \infty$. We see that the quality of the membrane polarisation can be improved much more efficiently by dissipating power in the binding cycle than by transporting the proteins on the filament.

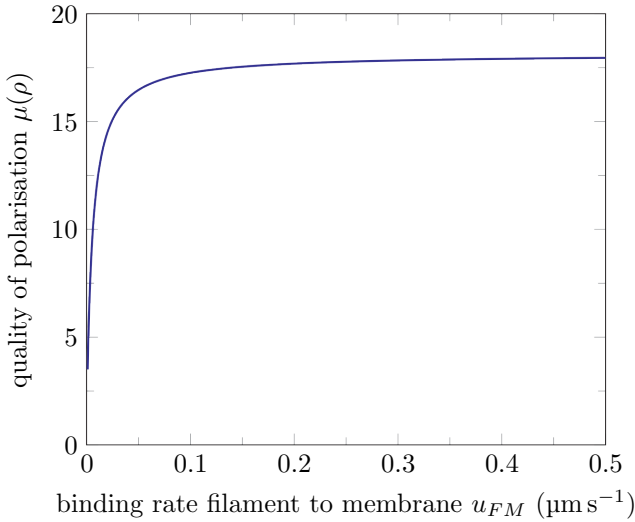


Figure 6.11: The quality of polarisation as a function of the rate to move from the filament to the membrane, u_{FM} . All other parameter values are listed in Table 6.1. Increasing u_{FM} to a value larger than $v_F = 0.5 \mu\text{m s}^{-1}$ has no influence on the high density spot on the membrane, only reducing the crowding at the end of the filament.

transport on the filament $P_{\text{exact},F}$ decreases more strongly than $P_{\text{exact},F}$ increases when we increase u_{FM} , leading to a lower overall power consumption.

The boundary condition Eq. 6.6 indicates that the derivative of $f(z)$ at $z = 0$, the density on the filament near the membrane, becomes less negative or even positive when u_{FM} increases. Faster transmission of the particles from the filament to the membrane lowers the high density peak on the filament, which is the spike at $z = 0$ in Fig. 6.7. However, if u_{FM} becomes much larger than v_F , the density $f(0)$ becomes zero, and the flux to the membrane becomes limited by the speed at which new particles are transported by the motor proteins. Fig. 6.11 shows that the quality of membrane polarisation $\mu(\rho)$ reaches an asymptote before reaching a value of $u_{FM} \approx v_F$. Even though increasing u_{FM} increases polarisation at almost no cost, it is only beneficial as long as $u_{FM} < v_F$.

To further investigate if increasing the dissipation in the binding cycle is efficient, we choose to vary the rate to bind from the bulk to the filament, u_{BF} . In Sec. 6.2, we showed that there is some freedom in choosing this rate. We increase the rate from $u_{BF} = 100 \mu\text{m s}^{-1}$ to $350 \mu\text{m s}^{-1}$, while setting $u_{FM} = v_F = 0.5 \mu\text{m s}^{-1}$. As shown in Fig. 6.10 (yellow line, 1), the quality of polarisation $\mu(\rho)$ increases exponentially with the power dissipated, which is more efficient than simply increasing the drift velocity on the filament. The dissipation mainly increases because the number of particles on the filament increases with u_{BF} , and this leads to a larger dissipation by the motor proteins.

To see if a non-equilibrium binding cycle can cause a polarised distribution of particles on the membrane, we also vary u_{BF} while keeping $v_F = 0$. Fig. 6.10 (red line, 2) shows the model does show a strong polarisation when only the binding cycle breaks

detailed balance, and that the free-energy dissipation is orders of magnitude lower than with a finite drift velocity. For $u_{BF} = 4300\mu\text{m s}^{-1}$ and $v_F = 0$, we find $\mu(\rho) = 60$ and $P_{\text{exact}} = 0.02\text{ k}_B\text{T/s}$, whereas for $u_{BF} = 350\mu\text{m s}^{-1}$ and $v_F = 0.5\mu\text{m s}^{-1}$, we find the same polarisation $\mu(\rho) = 60$ but with a dissipated power of $P_{\text{exact}} = 7.8\text{ k}_B\text{T/s}$. Hence, by driving the binding cycle out of equilibrium, via e.g. a phosphorylation-dephosphorylation cycle as in the Pom1/Tea1/Tea4 system, the cell can make the binding from the filament to the membrane more likely without increasing the backward rate from the membrane to the filament. This process is probably highly efficient in terms of its free-energy consumption.

6.6. DISCUSSION

Cytoskeletal filaments are often organised in non-homogeneous structures within the cell. For example, the mitotic spindle is a structure in which microtubules point radially outward from two microtubule organising centres. Together with the intrinsically polarised structure of the filaments, the cell can use its cytoskeleton to provide directional transport of other particles and break the symmetry of the distribution of particles. Fission yeast makes use of microtubule based transport of Tea1 and Tea4 to polarise the distribution of Pom1 on its membrane [19], and budding yeast transports vesicles with membrane-bound Cdc42 along actin cables, leading to a polarised distribution of Cdc42 on the outer membrane [20, 166]. Hence, if the filaments point towards the membrane and the transported cargoes bind to the membrane, transport by motor proteins along filaments offers a mechanism to polarise a distribution of proteins on the membrane of the cell. Using a minimal model, we showed that transport along a filament can create a polarised steady state distribution on the membrane, and that the motor proteins dissipate a reasonable amount of chemical free energy to maintain this non-equilibrium state. Using biologically relevant parameter values, the protein concentration on the membrane can increase by a factor 12 compared to the equilibrium density on the membrane, forming a high density spot close to the filament while the cell dissipates on average $2.6\text{ k}_B\text{T/s}$ of chemical free energy per particle. In comparison, the hydrolysis of a single ATP molecule releases roughly $18\text{ k}_B\text{T}$ [179], so a motor protein moving at $0.5\mu\text{m s}^{-1}$ that hydrolyses one ATP molecule per 8 nm step dissipates more than $1000\text{ k}_B\text{T/s}$. Hence, a polarised distribution of filament orientations that is used for directed transport can be sufficient to create a polarised distribution of cargo proteins on the membrane.

The model also includes a second mechanism to break detailed balance besides active transport. The particles transition reversibly between the bulk (cytosol) and filament, between the filament and membrane, and between the membrane and bulk. Those reactions can break detailed balance by modifying the particles as they pass through the loop. For example, Pom1 is dephosphorylated before it binds to the membrane in fission yeast, but its autophosphorylation then increases its dissociation rate from the membrane [19, 20]. Furthermore, Cdc42 switches between GDP and GTP bound states, binding to the membrane as Cdc42-GDP and unbinding after Cdc24 and Bem1 exchanges the bound nucleotide for GTP [166]. The model shows that such a non-equilibrium binding cycle would dissipate around $7 \times 10^{-3}\text{ k}_B\text{T/s}$ per particle to generate the same level of polarisation ($\mu(\rho) = 12$) as active transport, which dissipates $2.6\text{ k}_B\text{T/s}$ per parti-

cle. Even though a driven binding cycle can thus dissipate orders of magnitude less free-energy than active transport along the filament to create the same membrane spot, the absolute dissipation of active transport could still be low compared to other cellular processes such as protein translation, and therefore evade evolutionary selection pressure. Previously, it was estimated that budding yeast experiences selection pressure against genes that require more than 1×10^4 molecules of ATP per cell cycle [180]. We can make an estimate of the energy costs of cell polarisation via transport alone by assuming that the polarisation machinery is active for 30 min per cell cycle, which is a quarter of the minimal duration of the cell cycle of yeast [180]. Furthermore, we assume that 1000 copies of the polarising protein are involved, similar to the copy number of Cdc42 in budding yeast [181], and that ATP hydrolysis releases $18k_B T$ [179]. Then, the power predicted by our model in the biologically relevant regime ($2.6k_B T/s$) leads to the estimate that active transport would hydrolyse around 2.6×10^5 molecules of ATP per cell cycle to create cell polarisation. Hence, ignoring other fitness effects of the different polarisation mechanisms, the energetic requirements alone can be sufficient to stimulate the formation of a driven binding cycle.

In fact, our work provides a new perspective on the design logic of these systems. In particular, experiments indicate that Pom1 itself is not actively transported along the microtubule filaments [19, 20]. Instead, the filaments only mark the location where Pom1 is delivered to the membrane by transporting Tea4 to the microtubule tip, specifying the position where the phosphatase Dis2 becomes active in dephosphorylating Pom1, allowing Pom1 to bind to the membrane [19, 20]. The filaments could in principle also be used to actively transport Pom1, but our work suggests that this would only marginally enhance polarisation while it would significantly increase energy dissipation. When active transport of the polarising protein does occur, this transport may be sufficient to create a polarised protein density on the membrane, but it is still more efficient to implement an additional driven binding cycle, which is the case for the Cdc42 system in budding yeast.

A non-equilibrium binding cycle is more efficient because the particles only dissipate free-energy when they participate in the flux that moves from the filament to the membrane, and it is this flux that causes the spot on the membrane. In contrast, the motor proteins drive proteins along the entire filament, and many unbind from the filament before they reach the membrane. These cycles waste the free energy that was invested by the motor proteins, because the high diffusion constant in the bulk almost immediately homogenises the protein distribution in the bulk again. However, the binding cycle will likely also lead to the wasteful release of chemical free energy that is not captured by our model. For example, a phosphorylation cycle will typically include erroneous dephosphorylation steps, dissipating the free energy obtained from hydrolysing an NTP molecule. Integrating such wasteful processes in the minimal model presented here, it is likely that breaking detailed balance in the cycle of binding reactions also leads to a significant free-energy cost. In addition, simulations show that the transport along filaments is less wasteful when the finite magnitude of the diffusion constant in the bulk is taken into account, bringing the efficiencies of transport and binding closer together. Nonetheless, it is fundamentally difficult to create a membrane spot when binding is in equilibrium, because detailed balance causes the binding rate from the bulk to the mem-

brane to be large when the binding rate from the filament to the membrane is large. This increased binding rate from the bulk leads to a large homogeneous equilibrium concentration of proteins on the membrane, lowering the relative effect of the proteins deposited by the filament. Furthermore, we saw in Fig. 6.7 that transport generates a high density spot on the membrane via a direct reversible interchange of particles between this membrane spot and a strongly compressed density of particles on the tip of the filament. When exclusion effects between the proteins on the filament are taken into account, it may not be possible to create such a high density concentration on the tip of the filament [182, 183], preventing the formation of a membrane spot. In Sec. 6.5, we show that increasing the rate to bind from the filament to the membrane reduces the protein density at the front of the filament, but then an active binding cycle is required to still create a significant spot on the membrane. Hence, it is theoretically possible to create a polarised distribution of proteins on the membrane by active transport alone, but both in cells or in synthetic systems, membrane polarisation would likely be superior using a dissipative mechanism that biases the binding from the filament to the membrane.

Filament radius r	$0.0125 \mu\text{m}$
Container radius R	$10.0125 \mu\text{m}$
Filament length L	$10 \mu\text{m}$
Diffusion constant on filament D_F	$0.004 \mu\text{m}^2 \text{s}^{-1}$
Driving velocity on filament v_F	$0.5 \mu\text{m s}^{-1}$
Diffusion constant on membrane D_M	$5 \mu\text{m}^2 \text{s}^{-1}$
Diffusion constant in bulk D_B	$60 \mu\text{m}^2 \text{s}^{-1}$
Binding rate to the filament u_{BF}	$100 \mu\text{m s}^{-1}$
Unbinding rate from filament k_{FB}	0.5s^{-1}
Binding rate to membrane u_{BM}	$0.01 \mu\text{m s}^{-1}$
Unbinding rate from membrane k_{MB}	0.1s^{-1}
Rate of deposit on the membrane u_{FM}	$0.01 \mu\text{m s}^{-1}$
Reverse rate from the membrane u_{MF}	$20 \mu\text{m s}^{-1}$

Table 6.1: Model parameters and values, as derived in Sec. 6.2. For most parameters, we found a biologically relevant value in the literature, while for u_{BF} we chose a value that allows for the formation of a pronounced membrane spot, and u_{MF} is set by detailed balance.

Filament radius ρ	1.8×10^{-3}
Container radius P	1.4
Filament length Λ	112
Drift velocity α	11
Filament-membrane transition rate β	0.22
Membrane-filament transition rate γ	28
Binding driven factor δ	1

Table 6.2: The values of the dimensionless parameters, defined in Eq. 6.10, given by the values listed in Table 6.1.

APPENDIX

6.A. INTEGRATION CONSTANTS OF ANALYTICAL SOLUTIONS

In the Eq. 6.12 and Eq. 6.13, we found two ordinary differential equations for the non-dimensionalised protein densities on the filament and on the membrane. These equations are valid in steady state, and when the diffusion constant in the bulk D_B is very large, such that there are no density fluctuations in the bulk. The solutions for the dimensionless density on the filament $\varphi(\lambda)$ and the dimensionless density on the membrane $\mu(\sigma)$ are given in Eq. 6.18 and Eq. 6.19, respectively. These solutions involve the integration constants C_1 , C_2 , C_3 , and C_4 , which are determined by the four boundary conditions Eqs. 6.14–6.17. The boundary conditions provide a set of linear equations on the integration constants, which can be solved by standard linear algebra. Using that the

Longitudinal reaction length l_{long}	$5 \times 10^{-3} \mu\text{m}$
Radial reaction length l_{rad}	$5 \times 10^{-3} \mu\text{m}$
Time step δt	$1 \times 10^{-6} \text{s}$

Table 6.3: The parameter values used for the simulations of a system with a finite bulk diffusion constant. The reaction lengths were chosen such that they are (much) smaller than all length scales in the system, but large enough that a diffusing particle with diffusion constant D_B that comes close to the membrane has a significant probability to be within a reaction volume during a time step δt . The time step was chosen such that all reaction rates lead to a small (<1%) probability of performing a reaction each time step.

modified Bessel functions obey the relations

$$\partial_\sigma I_0(\sigma) = I_1(\sigma), \quad (6.49)$$

$$\partial_\sigma K_0(\sigma) = -K_1(\sigma), \quad (6.50)$$

we find the following integration constants,

6

$$\begin{aligned}
C_1 = \frac{1}{\mathcal{N}} & \left\{ (I_1(\text{P}) K_1(\rho) - K_1(\text{P}) I_1(\rho)) \right. \\
& \cdot \left[\alpha (\sqrt{4 + \alpha^2} + \alpha) \left(1 - \exp \left[\frac{\Lambda}{2} (\sqrt{4 + \alpha^2} - \alpha) \right] \right) \right] \\
& + \beta (1 - \delta) (\sqrt{4 + \alpha^2} + \alpha) \exp \left[\frac{\Lambda}{2} (\sqrt{4 + \alpha^2} - \alpha) \right] - 2\alpha\beta \\
& + \alpha\gamma (I_1(\text{P}) K_0(\rho) + K_1(\text{P}) I_0(\rho)) \\
& \left. \cdot (\sqrt{4 + \alpha^2} + \alpha) \left(1 - \exp \left[\frac{\Lambda}{2} (\sqrt{4 + \alpha^2} - \alpha) \right] \right) \right\}, \quad (6.51)
\end{aligned}$$

$$\begin{aligned}
C_2 = \frac{1}{\mathcal{N}} & \left\{ (I_1(\text{P}) K_1(\rho) - K_1(\text{P}) I_1(\rho)) \right. \\
& \cdot \left[\alpha (\sqrt{4 + \alpha^2} - \alpha) \left(1 - \exp \left[-\frac{\Lambda}{2} (\sqrt{4 + \alpha^2} + \alpha) \right] \right) \right] \\
& + \beta (1 - \delta) (\sqrt{4 + \alpha^2} - \alpha) \exp \left[-\frac{\Lambda}{2} (\sqrt{4 + \alpha^2} + \alpha) \right] + 2\alpha\beta \\
& + \alpha\gamma (I_1(\text{P}) K_0(\rho) + K_1(\text{P}) I_0(\rho)) \\
& \left. \cdot (\sqrt{4 + \alpha^2} - \alpha) \left(1 - \exp \left[-\frac{\Lambda}{2} (\sqrt{4 + \alpha^2} + \alpha) \right] \right) \right\}, \quad (6.52)
\end{aligned}$$

$$\begin{aligned}
C_3 = \frac{\gamma I_1(\mathbf{P})}{\delta \mathcal{N}} & \left\{ (1 - \delta) \right. \\
& \cdot \left(-2 \exp \left[\frac{\Lambda}{2} (\sqrt{4 + \alpha^2} - \alpha) \right] + 2 \exp \left[-\frac{\Lambda}{2} (\sqrt{4 + \alpha^2} + \alpha) \right] \right) \\
& - \alpha \left[(\sqrt{4 + \alpha^2} + \alpha) \exp \left[\frac{\Lambda}{2} (\sqrt{4 + \alpha^2} - \alpha) \right] \right. \\
& \quad \left. + (\sqrt{4 + \alpha^2} - \alpha) \exp \left[-\frac{\Lambda}{2} (\sqrt{4 + \alpha^2} + \alpha) \right] \right] + 2\alpha \sqrt{4 + \alpha^2} \left. \right\}, \quad (6.53)
\end{aligned}$$

$$\begin{aligned}
C_4 = \frac{\gamma K_1(\mathbf{P})}{\delta \mathcal{N}} & \left\{ (1 - \delta) \right. \\
& \cdot \left(-2 \exp \left[\frac{\Lambda}{2} (\sqrt{4 + \alpha^2} - \alpha) \right] + 2 \exp \left[-\frac{\Lambda}{2} (\sqrt{4 + \alpha^2} + \alpha) \right] \right) \\
& - \alpha \left[(\sqrt{4 + \alpha^2} + \alpha) \exp \left[\frac{\Lambda}{2} (\sqrt{4 + \alpha^2} - \alpha) \right] \right. \\
& \quad \left. + (\sqrt{4 + \alpha^2} - \alpha) \exp \left[-\frac{\Lambda}{2} (\sqrt{4 + \alpha^2} + \alpha) \right] \right] + 2\alpha \sqrt{4 + \alpha^2} \left. \right\}. \quad (6.54)
\end{aligned}$$

To prevent repetition, we have defined the denominator \mathcal{N} ,

$$\begin{aligned}
\mathcal{N} = & (I_1(\mathbf{P}) K_1(\rho) - K_1(\mathbf{P}) I_1(\rho)) \left\{ \right. \\
& - 2 \exp \left[\frac{\Lambda}{2} (\sqrt{4 + \alpha^2} - \alpha) \right] + 2 \exp \left[-\frac{\Lambda}{2} (\sqrt{4 + \alpha^2} + \alpha) \right] \\
& - \beta \left[(\sqrt{4 + \alpha^2} + \alpha) \exp \left[\frac{\Lambda}{2} (\sqrt{4 + \alpha^2} - \alpha) \right] \right. \\
& \quad \left. + (\sqrt{4 + \alpha^2} - \alpha) \exp \left[-\frac{\Lambda}{2} (\sqrt{4 + \alpha^2} + \alpha) \right] \right] \left. \right\} \\
& + \gamma (I_1(\mathbf{P}) K_0(\rho) + K_1(\mathbf{P}) I_0(\rho)) \left\{ \right. \\
& - 2 \exp \left[\frac{\Lambda}{2} (\sqrt{4 + \alpha^2} - \alpha) \right] + 2 \exp \left[-\frac{\Lambda}{2} (\sqrt{4 + \alpha^2} + \alpha) \right] \left. \right\}. \quad (6.55)
\end{aligned}$$

Using these definitions and Eq. 6.18 and Eq. 6.19, we now have a full analytical solution for the protein densities on the filament and the membrane.

6.B. REFLECTING BOUNDARY ALGORITHMS

The Monte Carlo algorithm that simulates the diffusion of the particle in each of the system parts makes a finite spatial step every time step. If the particle is at the longitudinal position z_0 in the bulk or on the filament, then the algorithm proposes a new position z'_1 by taking a step δz ,

$$z'_1 = z_0 + \delta z, \quad (6.56)$$

where the difference is drawn from a normal distribution, $\delta z \sim \mathcal{N}\left(0, \sqrt{2D\delta t}\right)$ and D is the appropriate diffusion constant. If this proposed position z'_1 is outside the container, it is reflected back in the boundary. Assuming that $L \gg \sqrt{2D\delta t}$, such that a particle is never reflected twice, we can summarise the diffusive algorithm by

$$z_1 = z'_1 \quad \text{if } 0 \leq z'_1 \leq L, \quad (6.57)$$

$$z_1 = -z'_1 \quad \text{if } z'_1 < 0, \quad (6.58)$$

$$z_1 = 2L - z'_1 \quad \text{if } z'_1 > L. \quad (6.59)$$

These reflections are reversible. For example, a particle that is close to $z = 0$ can move from $z_0 > 0$ to $z_1 > 0$ directly, or it can move to $z'_1 = -z_1$ after which it is reflected to z_1 . If we denote the probability density function of $\mathcal{N}\left(0, \sqrt{2D\delta t}\right)$ by $n(z)$, then the total probability density for the transition equals

$$p(z_0 \rightarrow z_1) = n(z_1 - z_0) + n(z'_1 - z_0) = n(z_0 - z_1) + n(z'_0 - z_1) = p(z_1 \rightarrow z_0), \quad (6.60)$$

where we used that $z'_1 = -z_1$ and $z'_0 = -z_0$. Since the probability density function of the normal distribution only depends on the traversed distance and not on the direction (sign) of the step, and because reflections preserve distance, the reflective algorithm obeys detailed balance.

When the particle is in the bulk or on the membrane, it makes two dimensional diffusive steps in the $x - y$ plane, where the radial coordinate $s = \sqrt{x^2 + y^2}$. Starting from a position \mathbf{s}_0 , a new position $\mathbf{s}'_1 = \mathbf{s}_0 + \delta \mathbf{s}$ is proposed, where both Cartesian coordinates of the difference vector $\delta \mathbf{s}$ are drawn from a normal distribution with standard deviation $\sqrt{2D\delta t}$. The proposed position can be inside the inner circle that represents the filament, $\|\mathbf{s}'_1\| < r$, or outside the outer circle that borders the container, $\|\mathbf{s}'_1\| > R$. As shown in Fig. 6.12, a path that crosses the outer circle is reflected in tangent line to the circle. To find the reflection point \mathbf{p} , we define points along the line $\mathbf{s}_0 - \mathbf{s}'_1$ as

$$\mathbf{l}(\lambda) = \mathbf{s}_0 + \lambda (\mathbf{s}'_1 - \mathbf{s}_0), \quad (6.61)$$

where $\mathbf{s}_0 = \mathbf{l}(0)$ and $\mathbf{s}'_1 = \mathbf{l}(1)$. Then, \mathbf{p} is the point where this line intersects the outer circle, providing the quadratic equation

$$\|\mathbf{l}(\lambda)\|^2 = R^2. \quad (6.62)$$

Then, the reflection point is given by the positive root of this equation, $\mathbf{p} = \mathbf{l}(\lambda_+)$, with

$$\lambda_+ = \frac{1}{\|\mathbf{s}'_1 - \mathbf{s}_0\|^2} \left[\sqrt{(\mathbf{s}_0 \cdot (\mathbf{s}'_1 - \mathbf{s}_0))^2 + (R^2 - \|\mathbf{s}_0\|^2) \|\mathbf{s}'_1 - \mathbf{s}_0\|^2} - \mathbf{s}_0 \cdot (\mathbf{s}'_1 - \mathbf{s}_0) \right]. \quad (6.63)$$

Knowing \mathbf{p} , we define the unit vector $\hat{\mathbf{p}} = \mathbf{p}/R$. The proposed point \mathbf{s}'_1 is reflected by moving it in the direction of $\hat{\mathbf{p}}$,

$$\mathbf{r}''_1 = \mathbf{r}'_1 - 2[\hat{\mathbf{p}} \cdot \mathbf{r}'_1 - R] \hat{\mathbf{p}}. \quad (6.64)$$

As shown in Fig. 6.12, it is not guaranteed that $\|\mathbf{r}''_1\| \leq R$, so the algorithm checks whether the newly proposed point is inside the container, and if not it repeats the previous steps

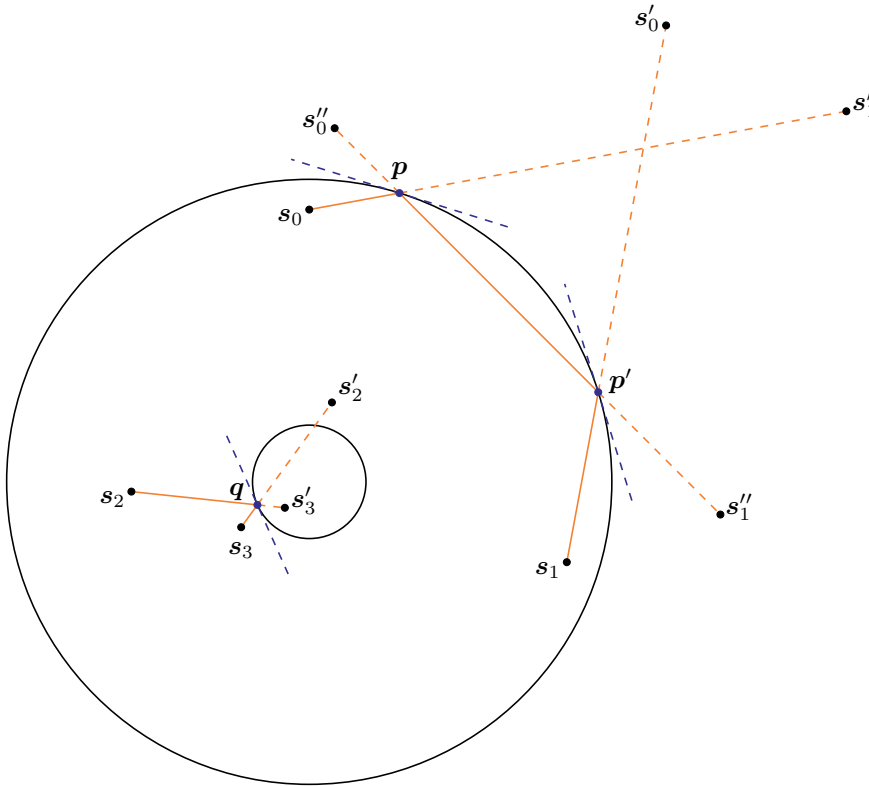


Figure 6.12: Starting from a position s_0 , the diffusion algorithm can propose a new point s'_1 outside of the container. To bring the proposed point back into the outer circle, we find the point p where the line $s_0-s'_1$ intersects the outer circle, and reflect s'_1 in the line tangent to the circle through p . The resulting point, s''_1 , still lies outside the circle in this example, so we repeat the procedure, reflecting s''_1 in the tangent line through p' , giving s_1 . Starting from s_1 , taking the proposed point s'_0 leads to the exact reverse of the first path. Similarly, we can start from a position s_2 and propose a point s'_3 that lies inside the inner circle. Again, we find the intersection point q and reflect the point in the tangent line through q to find s_3 . The reverse transition from s_3 to s_2 occurs when we propose a point s'_2 that is outside of the inner circle, showing that we have to reflect any line that passes through the inner circle to guarantee reversibility of all paths.

replacing the old point \mathbf{r}_0 with \mathbf{p} and replacing the proposed point \mathbf{r}'_1 with \mathbf{r}''_1 . The algorithm ends when the proposed point is inside the container, setting \mathbf{r}_1 .

Fig. 6.12 shows that we perform similar reflections in the inner circle with radius r that represents the filament. Starting from an initial position \mathbf{s}_2 inside the container, a proposed point \mathbf{s}'_3 can be inside the filament. Furthermore, the line $\mathbf{s}_2\text{—}\mathbf{s}'_3$ can cross the inner circle even when the proposed point is outside the filament. In both cases, we reflect the line in the first point that crosses the inner circle. Defining the reflection point \mathbf{q} as the first intersection point between the inner circle and the line

$$\mathbf{l}(\lambda) = \mathbf{s}_2 + \lambda (\mathbf{s}'_3 - \mathbf{s}_2), \quad (6.65)$$

the reflection point follows from the smallest solution of the quadratic equation

$$\|\mathbf{l}(\lambda)\|^2 = r^2. \quad (6.66)$$

To test whether a reflection is necessary, we first check if $\|\mathbf{s}'_3 - \mathbf{s}_2\| > \|\mathbf{s}_2\| - r$. If that is not the case, then the line $\mathbf{s}_2\text{—}\mathbf{s}'_3$ is not long enough to reach the circle. If this test is positive, we calculate the discriminant of the second order polynomial in λ given by Eq. 6.66. If the discriminant is negative or zero, then the extended line through \mathbf{s}_2 and \mathbf{s}'_3 never crosses the inner circle or only touches it in one point, respectively. In either case, no reflection is necessary. If a reflection is still possible at that point, we calculate the smallest root of Eq. 6.66,

$$\lambda_- = \frac{1}{\|\mathbf{s}'_3 - \mathbf{s}_2\|^2} \left[-\sqrt{(\mathbf{s}_2 \cdot (\mathbf{s}'_3 - \mathbf{s}_2))^2 - (\|\mathbf{s}_2\|^2 - r^2) \|\mathbf{s}'_3 - \mathbf{s}_2\|^2} - \mathbf{s}_2 \cdot (\mathbf{s}'_3 - \mathbf{s}_2) \right]. \quad (6.67)$$

Finally, we test if $\lambda_- < 0$ or if $\lambda_- \geq 1$, which together with the assumption that $\|\mathbf{s}_2\| \geq r$ implies that the line $\mathbf{s}_2\text{—}\mathbf{s}'_3$ never crosses the circle. If $0 \leq \lambda_- < 1$, we know that the line has crossed the circle, and we perform a reflection in the point $\mathbf{q} = \mathbf{l}(\lambda_-)$. Defining the unit vector $\hat{\mathbf{q}} = \mathbf{q}/r$, the reflected point is located at

$$\mathbf{s}_3 = \mathbf{s}'_3 + 2 [r - \hat{\mathbf{q}} \cdot \mathbf{s}'_3] \hat{\mathbf{q}}. \quad (6.68)$$

This reflection is guaranteed to lie outside of the inner circle, completing our diffusive algorithm.

REFERENCES

- [1] P. A. Janmey, *The Cytoskeleton and Cell Signaling: Component Localization and Mechanical Coupling*, *Physiol. Rev.* **78**, 763 (1998).
- [2] O. Moujaber and U. Stochaj, *The Cytoskeleton as Regulator of Cell Signaling Pathways*, *Trends Biochem. Sci.* **45**, 96 (2020).
- [3] C. A. Henderson, C. G. Gomez, S. M. Novak, L. Mi-Mi, and C. C. Gregorio, *Overview of the Muscle Cytoskeleton*, *Comprehensive Physiology*, 891 (2017).
- [4] S. Seetharaman and S. Etienne-Manneville, *Cytoskeletal Crosstalk in Cell Migration*, *Trends Cell Biol.* **30**, 720 (2020).
- [5] T. D. Pollard, *Mechanics of cytokinesis in eukaryotes*, *Curr. Opin. Cell Biol.* **22**, 50 (2010).
- [6] T. K. Akhshi, D. Wernike, and A. Piekny, *Microtubules and actin crosstalk in cell migration and division*, *Cytoskeleton (Hoboken)* **71**, 1 (2014).
- [7] C. H. Tan, I. Gasic, S. P. Huber-Reggi, D. Dudka, M. Barisic, H. Maiato, and P. Meraldi, *The equatorial position of the metaphase plate ensures symmetric cell divisions*, *eLife* **4**, e05124 (2015).
- [8] S. Inoué, *Cell division and the mitotic spindle*, *J. Cell Biol.* **91**, 131s (1981).
- [9] B. Alberts, D. Bray, J. Lewis, M. Raff, K. Roberts, J. D. Watson, B. Alberts, D. Bray, J. Lewis, M. Raff, K. Roberts, and J. D. Watson, *Molecular Biology of the Cell*, 3rd ed. (Garland Science, 1994).
- [10] T. H. Cheffings, N. J. Burroughs, and M. K. Balasubramanian, *Actomyosin Ring Formation and Tension Generation in Eukaryotic Cytokinesis*, *Curr. Biol.* **26**, R719 (2016).
- [11] M. Stewart, *Intermediate filaments: structure, assembly and molecular interactions*, *Curr. Opin. Cell Biol.* **2**, 91 (1990).
- [12] R. H. Wade and A. A. Hyman, *Microtubule structure and dynamics*, *Curr. Opin. Cell Biol.* **9**, 12 (1997).
- [13] L. Haviv, N. Gov, Y. Ideses, and A. Bernheim-Groswasser, *Thickness distribution of actin bundles in vitro*, *Eur. Biophys. J.* **37**, 447 (2008).
- [14] M. Melak, M. Plessner, and R. Grosse, *Actin visualization at a glance*, *J. Cell Sci.* **130**, 525 (2017).

- [15] Q. Wen and P. A. Janmey, *Polymer physics of the cytoskeleton*, *Curr. Opin. Solid State Mater. Sci.* **15**, 177 (2011).
- [16] A. A. Hyman, S. Salser, D. N. Drechsel, N. Unwin, and T. J. Mitchison, *Role of GTP hydrolysis in microtubule dynamics: information from a slowly hydrolyzable analogue, GMPCPP*, *Mol. Biol. Cell* **3**, 1155 (1992).
- [17] U. Seifert, *Stochastic thermodynamics, fluctuation theorems and molecular machines*, *Rep. Prog. Phys.* **75**, 126001 (2012).
- [18] Z. Lansky, M. Braun, A. Lüdecke, M. Schlierf, P. R. ten Wolde, M. E. Janson, and S. Diez, *Diffusible Crosslinkers Generate Directed Forces in Microtubule Networks*, *Cell* **160**, 1159 (2015).
- [19] O. Hachet, M. Berthelot-Grosjean, K. Kokkoris, V. Vincenzetti, J. Moosbrugger, and S. G. Martin, *A phosphorylation cycle shapes gradients of the DYRK family kinase Pom1 at the plasma membrane*, *Cell* **145**, 1116 (2011).
- [20] S. G. Martin and R. A. Arkowitz, *Cell polarization in budding and fission yeasts*, *FEMS Microbiol. Rev.* **38**, 228 (2014).
- [21] J. Kierfeld, K. Frentzel, P. Kraikivski, and R. Lipowsky, *Active dynamics of filaments in motility assays*, *Eur. Phys. J. Spec. Top.* **157**, 123 (2008).
- [22] E. T. Jaynes, *Information Theory and Statistical Mechanics*, *Phys. Rev.* **106**, 620 (1957).
- [23] J. C. Maxwell, *IV. On the dynamical theory of gases*, *Philos. Trans. Royal Soc.* **157**, 49 (1867).
- [24] C. Maes, K. Netočný, and B. Wynants, *On and beyond entropy production: the case of Markov jump processes*, *Markov. Process. Relat.* **14**, 445 (2008).
- [25] C. Maes, *Local detailed balance*, (2020).
- [26] A. D. Fokker, *Die mittlere Energie rotierender elektrischer Dipole im Strahlungsfeld*, *Ann. Phys.* **348**, 810 (1914).
- [27] M. Planck, *Über einen Satz der statistischen Dynamik und seine Erweiterung in der Quantentheorie*, *Sitzungsber. Königl. Preuss. Akad. Wiss. Berlin* **24**, 324 (1917).
- [28] A. Einstein, *Über die von der molekularkinetischen Theorie der Wärme geforderte Bewegung von in ruhenden Flüssigkeiten suspendierten Teilchen*, *Ann. Phys. (Berl.)* **322**, 549 (1905).
- [29] A. Kolmogoroff, *Über die analytischen Methoden in der Wahrscheinlichkeitsrechnung*, *Math. Ann.* **104**, 415 (1931).
- [30] H. A. Kramers, *Brownian motion in a field of force and the diffusion model of chemical reactions*, *Physica* **7**, 284 (1940).

- [31] L. Sjögren, *Lecture notes Stochastic processes*, Accessed online on 2020-08-07.
- [32] B. Peters, *Reaction Coordinates and Mechanistic Hypothesis Tests*, *Annu. Rev. Phys. Chem.* **67**, 669 (2016).
- [33] G. Hummer, *From transition paths to transition states and rate coefficients*, *J. Chem. Phys.* **120**, 516 (2004).
- [34] P. Hänggi, P. Talkner, and M. Borkovec, *Reaction-rate theory: fifty years after Kramers*, *Rev. Mod. Phys.* **62**, 251 (1990).
- [35] H. Wierenga and P. R. ten Wolde, *Diffusible Cross-linkers Cause Superexponential Friction Forces*, *Phys. Rev. Lett.* **125**, 078101 (2020).
- [36] A. Yamashita, M. Sato, A. Fujita, M. Yamamoto, and T. Toda, *The Roles of Fission Yeast Ase1 in Mitotic Cell Division, Meiotic Nuclear Oscillation, and Cytokinesis Checkpoint Signaling*, *Mol. Biol. Cell* **16**, 1378 (2005).
- [37] I. Loïdice, J. Staub, T. G. Setty, N.-P. T. Nguyen, A. Paoletti, and P. T. Tran, *Ase1p Organizes Antiparallel Microtubule Arrays during Interphase and Mitosis in Fission Yeast*, *Mol. Biol. Cell* **16**, 1756 (2005).
- [38] M. E. Janson, R. Loughlin, I. Loïdice, C. Fu, D. Brunner, F. J. Nédélec, and P. T. Tran, *Crosslinkers and Motors Organize Dynamic Microtubules to Form Stable Bipolar Arrays in Fission Yeast*, *Cell* **128**, 357 (2007).
- [39] T. Courthouex, G. Gay, Y. Gachet, and S. Tournier, *Ase1/Prc1-dependent spindle elongation corrects merotelically attached chromosomes during anaphase in fission yeast*, *J. Cell Biol.* **187**, 399 (2009).
- [40] R. Subramanian, E. M. Wilson-Kubalek, C. P. Arthur, M. J. Bick, E. A. Campbell, S. A. Darst, R. A. Milligan, and T. M. Kapoor, *Insights into antiparallel microtubule crosslinking by PRC1, a conserved nonmotor microtubule binding protein*, *Cell* **142**, 433 (2010).
- [41] P. Bieling, I. A. Telley, and T. Surrey, *A minimal midzone protein module controls formation and length of antiparallel microtubule overlaps*, *Cell* **142**, 420 (2010).
- [42] C. Hentrich and T. Surrey, *Microtubule organization by the antagonistic mitotic motors kinesin-5 and kinesin-14*, *J. Cell Biol.* **189**, 465 (2010).
- [43] M. Braun, Z. Lansky, G. Fink, F. Ruhnnow, S. Diez, and M. E. Janson, *Adaptive braking by Ase1 prevents overlapping microtubules from sliding completely apart*, *Nat. Cell Biol.* **13**, 1259 (2011).
- [44] R. Subramanian, S.-C. Ti, L. Tan, S. A. Darst, and T. M. Kapoor, *Marking and measuring single microtubules by PRC1 and kinesin-4*, *Cell* **154**, 377 (2013).
- [45] D. Johann, D. Goswami, and K. Kruse, *Assembly of bipolar microtubule structures by passive cross-linkers and molecular motors*, *Phys. Rev. E* **93**, 062415 (2016).

- [46] R. Blackwell, C. Edelmaier, O. Sweezy-Schindler, A. Lamson, Z. R. Gergely, E. O'Toole, A. Crapo, L. E. Hough, J. R. McIntosh, M. A. Glaser, and M. D. Betterton, *Physical determinants of bipolar mitotic spindle assembly and stability in fission yeast*, *Sci. Adv.* **3**, e1601603 (2017).
- [47] S. A. Rincon, A. Lamson, R. Blackwell, V. Syrovatkina, V. Fraissier, A. Paoletti, M. D. Betterton, and P. T. Tran, *Kinesin-5-independent mitotic spindle assembly requires the antiparallel microtubule crosslinker Ase1 in fission yeast*, *Nat. Commun.* **8**, 15286 (2017).
- [48] S. Wijeratne and R. Subramanian, *Geometry of antiparallel microtubule bundles regulates relative sliding and stalling by PRC1 and Kif4A*, *eLife* **7**, e32595 (2018).
- [49] J. Hannabuss, M. Lera-Ramirez, N. I. Cade, F. J. Fourniol, F. J. Nédélec, and T. Surrey, *Self-Organization of Minimal Anaphase Spindle Midzone Bundles*, *Curr. Biol.* **29**, 2120 (2019).
- [50] A. R. Lamson, C. J. Edelmaier, M. A. Glaser, and M. D. Betterton, *Theory of Cytoskeletal Reorganization during Cross-Linker-Mediated Mitotic Spindle Assembly*, *Biophys. J.* **116**, 1719 (2019).
- [51] Z. Xue and A. M. Sokac, *-Back-to-back mechanisms drive actomyosin ring closure during Drosophila embryo cleavage*, *J. Cell Biol.* **215**, 335 (2016).
- [52] R. Neujahr, C. Heizer, and G. Gerisch, *Myosin II-independent processes in mitotic cells of Dictyostelium discoideum: redistribution of the nuclei, re-arrangement of the actin system and formation of the cleavage furrow*, *J. Cell Sci.* **110**, 123 (1997).
- [53] X. Ma, M. Kovács, M. A. Conti, A. Wang, Y. Zhang, J. R. Sellers, and R. S. Adelstein, *Nonmuscle myosin II exerts tension but does not translocate actin in vertebrate cytokinesis*, *Proc. Natl. Acad. Sci. U.S.A.* **109**, 4509 (2012).
- [54] O. Kučera, D. Janda, V. Siahhan, S. H. Dijkstra, E. Pilátová, E. Zatecka, S. Diez, M. Braun, and Z. Lansky, *Anillin propels myosin-independent constriction of actin rings*, (2020).
- [55] S. Walcott and S. X. Sun, *Active force generation in cross-linked filament bundles without motor proteins*, *Phys. Rev. E* **82**, 050901 (2010).
- [56] A. Ward, F. Hilitski, W. Schwenger, D. Welch, A. W. C. Lau, V. Vitelli, L. Mahadevan, and Z. Dogic, *Solid friction between soft filaments*, *Nat. Mater.* **14**, 583 (2015).
- [57] S. Mukhina, Y.-L. Wang, and M. Murata-Hori, *Alpha-actinin is required for tightly regulated remodeling of the actin cortical network during cytokinesis*, *Dev. Cell* **13**, 554 (2007).
- [58] E. M. Reichl, Y. Ren, M. K. Morphew, M. Delannoy, J. C. Effler, K. D. Girard, S. Divi, P. A. Iglesias, S. C. Kuo, and D. N. Robinson, *Interactions between Myosin and Actin Crosslinkers Control Cytokinesis Contractility Dynamics and Mechanics*, *Curr. Biol.* **18**, 471 (2008).

- [59] S. Forth, K.-C. Hsia, Y. Shimamoto, and T. M. Kapoor, *Asymmetric Friction of Non-motor MAPs Can Lead to Their Directional Motion in Active Microtubule Networks*, *Cell* **157**, 420 (2014).
- [60] Y. Ezber, V. Belyy, S. Can, and A. Yildiz, *Dynein harnesses active fluctuations of microtubules for faster movement*, *Nat. Phys.* **16**, 312 (2020).
- [61] A. Vanossi, N. Manini, M. Urbakh, S. Zapperi, and E. Tosatti, *Colloquium: Modeling friction: From nanoscale to mesoscale*, *Rev. Mod. Phys.* **85**, 529 (2013).
- [62] V. Bormuth, V. Varga, J. Howard, and E. Schäffer, *Protein Friction Limits Diffusive and Directed Movements of Kinesin Motors on Microtubules*, *Science* **325**, 870 (2009).
- [63] H. Suda, *Origin of Friction Derived from Rupture Dynamics*, *Langmuir* **17**, 6045 (2001).
- [64] A. F. Huxley, *Muscle structure and theories of contraction*, *Prog. Biophys. Biophys. Chem.* **7**, 255 (1957).
- [65] C. S. Peskin, *An Inverse Problem in Muscle Mechanics*, in *Partial differential equations in biology* (Courant Institute of Mathematical Sciences, New York University, 1976).
- [66] H. M. Lacker, *Cross-bridge dynamics in skeletal muscle: Mathematical methods for determining the reaction rate and force-extension curves of cross-bridges from the macroscopic behavior of muscle*, Ph.D. thesis, New York University, New York (1977).
- [67] H. M. Lacker and C. S. Peskin, *A mathematical method for the unique determination of cross-bridge properties from steady-state mechanical and energetic experiments on macroscopic muscle*, in *Some Mathematical Questions in Biology—Muscle Physiology*, Lectures on Mathematics in the Life Sciences, Vol. 16 (AMS, 1986) pp. 121–153.
- [68] T. a. J. Duke, *Molecular model of muscle contraction*, *Proc. Natl. Acad. Sci. U.S.A.* **96**, 2770 (1999).
- [69] M. Srinivasan and S. Walcott, *Binding site models of friction due to the formation and rupture of bonds: State-function formalism, force-velocity relations, response to slip velocity transients, and slip stability*, *Phys. Rev. E* **80**, 046124 (2009).
- [70] S. Walcott and S. X. Sun, *A mechanical model of actin stress fiber formation and substrate elasticity sensing in adherent cells*, *Proc. Natl. Acad. Sci. U.S.A.* **107**, 7757 (2010).
- [71] S. Forth and T. M. Kapoor, *The mechanics of microtubule networks in cell division*, *J. Cell Biol.* **216**, 1525 (2017).

- [72] K. Tawada and K. Sekimoto, *Protein friction exerted by motor enzymes through a weak-binding interaction*, J. Theor. Biol. **150**, 193 (1991).
- [73] S. Leibler and D. A. Huse, *Porters versus rowers: a unified stochastic model of motor proteins*. J. Cell Biol. **121**, 1357 (1993).
- [74] M. Lera-Ramirez and F. J. Nédélec, *Theory of antiparallel microtubule overlap stabilization by motors and diffusible crosslinkers*, Cytoskeleton (Hoboken) **76**, 600 (2019).
- [75] B. Harland, S. Walcott, and S. X. Sun, *Adhesion dynamics and durotaxis in migrating cells*, Phys. Biol. **8**, 015011 (2011).
- [76] L. A. Amos and A. Klug, *Arrangement of Subunits in Flagellar Microtubules*, J. Cell Sci. **14**, 523 (1974).
- [77] E. H. Kellogg, S. Howes, S.-C. Ti, E. Ramírez-Aportela, T. M. Kapoor, P. Chacón, and E. Nogales, *Near-atomic cryo-EM structure of PRC1 bound to the microtubule*, Proc. Natl. Acad. Sci. U.S.A. **113**, 9430 (2016).
- [78] S. Jeney, E. H. K. Stelzer, H. Grubmüller, and E.-L. Florin, *Mechanical Properties of Single Motor Molecules Studied by Three-Dimensional Thermal Force Probing in Optical Tweezers*, ChemPhysChem **5**, 1150 (2004).
- [79] M. Schlierf and M. Rief, *Temperature Softening of a Protein in Single-molecule Experiments*, J. Mol. Biol. **354**, 497 (2005).
- [80] H. Ahmadzadeh, D. H. Smith, and V. B. Shenoy, *Viscoelasticity of Tau Proteins Leads to Strain Rate-Dependent Breaking of Microtubules during Axonal Stretch Injury: Predictions from a Mathematical Model*, Biophys. J. **106**, 1123 (2014).
- [81] A. J. Hunt, F. Gittes, and J. Howard, *The force exerted by a single kinesin molecule against a viscous load*. Biophys. J. **67**, 766 (1994).
- [82] A. Prados, J. J. Brey, and B. Sánchez-Rey, *A dynamical monte carlo algorithm for master equations with time-dependent transition rates*, J. Stat. Phys. **89**, 709 (1997).
- [83] S. Arrhenius, *Über die Reaktionsgeschwindigkeit bei der Inversion von Rohrzucker durch Säuren*, Z. Phys. Chem. **4U**, 226 (1889).
- [84] P. Milewski, *Derivation of Gaussian Distribution from Binomial*, (2007), accessed online on 2018-11-22.
- [85] M. C. Uçar and R. Lipowsky, *Collective Force Generation by Molecular Motors Is Determined by Strain-Induced Unbinding*, Nano Lett. **20**, 669 (2020).
- [86] L. C. Kapitein, M. E. Janson, S. M. J. L. van den Wildenberg, C. C. Hoogenraad, C. F. Schmidt, and E. J. G. Peterman, *Microtubule-Driven Multimerization Recruits *ase1p* onto Overlapping Microtubules*, Curr. Biol. **18**, 1713 (2008).

- [87] L. C. Kapitein, E. J. G. Peterman, B. H. Kwok, J. H. Kim, T. M. Kapoor, and C. F. Schmidt, *The bipolar mitotic kinesin Eg5 moves on both microtubules that it crosslinks*, *Nature* **435**, 114 (2005).
- [88] C. Fu, J. J. Ward, I. Loiodice, G. Velve-Casquillas, F. J. Nédélec, and P. T. Tran, *Phospho-regulated interaction between kinesin-6 Klp9p and microtubule bundler Ase1p promotes spindle elongation*, *Dev. Cell* **17**, 257 (2009).
- [89] Y. Shimamoto, S. Forth, and T. M. Kapoor, *Measuring Pushing and Braking Forces Generated by Ensembles of Kinesin-5 Crosslinking Two Microtubules*, *Dev. Cell* **34**, 669 (2015).
- [90] C. Edelmaier, A. R. Lamson, Z. R. Gergely, S. Ansari, R. Blackwell, J. R. McIntosh, M. A. Glaser, and M. D. Betterton, *Mechanisms of chromosome biorientation and bipolar spindle assembly analyzed by computational modeling*, *eLife* **9**, e48787 (2020).
- [91] C. Leduc, F. Ruhnnow, J. Howard, and S. Diez, *Detection of fractional steps in cargo movement by the collective operation of kinesin-1 motors*, *Proc. Natl. Acad. Sci. U.S.A.* **104**, 10847 (2007).
- [92] K. C. Neuman and A. Nagy, *Single-molecule force spectroscopy: optical tweezers, magnetic tweezers and atomic force microscopy*, *Nat. Methods* **5**, 491 (2008).
- [93] M. Innerbichler, G. Menzl, and C. Dellago, *State-dependent diffusion coefficients and free energies for nucleation processes from Bayesian trajectory analysis*, *Mol. Phys.* **116**, 2987 (2018).
- [94] N. M. Temme, *Speciale functies in de mathematische fysica*, wetenschappelijke reeks No. 15 (Epsilon Uitgaven, Utrecht, 1990).
- [95] H. Li, D. J. DeRosier, W. V. Nicholson, E. Nogales, and K. H. Downing, *Microtubule Structure at 8 Å Resolution*, *Structure* **10**, 1317 (2002).
- [96] L. A. Amos, *Microtubule structure and its stabilisation*, *Org. Biomol. Chem.* **2**, 2153 (2004).
- [97] Z. J. Donhauser, W. B. Jobs, and E. C. Binka, *Mechanics of Microtubules: Effects of Protofilament Orientation*, *Biophys. J.* **99**, 1668 (2010).
- [98] A. Mitra, L. Meißner, R. Gandhimathi, R. Renger, F. Ruhnnow, and S. Diez, *Kinesin-14 motors drive a right-handed helical motion of antiparallel microtubules around each other*, *Nat. Commun.* **11**, 2565 (2020).
- [99] B. R. Graziano and O. D. Weiner, *Self-organization of protrusions and polarity during eukaryotic chemotaxis*, *Curr. Opin. Cell Biol.* **30**, 60 (2014).
- [100] R. Sunyer and X. Trepap, *Durotaxis*, *Curr. Biol.* **30**, R383 (2020).
- [101] X. Wu, A. Kodama, and E. Fuchs, *ACF7 Regulates Cytoskeletal-Focal Adhesion Dynamics and Migration and Has ATPase Activity*, *Cell* **135**, 137 (2008).

- [102] G. M. Cammarata, E. A. Bearce, and L. A. Lowery, *Cytoskeletal social networking in the growth cone: How +TIPs mediate microtubule-actin cross-linking to drive axon outgrowth and guidance*, *Cytoskeleton* (Hoboken) **73**, 461 (2016).
- [103] S. Etienne-Manneville, *Microtubules in cell migration*, *Annu. Rev. Cell Dev. Biol.* **29**, 471 (2013).
- [104] C. Garcin and A. Straube, *Microtubules in cell migration*, *Essays Biochem.* **63**, 509 (2019).
- [105] M. Dogterom and G. H. Koenderink, *Actin–microtubule crosstalk in cell biology*, *Nat. Rev. Mol. Cell Biol.* **20**, 38 (2019).
- [106] O. C. Rodriguez, A. W. Schaefer, C. A. Mandato, P. Forscher, W. M. Bement, and C. M. Waterman-Storer, *Conserved microtubule–actin interactions in cell movement and morphogenesis*, *Nat. Cell Biol.* **5**, 599 (2003).
- [107] M. P. López, F. Huber, I. Grigoriev, M. O. Steinmetz, A. Akhmanova, G. H. Koenderink, and M. Dogterom, *Actin–microtubule coordination at growing microtubule ends*, *Nat. Commun.* **5**, 4778 (2014).
- [108] I. Kaverina, K. Rottner, and J. V. Small, *Targeting, capture, and stabilization of microtubules at early focal adhesions*, *J. Cell Biol.* **142**, 181 (1998).
- [109] S. Stehbens and T. Wittmann, *Targeting and transport: how microtubules control focal adhesion dynamics*, *J. Cell Biol.* **198**, 481 (2012).
- [110] N. B. M. Rafiq, Y. Nishimura, S. V. Plotnikov, V. Thiagarajan, Z. Zhang, S. Shi, M. Natarajan, V. Viasnoff, P. Kanchanawong, G. E. Jones, and A. D. Bershadsky, *A mechano-signalling network linking microtubules, myosin IIA filaments and integrin-based adhesions*, *Nat. Mater.* **18**, 638 (2019).
- [111] J. L. Henty-Ridilla, A. Rankova, J. A. Eskin, K. Kenny, and B. L. Goode, *Accelerated actin filament polymerization from microtubule plus ends*, *Science* **352**, 1004 (2016).
- [112] N. Efimova, C. Yang, J. X. Chia, N. Li, C. J. Lengner, K. L. Neufeld, and T. M. Svitkina, *Branched actin networks are assembled on microtubules by adenomatous polyposis coli for targeted membrane protrusion*, *J. Cell Biol.* **219** (2020), 10.1083/jcb.202003091.
- [113] D. van de Willige, J. J. Hummel, C. Alkemade, O. I. Kahn, F. K. Au, R. Z. Qi, M. Dogterom, G. H. Koenderink, C. C. Hoogenraad, and A. Akhmanova, *Cytolinker Gas2L1 regulates axon morphology through microtubule-modulated actin stabilization*, *EMBO Rep.* **20**, e47732 (2019).
- [114] J. Alves-Silva, N. Sánchez-Soriano, R. Beaven, M. Klein, J. Parkin, T. H. Millard, H. J. Bellen, K. J. T. Venken, C. Ballestrem, R. A. Kammerer, and A. Prokop, *Spectraplakins Promote Microtubule-Mediated Axonal Growth by Functioning As Structural Microtubule-Associated Proteins and EB1-Dependent +TIPs (Tip Interacting Proteins)*, *J. Neurosci.* **32**, 9143 (2012).

- [115] S. Chakraborty, J. Mahamid, and W. Baumeister, *Cryoelectron Tomography Reveals Nanoscale Organization of the Cytoskeleton and Its Relation to Microtubule Curvature Inside Cells*, *Structure* **28**, 991 (2020).
- [116] T. L. Hill, *Theoretical problems related to the attachment of microtubules to kinetochores*, *Proc. Natl. Acad. Sci. U.S.A.* **82**, 4404 (1985).
- [117] C. S. Peskin, G. M. Odell, and G. F. Oster, *Cellular motions and thermal fluctuations: the Brownian ratchet*. *Biophys. J.* **65**, 316 (1993).
- [118] R. Zandi, D. Reguera, J. Rudnick, and W. M. Gelbart, *What drives the translocation of stiff chains?* *Proc. Natl. Acad. Sci. U.S.A.* **100**, 8649 (2003).
- [119] R. Rodríguez-García, V. A. Volkov, C.-Y. Chen, E. A. Katrukha, N. Olieric, A. Aher, I. Grigoriev, M. P. López, M. O. Steinmetz, L. C. Kapitein, G. Koenderink, M. Dogterom, and A. Akhmanova, *Mechanisms of Motor-Independent Membrane Remodeling Driven by Dynamic Microtubules*, *Curr. Biol.* **30**, 972 (2020).
- [120] G. Lan, B. R. Daniels, T. M. Dobrowsky, D. Wirtz, and S. X. Sun, *Condensation of FtsZ filaments can drive bacterial cell division*, *Proc. Natl. Acad. Sci. U.S.A.* **106**, 121 (2009).
- [121] M. Kwon, M. Bagonis, G. Danuser, and D. Pellman, *Direct Microtubule-Binding by Myosin-10 Orients Centrosomes toward Retraction Fibers and Subcortical Actin Clouds*, *Dev. Cell* **34**, 323 (2015).
- [122] J. Feng, Z. Hu, H. Chen, J. Hua, R. Wu, Z. Dong, L. Qiang, Y. Liu, P. W. Baas, and M. Liu, *Depletion of kinesin-12, a myosin-IIB-interacting protein, promotes migration of cortical astrocytes*, *J. Cell Sci.* **129**, 2438 (2016).
- [123] F. J. Ahmad, J. Hughey, T. Wittmann, A. Hyman, M. Greaser, and P. W. Baas, *Motor proteins regulate force interactions between microtubules and microfilaments in the axon*, *Nat. Cell Biol.* **2**, 276 (2000).
- [124] D. L. Beach, J. Thibodeaux, P. Maddox, E. Yeh, and K. Bloom, *The role of the proteins Kar9 and Myo2 in orienting the mitotic spindle of budding yeast*, *Curr. Biol.* **10**, 1497 (2000).
- [125] H. Yin, D. Pruyne, T. C. Huffaker, and A. Bretscher, *Myosin V orientates the mitotic spindle in yeast*, *Nature* **406**, 1013 (2000).
- [126] S. P. Maurer, P. Bieling, J. Cope, A. Hoenger, and T. Surrey, *GTP γ S microtubules mimic the growing microtubule end structure recognized by end-binding proteins (EBs)*, *Proc. Natl. Acad. Sci. U.S.A.* **108**, 3988 (2011).
- [127] A. Akhmanova and M. O. Steinmetz, *Control of microtubule organization and dynamics: two ends in the limelight*, *Nat. Rev. Mol. Cell Biol.* **16**, 711 (2015).
- [128] C. Duellberg, N. I. Cade, D. Holmes, and T. Surrey, *The size of the EB cap determines instantaneous microtubule stability*, *eLife* **5**, e13470 (2016).

- [129] M. J. Schnitzer, K. Visscher, and S. M. Block, *Force production by single kinesin motors*, *Nat. Cell Biol.* **2**, 718 (2000).
- [130] J. Fink, N. Carpi, T. Betz, A. Bétard, M. Chebah, A. Azioune, M. Bornens, C. Sykes, L. Fetler, D. Cuvelier, and M. Piel, *External forces control mitotic spindle positioning*, *Nat. Cell Biol.* **13**, 771 (2011).
- [131] J. D. Fenn, C. M. Johnson, J. Peng, P. Jung, and A. Brown, *Kymograph analysis with high temporal resolution reveals new features of neurofilament transport kinetics*, *Cytoskeleton (Hoboken)* **75**, 22 (2018).
- [132] C. Hookway, L. Ding, M. W. Davidson, J. Z. Rappoport, G. Danuser, and V. I. Gelfand, *Microtubule-dependent transport and dynamics of vimentin intermediate filaments*, *Mol. Biol. Cell* **26**, 1675 (2015).
- [133] C. Leduc and S. Etienne-Manneville, *Regulation of microtubule-associated motors drives intermediate filament network polarization*, *J. Cell Biol.* **216**, 1689 (2017).
- [134] A. Robert, P. Tian, S. A. Adam, M. Kittisopikul, K. Jaqaman, R. D. Goldman, and V. I. Gelfand, *Kinesin-dependent transport of keratin filaments: a unified mechanism for intermediate filament transport*, *FASEB J.* **33**, 388 (2019).
- [135] J. Lutkenhaus, *The ParA/MinD family puts things in their place*, *Trends Microbiol.* **20**, 411 (2012).
- [136] A. G. Vecchiarelli, K. Mizuuchi, and B. E. Funnell, *Surfing biological surfaces: exploiting the nucleoid for partition and transport in bacteria*, *Mol. Microbiol.* **86**, 513 (2012).
- [137] A. G. Vecchiarelli, Y. Seol, K. C. Neuman, and K. Mizuuchi, *A moving ParA gradient on the nucleoid directs subcellular cargo transport via a chemophoresis force*, *Bioarchitecture* **4**, 154 (2014).
- [138] M. Preciado López, F. Huber, I. Grigoriev, M. O. Steinmetz, A. Akhmanova, M. Dogterom, and G. H. Koenderink, *Chapter Seventeen - In Vitro Reconstitution of Dynamic Microtubules Interacting with Actin Filament Networks*, in *Methods in Enzymology*, Reconstituting the Cytoskeleton, Vol. 540, edited by R. D. Vale (Academic Press, 2014) pp. 301–320.
- [139] J. D. Pardee and J. Aspidich, *Chapter Eighteen - Purification of Muscle Actin*, in *Methods in Enzymology*, Structural and Contractile Proteins Part B: The Contractile Apparatus and the Cytoskeleton, Vol. 85 (Academic Press, 1982) pp. 164–181.
- [140] S. Honnappa, S. M. Gouveia, A. Weisbrich, F. F. Damberger, N. S. Bhavesh, H. Jawhari, I. Grigoriev, F. J. A. van Rijssel, R. M. Buey, A. Lawera, I. Jelesarov, F. K. Winkler, K. Wüthrich, A. Akhmanova, and M. O. Steinmetz, *An EB1-Binding Motif Acts as a Microtubule Tip Localization Signal*, *Cell* **138**, 366 (2009).

- [141] J. Schindelin, I. Arganda-Carreras, E. Frise, V. Kaynig, M. Longair, T. Pietzsch, S. Preibisch, C. Rueden, S. Saalfeld, B. Schmid, J.-Y. Tinevez, D. J. White, V. Hartenstein, K. Eliceiri, P. Tomancak, and A. Cardona, *Fiji: an open-source platform for biological-image analysis*, *Nat. Methods* **9**, 676 (2012).
- [142] P. Bieling, L. Laan, H. Schek, E. L. Munteanu, L. Sandblad, M. Dogterom, D. Brunner, and T. Surrey, *Reconstitution of a microtubule plus-end tracking system in vitro*, *Nature* **450**, 1100 (2007).
- [143] V. A. Volkov, P. J. Huis in 't Veld, M. Dogterom, and A. Musacchio, *Multivalency of NDC80 in the outer kinetochore is essential to track shortening microtubules and generate forces*, *eLife* **7**, e36764 (2018).
- [144] M. Castoldi and A. V. Popov, *Purification of brain tubulin through two cycles of polymerization–depolymerization in a high-molarity buffer*, *Protein Expr. Purif.* **32**, 83 (2003).
- [145] A. Hyman, D. Drechsel, D. Kellogg, S. Salser, K. Sawin, P. Steffen, L. Wordeman, and T. Mitchison, *Preparation of modified tubulins*, in *Methods in Enzymology, Molecular Motors and the Cytoskeleton*, Vol. 196 (Academic Press, 1991) pp. 478–485.
- [146] M. P. López, *In vitro studies of actin-microtubule coordination*, Dissertation, Vrije Universiteit, Amsterdam (2015).
- [147] A. Vijaykumar, P. G. Bolhuis, and P. R. t. Wolde, *The intrinsic rate constants in diffusion-influenced reactions*, *Faraday Discuss.* **195**, 421 (2017).
- [148] S. P. Maurer, N. I. Cade, G. Bohner, N. Gustafsson, E. Boutant, and T. Surrey, *EB1 Accelerates Two Conformational Transitions Important for Microtubule Maturation and Dynamics*, *Curr. Biol.* **24**, 372 (2014).
- [149] T. A. Reid, C. Coombes, S. Mukherjee, R. R. Goldblum, K. White, S. Parmar, M. McClellan, M. Zanic, N. Courtemanche, and M. K. Gardner, *Structural state recognition facilitates tip tracking of EB1 at growing microtubule ends*, *eLife* **8**, e48117 (2019).
- [150] N. B. Gudimchuk, E. V. Ulyanov, E. O'Toole, C. L. Page, D. S. Vinogradov, G. Morgan, G. Li, J. K. Moore, E. Szczesna, A. Roll-Mecak, F. I. Ataullakhanov, and J. Richard McIntosh, *Mechanisms of microtubule dynamics and force generation examined with computational modeling and electron cryotomography*, *Nat. Commun.* **11**, 3765 (2020).
- [151] D. Boyer, *Optimal estimates of the diffusion coefficient of a single Brownian trajectory*, *Phys. Rev. E* **85** (2012), 10.1103/PhysRevE.85.031136.
- [152] D. Boyer and D. S. Dean, *On the distribution of estimators of diffusion constants for Brownian motion*, *J. Phys. A-Math. Theor.* **44**, 335003 (2011).

- [153] A. W. Avery, M. E. Fealey, F. Wang, A. Orlova, A. R. Thompson, D. D. Thomas, T. S. Hays, and E. H. Egelman, *Structural basis for high-affinity actin binding revealed by a β -III-spectrin SCA5 missense mutation*, Nat. Commun. **8** (2017), 10.1038/s41467-017-01367-w.
- [154] Y. Wang, K. Ajtai, and T. P. Burghardt, *Ventricular Myosin Modifies In Vitro Step-Size When Phosphorylated*, J. Mol. Cell Cardiol. **72**, 231 (2014).
- [155] V. E. Galkin, A. Orlova, M. R. Vos, G. F. Schröder, and E. H. Egelman, *Near-Atomic Resolution for One State of F-Actin*, Structure **23**, 173 (2015).
- [156] S. Broersma, *Viscous Force Constant for a Closed Cylinder*, J. Chem. Phys. **32**, 1632 (1960), publisher: American Institute of Physics.
- [157] S. Broersma, *Viscous force and torque constants for a cylinder*, J. Chem. Phys. **74**, 6989 (1981).
- [158] G. Li, Q. Wen, and J. X. Tang, *Single filament electrophoresis of F-actin and filamentous virus fd*, J. Chem. Phys. **122**, 104708 (2005).
- [159] T. F. Chan, G. H. Golub, and R. J. LeVeque, *Updating Formulae and a Pairwise Algorithm for Computing Sample Variances*, in *COMPSTAT 1982 5th Symposium held at Toulouse 1982*, edited by H. Caussinus, P. Ettinger, and R. Tomassone (Physica-Verlag HD, 1982) pp. 30–41.
- [160] B. P. Welford, *Note on a Method for Calculating Corrected Sums of Squares and Products*, Technometrics **4**, 419 (1962).
- [161] J. P. Campanale, T. Y. Sun, and D. J. Montell, *Development and dynamics of cell polarity at a glance*, J. Cell Sci. **130**, 1201 (2017).
- [162] R. Li and G. G. Gundersen, *Beyond polymer polarity: how the cytoskeleton builds a polarized cell*, Nat. Rev. Mol. Cell Biol. **9**, 860 (2008).
- [163] L. J. Pillitteri, X. Guo, and J. Dong, *Asymmetric cell division in plants: mechanisms of symmetry breaking and cell fate determination*, Cell. Mol. Life Sci. **73**, 4213 (2016).
- [164] W.-J. Rappel and L. Edelstein-Keshet, *Mechanisms of Cell Polarization*, Curr. Opin. Syst. Biol. **3**, 43 (2017).
- [165] R. Raman, C. S. Pinto, and M. Sonawane, *Polarized Organization of the Cytoskeleton: Regulation by Cell Polarity Proteins*, J. Mol. Biol. Cell Polarity Regulation, **430**, 3565 (2018).
- [166] K. P. Harris and U. Tepass, *Cdc42 and Vesicle Trafficking in Polarized Cells*, Traffic **11**, 1272 (2010).
- [167] V. Varga, J. Helenius, K. Tanaka, A. A. Hyman, T. U. Tanaka, and J. Howard, *Yeast kinesin-8 depolymerizes microtubules in a length-dependent manner*, Nat. Cell Biol. **8**, 957 (2006).

- [168] V. Varga, C. Leduc, V. Bormuth, S. Diez, and J. Howard, *Kinesin-8 Motors Act Cooperatively to Mediate Length-Dependent Microtubule Depolymerization*, *Cell* **138**, 1174 (2009).
- [169] J. M. Mitchison and P. Nurse, *Growth in cell length in the fission yeast *Schizosaccharomyces pombe**, *J. Cell Sci.* **75**, 357 (1985).
- [170] S.-K. Guo, W.-C. Wang, P.-Y. Wang, and P. Xie, *Force Dependence of Velocity and Run Length of Kinesin-1, Kinesin-2 and Kinesin-5 Family Molecular Motors*, *Molecules* **24**, 287 (2019).
- [171] Y. Okada and N. Hirokawa, *A Processive Single-Headed Motor: Kinesin Superfamily Protein KIF1A*, *Science* **283**, 1152 (1999).
- [172] V. Bormuth, V. Varga, J. Howard, and E. Schäffer, *Breaking of bonds between a kinesin motor and microtubules causes protein friction*, in *Optical Trapping and Optical Micromanipulation VII*, Vol. 7762 (International Society for Optics and Photonics, 2010) p. 776208.
- [173] K. Weiß, A. Neef, Q. Van, S. Kramer, I. Gregor, and J. Enderlein, *Quantifying the diffusion of membrane proteins and peptides in black lipid membranes with 2-focus fluorescence correlation spectroscopy*, *Biophys. J.* **105**, 455 (2013).
- [174] T. Fujiwara, K. Ritchie, H. Murakoshi, K. Jacobson, and A. Kusumi, *Phospholipids undergo hop diffusion in compartmentalized cell membrane*, *J. Cell Biol.* **157**, 1071 (2002).
- [175] T. Kühn, T. O. Ihalainen, J. Hyväluoma, N. Dross, S. F. Willman, J. Langowski, M. Vihinen-Ranta, and J. Timonen, *Protein Diffusion in Mammalian Cell Cytoplasm*, *PLOS ONE* **6** (2011), 10.1371/journal.pone.0022962.
- [176] S.-K. Guo, X.-X. Shi, P.-Y. Wang, and P. Xie, *Force dependence of unbinding rate of kinesin motor during its processive movement on microtubule*, *Biophys. Chem.* **253**, 106216 (2019).
- [177] J. L. Johnson, J. W. Erickson, and R. A. Cerione, *New Insights into How the Rho Guanine Nucleotide Dissociation Inhibitor Regulates the Interaction of Cdc42 with Membranes*, *J. Biol. Chem.* **284**, 23860 (2009).
- [178] D. D. Hackney, *Implications of diffusion-controlled limit for processivity of dimeric kinesin head domains*, *Biophys. J.* **68**, 267S (1995).
- [179] Q. H. Tran and G. Udden, *Changes in the proton potential and the cellular energetics of *Escherichia coli* during growth by aerobic and anaerobic respiration or by fermentation*, *Eur. J. Biochem.* **251**, 538 (1998).
- [180] M. Lynch and G. K. Marinov, *The bioenergetic costs of a gene*, *Proc. Natl. Acad. Sci. U.S.A.* **112**, 15690 (2015).

- [181] P.-J. Lahtvee, B. J. Sánchez, A. Smialowska, S. Kasvandik, I. E. Elsemman, F. Gatto, and J. Nielsen, *Absolute Quantification of Protein and mRNA Abundances Demonstrate Variability in Gene-Specific Translation Efficiency in Yeast*, *Cell Syst.* **4**, 495 (2017).
- [182] C. Leduc, K. Padberg-Gehle, V. Varga, D. Helbing, S. Diez, and J. Howard, *Molecular crowding creates traffic jams of kinesin motors on microtubules*, *Proc. Natl. Acad. Sci. U.S.A.* **109**, 6100 (2012).
- [183] M. Rank and E. Frey, *Crowding and Pausing Strongly Affect Dynamics of Kinesin-1 Motors along Microtubules*, *Biophys. J.* **115**, 1068 (2018).

SUMMARY

In chapter 1, we summarise some of the key concepts from thermodynamics and statistical physics that are used in this thesis. Starting from the Boltzmann distribution, we describe the local detailed balance relation that is used to connect free-energy differences to the dynamics of discrete Markovian systems, even when the systems are not in equilibrium. This description is then extended to continuous Markovian systems, by viewing the continuous system as a limiting case of having many small discrete states that are connected smoothly. These continuous systems are described by Fokker-Planck equations, and the local detailed balance relation is transformed into the Einstein relation which connects the dynamics of the system to the forces acting on it. Finally, we focus on the opposite direction where a continuous system shows discrete behaviour. This occurs when the continuous dynamics leads to a discrete number of attractor regions that are separated by free-energy barriers. To find the Markovian dynamics in this reduced discrete system, we apply Kramers theory, which attempts to find transition rates from the underlying diffusive dynamics and the free-energy profile.

Then, we apply these techniques to a biologically motivated problem in chapter 2. Here, we investigate a model system that was previously successful in explaining the entropic force generation when two microtubules are connected by diffusible cross-linking proteins called Ase1. It was observed in simulations and in experiments that the friction between the microtubules scales exponentially with the number of cross-linkers, but an explanation of this phenomenon remained lacking. We show that the nonlinear scaling of the friction coefficient is caused by having a lattice of binding sites on the microtubules, together with the relatively high stiffness of the cross-linkers with respect to the lattice constant. These properties lead to a lattice of optimal positions for the microtubules that are 8 nm apart, with free-energy barriers separating these basins of attraction. The friction between the microtubules is caused by the height of the free-energy barriers, and we show that these barriers grow linearly with the number of cross-linkers. Furthermore, we observe that when the density of cross-linkers becomes higher, the height of the barrier scales even faster with the number of cross-linkers. This super-exponential increase of the friction can have implications in the non-equilibrium networks of microtubules that occur in the mitotic spindle, since motor proteins can drive microtubule overlaps to decrease, thereby increasing the densities of cross-linkers. Furthermore, the model can also be applied to other cytoskeletal systems such as the actin cytokinetic ring.

While the previous chapter predicts how the the friction coefficient scales, chapter 3 looks at the absolute value of this friction coefficient. Since the friction coefficient follows directly from the rate at which the microtubule jumps in equilibrium, we apply Kramers theory to estimate the prefactor of this jump rate. First, we estimate the effective diffusion constant at the peak of the barrier, and confirm the expression using simulations. Even though the free-energy profile and the reaction coordinate are well

established, and the diffusion constant is also predicted relatively well, Kramers theory does not predict the prefactor over the full range of cross-linker numbers and overlap lengths. The predicted prefactor works well for low densities, and does generally give the right order of magnitude as compared to the simulation results, but it predicts the prefactor to scale exponentially with the density of cross-linkers while the simulations actually show a decreasing prefactor. By examining all assumptions of Kramers theory one at a time, we reach the conclusion that the errors of Kramers theory are caused by the breakdown of the validity of the Fokker-Planck equation during the small time scales in which barrier crossings occur.

Chapter 4 uses the friction model established in the previous chapters to investigate how two partially overlapping microtubules move when subject to either entropic or condensation forces. It was previously established that when the cross-linkers cannot bind or unbind, such that their number remains constant, the overlap length grows due to the increase of entropy when diffusing cross-linkers can explore a larger overlap. From the expressions of the entropic force and the friction coefficient, we predict the overlap length to grow with the square root of time, which is also observed in simulations. When binding and unbinding are allowed, the overlap also expands due to the condensation force that is driven by the binding affinity of the cross-linkers for the overlap between the microtubules. Here, we expect the overlap to scale logarithmically in time, but simulations show that the overlap expansion can be fast initially and then stall much more rapidly. We show that this behaviour is explained by the slow (un)binding rates of the cross-linkers, which fail to equilibrate within the small overlap when it is moving fast. Then, we also discuss the effects that cooperative binding and multiple protofilaments have on the balance of forces.

In chapter 5, we look at another system in which condensation and friction forces interact in a new way. Using an engineered cross-linking protein called TipAct, which has affinity for microtubule tip regions and for actin filaments, *in vitro* experiments show that growing microtubules can transport actin filaments. The binding of the cross-linking TipAct proteins simultaneously causes a condensation force and a counteracting friction force. We show that in this case, because of a low effective spring constant, the friction between the two filaments scales linearly with the number of cross-linkers. In experiments, the transport events end in one of three ways: the actin filament can unbind from the tip of the microtubule, the microtubule can have a catastrophe event, or the actin filament can fall behind the tip region and diffuse on the microtubule lattice due to a low affinity of TipAct for the microtubule lattice. We create a theoretical description for these three events, where the unbinding rate decreases exponentially with the overlap length, the catastrophes occur at a fixed rate, and the actin falling behind the microtubule tip region is a barrier crossing event which occurs more often for longer actin filaments and for faster growing microtubules. Using Kramers theory to estimate the time until the barrier crossings, we can compare our theoretical predictions directly to experiments, confirming that our proposed mechanism can quantitatively explain the transport of actin filaments by growing microtubules.

Finally, we study a different cytoskeletal system where thermodynamics plays a strong role in chapter 6. Cell polarisation is a necessary condition for the correct biological functioning and reproduction of many cells, and it remains an interesting question how

cell polarisation can be established. One mechanism by which a protein concentration can be polarised makes use of cytoskeletal filaments, which are intrinsically polarised filaments and can be used as tracks for motor proteins to transport other proteins to their plus ends. Assuming that the cell manages to polarise the distribution of cytoskeletal filaments to point them towards a point on the cell membrane where a specific protein needs to be concentrated, we ask whether the transport of the proteins is enough to create a polarising spot. Using a minimal model of a single microtubule in a cylinder with a membrane on one side, we use Fokker-Planck equations to describe the polarisation of a protein concentration on the cell membrane. We show that polarisation is possible, but has very significant energetic costs when it is only driven by motor proteins. However, when the proteins themselves undergo a chemical modification that biases their binding to the microtubule or their unbinding from the membrane, polarisation is enhanced at a much lower energetic cost. The change in dissipation of chemical free energy between transport and non-equilibrium binding may be sufficient to lead to selection pressures in some organisms, for example providing insight in the design mechanisms of the Pom1/Tea1/Tea4 system in fission yeast or the Cdc42 system in budding yeast.

SAMENVATTING

In hoofdstuk 1 vatten we enkele belangrijke concepten uit de thermodynamica en statistische fysica samen die in dit proefschrift worden gebruikt. Na een afleiding te hebben gegeven van de Boltzmann-verdeling beschrijven we de lokale evenwichtsconditie. Deze conditie definieert vrije-energieverschillen in Markovprocessen in een discrete ruimte, zelfs wanneer deze Markovketens niet in evenwicht zijn. Daarna breiden we de toepasbaarheid van deze beschrijving uit naar Markovprocessen in een continue ruimte door deze ruimte te zien als de limiet van discrete punten die op een gladde manier verbonden zijn. Deze continue Markovprocessen worden beschreven met een Fokker-Planck vergelijking, en de continue limiet transformeert de lokale evenwichtsconditie voor discrete systemen tot de zogenaamde Einstein relatie die de dynamica van het systeem verbindt met de krachten die erop uitgeoefend worden. Als laatste beschouwen we een limiet in de andere richting, waarin een continu systeem zich gedraagt als een verzameling van discrete punten. Dit komt voor wanneer de continue dynamica zich over eindige tijden beperkt binnen enkele attractorposities die gescheiden worden door vrije-energiebarrières. Om de Markovdynamica te vinden in dit gereduceerde discrete systeem passen we de Kramers theorie toe, welke de transitiesnelheden probeert te vinden vanuit de onderliggende diffusieve dynamica en het vrije-energieprofiel.

Daarna passen we deze technieken toe op een biologisch gemotiveerd probleem in hoofdstuk 2. Hier onderzoeken we een modelsysteem dat eerder succesvol was in het beschrijven van de generatie van entropische krachten wanneer twee microtubuli verbonden zijn via de diffusieve crosslinkers Ase1. Zowel experimenten als simulaties lieten zien dat de wrijving tussen de microtubuli exponentieel schaalt met het aantal crosslinkers, maar er bestond geen verklaring voor dit fenomeen. We laten zien dat de niet-lineaire schaling van de wrijvingscoëfficiënt veroorzaakt wordt door de combinatie van een rooster van bindingsplaatsen op de microtubuli en de relatief hoge veerconstante van de crosslinkers op de schaal van de roosterconstante. Deze eigenschappen leiden tot een rooster van optimale posities voor de microtubuli die 8 nm van elkaar verwijderd zijn, en deze attractorposities worden gescheiden door vrije-energiebarrières. De wrijving tussen de microtubuli wordt veroorzaakt door de hoogte van deze vrije-energiebarrières, en we laten zien dat de barrières lineair hoger worden wanneer het aantal crosslinkers toeneemt. Daarnaast zien we dat de hoogte van de barrière nog sneller schaalt wanneer de dichtheid van crosslinkers hoger wordt. Deze superexponentiële toename van de wrijving kan implicaties hebben in de niet-evenwichtsnetwerken van microtubuli die in de spoelfiguur voorkomen, omdat motoreiwitten de overlap tussen microtubuli daar laten krimpen en zo de dichtheid van de crosslinkers laten toenemen. Verder kan ons model ook worden toegepast op andere structuren in het cytoskelet, zoals de actine-ring die wordt gevormd tijdens cytokinese.

Terwijl het vorige hoofdstuk voorspelt hoe de wrijvingscoëfficiënt schaalt, kijkt hoofdstuk 3 naar de absolute waarde van deze wrijvingscoëfficiënt. Omdat de wrijvingsco-

efficiënt direct kan worden berekend vanuit de frequentie waarmee een microtubulus rondspringt wanneer deze in thermisch evenwicht is, kunnen we Kramers theorie gebruiken om de voorfactor van deze frequentie te berekenen. Eerst schatten we de diffusieconstante op de piek van de barrière af en bevestigen we de functionele afhankelijkheid van deze diffusieconstante met behulp van computersimulaties. Terwijl het vrije-energieprofiel en de reactiecoördinaat vastliggen en ook de effectieve diffusieconstante bij benadering goed wordt beschreven, komt de voorspelling door Kramers theorie niet overeen met de gevonden sprongfrequenties over het hele domein van crosslinkeraantallen en overlaplengtes. Voor lage dichtheden van crosslinkers komt de voorfactor van de sprongfrequentie goed overeen met de voorspelde absolute waarde, maar voor hoge crosslinkerdichtheden groeit de voorspelde voorfactor exponentieel terwijl de simulaties een lichte daling laten zien. Door achtereenvolgens alle aannames in Kramers theorie te doorlopen en uit te sluiten concluderen we dat de fouten in de voorspelde waardes worden veroorzaakt door het falen van de toepasbaarheid van de Fokker-Planck vergelijking op de kleine tijdschalen waarbinnen de barrièretransities plaatsvinden.

In hoofdstuk 4 gebruiken we het wrijvingsmodel dat we in de voorgaande hoofdstukken hebben bestudeerd om te onderzoeken hoe twee deels overlappende microtubuli ten opzichte van elkaar bewegen wanneer ze onderhevig zijn aan entropische- of condensatiekrachten. Eerder onderzoek stelde vast dat wanneer de crosslinkers niet kunnen binden of ontbinden, zodat het aantal crosslinkers vastligt, de overlaplengte tussen de microtubuli uitdijt door een toename van de entropie van de crosslinkers die een grotere overlap kunnen verkennen. Met behulp van de uitdrukkingen voor de entropische kracht en de wrijvingscoëfficiënt voorspellen we dat de overlaplengte groeit met de vierkantswortel van de tijd, wat wordt bevestigd in simulaties. Wanneer het binden en ontbinden van crosslinkers is toegestaan dijt de overlap uit onder invloed van een condensatiekracht die voortkomt uit de bindingsaffiniteit van de crosslinkers voor de overlap tussen de microtubuli. Hier verwachten we dat de overlap logaritmisch groeit met de tijd, maar simulaties laten zien dat de overlaplengte soms initieel snel uitdijt en dan abrupt stil komt te staan. We laten zien dat dit wordt veroorzaakt door de lage (ont)bindingssnelheden van de crosslinkers, die de snelle expansie van de korte overlappen niet bij kunnen benen en daardoor niet in evenwicht komen. Ten slotte bespreken we ook de effecten die coöperatieve interacties en meerdere protofilamenten hebben op de krachtenbalans tussen microtubuli.

In hoofdstuk 5 beschouwen we een ander systeem waarin condensatiekrachten en wrijvingskrachten op een nieuwe manier wisselwerken. Gebruikmakend van het artificiële crosslinkeiwit TipAct dat een affiniteit heeft voor zowel het uiteinde van microtubuli als voor actinefilamenten, laten in vitro experimenten zien dat groeiende microtubuli actinefilamenten kunnen transporteren. De binding van de crosslinkende TipAct-eiwitten creëert tegelijkertijd een condensatiekracht en een tegenwerkende wrijvingskracht op de actinefilamenten. We laten zien dat, beïnvloed door de lage veerconstante van de crosslinkers, de wrijvingsconstante tussen de filamenten lineair schaalt met het aantal crosslinkers. Experimenten tonen dat het transport van de actinefilamenten op drie manieren eindigt: de filamenten ontbinden van het uiteinde van de microtubulus, de microtubulus ondergaat een catastrofe, of het actinefilament raakt achter op het groeiende uiteinde van de microtubulus en diffundeert langs het rooster van de microtubulus

door de lage bindingsaffiniteit van het actinefilament voor dit rooster. In dit hoofdstuk vormen we een theoretische beschrijving voor elk van deze drie processen, waarin de ontbindingssnelheid exponentieel afneemt met de overlaplengte, de catastrofes met een vaste frequentie plaatsvinden, en het achterblijven van de actinefilamenten wordt beschreven als een oversteken van een vrije-energiebarrière, wat vaker voorkomt voor langere actinefilamenten en voor sneller groeiende microtubuli. Met Kramers theorie kunnen we de gemiddelde tijd berekenen tot de volgende sprong over de barrière, en we vergelijken onze voorspellingen direct met de experimenten. Deze vergelijking bevestigt dat het door ons voorgestelde mechanisme het transport van actinefilamenten door groeiende microtubuli goed beschrijft.

Tot slot beschouwen we in hoofdstuk 6 een ander systeem waarin zowel het cytoskelet als thermodynamica een sterke rol spelen. Celpolarisatie is een voorwaarde voor de biologische functie en reproductie van veel cellen, en het blijft een interessante vraag hoe celpolarisatie kan worden bewerkstelligd. Eén mechanisme waarmee een eiwitconcentratie kan worden gepolariseerd is via filamenten uit het cytoskelet, welke intrinsiek gepolariseerd zijn en als spoor kunnen worden gebruikt voor moleculaire motoren om andere eiwitten te transporteren. Ervan uitgaande dat een cel zijn cytoskelet weet te organiseren zodat de individuele filamenten naar de plek op het celmembraan georiënteerd staan waar membraaneiwitten geconcentreerd moeten worden, stellen we de vraag of actief transport van de eiwitten langs een filament voldoende zijn om een gepolariseerde distributie van membraaneiwitten te veroorzaken. Met een minimaal model van een enkel filament in het centrum van een cilinder met het membraan op de zijkant gebruiken we een Fokker-Planck vergelijking om de polarisatie van een eiwitconcentratie op het celmembraan te beschrijven. We laten zien dat polarisatie mogelijk is, maar dat het energetisch kostbaar is wanneer deze alleen door transport langs het filament wordt gedreven. Echter, wanneer de membraaneiwitten ook zelf een chemische modificatiecyclus ondergaan die het binden naar het filament of het ontbinden van het membraan bevordert kan celpolarisatie worden verwezenlijkt met een veel lager energetische budget. Het verschil in de dissipatie van chemische vrije energie tussen het transport en het niet-evenwichtsbinden van eiwitten kan voldoende zijn om tot een selectiedruk te komen in bepaalde organismen, wat bijvoorbeeld inzicht geeft in de ontwerpprincipes van het Pom1/Tea1/Tea4 systeem in slijtingsgist of het Cdc42 systeem in biergist.

CURRICULUM VITÆ

Harmen WIERENGA

06-02-1992 Born in Zutphen, Netherlands.

EDUCATION

2004–2010 Gymnasium
Baudartius College, Zutphen

2010–2013 Bachelor's Physics and Astronomy
Universiteit Utrecht

2013–2016 Master's Theoretical Physics
Universiteit van Amsterdam
Erasmus exchange Universität Bonn (2014–2015)

2016–2021 PhD student
Based at AMOLF, Amsterdam
Employed by TU Delft

LIST OF PUBLICATIONS

Appearing in this thesis:

Harmen Wierenga and Pieter Rein ten Wolde, *Diffusible Cross-linkers Cause Superexponential Friction Forces*, Physical Review Letters **125**, 078101 (2020).

Celine Alkemade*, **Harmen Wierenga***, Vladimir A. Volkov, Magdalena Preciado-López, Anna Akhmanova, Pieter Rein ten Wolde, Marileen Dogterom, and Gijsje H. Koenderink, *Passive cross-linkers drive actin transport by growing microtubules*, in preparation (*shared first author).

Harmen Wierenga and Pieter Rein ten Wolde, *Energetic constraints on filament mediated membrane polarisation*, in preparation.

Other publications:

Harmen Wierenga, Pieter Rein ten Wolde, and Nils B. Becker, *Quantifying fluctuations in reversible enzymatic cycles and clocks*, Physical Review E **97**, 042404 (2018).

Yuval Mulla, **Harmen Wierenga**, Celine Alkemade, Pieter Rein ten Wolde, and Gijsje H. Koenderink, *Frustrated binding of biopolymer crosslinkers*, Soft Matter **15**, 3036–3042 (2019).

ACKNOWLEDGEMENTS

As I sit down behind the table at home to write the last section of this thesis, I try to think back of all the different people and events that have occurred since the day I started to work as a Master's student at AMOLF nearly six years ago. This table has been the place where I eat, work, write, watch series, have virtual tea breaks, and break my head over equations for a year since the first lockdown started. Still, the time at my desk at AMOLF has left a far greater impression on me.

First I would like to thank Pieter Rein for motivating me to get through the parts of my PhD where I struggled, especially with the writing of papers. I also thank you for providing me with both autonomy and guidance when I needed it, and for the infinite supply of energy that you brought to every meeting. Your drive does not seem to adhere to the constraints set by thermodynamics.

Marileen, thank you for allowing me to stick around at AMOLF for so many years, and for creating an environment in which even the most stubborn theoretician can become grounded in the real world.

Then my paranymphs, Lucia and Mareike, thank you for supporting me as I finish my PhD, and for enduring me whenever I bombarded you with random facts, news stories, or observations while you were trying to get some work done. Lucia, I am very happy that when I asked Clyde to put another PhD student in my office, you came through the door. I always enjoy your sense of humour, your passion for science, and your kindness, and I will never forget the horrendous photoshops, the nice tea breaks, and your amazing birthday cakes. It was sad when I learned that you were going to leave AMOLF and the office, but luckily you did not move far and I could still run into you in Delft. I am sure that you will make a great professor one day. Mareike, to you I will hand over the baton of being the oldest PhD student in the group. I was very happy when you joined the group, seeing your positivity and your great work ethic. Luckily you were willing to let me into the office, and our summer as the 'Delta Daltons' was a great one. Also your social skills are legendary, I remember the party you threw just after you arrived in Amsterdam from Munich, and already you knew more people there than I did. The group is very lucky to have you!

Next I would like to thank Bela, the little boss, for always picking me up for tea or lunch, for the nice discussions, and for your sharp remarks and knowledge of mathematics and programming. I will always associate AMOLF with your smile, and you are the living proof that a successful professor can also be approachable and fun to be around.

Ramon, your presence always increases the intellectual level of any conversation. And I will think back to your bachelor party sometimes and smile. Johannes, thank you for letting me be one of your paranymphs, and for all the stimulating discussions. Joris, Giulia, Michele, Adithya, Yao, thank you for making the group a welcoming and great place to work in. I will remember Sinterklaas at Pieter Rein's.

Marco and Celine, I was happy to share my PhD experience with you. Celine, I am proud of the paper that we are writing together, and I have fond memories of the parties at the Veldhoven conference or the Microtubule Meeting. Marco, the trip to Buenos Aires was one that will leave an impression, and it was great to share this experience with you.

I shared the office with countless people, whom I will now try to count: Rasa, Felicio, Rayan, Nadia, Zubayda, Lisa, Simon, Gerard, Tom van der Mijn, and Alex, you were great. Lisa, Xavi, and Happatat (Matthijs), I cannot see a duck without thinking of that summer. And Xavi, everybody hurts, sometimes. Faan, I remember the 'borrel' on the day that you joined AMOLF where before you knew it you were playing beerpong with your supervisor. Alex, you are a great addition to the group and I am only slightly worried that the combination of your books and your power tower will turn you into a superhuman being. To the new group members, Manuel and Age, I wish you all the best in your PhDs, and I hope that you will enjoy it as much as I did. And the Pythagoras lunch group, I will think back of the many conversations about politics, history, and science we had.

To Yuval, Keita, Mathijs, Federica, Melle, Steffen, Verena, Martijn, Lotte, Jeroen Goedhart, Christian, Joleen, Tom Clement, Fotios, Floortje, and all those others at AMOLF with whom I have shared lunches, tea breaks, conversations, meetings, sports days with drinks, open days with know-it-all children, and Christmas lunches with steaming silent discos, thank you for making AMOLF an amazing place to work. A special thanks goes to Michiel and Gerben, who have brought the Linux support at AMOLF to a higher level, and who have helped me with every problem I could throw at them.

To the members of the Dogterom Lab in Delft, Kim, Renu, Vladimir, Maurits, Eli, Esengül, thank you for letting me break into your group meetings, for asking me the right questions, and for the nice time we had in Brussels and Heidelberg.

Then my friends in Utrecht, Roel, Robert, Lucas, Oskar, Sjoerd, Eric, en Michiel, thank you for all the Tuesday evening dinners, and the parties, concerts, and festivals. Your friendship gave me the energy to get this thesis done.

Joris, Mehran, Djoeke, Manon, Onno, it was great to talk to you about our PhD experiences, and to meet with you in Amsterdam, Utrecht, Delft, or Munich. And Joris, after sharing the last eleven years at the UU, the UvA and the Science Park, I will gladly take a detour to visit you in Konstanz!

To my parents, Bert and Heidi, and to Lex and Eline, you have always supported me, and I would not have gotten to this point without you. I will cherish our trips to Callantsoog and the weekends in Hengelo.

Lydia et Lily, les vacances chez vous étaient très bonnes pour me reposer, merci !

Audrey, you have been my greatest support during these years. The trips I made with you were always special, and I am grateful for having you in my life.

